Instability of non-uniform viscoelastic liquid jets

by

Abdullah Madhi Alsharif

A thesis submitted to
The University of Birmingham
for the degree of
Doctor of Philosophy

School of Mathematics
The University of Birmingham
October 2014

Abstract

The industrial prilling process is a common technique to produce small pellets which are generated from the break-up of rotating liquid jets. In many cases the fluids used are molten liquid and/or contain small quantities of polymers and thus typically can be modelled as non-Newtonian liquids. Industrial scale set-ups are costly to run and thus mathematical modelling provides an opportunity to assess methods to improve efficiency and introduce greater levels of precision. In order to understand this process, we consider a mathematical model to capture the essential physics related to a cylindrical drum which is rotated about its axis and from which a slender liquid jet emerges from a hole placed on the side of the drum. Furthermore, surfactants my be used in such process to manipulate the size of the resulting droplets. In this thesis, we model the viscoelastic nature of the fluid using the Oldroyd-B model. An asymptotic approach is used to simplify the governing equations and then we consider a linear temporal stability analysis of the resulting set of equations.

The effect of gravity on viscoelastic liquid jets has been discussed both with rotation and without rotation. The trajectory of this problem has been plotted in three dimensions. Our results show the effect of many non-dimensional parameters on the linear instability of a viscoelastic curved liquid with gravity and without gravity.

Acknowledgements

In the beginning, I would like to take this opportunity to deeply thank my supervisors Prof. Stephen Decent and Dr. Jamal Uddin for guiding me towards this topic and for their support, patience and guidance in completing this thesis. I have received lots of support from them.

I would also like to thank my parents; without their prayers and best wishes this work would be impossible to finish. I would also like to thank my wife and my children for being more patient and giving me moral support during this time of my life. Further thanks to all my family for encouraging me throughout the course of my Ph.D.

I would also like to thank Faheem Afzaal for his support and the collaboration during this course.

I would also like to thank the Government of Saudi Arabia for the financial support which allowed this work to become a reality.

Contents

List of Figures

Chapter 1

Introduction

Liquid jets have attracted the attention of many researchers in a wide range of disciplines from nuclear fission to DNA sampling. Scientists and researchers have investigated phenomena associated with liquid jets, including the process of break-up, drop formation and rupture, because of their relevance to many different industrial applications, such as fertilizer and ink jet printing. A deep understanding of the mechanisms of break-up of liquid jets and the associated flow dynamics is heavily dependent on the nature or constitution of the fluid and for this some knowledge of different fluids used in industry are required. Knowledge associated with complex fluid flows also has relevance in determining the actual process or techniques used to generate droplets. In all such cases, whilst experiments provide data and quantitative relationships between fluid properties and for example droplet sizes, analytical techniques can almost always be used to better understand these processes.

First of all, this thesis will start by giving a general explanation of liquid jets and it will give some applications for the occurrence of this phenomenon, both in everyday life, such as domestically, in kitchens and showers, or in industry with ink-jet printing problems. Then the literature for studies in inviscid jets will be examined which includes studies by Savart (1833) and Rayleigh (1878). After that, an analysis of viscous jets will

be given which was initiated by Weber (1836). Recent studies were conducted which were investigated by Wallwork (2002a) and Uddin (2007) for liquid curved jets and many others, as can be seen in section (2.1). In section (2.2), we will also look at the background of viscoelastic jets which is the subject of this thesis. We also present in this chapter break-up regimes and nonlinear dynamics.

In Chapter 3, the prilling process is introduced and some details are given about the theoretical and experimental work carried out more recently at the University of Birmingham.

To give a better understanding about viscoelastic fluids, we start Chapter 4 by giving the meaning of the term of viscoelastic and some examples of this phenomenon. It will be seen in this chapter that there are many models which can be used for non-Newtonian fluids. These constitutive models provide a mathematical description of the how the stress in a non-Newtonian fluid relates to the strain can affect on the behaviour of these fluids. In this thesis, we have used the simplest model to investigate the instability of viscoelastic liquid jets, which is Maxwell-Upper convected model, known as Oldroyd-B.

In Chapter 5, we examine the temporal instability of straight viscoelastic liquid jets falling under the influence of gravity. An asymptotic analysis is used to obtain the steady state solutions, and then we derive the dispersion relation.

Chapter 6 gives more details about the prilling process in terms of mathematical formulation of non-Newtonian liquids for studying the linear instability of this problem. Most of the studies are related to Newtonian fluids. However, non-Newtonian fluids need more examination, because many industrial liquids, even those which are involved in the production of fertilizers, are non-Newtonian. In the University of Birmingham, there are many researchers who have studied the prilling process in Newtonian fluids and have developed a procedure to examine non-Newtonian fluids. Therefore, in this thesis, we will

utilize an alternative non-Newtonian model to study non-Newtonian fluids, especially viscoelastic liquid jets in the spiralling process. An asymptotic analysis is used to derive the equations of motion and boundary conditions at leading order. We also examined the temporal instability to obtain the dispersion relation for viscoelastic liquid curved jets. We present some results at the end of this chapter.

In Chapter 7, we investigate nonlinear instability of viscoelastic curved jets by using a finite difference scheme which is based on the two-step Lax-Wendroff method. We therefore discuss break-up lengths, the break-up time, main and satellite droplet sizes.

In Chapter 8, we extend Chapter 6 by considering the liquid emerging from the orifice and falling under gravity. We present the trajectory of the centerline of liquid jets in three dimensions. Moreover, we study the linear analysis as we did in that chapter.

In Chapter 9, we study linear and nonlinear instability of viscoelastic liquid curved jets by including surfactants. In this chapter, we can see that surfactants decrease the surface tension which means that growth rates, break-up lengths and droplets formation changes by changing the initial surfactant concentration. In Chapter 10, we give some conclusions and future work which we can study.

1.1 Articles extracting from this thesis

• Alsharif, A., M., Uddin, J. and Afzaal, M. F. Instability of Viscoelastic Liquid Curved Jets, submitted to Journal of Applied Mathematical Modelling, December 2013 (Chapter 6 and 7).

• Alsharif, A., M. & Uddin, J. 2013, The Influence of Gravity on The Temporal Instability of Viscoelastic Liquid Curved Jet, World Academy of Science, Engineering and Technology, 79, 1742-1748 (Chapter 8).

• Alsharif, A., M. & Uddin, J. Instability of Viscoelastic Liquid Curved Jets with Surfactants, submitted to the Journal of Non-Newtonian Fluid Mechanics, April 2014 (Chapter 9).

Chapter 2

Literature Review

2.1 Introduction

A jet is a stream of liquid which emerges from a nozzle and has a column shape. In this thesis, we will focus on the break-up of liquid jets, which has applications in many areas. For example, we can see the liquid jet in kitchens, when water emerges from a tap, in agriculture when a farmer irrigates his field, in powder technology, and in ink-jet printing.

Liquid jet dynamics is also relevant to fields which deal with small-scale phenomena, even on the nanometer scale, such as DNA sampling, and can have pharmaceutical applications. For example, pharmaceutical companies use the freeze-drying process to produce tablets. In all such cases the classical approach to studying the theory of the instability of liquid jets has been investigated by Rayleigh (1878) for inviscid liquid jets.
In order to understand these phenomena, it is important to study the break-up of liquid jets theoretically and verify it experimentally. It is also necessary to investigate drop sizes in order to reduce liquid quantity costs.

2.2 Inviscid and Viscous Jets

The earliest experimental work on the break-up of a liquid jet was conducted by Savart (1833) who observed that the break-up of a liquid jet depends on a feature intrinsic of the fluid motion. He also noticed that there is a small drop (satellite) between main drops. Another experiment was conducted by Plateau (1873) who found that the crucial role of the jet break-up is the surface tension, which can be considered as the energy per unit area of interface . Lord Rayleigh (1878) carried out the first theoretical treatment for the instability of an incompressible inviscid liquid jet and found that the driving force for the jet break-up is the surface tension. He investigated the effect of the capillary force on a cylindrical jet which has radius $r = a$ and studied the traveling wave modes of the form $exp(\omega t - i(kz - n\theta))$, where ω is the growth rate, k is the wavenumber, θ is the azimuthal coordinate and t is the time. Rayleigh found that when a perturbation to inviscid liquid jets is made, the dispersion relation, which describes the relationship between ω and k, takes the form

$$\omega^2 = \frac{\gamma(ka)}{\rho a^3}(1 - n^2 - (ka)^2)\,\frac{I_n^{'}(ka)}{I_n(ka)}, \tag{2.1}$$

where γ is the surface tension and I_n is the modified Bessel function of order n. The disturbances are axisymmetric for $n = 0$ so that the previous equation becomes

$$\omega^2 = \frac{\gamma(ka)}{\rho a^3}(1 - (ka)^2)\,\frac{I_1(ka)}{I_0(ka)}. \tag{2.2}$$

For $ka > 1$, the jet is stable which means the disturbances will not grow. Rayleigh found that the maximum growth occurs at $ka = 0.697$ with a corresponding wavelength $\omega \approx 2\pi R/0.697 \approx 9R$. When $n \neq 0$ this means the growth rate (ω) is imaginary and does not grow with time.

There are many references which go into detail about the instability of liquid jets and the reader is referred to Eggers (1997), Middleman (1995) and Lin (2003). The viscosity of the jet was considered in the case of a cylinder of incompressible liquid by Weber (1936) who found that the wavelength of most unstable waves is increased by the viscosity. Weber (1936) followed the same analysis as for the inviscid liquid jet (for $n = 0$) to obtain the dispersion relation which is

$$\omega^2 + \omega \frac{2\,\mu\,k^2}{I_0(kR)}\Big[I_1^{'}(kR) - \frac{k\tilde{k}I_1(kR)I_1^{'}(\tilde{k}R)}{(k^2+\tilde{k}^2 I_1(\tilde{k}R)}\Big] = \frac{\sigma R}{\rho\mu^2}\,\frac{kR(k^2-\tilde{k}^2)I_1(kR)}{(k^2+\tilde{k}^2)I_0(kR)}\,(1-k^2R^2), \quad (2.3)$$

where $\tilde{k}^2 = k^2 + \frac{\omega}{\mu}$.

This quadratic equation has a positive solution at the maximum wavenumber which is $ka = \frac{1}{\sqrt{2(1+3\,Oh)}}$, where $Oh = \frac{\mu}{\sqrt{\rho\sigma a}}$ is the Ohnesorge number. This result shows the effect of viscosity, which is μ, on the system. When $\mu = 0$ we obtain the dispersion relation for inviscid liquid jets, which takes the form $ka = \frac{1}{\sqrt{2}} \approx 0.707$. This result differs from the inviscid case.

Tomotika (1935) investigated the linear instability of a cylindrical thread of a viscous liquid jet into another viscous liquid. He found that the linear instability depends upon the viscosity and density ratios of two fluids. He also discussed the effect of surface tension on both viscous liquid jets.

A more rigorous asymptotic approach has been applied by Papageorgiou (1995) to the system governing the dynamics of a liquid jet to search for a nonlinear solution. He also found that there are good agreements between theoretical and asymptotic solutions. In addition to this, he investigated the break-up behaviour for viscous liquid threads for different initial conditions.

Typically, for instability in liquid threads or jets two types of instabilities are presented; firstly, temporal instability, which is the cases considered above in Rayleigh's analysis

where k is real and the growth rate is complex; and secondly, spatial instability. This was discussed by Keller, Rubino & Tu (1973). They suggested that waves might grow in space and thus investigated disturbances with complex k and times realized that spatially growing waves do exist. Their studies were on a cylindrical liquid jet which emerged from a nozzle, and followed Rayleigh's analysis.

Newtonian jet stability was examined by Grant & Middleman (1965) in terms of predicting the stability in turbulent and laminar jets which emerged from a nozzle. They have also modified Weber's theory to study the break-up of laminar liquid jets. The nonlinear temporal instability of capillary liquid jets was investigated by Ashgriz & Mashayek (1995) and it was found that when the Reynolds number is very small, the satellite drops are not observed, and the satellite drops can be seen when the Reynolds number is high.

Wallwork (2002a) used a mathematical model to investigate the prilling process, because this process has many industrial applications, such as producing urea pellets fertilizer. The work of Wallwork *et al.* (2002b) examines the trajectory and stability of inviscid curved liquid jets; their investigation revealed temporal and spatial stability in the case of steady state solutions. They also conducted some experiments for inviscid rotating liquid jets and found agreement between the theoretical and experimental work. Decent *et al.* (2002) extended the previous work to include gravity in the examination of linear stability by Wallwork (2002a). Moreover, the influence of viscosity on the trajectory and stability of the break-up of rotating liquid jets has been examined by Decent *et al.* (2009) and the experiments agree with the theoretical work.

The influence of gravity on capillary jet instability was investigated by Cheong *et al.* (2004) and they found drop formation by using a finite difference solution. They also conducted experiments to compare with the numerical results, and found that the increase in gravity decreases disturbance frequency and, without including gravity, the maximum wave number is $k = 0.697$, which agrees with Rayleigh's result. The linear analysis of a

vertical viscous liquid jet falling under gravity was discussed by Sauter & Buggisch (2005). There is an article which reviews surface instabilities for different types of instabilities which is done by Malkin (2008).

2.3 Viscoelastic Jets

It is important to understand the behaviour of non-Newtonian jets because such jets have many industrial applications, such as ink jet printing, fertilizers, roll coating and paint leveling. Zhang *et al.* (2002) discussed the surfactant with viscoelastic film by using the Oldroyd-B model. non-Newtonian fluids have been investigated by Uddin *et al.* (2006) by using the power-law model to examine the linear instability of a rotating liquid jet. Uddin *et al.* (2006), also derived the dispersion relation to study the growth rate and wavenumber. The linear instability predicts that the drop sizes are uniform. However, the nonlinear instability gives non-uniform sizes, which are known as satellite droplets. Uddin *et al.* (2008a) studied nonlinear temporal solutions by using the Lax-Wendroff method for non-Newtonian liquid curved jets. In the same paper, these researchers used the simplest model which is the Power-Law for studying non-Newtonian fluids, which is used widely in many areas, especially in engineering. Uddin *et al.* (2008b) also studied the instability of liquid curved jets with surfactant. They found that break-up lengths increase, when the rotation rates increase. They also observed that satellite droplets decrease, when the effectiveness of surfactants(which is β see Chapter 9) increases. Another finding is that increasing the surfactant concentration leads to delay in the jet break-up. The linear and nonlinear instability were discussed by Uddin & Decent (2009) for non-Newtonian liquid curved jets with surfactant by using the Power-Law model. Following this, Uddin & Decent (2012) examined drop formation for non-Newtonian liquid curved jets with surfactant by using a finite difference scheme known as the Lax-Wendroff method(see Press *et al.* (2001)). Goren & Gottlieb (1982) investigated the theory of linear stability on break-

up of viscoelastic liquid jets by using Oldroyd's 8-constant model. They found agreement in this theory with previous studies; for example, if the elastic tension is not included, the shear-thinning liquid jets are less stable than Newtonian liquids. A numerical approach has been used by Renardy (1995) to investigate break-up of Newtonian and viscoelastic liquid jets for the Giesekus model and upper convected Maxwell model. The stability of viscoelastic jets has been examined by Middleman (1965) who compared growth rates of disturbances along viscous and viscoelastic liquid jets and found that a viscoelastic liquid jet is less stable than a Newtonian liquid jet. Goldin *et al.* (1969) considered the instability of viscoelastic liquid threads and identified the presence of thin ligaments between droplets which they attributed to the effects of stress on the fluid. They also compared the linear stability between inviscid, Newtonian and viscoelastic liquid jets, and found that the growth rate of viscoelastic liquid jets is higher than that of Newtonian liquid jets and smaller than that of inviscid liquid jets for the same zero shear viscosity fluid. Mageda & Larson (1988) have used the Oldroyd-B model (see section 4.4 for more details) for ideal elastic liquids, called Boger fluids, for investigating the rheological behavior of polyisobutylene and polystyrene when the shear rates are low. They found that this model gives a good description of recovery of shear rates and relaxation time of the fluid.

Schummer & Thelen (1988) studied the break-up of a viscoelastic liquid jet by using an upper-convected Jeffrey's model (for more details see section 4.7), and also investigated its linear stability. Larson (1992) wrote an article reviewing instability in viscoelastic flows in which he described the simplest model for studying the viscoelastic jets, which is the Oldroyd-B model. This model will be used for studying the break-up of viscoelastic liquid jets in the next chapter. However, according to Larson (1992), the Oldroyd-B model has two limitations. One of them is that the model has only one relaxation time, whereas fluids have spectrum of time. The other one is that prediction of the growth rate

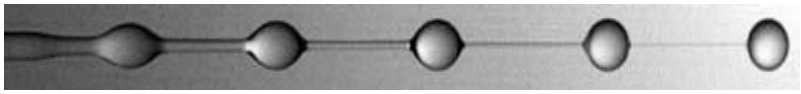

Figure 2.1: A viscoelastic liquid jet which is aqueous polyacrylamide solution at high-speed video under Capillary force where the surface tension is $\gamma = 62\text{m}Nm^{-1}$, the velocity of the jet is $30\text{cm}s^{-1}$, the contribution of the polymer is $\eta_p = 0.0119\,Pas$, the polymer time is $\lambda = 0.012$ s , and the Deborah number is $De = 18.2$. The orifice is at the left of the image (see Clasen *et al.* (2006)).

is unlimited in this model. Larson (1992) also illustrated the linear and nonlinear instability for Newtonian and non-Newtonian fluids. The asymptotic analysis and numerical computation was applied to stretching of viscoelastic jets to study linear stability and onset of stretching dynamics by Chang (1999), using the Oldroyd-B and FENE model to describe the viscoleastic structure of the fluid. The resulting dispersion relation was found to be a cubic equation, which was solved to investigate the stability of a filament near pinch-off where fluid is drained from ligaments into beads.

The beads-on-string structure of viscoelastic jets means that we have large droplets which are connected by thin threads as can be seen in Fig. 2.1. This phenomenon was examined by Clasen *et al.* (2006) using the Oldroyd-B model.

They also used the Oldroyd-B model, which is described as one dimensional, to examine the dilute polymer solution (see section 4.4 for more details about this model). Their study described the behaviour of this model for different initial conditions and compared it to the experimental work. The numerical study was conducted by Li & Fontelos (2003) for the beads-on-string structure of viscoelastic liquid jets by using an explicit finite difference method. They found that the variation of elastic force is larger than the variation of the capillary force by approximately four times.

Fontelos (2003) investigated the break-up of viscoelastic jets by using the Johnson-Segalman model. He discussed three assumptions, which were the boundary conditions

for polymeric fluids, the polymeric contribution (which is very high or very low), and the traveling wave solution. Fontelos & Li (2004) studied the evolution and break-up of viscoelastic liquid jets for two models: the Giesekus model and FENE-P type. They found that the radius of the jet decreases linearly close to the break-up. Temporal linear instability of a viscoelastic jet immersed in a Newtonian fluid was conducted by Gunawan *et al.* (2005), who used the constitutive model for the fluid as Jeffrey's model. The numerical study for pendant drop formation of viscoelastic liquid jets in air which emerged from a nozzle was examined by Davidson *et al.* (2006). They used the Oldroyd-B model and compared the drop shapes numerically with experimental work. Cooper-White *et al.* (2002) investigated the effects on elasticity of the drop of the liquid jet caused by gravity. They found that the comparison between numerical and experimental work was the same, but that the presence of elasticity led to different results, specifically towards the onset of pinch-off.

Roy *et al.* (2006) used the Fredholm-alternative theorem to obtain the equation of motion in order to study viscoelastic filament behavior by using the Oldroyd-B model. They discovered that the falling and rising behavior of viscoelastic liquid jets is different from that of Newtonian liquid jets. The beads-on-string structure of viscoelastic threads was discussed by Clasen *et al.* (2006). They used the Oldroyd-B model to this problem to study the beads-on-string and liquid bridge. This article is well-presented, and explains the theoretical analysis and experimental study. The viscoelastic jets were examined without rotation. Renardy (2008) studied the linear stability of viscoelastic shear flow in the limit of high Weissenberg and Reynolds numbers by using Maxwell upper convected fluid. The behavior of linear instability of three dimensional non-Newtonian liquid jets was discussed by Liu & Liu (2006). Liu & Liu (2008) discussed the temporal instability of viscoelastic liquid jets for axisymmetric and asymmetric disturbances. They found that the growth rate of viscoelastic jets is larger than the growth rate of Newtonian fluid and

smaller than the inviscid one for axisymmetric and asymmetric disturbances.

The dynamics of beads-on-string structure and filament thread have been discussed by Ardekani *et al.* (2010) for weakly viscoelastic jets by using the Giesekus constitutive equation (see section 4.8 for more details) and the results were compared with those of the Oldroyd-B model (when $\alpha = 0$). They found that the mobility factor α, which is a dimensionless parameter corresponding to the anisotropy of the hydrodynamic drag on the polymer molecules (Giesekus 1982), has an influence on the neck of droplets. Morrison *et al.* (2010) studied the viscoelasticity of the drop of ink which emerged from the nozzle. Axisymmetric instabilities for viscoelastic liquid jets were analysed by Carroll & Joo (2008) theoretically and experimentally in the presence of an electric field. The FENE-CR (Chilcott and Rallison (1988)) constitutive equation was used for modeling the problem and they found good agreements between the experimental studies and the numerical results. Moreover, the temporal linear stability was studied by Li *et al.* (2011) for an electrical viscoelastic liquid jet by using the Oldroyd-B model. In terms of electrical conductivity, they used the Taylor-Melcher theory. The dispersion relation was derived theoretically and examined in many cases, which were: without electrical field, with electrical field, and when considering the influence of liquid elasticity on the linear stability. They found that the normal electric field destabilizes the axisymmetric and non-symmetric disturbances for viscoelastic liquid jets. The equivalent case with viscosity was investigated by Hohman *et al.* (2001a, 2001b).

Brenn *et al.* (2000) investigated linear analysis of axisymmetric non-Newtonian liquid jets by using the corotational Oldroyd 8-constant model (for more details see section 4.9). They pointed out that at the same value of the Ohnesorge number, the growth rate of viscoelastic jets becomes larger than the growth rate of Newtonian jets, which suggests that viscoelastic liquid jets are more unstable than the Newtonian liquid jets due to the interaction between viscosity of the liquid and elastic effects inherent within the fluid.

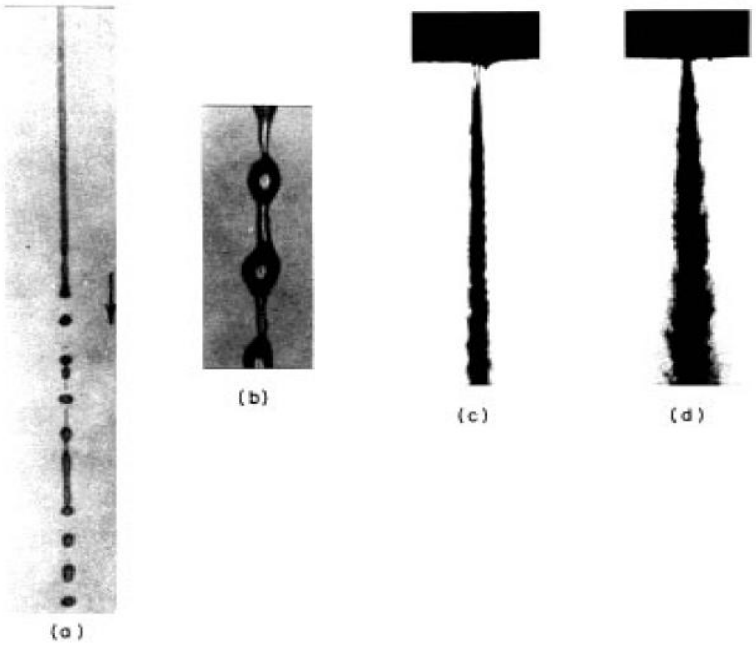

Figure 2.2: Four types of break-up regimes which are: (a) Rayleigh regime, (b) first-induced regime, (c) second-induced regime and (d) atomization regime. Taken from Lin and Reits (1998)

According to Funada & Joseph (2003), there are two dimensionless numbers, namely the Reynolds and the Deborah numbers, which are instrumental in determining the rate at which a column of fluid disintegrates into droplets.

2.4 Break-up Regimes

When the liquid emerges from a circular nozzle, the break-up occurs and it becomes liquid droplets. There are four types of break-up and each one has different characteristics. Rayleigh regime and first wind-induced regime happen when the speed is low, and from these two regimes the break-up does not happen near the orifice. The third one is second wind-induced regime which does happen near the orifice. The last one is the atomization regime, which is similar to the third one, as both occur at high speed. These regimes are presented in Fig. 2.2. We are interested in investigating the first regime which is the Rayleigh regime. Linear instability can be used to predict the break-up length of

a liquid jet by examining either short or long wavelength disturbances (see Decent*et al.* (2009)). Investigations of short wavelength disturbances render the governing equations more intractable than the equivalent analysis based on long wavelengths, where the slenderness of the jet can be used to form a small dimensionless parameter, which in turn is used to reduce the governing equations into a set of simpler equations using asymptotic theory. In this thesis we therefore adopt the latter approach and examine long wavelength disturbances.

2.5 The Non-Linear Dynamics of Break-up

Linear stability analysis predicts that liquid jets break up and produce uniform drop sizes along the axis of approximately the same wavelength of the initial disturbance. However, according to Chaudhary & Maxworthy (1980a, 1980b), by investigating the nonlinear phenomena, it can be observed that a number of smaller satellite droplets appeared in this case which are not equal in size. The first attempt at making a numerical simulation for studying break-up of inviscid liquid jets was made by Lee (1974) and presented the main and satellite droplet sizes. Pimbley & Lee (1977) studied the behavior of satellite droplet sizes theoretically and experimentally by considering the spatial instability analysis. Rutland & Jameson (1971) studied the non-linear effect of liquid jet break-up to predict the size of the main and primary (satellite) droplets experimentally in order to compare their results with Yuen (1968) in which they found good agreement. They also found a good agreement between the theoretical and experimental behavior examined by Bousfield (1986) for studying the non-linear analysis of break-up of viscoelastic filaments. Kang & Chen (1995) performed a non-linear instability analysis for viscoelastic film affected by gravity using the Oldroyd-B model.

In order to study nonlinear instability, a full analysis of the governing equations with free surface boundary conditions is an extremely difficult set of equations to solve analytically

and numerically. For this reason, we use an asymptotic approach to reduce the equations to one-dimensional models. Eggers & Dupont (1994) examined drop formation in a one-dimensional equation for viscous liquid jets. They investigated a one-dimensional equation by expanding a Taylor series with respect r as follows

$$
\begin{aligned}
v(z,r,t) &= v_0(z,t) + r^2 v_2(z,t) + ... \\
u(z,r,t) &= -\frac{1}{2} r v_{0z}(z,t) - \frac{1}{4} v_{2z}(z,t) + ... \\
p(z,r,t) &= p_0(z,t) + r^2 p_2(z,t) + ...
\end{aligned}
$$

where v, u and p are the axial velocity, radial velocity and pressure fields respectively. Substituting these expressions into the Navier-Stokes and the free boundary surface, the non-linear system are

$$
\begin{aligned}
v_t &= -v v_z - \frac{p_z}{\rho} + \frac{3\nu(h^2 v_z)_z}{h_z}, \\
p &= \gamma\left(\frac{1}{h(1+h_z^2)^{\frac{1}{2}}} - \frac{h_{zz}}{(1+h_z^2)^{\frac{3}{2}}}\right), \\
h_t &= -v h_z - \frac{1}{2} v_z h,
\end{aligned}
$$

where $h(z,t)$ is the position of the free surface, and $\nu = \mu/\rho$ is the kinematic viscosity. In this thesis, we will derive equations similar to the above for viscoelastic liquid curved jets.

Chapter 3

Theoretical work

3.1 Prilling Process

Prilling is an industrial process which is used to produce fertilizer pellets with a very small diameter, and these pellets have a different size owing to the break-up. This process can be applied either to fertilizer products, such as urea and ammonium nitrate, or to chemical products as an example NaOH (sodium hydroxide). When the liquid emerges from orifices, small satellite drops are wasted, so that manufacturers which produce the product need to save money by making the droplets uniform in size. The largest company for producing fertilizer pellets using industrial prilling during the last decade was Norsk Hydro based in Norway. In their set-up, they used a cylindrical drum to hold the molten urea, measuring 1 m in height and 0.5 m in the diameter. This can has 2000 small orifices and rotates at approximately 320-450 revolutions per minute (rpm). Therefore, the liquid emerges from these orifices and breaks up into small satellite droplets. The photograph for this prilling can from Norsk Hydro is shown in Figs. 3.1 and 3.2. In order to investigate the full production scale model in more detail a slightly smaller drum was constructed in the School of Chemical Engineering at the University of Birmingham, which in fact replaced a much smaller scale 'table-top' experiment within the School of Mathematics

Figure 3.1: Photograph of a prilling can. Courtesy of GEA Niro A S

where a small baked beans can was used as the drum!

3.2 Theoretical Work

In order to motivate a theoretical analysis of the industrial prilling process we consider a cylindrical container, containing a viscoelastic fluid, which has radius s_0 and rotates about its axis with angular velocity Ω. A small orifice with radius a is located on the curved face of the container and subsequently a slender jet emerges from the container due to hydrostatic pressure and centrifugal forces. The governing equations which describe the change in momentum and conservation of mass may be derived in non-dimensional

Figure 3.2: Photograph showing multiple jets emerging from a can (which is the dark shape at the bottom of this picture) in the prilling process. It can be seen that there are some droplets at the top of this picture. Taken from Wallwork (2002a).

form and these are found to be similar to those presented in Uddin (2007). However, in the present problem we have a more complex fluid which requires a number of additional features in the governing equations. In particular, we model the viscoelastic nature of the jet using the Oldroyd-B model. We use a curvilinear coordinate system (s, n, ϕ), where s is the arc-length of the jet and (n, ϕ) are plane polar coordinates in any cross section of the jet. In addition, the centerline of the jet is represented by Cartesian coordinates (X, Y, Z). A schematic of the set-up modelled together with a diagram showing pictorially the coordinate system used is shown in Figs. 3.3 and 3.4. This was used by Wallwork

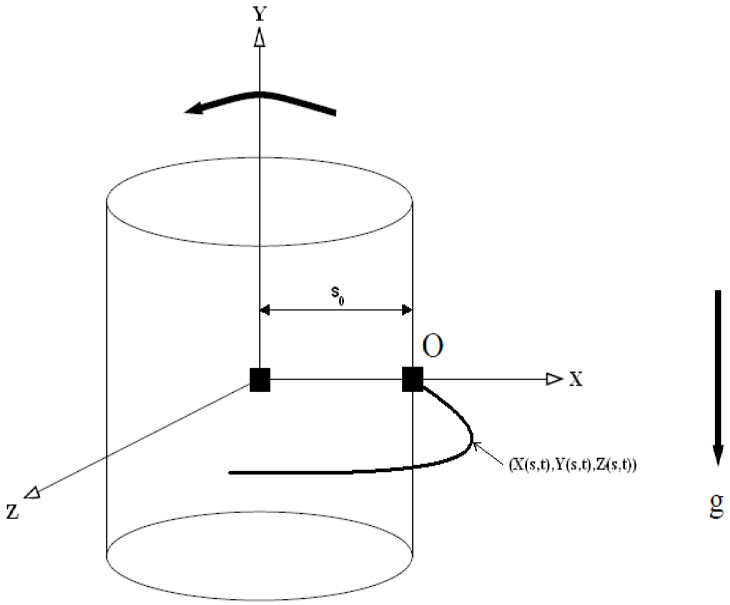

Figure 3.3: Sketch of coordinate system which uses the X, Y, Z axis. O represents the orifice from which the liquid emerges (see Wallwork (2002a)).

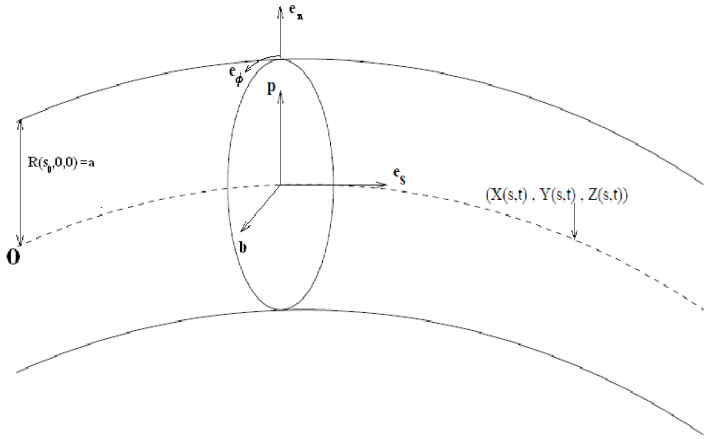

Figure 3.4: The centerline of the jet (see Wallwork (2002a)).

(2002a), $X = X(s,t)$ and $Z = Z(s,t)$ where t is the time. We use

$$\boldsymbol{e_s} = X_{i,s}\boldsymbol{e_i}, \tag{3.1}$$

the unit vectors in this coordinate system are calculated by using a principal normal vector $\mathbf{p}$ and a binormal vector$\mathbf{b}$ to the centerline (see Wallwork (2002a))

$$\boldsymbol{p} = \frac{\boldsymbol{e_{s,s}}}{|\boldsymbol{e_{s,s}}|} = \frac{X_{i,ss}\boldsymbol{e_i}}{\sqrt{X_{j,ss}X_{j,ss}}}$$

and

$$\boldsymbol{b} = \boldsymbol{p} \times \boldsymbol{e_s} = \frac{\varepsilon_{ijk}X_{j,ss}X_{k,s}\boldsymbol{e_i}}{\sqrt{X_{L,ss}X_{L,ss}}}.$$

There are another two vectors $\boldsymbol{e_n}$ and $\boldsymbol{e_\phi}$, which are defined as

$$\boldsymbol{e_n} = \cos\phi\boldsymbol{p} + \sin\phi\boldsymbol{b}, \tag{3.2}$$

and

$$\boldsymbol{e_\phi} = -\sin\phi\boldsymbol{p} + \cos\phi\boldsymbol{b}. \tag{3.3}$$

Now substitutions are made for $\boldsymbol{p}$ and $\boldsymbol{b}$ into the previous two equations and the unit vectors are obtained as follows

$$\boldsymbol{e_n} = \frac{1}{\sqrt{X_{L,ss}X_{L,ss}}}\Big(\cos\phi X_{i,ss} + \sin\phi\,\varepsilon_{ijk}\,X_{j,ss}X_{k,s}\Big)\boldsymbol{e_i}, \tag{3.4}$$

$$\boldsymbol{e_\phi} = \frac{1}{\sqrt{X_{L,ss}X_{L,ss}}}\Big(-\sin\phi X_{i,ss} + \cos\phi\,\varepsilon_{ijk}\,X_{j,ss}X_{k,s}\Big)\boldsymbol{e_i}. \tag{3.5}$$

For this coordinate system, we need to determine the structure functions, h_s, h_n and h_ϕ, which are defined as

$$h_i = \left|\frac{\partial r}{\partial i}\right| \quad \text{for} \quad i = s, n, \phi.$$

To describe the flow, we use a vector field as $\boldsymbol{u} = u\mathbf{e_s} + v\mathbf{e_n} + w\mathbf{e}_\phi$, then we can find that $\boldsymbol{\nabla} u$, $\boldsymbol{\nabla \cdot u}$, $\boldsymbol{\nabla \times u}$ and $\boldsymbol{\nabla^2} u$ are

$$\boldsymbol{\nabla} u = \frac{1}{h_s}\frac{\partial u}{\partial s}\mathbf{e_s} + \frac{\partial v}{\partial n}\mathbf{e_n} + \frac{1}{n}\frac{\partial w}{\partial \phi}\mathbf{e}_\phi,$$

$$\boldsymbol{\nabla \cdot u} = \frac{1}{nh_s}\left[\frac{\partial}{\partial s}(nu) + \frac{\partial}{\partial n}(nh_s v) + \frac{\partial}{\partial \phi}(h_s w)\right],$$

$$\boldsymbol{\nabla \times u} = \frac{1}{nh_s}\begin{vmatrix} h_s\mathbf{e_s} & \mathbf{e_n} & n\mathbf{e}_\phi \\ \frac{\partial}{\partial s} & \frac{\partial}{\partial n} & \frac{\partial}{\partial \phi} \\ h_s u & v & nw \end{vmatrix},$$

and

$$\boldsymbol{\nabla^2} u = \frac{1}{nh_s}\left[\frac{\partial}{\partial s}\left(\frac{n}{h_s}\frac{\partial u}{\partial s}\right) + \frac{\partial}{\partial n}\left(nh_s\frac{\partial u}{\partial n}\right) + \frac{\partial}{\partial \phi}\left(\frac{h_s}{n}\frac{\partial u}{\partial \phi}\right)\right].$$

It can be seen from Batchelor (1967), p. 600, that the components of the stress tensor σ in the curvilinear coordinate system take the form

$$\tau_{11} = \frac{1}{h_1}\frac{\partial u_1}{\partial \xi_1} + \frac{u_2}{h_1 h_2}\frac{\partial h_1}{\partial \xi_2} + \frac{u_3}{h_3 h_2}\frac{\partial h_1}{\partial \xi_3},$$

$$\tau_{23} = \frac{h_3}{2h_2}\frac{\partial}{\partial \xi_2}\left(\frac{u_3}{h_3}\right) + \frac{h_2}{2h_3}\frac{\partial}{\partial \xi_3}\left(\frac{u_2}{h_2}\right).$$

For this problem we choose $\xi_1 = s$, $\xi_2 = n$, $\xi_3 = \phi$ and $h_1 = h_s = 1 + n\cos\phi(X_s Z_{ss} - X_{ss} Z_s), h_2 = 1, h_3 = n$ (see Wallwork *et al.* (2002b)) and the total stress tensor is given by

$$\mathbf{\Pi} = -p\mathbf{I} + \boldsymbol{\tau},$$

$$\Pi_{ss} = -p + 2\mu.\frac{1}{h_s}.\left[\frac{\partial u}{\partial s} + (\upsilon\cos\phi - w\sin\phi)(X_s Z_{ss} - X_{ss} Z_s)\right],$$

$$\Pi_{nn} = -p + 2\mu\frac{\partial \upsilon}{\partial n},$$

$$\Pi_{\phi\phi} = -p + 2\mu.\frac{1}{n}.\left(\frac{\partial w}{\partial \phi} + \upsilon\right),$$

$$\Pi_{sn} = \Pi_{ns} = \mu\left[\frac{1}{h_s}\frac{\partial \upsilon}{\partial s} + \frac{\partial u}{\partial n} - \frac{u}{h_s}\cos\phi(X_s Z_{ss} - X_{ss} Z_s)\right],$$

$$\Pi_{n\phi} = \Pi_{\phi n} = \mu\left(\frac{\partial w}{\partial n} - \frac{w}{n} + \frac{1}{n}.\frac{\partial \upsilon}{\partial \phi}\right)$$

and

$$\Pi_{s\phi} = \Pi_{\phi s} = \mu\left[\frac{1}{n}.\frac{\partial u}{\partial \phi} + \frac{u}{h_s}\sin\phi(X_s Z_{ss} - X_{ss} Z_s) + \frac{1}{h_s}.\frac{\partial w}{\partial s}\right].$$

The position vector is known as

$$\mathbf{r} = \int_0^s \mathbf{e_s}\, ds + n\, \mathbf{e_n}, \tag{3.6}$$

where $\mathbf{e_s}$ and $\mathbf{e_n}$ are in equations (3.3) and (3.4) respectively. After substituting these equations into equation (3.6), we obtain

$$\mathbf{r} = (X + n\, \cos\phi\, Z_s)\mathbf{e_i} - n\, \sin\phi \mathbf{e_j} + (Z - n\, \cos\phi\, X_s)\mathbf{e_k}.$$

Părău *et al.* (2007) found expressions for u, v and w as follows. First,

$$\frac{d\mathbf{r}}{dt} = u\mathbf{e_s} + v\mathbf{e_n} + w\mathbf{e}_\phi = (uX_s + v\, \cos\phi\, Z_s)e_i -$$
$$(v\, \sin\phi + w\, \cos\phi)e_j + (uZ_s - v\, \cos\phi\, X_s + w\, \sin\phi\, X_s)e_k. \tag{3.7}$$

However, we have the velocity field in the form

$$\frac{d\mathbf{r}}{dt} = (X_s\frac{\partial s}{\partial t} + X_t + \frac{\partial n}{\partial t}\cos\phi\, Z_s - \frac{\partial \phi}{\partial t} n \sin\phi Z_s + \phi n \cos\phi Z_{ss}\frac{\partial s}{\partial t} + n\cos\phi\, Z_{st})\mathbf{e_i} -$$
$$(\frac{\partial n}{\partial t}\sin\phi + \frac{\partial \phi}{\partial t} n\cos\phi)\mathbf{e_j}$$
$$+(Z_s\frac{\partial s}{\partial t} + Z_t - \frac{\partial n}{\partial t}\cos\phi X_s + \frac{\partial \phi}{\partial t} n \sin\phi X_s - n\, \cos\phi X_{ss}\frac{\partial s}{\partial t} - n\cos\phi X_{st})\mathbf{e_k}. \tag{3.8}$$

By equating the unit vectors (3.7) and (3.8), we find

$$uX_s + v\cos\phi Z_s - w\sin\phi Z_s = X_s\frac{\partial s}{\partial t} + X_t + \frac{\partial n}{\partial t}\cos\phi Z_s - \frac{\partial \phi}{\partial t}n\sin\phi Z_s +$$
$$n\cos\phi Z_{ss}\frac{\partial s}{\partial t} + n\cos\phi Z_{st} \tag{3.9}$$
$$v\sin\phi + w\cos\phi = \frac{\partial n}{\partial t}\sin\phi + \frac{\partial \phi}{\partial t}n\cos\phi \tag{3.10}$$
$$uZ_s - v\cos\phi X_s + w\sin\phi X_s = Z_s\frac{\partial s}{\partial t} + Z_t - \frac{\partial n}{\partial t}\cos\phi X_s +$$
$$\frac{\partial \phi}{\partial t}n\sin\phi X_s - n\cos\phi X_{ss}\frac{\partial s}{\partial t} - n\cos\phi X_{st}, \tag{3.11}$$

and after solving the last three equations, we obtain (as seen in Părău *et al.* (2007))

$$u = \frac{\partial s}{\partial t}\left(1 + n\cos\phi(X_sZ_{ss} - X_{ss}Z_s)\right) + X_tX_s + Z_tZ_s + n\cos\phi(X_sZ_{st} - X_{st}Z_s), \tag{3.12}$$

$$v = \frac{\partial n}{\partial t} + \cos\phi(X_tZ_s - X_sZ_t), \tag{3.13}$$

$$w = n\frac{\partial \phi}{\partial t} - \sin\phi(X_tZ_s - X_sZ_t). \tag{3.14}$$

We use these equations (3.12)-(3.14) to derive the kinematic condition (see Eq. 6.27).

Now we turn our attention to the governing equations which are the continuity equation and Navier-Stokes equations respectively (see Wallwork (2002a))

$$\boldsymbol{\nabla}\cdot\boldsymbol{u} = 0,$$

$$\rho\left(\frac{\partial \boldsymbol{u}}{\partial t} + \boldsymbol{u}\cdot\boldsymbol{\nabla}\boldsymbol{u}\right) = -\boldsymbol{\nabla}p + \nu\boldsymbol{\nabla^2}\boldsymbol{u} - 2\,\boldsymbol{w}\times\boldsymbol{u} - \boldsymbol{w}\times(\boldsymbol{w}\times\boldsymbol{r'}), \tag{3.15}$$

where ρ is the density, p is the pressure, ν is the kinematic viscosity, $\boldsymbol{r}'$ is the position vector and the velocity field is $\boldsymbol{u} = u\mathbf{e_s} + v\mathbf{e_n} + w\mathbf{e}_\phi$. For this system of equations, we have boundary conditions which are firstly the kinematic condition

$$\frac{D}{Dt}\Big(R(s,\phi,t) - n\Big) = 0 \quad \text{for} \quad n = R(s,\phi,t) \tag{3.16}$$

where $R(s,\phi,t)$ is a function which gives the free surface position, we can write the previous equation as

$$\frac{\partial R}{\partial t} + \frac{\partial R}{\partial s}\frac{\partial s}{\partial t} + \frac{\partial R}{\partial \phi}\frac{\partial \phi}{\partial t} - \frac{\partial n}{\partial t} = 0. \tag{3.17}$$

And, secondly, the tangential stress condition and the normal stress condition are respectively, $\boldsymbol{t_i}\cdot\boldsymbol{\Pi}\cdot\boldsymbol{n} = \boldsymbol{t_i}\cdot\nabla\sigma$ for $i = 1, 2$ and $\boldsymbol{n}\cdot\boldsymbol{\Pi}\cdot\boldsymbol{n} = \sigma\kappa$, where σ is the surface tension, $\boldsymbol{n}$ is the normal unit vector and κ is the mean curvature of the free surface and $\boldsymbol{\Pi}$ is the total stress tensor which is obtained from $-p\boldsymbol{I} + \mu(\nabla\boldsymbol{u} + (\nabla\boldsymbol{u})^T)$. We have another condition for this problem which is the arc-length condition

$$X_s^2 + Z_s^2 = 1.$$

We apply the transformation as Wallwork (2002a) did to obtain the non-dimensionalization. We use an asymptotic analysis, as in Wallwork (2002a), to solve and find the steady state

for this problem by assuming that

$$u = u_0(s,t) + (\varepsilon n)u_1(s,n,\phi,t) + O(\varepsilon^2)$$

$$v = (\varepsilon n)v_1(s,\phi,t) + (\varepsilon n)^2 v_2(s,\phi,t) + O(\varepsilon^3)$$

$$w = (\varepsilon n)w_1(s,\phi,t) + (\varepsilon n)^2 w_2(s,\phi,t) + O(\varepsilon^3)$$

$$p = p_0(s,t) + (\varepsilon n)p_1(s\phi,t) + O(\varepsilon^2)$$

$$R = R_0(s,t) + (\varepsilon n)R_1(s\phi,t) + O(\varepsilon^2)$$

$$X = X_0(s,t) + \varepsilon X_1(s,n,\phi,t) + O(\varepsilon^2)$$

$$Z = Z_0(s,t) + \varepsilon Z_1(s,n,\phi,t) + O(\varepsilon^2).$$

From these assumptions, we find the equations which we use to determine the trajectory. These equations, derived by Wallwork (2002a), state that

$$u_0 = \left(1 - \frac{1}{Rb^2}(X^2 + 2X + Z^2) + \frac{2}{We}(1 - \frac{1}{R_0})\right)^{\frac{1}{2}} \tag{3.18}$$

$$\frac{dR_0}{ds} = -\frac{WeR_0^2((X+1)X_s + ZZ_s)}{Rb^2(1 + 2WeR_0u_0^2)} \tag{3.19}$$

$$Z_{ss} = \frac{WeR_0X_s}{WeR_0u_0^2 - 1}\left(\frac{2u_0}{Rb} + \frac{ZX_s - (X+1)Z_s}{Rb^2}\right) \tag{3.20}$$

$$X_s^2 + Z_s^2 = 1, \tag{3.21}$$

where $X_0 = X$, $Z_0 = Z$, Rb is the Rossby number, $Rb = \frac{U}{s_0\Omega}$ and We is the Weber number, $We = \frac{\rho U^2 a}{\sigma}$. To solve the previous equations, we need to have initial conditions which are

$X = Z = Z_s = 0, X_s = R_0 = u_0 = 1$ *at* $s = 0$. By using a Runge-Kutta method, these equations are solved numerically by using the ODE45 package in MATLAB to obtain the trajectory of the centerline of the curved jet. This method will be used in Chapter 6 to determine the trajectory of viscoelastic curved jets. To investigate the linear temporal

stability of disturbances about the base steady state, we use the following approach

$$u = \overline{u}(s, n, \phi, \varepsilon) + \delta\tilde{u}(s, \overline{s}, n, \phi, t, \overline{t}) + O(\delta^2)$$
$$p = \overline{p}(s, n, \phi, \varepsilon) + \delta\tilde{p}(s, \overline{s}, n, \phi, t, \overline{t}) + O(\delta^2)$$
$$R = \overline{R}(s, n, \phi, \varepsilon) + \delta\tilde{R}(s, \overline{s}, n, \phi, t, \overline{t}) + O(\delta^2)$$
$$X = \overline{X}(s, \varepsilon) + \delta\varepsilon\tilde{X}(s, \overline{s}, t, \overline{t}) + O(\delta^2)$$

where first terms of these equations are the steady state solutions obtained by solving (3.18)-(3.21), whereas the variables with tilde are unsteady variables obtained after making perturbations to this system of equations. It can be considered that the traveling modes take the form $exp(ik\overline{s} + \omega\overline{t})$, where $\overline{s} = \frac{t}{\varepsilon}$, $\overline{t} = \frac{t}{\varepsilon}$, k is the wave number and ω is the wave growth rate. It can be noticed that we use Fourier series for expanding the velocity, pressure and radius in ϕ, and find eigenvalue relationships, each associated with $\cos(n\phi)$ and $\sin(n\phi)$ where n is integer.

Wallwork *et al.* (2002b) derived the linear stability for inviscid liquid jets and obtained the relationship

$$(\omega + iku_0)^2 = \frac{1}{We}\left(\frac{1}{R_0^2}(1 - n^2) - k^2\right) k\frac{I_n^{'}(kR_0)}{I_n(kR_0)},$$

where I_n is the nth order modified Bessel function. When $n = 0$ which means the disturbances are axisymmetric, we obtain the dispersion relation as follows

$$\omega + iku_0 = \sqrt{\frac{1}{We}\left(\frac{1}{R_0^2} - k^2\right) k\frac{I_1(kR_0)}{I_0(kR_0)}}$$

which is similar to the classic Rayleigh mode. The modes become unstable when $0 < kR_0 < 1$. The most unstable wavenumber k^* can be determined from the above equation and is found to have the form $k^* = \frac{0.697}{R_0(s)}$ where $R_0(s)$ is the solution found by solving the

equations (3.18)-(3.12).

According to Wallwork (2002a), the dispersion relation for viscous liquid jets takes the form

$$\omega^2 + \frac{3\mu k^2}{\rho}\omega = \frac{\sigma k}{\rho a^2}\left(1 - (kR_0)^2\right)\frac{I_1'(kR_0)}{I_0(kR_0)},$$

from the last equation, we can find the most unstable wave number from the form

$$k^*(s) = \frac{1}{2^{1/4}R_0^{3/4}(s)\sqrt{\sqrt{2R_0(s)} + 3Oh}} \tag{3.22}$$

where Oh $(= \frac{\mu}{\sqrt{\sigma a \rho}}$) is the Ohnesorge number. From the above equation it can be seen that for the case where viscosity is absent, i.e. when $Oh = 0$, the expression obtained corresponds to the most unstable wavenumber found for the inviscid case by Rayleigh as one would expect.

3.3 Experimental Work

There was an attempt to investigate the dynamics of the breakup of jets which emerged from orifice. This spiraling process was conducted by Wong *et al.* (2004) at University of Birmingham school of Mathematics. The apparatus of this experiment was a cylindrical can with a diameter of 0.085 m and height of 0.115 m. This can rotated about its axis. It also had two sizes of orifice, which were 0.001 m and 0.003 m. A peristaltic pump was used (Waltson-Mason 505 s) for filling up the can with wasted liquid. A high speed camera was also used for studying the trajectory of the jet, which is capable of capturing 10,000 frames per second. Additionally, Wong *et al.* (2004) used a personal computer to download the images. The dimensionless groups which were used were Reynolds number ($Re = \frac{\rho U a}{\mu}$), Rosby number ($Rb = \frac{U}{s_0\Omega}$),Weber's number ($We = \frac{\rho U^2 a}{\sigma}$) and Ohnesorge's number ($Oh = \frac{\mu}{\sqrt{\sigma a \rho}}$). The ranges of these parameters taken in the experiment were

$1 < Re < 10^3$, $0.2 < Rb < 4.5$, $0.5 < We < 2.5$ and $5 \times 10^{-3} < Oh < 4 \times 10^{-1}$. The exit velocity was calculated by the total volume of liquid collected during 1 minute by the cross-sectional area. Different fluids were used in this experiment for discovering physical properties, such as water and glycerol. They have investigated four modes for breakup which were indicated as M1, M2, M3 and M4.

Mode M1 (Figs. 3.7 and 3.8) shows rapid formation with few or absent satellite

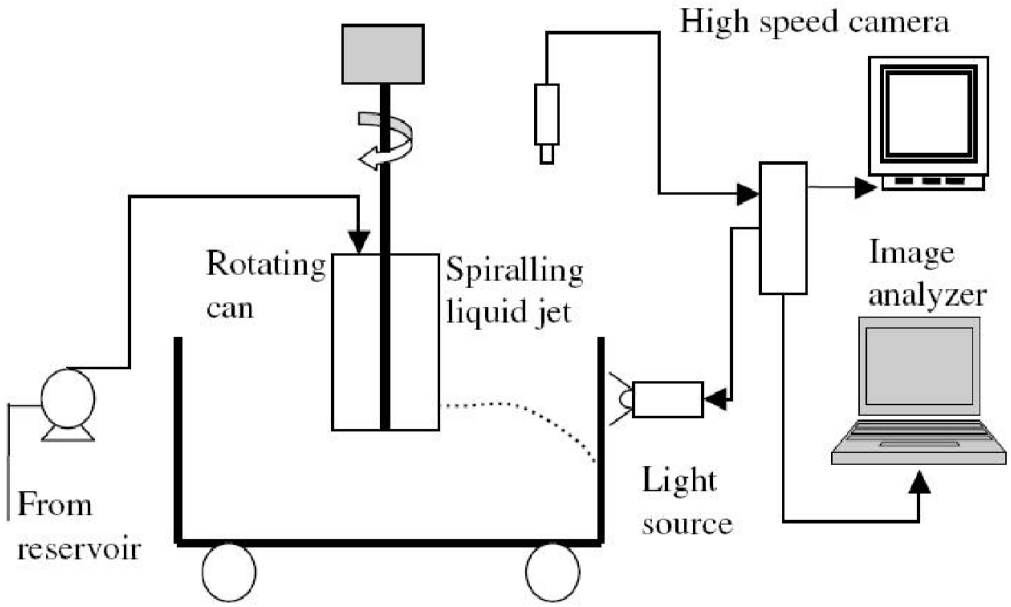

Figure 3.5: Diagram of the experimental laboratory scale setup

droplets and surface tension convected downstream. In this mode the breakup occurs for water jets which emerged from a 0.001 m orifice. Mode M2 (Figs. 3.9 and 3.10) represents short wavelength and satellite drops which are formed in between the drops because of capillary pinch-off. When the velocity of the exit jet was increased the breakup mode changed from M1 to M2. Mode M3 (Figs. 3.11 and 3.12) showing long wavelength and jet breakup, happens simultaneously along the jet. By using fluids which have high viscosity with high exit velocity the break-up for this mode occurs. Mode M4 (Figs. 3.13 and 3.14) is nonlinear disintegration and bends away from the centerline. This mode

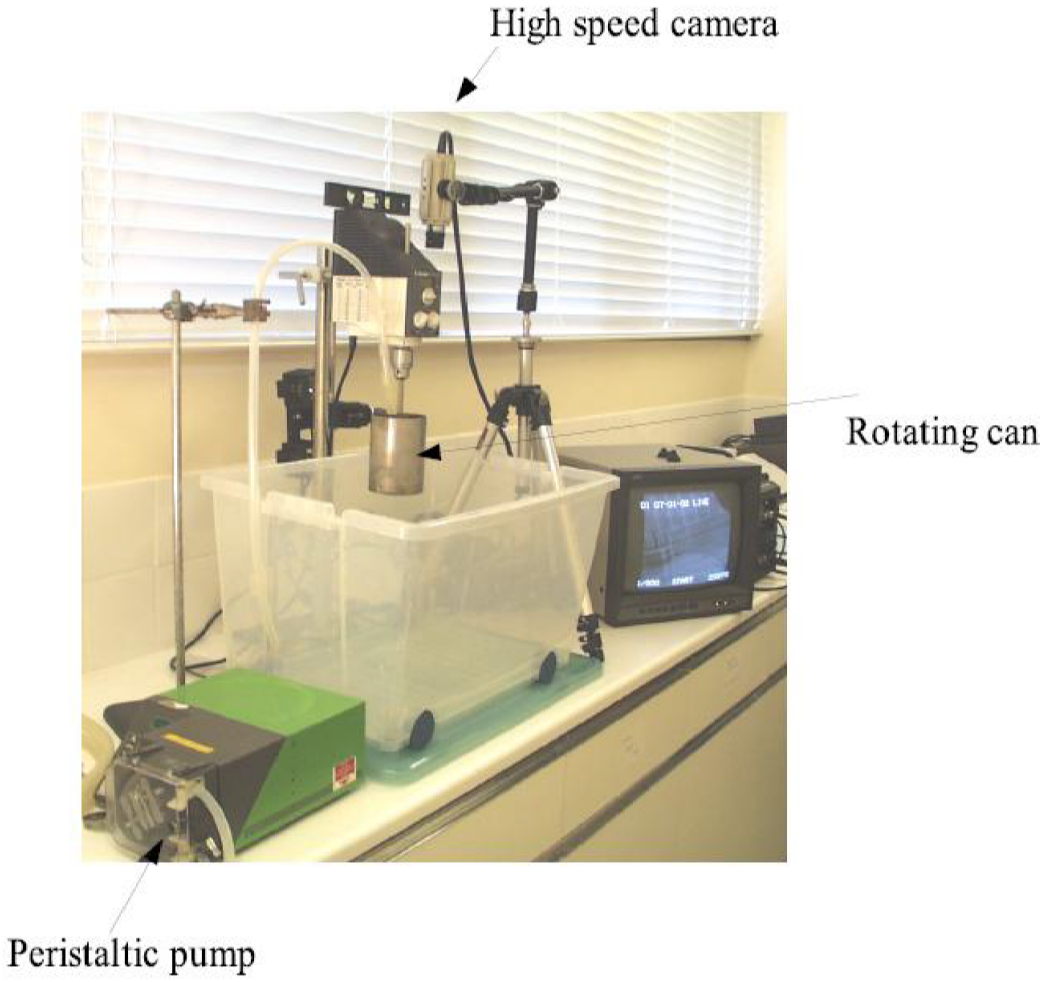

Figure 3.6: Photograph of the experimental laboratory scale setup

happens as a result of using fluids which have high viscosity with low exit velocity. The theoretical prediction for this experiment was investigated by Wallwork *et al.* (2002b) for inviscid liquid jets. Decent *et al.* (2009) extends this work to include the influence of viscosity and gravity and studied the temporal and spatial stability. Wong *et al.* (2004) reported that the experimental data for some modes showed the linear stability is not enough for predicting breakup. However, it appears that non-linear analysis is required to give better results. Părău *et al.* (2006, 2007) studied the non-linear viscous liquid jets. The preceding discussion about experiments has been concerned with rotating Newtonian

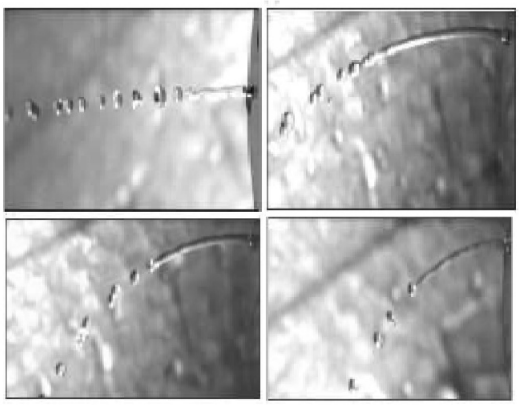

Figure 3.7: Experimental photos of a spiralling liquid jet for different rotation rates. The fluid here is Newtonian and the rotation rates from top to bottom and left to right are 0 rpm, 50 rpm, 100 rpm and 200 rpm respectively. Taken from Uddin (2007)

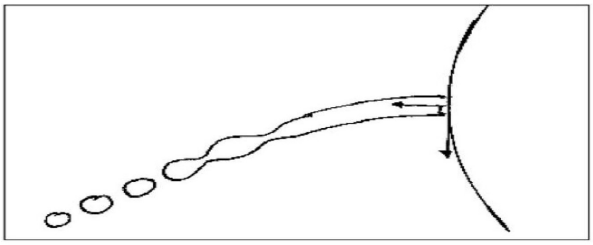

Figure 3.8: Sketch showing Mode 1 break-up (see Wong *et al.* (2004)).

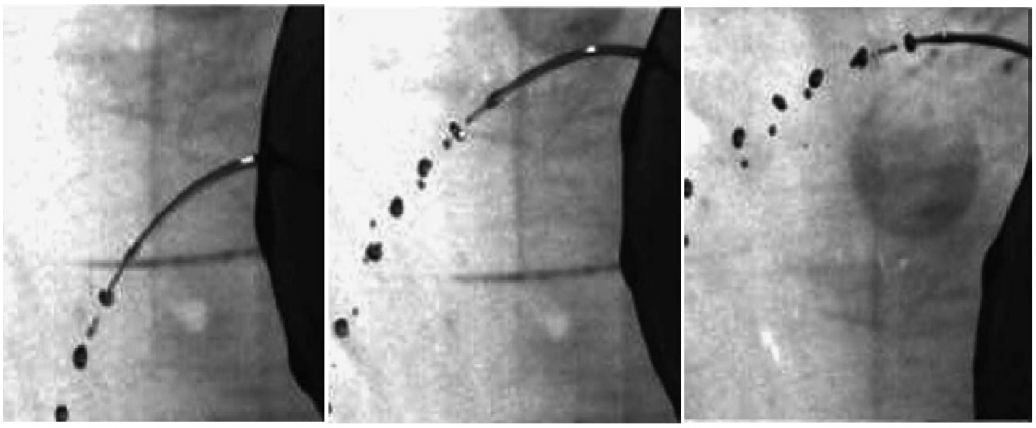

Figure 3.9: Photographs showing Mode 2 break-up (see Wong *et al.* (2004)).

liquid jets. However, more recently experiments involving spiraling non-Newtonian liquid jets were conducted by Hawkins *et al.* (2007) which are presented in Fig. 3.15.

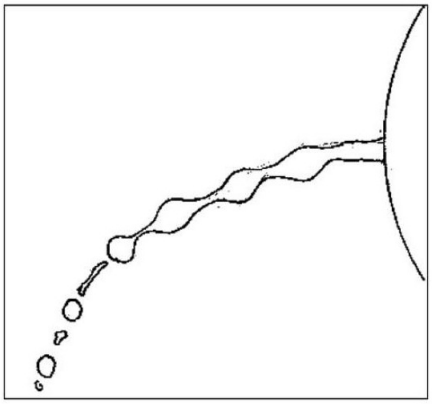

Figure 3.10: Sketch showing Mode 2 break-up (see Wong *et al*. (2004)).

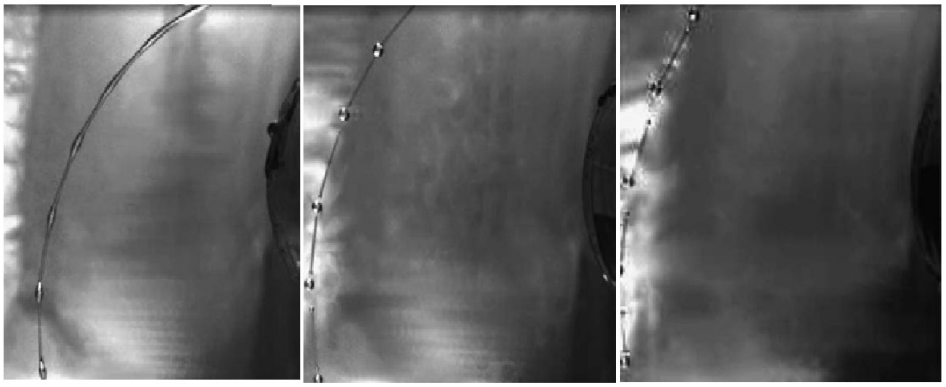

Figure 3.11: Photograph showing Mode 3 break-up (see Wong *et al*. (2004)).

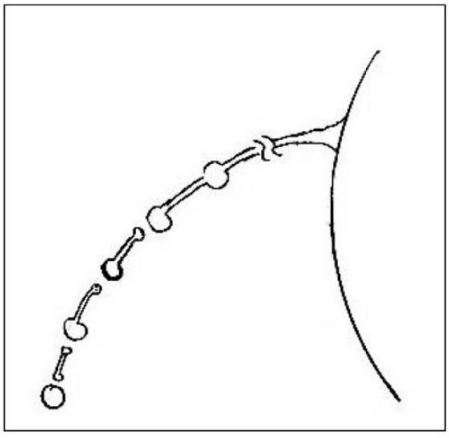

Figure 3.12: Sketch showing Mode 3 break-up (see Wong *et al*. (2004)).

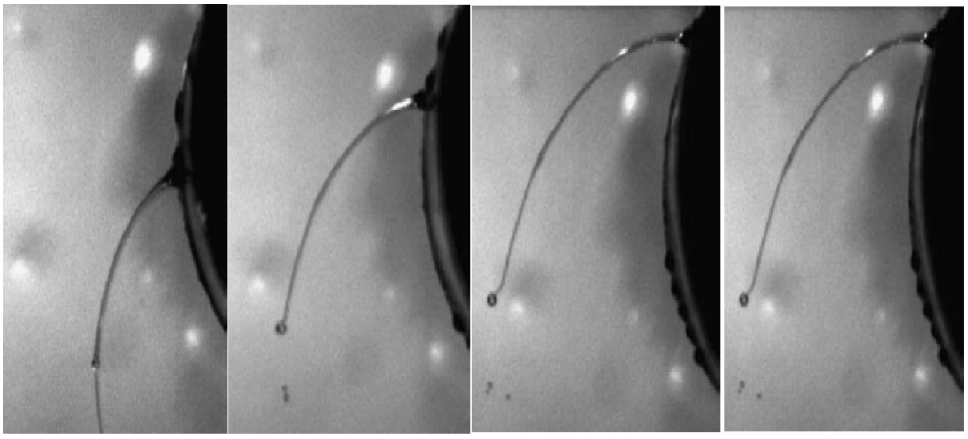

Figure 3.13: Photographs showing Mode 4 break-up (see Wong *et al*. (2004)).

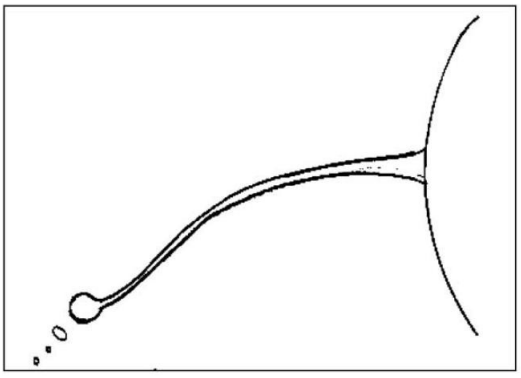

Figure 3.14: Sketch showing Mode 4 break-up (see Wong *et al*. (2004)).

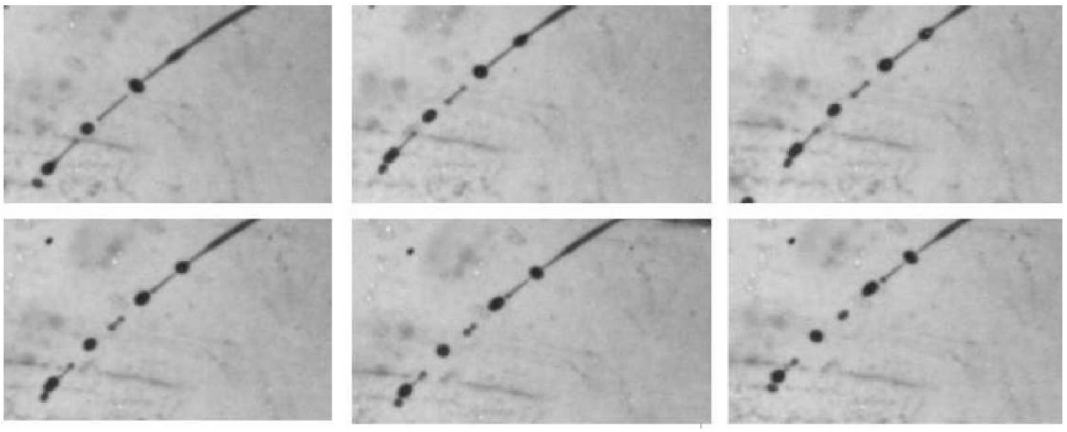

Figure 3.15: Experimental image of pendant drop formation in rotating shear thinning jets. $We = 16.06$, $Rb = 1.9049$, $Oh = 0.0220$, $Re = 181.98$, $\rho = 1025.05$ Kg m^{-3}, $k = 0.01197\ Pas$, $\alpha = 0.920$. See Hawkins *et al.* (2007) for more details.

Chapter 4

Viscoelastic Models

4.1 Introduction

In nature there exist some types of fluids which have characteristics shared by both ideal fluids, which have no resistance to shear flow, and elastic solids which retain their original shape after being stretched. These fluids are called viscoelastic fluids. For example, mayonnaise takes a different shape when a small disturbance is applied. After disturbing the mayonnaise, it will keep the same shape for a long time. This fluid has both a viscous behaviour and an elastic behaviour (see Morrison (2001)).

In addition, viscoelastic fluids are susceptible to deformations and stresses. These fluids have energy stored within their structure as a strain energy. When a deforming stress is removed, these fluids will show an elastic recovery time. This time is called relaxation time which we express in this thesis as λ.

Newtonian fluids are characterised by fluids where the viscosity does not change, but the viscosity of non-Newtonian fluids will vary with the shear rate. Moreover, the governing equations for incompressible Newtonian fluids which are equation of motion, equation of

continuity and constitutive equation are

$$\rho\left(\frac{\partial \boldsymbol{u}}{\partial t} + \boldsymbol{u}\cdot\nabla\boldsymbol{u}\right) = -\nabla p + \nabla\cdot\boldsymbol{\tau} + \rho\mathbf{g}, \tag{4.1}$$

$$\nabla\cdot\boldsymbol{u} = 0, \tag{4.2}$$

$$\boldsymbol{\tau} = \mu\left(\nabla\boldsymbol{u} + (\nabla\boldsymbol{u})^T\right), \tag{4.3}$$

where $\boldsymbol{u}$ is the velocity, p is the pressure, $\mathbf{g}$ is the external force, $\boldsymbol{\tau}$ is the stress tensor, ρ is the density and μ is the viscosity. When we consider a non-Newtonian fluid which is assumed incompressible the previous equations (4.1) and (4.2) will remain valid, however equation (4.3) will be modified as we will see in section 4.4. The study of deformation and flow is called rheology.

4.2 Non-Newtonian Fluids

Chhabra & Richardson (2008) have shown that a non-Newtonian fluid is one in which the flow curve, that is the relationship between stress and shear, is non-linear and therefore the viscosity is not constant. In addition to this, there are two differences between Newtonian fluids and non-Newtonian fluids in terms of modeling which are

1. For a Newtonian fluid the constitutive equation is

$$\boldsymbol{\tau} = \mu\left(\nabla\boldsymbol{u} + \nabla(\boldsymbol{u})^T\right) + (\frac{2}{3}\mu - \kappa)(\nabla\cdot\boldsymbol{u})I \tag{4.4}$$

where μ is the dynamic viscosity, $\boldsymbol{u}$ is the velocity gradient tensor, κ is the dilatation viscosity and I is the identity tensor. Since we model the fluid as incompressible we may ignore the divergence of $\boldsymbol{u}$. Then the equation (4.4) becomes

$$\boldsymbol{\tau} = \mu\left(\nabla\boldsymbol{u} + (\nabla\boldsymbol{u})^T\right) = \mu\boldsymbol{\gamma}, \tag{4.5}$$

where $\boldsymbol{\gamma}$ is the rate of strain tensor. The viscosity in non-Newtonian fluids is not constant. 2. Non-Newtonian fluid have a relaxation time (see Maxwell model eq. 4.11) which is responsible for the flow to respond at a delay time. This relaxation time is crucial to study in viscoelastic fluids.

4.3 Viscoelastic Fluids Behavior

From the classical theory of elasticity, there is a relationship between changes or deformations to a body and the force which are acting upon it; this is known as Hooke's Law. The mathematical description of this relationship for a fluid can be written as

$$\boldsymbol{\tau} = \mu\Big(\nabla \boldsymbol{w} + (\nabla \boldsymbol{w})^T\Big) = G\boldsymbol{\gamma}, \tag{4.6}$$

where G is the elastic modulus and $\boldsymbol{w}$ is the displacement vector. According to Chhabra & Richandson (2008), there are many materials which have the ability to keep and recover shear stress, such as polymer melts, soap and synovial fluids. These materials, when affected by stress and deformed, will return to the original shape when the stress is removed.

4.4 Constitutive Equations

The simplest constitutive equation for studying non-Newtonian fluids is the Oldroyd-B equation which is given by Oldroyd (1950). The extra stress tensor in this equation can be written as

$$\boldsymbol{\tau} = \boldsymbol{\tau}_s + \boldsymbol{\tau}_p,$$

where $\boldsymbol{\tau}_s$ is the viscous stress tensor and $\boldsymbol{\tau}_p$ is the polymeric contribution to the stress tensor. In this thesis, we will use Eq. (4.13) to present the polymeric contribution.

4.5 The Maxwell Model

According to Yamaguchi (2010), this model consists of viscous elements which are known as dashpot (η is the viscosity) and elastic elements assigned as a spring, where E is the modulus. Consider that the stress $\boldsymbol{\tau_1}$ in the spring is $E\boldsymbol{\gamma_1}$ and the stress in the dashpot is $\eta\left(\frac{\partial \boldsymbol{\gamma_2}}{\partial t}\right) = \eta\boldsymbol{\gamma_2}$ and $\boldsymbol{\tau} = \boldsymbol{\tau_1} = \boldsymbol{\tau_2}$. Then we can write the total strain of the system as

$$\boldsymbol{\gamma} = \boldsymbol{\gamma}_1 + \boldsymbol{\gamma}_2, \tag{4.7}$$

$$\frac{\partial \boldsymbol{\gamma}}{\partial t} = \frac{\partial \boldsymbol{\gamma}_1}{\partial t} + \frac{\partial \boldsymbol{\gamma}_2}{\partial t}, \tag{4.8}$$

$$\frac{\partial \boldsymbol{\gamma}}{\partial t} = \frac{\frac{\partial \boldsymbol{\tau}_1}{\partial t}}{E} + \frac{\boldsymbol{\tau}_2}{\eta}, \tag{4.9}$$

$$\frac{\partial \boldsymbol{\gamma}}{\partial t} = \frac{\frac{\partial \boldsymbol{\tau}}{\partial t}}{E} + \frac{\boldsymbol{\tau}}{\eta}, \tag{4.10}$$

$$\boldsymbol{\tau} + \lambda\frac{\partial \boldsymbol{\tau}}{\partial t} = \eta\boldsymbol{\gamma}, \tag{4.11}$$

where $\lambda = \frac{\eta}{E}$ is the relaxation time (see Fig. 4.1).

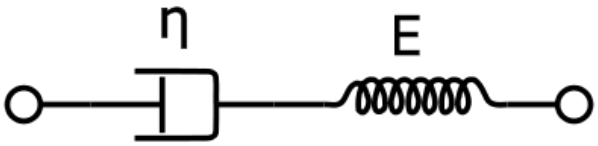

Figure 4.1: Maxwell Model

At steady state, equation (4.11) becomes the Newtonian constitutive equation. This equation is a differential equation model. There is another expression to calculate the stress which is in the form

$$\boldsymbol{\tau} = \frac{\eta}{\lambda}\int_{-\infty}^{t} exp\left(\frac{-(t-\tau)}{\lambda}\right)\frac{\partial \boldsymbol{\gamma}}{\partial t}d\sigma. \tag{4.12}$$

Moreover, Joseph (1990) discussed that there are two other models for this model which

are called Upper-Convected Maxwell (UCM) and Lower-Convected Maxwell (LCM) respectively

$$\boldsymbol{\tau} + \lambda \boldsymbol{\tau}^{\nabla} = \mu \boldsymbol{\gamma}, \tag{4.13}$$

$$\boldsymbol{\tau} + \lambda \boldsymbol{\tau}^{\triangle} = \mu \boldsymbol{\gamma}, \tag{4.14}$$

where the symbols ∇ and $\triangle$ are known upper convected derivative and lower convected derivative of an arbitrary tensor $\boldsymbol{A}$ respectively as

$$\boldsymbol{A}^{\nabla} = \frac{D\boldsymbol{A}}{DT} - (\nabla \boldsymbol{u})^T \cdot \boldsymbol{A} - \boldsymbol{A} \cdot \nabla \boldsymbol{u}, \tag{4.15}$$

$$\boldsymbol{A}^{\triangle} = \frac{D\boldsymbol{A}}{DT} + (\nabla \boldsymbol{u})^T \cdot \boldsymbol{A} + \boldsymbol{A} \cdot \nabla \boldsymbol{u}. \tag{4.16}$$

Yamaguchi (2010) explained that the lower-convected Maxwell (LCM) is not commonly used owing to disagreement between the theoretical and experimental work, whereas the upper-convected Maxwell (UCM) has good results compared to experimental work.

4.6 Co-rotational Maxwell Model

Another model, similar to the Maxwell Model considered above, takes the form

$$\boldsymbol{\tau} + \lambda \boldsymbol{\tau}^{\circ} = \mu \boldsymbol{\gamma}, \tag{4.17}$$

where $\boldsymbol{\tau}^{\circ}$ is defined as

$$\boldsymbol{\tau}^{\circ} = \boldsymbol{\tau} - \boldsymbol{w}^T \cdot \boldsymbol{\tau} - \boldsymbol{\tau} \cdot \boldsymbol{w}, \tag{4.18}$$

and the vorticity tensor is

$$\boldsymbol{w} = \frac{1}{2}\bigg(\nabla \boldsymbol{u} - (\nabla \boldsymbol{u})^T\bigg).$$

This model is called Jaumann time derivative or co-rotational (see Larson (1988)).

4.7 Jeffrey's Model

Morrison (2001) explained that in Maxwell's Model there is a linear term missing which is the time derivative of the rate of strain, so this model is

$$\boldsymbol{\tau} + \lambda \frac{\partial \boldsymbol{\tau}}{\partial t} = \mu\bigg(\boldsymbol{\gamma} + \lambda_r \frac{\partial \boldsymbol{\gamma}}{\partial t}\bigg), \tag{4.19}$$

when we use the two ways to present Jeffrey's equation as in upper-convected and lower-convected, so we obtain the Oldroyd-B and Oldroyd-A equations respectively (see Larson (1988)),

$$\boldsymbol{\tau} + \lambda \boldsymbol{\tau}^{\nabla} = \mu(\boldsymbol{\gamma} + \lambda_r \boldsymbol{\tau}^{\nabla}), \tag{4.20}$$

$$\boldsymbol{\tau} + \lambda \boldsymbol{\tau}^{\triangle} = \mu(\boldsymbol{\gamma} + \lambda_r \boldsymbol{\gamma}^{\triangle}), \tag{4.21}$$

where λ is the relaxation time and λ_r is the retardation time. It can be seen that when $\lambda_r = 0$, we obtain Maxwell's model. The constitutive equation for Oldroyd-B can be written as

$$\boldsymbol{\tau} = \boldsymbol{\tau}_s + \boldsymbol{\tau}_p, \tag{4.22}$$

where $\boldsymbol{\tau}_s(=\mu_s\boldsymbol{\gamma})$ is the solvent stress and $\boldsymbol{\tau}_p$ is the polymer stress which satisfies the UCM equation

$$\boldsymbol{\tau}_p + \lambda\boldsymbol{\tau}_p^{\nabla} = \mu_p\boldsymbol{\gamma}. \tag{4.23}$$

4.8 Giesekus's Model

Giesekus (1982) has given a simple constitutive model to model polymer fluids which are based on deformation-dependent mobility. This model has the form

$$\boldsymbol{\tau} + \lambda\boldsymbol{\tau}^{\nabla} + a\boldsymbol{\tau}^2 = \mu\boldsymbol{\gamma}. \tag{4.24}$$

We can notice that this model is the UCM plus an extra quadratic term, where a is the mobility factor.

4.9 Oldroyd Eight-Constant Equation

Oldroyd has produced a general constitutive equation from which we can derive the UCM, LCM, Giesekus and Jeffrey's model. According to Larson (1988), this equation has the form

$$\begin{aligned}\boldsymbol{\tau} + \lambda\boldsymbol{\tau}^{\circ} + \mu_0 tr(\boldsymbol{\tau})\boldsymbol{\gamma} - \mu_1(\boldsymbol{\tau}\cdot\boldsymbol{\gamma} + \boldsymbol{\gamma}\cdot\boldsymbol{\tau}) + \nu_1(\sigma:\boldsymbol{\tau})\boldsymbol{\delta} = \\ \mu_0\Big[\boldsymbol{\tau} + \lambda_r\boldsymbol{\gamma}^{\circ} - \mu_2\boldsymbol{\gamma}^2 + \nu_2\boldsymbol{\gamma}:\boldsymbol{\gamma}\boldsymbol{\delta}\Big],\end{aligned} \tag{4.25}$$

where

$$\begin{aligned}
\boldsymbol{\gamma} &= \nabla \boldsymbol{u} + (\nabla \boldsymbol{u})^T, \\
\boldsymbol{w} &= \nabla \boldsymbol{u} - (\nabla \boldsymbol{u})^T, \\
\boldsymbol{\tau}^{\circ} &= \frac{\partial \boldsymbol{\tau}}{\partial t} + (\boldsymbol{u} \cdot \nabla)\boldsymbol{\tau} + \frac{1}{2}(\boldsymbol{w} \cdot \boldsymbol{\tau} - \boldsymbol{\tau} \cdot \boldsymbol{w}), \\
\boldsymbol{\gamma}^{\circ} &= \frac{\partial \boldsymbol{\gamma}}{\partial t} + (\boldsymbol{u} \cdot \nabla)\boldsymbol{\gamma} + \frac{1}{2}(\boldsymbol{w} \cdot \boldsymbol{\tau} - \boldsymbol{\tau} \cdot \boldsymbol{w}).
\end{aligned} \tag{4.26}$$

4.10 Co-rotational Jeffrey Model

According to Larson (1988), there is another model corresponding to co-rotational Maxwell equation (CRM) which is co-rotational Jeffrey's equation, that can be found by adding retardation term to (CRM), in the form

$$\boldsymbol{\tau} + \lambda \boldsymbol{\tau}^{\circ} = \mu(\boldsymbol{\gamma} + \lambda_r \boldsymbol{\gamma}^{\circ}), \tag{4.27}$$

where $\boldsymbol{\gamma}^{\circ}$ is the co-rotational time derivative, defined as

$$\boldsymbol{\gamma}^{\circ} = \boldsymbol{\gamma}^{\cdot} - \boldsymbol{w}^T \cdot \boldsymbol{\gamma} - \boldsymbol{\gamma} \cdot \boldsymbol{w}. \tag{4.28}$$

4.11 Johnson-Segalman Model

This model is combined between the upper-convected and lower-convected Maxwell, so that the form is

$$\boldsymbol{\tau} + \lambda \boldsymbol{\tau}^{\diamond} = \mu \boldsymbol{\gamma}, \tag{4.29}$$

where $\boldsymbol{\tau}^{\diamond}$ is the combination of the upper-convected and lower-convected derivative

$$\begin{aligned}\boldsymbol{\tau}^{\diamond} &= \boldsymbol{\tau}^{\cdot} - \nabla\boldsymbol{u}^{T}\cdot\boldsymbol{\tau} - \boldsymbol{\tau}\cdot\nabla\boldsymbol{u} + a(\boldsymbol{\tau}\cdot\boldsymbol{\gamma} + \boldsymbol{\gamma}\cdot\boldsymbol{\tau}),\\ &= \boldsymbol{\tau}^{\cdot} - \boldsymbol{w}^{T}\cdot\boldsymbol{\tau} - \boldsymbol{\tau}\cdot\boldsymbol{w} - a(\boldsymbol{\tau}\cdot\boldsymbol{\gamma} + \boldsymbol{\gamma}\cdot\boldsymbol{\tau}),\end{aligned} \tag{4.30}$$

where a is the slip parameter. It can be shown that this model includes the upper-convected, lower-convected and co-rotational derivative (see Larson (1988)).

In this thesis, we will use the Maxwell model (see Eq. 4.13) to present the polymeric contribution for studying the linear and non-linear instability of viscoelastic liquid curved jets. This model is more commonly used in practice, because there are good agreements between the theoretical and experimental work.

Chapter 5

Temporal Instability of Viscoelastic Liquid jets Falling Under Gravity

As the aim of this thesis is to investigate the instability and behaviour of viscoelastic liquids under various non-uniform flow configurations, we begin with the simplest case where a liquid jet falls vertically under gravity. In this case, a non-uniform steady state of viscoelastic liquid jet will be affected by the gravitational force .

5.1 Problem Formulation

In this chapter, we will examine the linear instability of straight liquid jets falling under the influence of gravity. We assume that we have a column of an incompressible viscoelastic liquid jet emerging from an orifice which has radius a. We therefore consider this problem by using cylindrical coordinates (r, θ, z), where z lies along the axis of the jet, r is the radial direction and θ is the azimuthal direction. To begin with, we have to determine the equations of motion which are the continuity equation, momentum equation and constitutive equation. We use the Oldroyd-B model to study the viscoelastic liquid

jet. The equations of motion take the form

$$\boldsymbol{\nabla} \cdot \boldsymbol{u} = 0,$$

$$\rho\left(\frac{\partial \boldsymbol{u}}{\partial t} + \boldsymbol{u} \cdot \boldsymbol{\nabla} \boldsymbol{u}\right) = -\boldsymbol{\nabla} p + \boldsymbol{\nabla} \cdot \boldsymbol{\tau} + \rho \boldsymbol{g},$$

$$\boldsymbol{\tau} = \mu_s(\boldsymbol{\nabla} \boldsymbol{u} + (\boldsymbol{\nabla} \boldsymbol{u})^T) + \boldsymbol{T}$$

$$\lambda \boldsymbol{T}^{\triangledown} + \boldsymbol{T} = \mu_p \boldsymbol{\gamma}$$

$$\frac{\partial \boldsymbol{T}}{\partial t} + (\boldsymbol{u} \cdot \boldsymbol{\nabla})\boldsymbol{T} - \boldsymbol{T} \cdot \boldsymbol{\nabla} \boldsymbol{u} - (\boldsymbol{\nabla} \boldsymbol{u})^T \cdot \boldsymbol{T} = \frac{1}{\lambda}(\mu_p \boldsymbol{\gamma} - \boldsymbol{T}), \tag{5.1}$$

where $\boldsymbol{u}$ is the velocity in the form $\boldsymbol{u} = v\mathbf{e_z} + u\mathbf{e_r} + w\mathbf{e}_\phi$, ρ is the density of the fluid, p is the pressure, μ_s is the viscosity of the solvent, $\boldsymbol{g}$ is the acceleration due to gravity, $\boldsymbol{T}$ is the extra stress tensor that represents the elastic contribution to the stresses and μ_p is the viscosity of the polymer. Then the equations of motion are

$$\frac{\partial u}{\partial r} + \frac{\partial v}{\partial z} + \frac{u}{r} = 0, \tag{5.2}$$

$$\rho\left(\frac{\partial u}{\partial t} + v\frac{\partial u}{\partial r} + u\frac{\partial u}{\partial z}\right) = -\frac{\partial p}{\partial z} + \mu_s\left(\frac{1}{r}\frac{\partial}{\partial r}(r\frac{\partial u}{\partial r}) + \frac{\partial^2 u}{\partial z^2}\right) + \frac{\partial T_{zz}}{\partial z} + \rho g, \tag{5.3}$$

$$\rho\left(\frac{\partial v}{\partial t} + v\frac{\partial v}{\partial r} + u\frac{\partial v}{\partial z}\right) = -\frac{\partial p}{\partial r} + \mu_s\left(\frac{\partial}{\partial r}\left(\frac{1}{r}\frac{\partial}{\partial r}(rv)\right) + \frac{\partial^2 v}{\partial z^2}\right) + \frac{1}{r}\frac{\partial}{\partial r}\left(rT_{rr}\right), \tag{5.4}$$

$$\frac{\partial T_{rr}}{\partial t} + v\frac{\partial T_{rr}}{\partial r} + u\frac{\partial T_{rr}}{\partial z} - 2T_{rr}\frac{\partial v}{\partial r} = \frac{1}{\lambda}\left(2\mu_p\frac{\partial v}{\partial r} - T_{rr}\right), \tag{5.5}$$

$$\frac{\partial T_{zz}}{\partial t} + v\frac{\partial T_{zz}}{\partial r} + u\frac{\partial T_{zz}}{\partial z} - 2T_{zz}\frac{\partial u}{\partial z} = \frac{1}{\lambda}\bigg(2\mu_p\frac{\partial u}{\partial z} - T_{zz}\bigg). \tag{5.6}$$

The position of the free surface can be determined by $r - R(z,t) = 0$ and the normal vector is given by $\nabla(r - R(z,t))$, which gives

$$\boldsymbol{n} = \frac{1}{E}\bigg(-\frac{\partial R}{\partial z}\,\boldsymbol{e_z} + \boldsymbol{e_r}\bigg),$$

where

$$E = \bigg(1 + \bigg(\frac{\partial R}{\partial z}\bigg)^2\bigg)^{\frac{1}{2}}.$$

The normal stress condition is $\boldsymbol{n}\cdot\Pi\cdot\boldsymbol{n} = \sigma\kappa$, where Π is the total stress tensor given by $-p\mathbf{I} + \boldsymbol{\tau}$, which can be written as

$$p - 2\mu_s\bigg(\bigg(\frac{\partial R}{\partial z}\bigg)\bigg(\frac{\partial u}{\partial z} + \frac{T_{zz}}{2\mu_s}\bigg) + \frac{\partial v}{\partial r} + \frac{T_{rr}}{2\mu_s} - \frac{\partial R}{\partial z}\bigg(\frac{\partial u}{\partial r} + \frac{\partial v}{\partial z}\bigg)\bigg) = \sigma\kappa, \tag{5.7}$$

where σ is the isotropic surface tension and κ is the mean curvature of the free surface

$$\kappa = \frac{1}{r}\bigg(-\frac{\partial}{\partial z}\bigg(\frac{r}{E}\frac{\partial R}{\partial z}\bigg) + \frac{\partial}{\partial r}\bigg(\frac{r}{E}\bigg)\bigg),$$

the tangential condition $\boldsymbol{t}\cdot\Pi\cdot\boldsymbol{n} = 0$ is

$$\bigg(1 - \bigg(\frac{\partial R}{\partial z}\bigg)\bigg)\bigg(\frac{\partial v}{\partial z} + \frac{\partial u}{\partial r}\bigg) + 2\frac{\partial R}{\partial z}\bigg(\frac{\partial u}{\partial z} - \frac{\partial v}{\partial r} - \frac{1}{2}\bigg(T_{rr} - T_{zz}\bigg)\bigg) = 0, \tag{5.8}$$

and finally the kinematic condition $\frac{D}{Dt}(R(z,t) - r) = 0$ is

$$\frac{\partial R}{\partial t} - v + u\frac{\partial R}{\partial z} = 0. \tag{5.9}$$

5.2 Nondimensionalization

We non-dimensionalize our equations by using the following transformations

$$\overline{z} = \frac{z}{L}, \quad \overline{r} = \frac{r}{a}, \quad \overline{t} = \frac{U}{L}t, \quad \overline{p} = \frac{1}{U^2\rho}p, \quad \varepsilon = \frac{a}{L},$$

$$\overline{u} = \frac{u}{U}, \quad \overline{v} = \frac{v}{U}, \quad \overline{R} = \frac{R}{a}, \quad \overline{T} = \frac{L}{U\mu_0}T,$$

where u and v are the axial and the radial velocity components, U is the exit speed of the jet, a is radius of the orifice, L is an axial length scale, T is the extra stress tensor and μ_0 is the total of the viscosity, and then we drop overbars to get the following dimensionless parameters where $Re = \frac{U\rho a}{\mu_0}$ is the Reynolds number(= inertia force/viscosity force), $\alpha_s = \frac{\mu_s}{\mu_0}$ is the viscosity ratio, $We = \frac{\rho U^2 a}{\sigma}$ is the Weber number (= inertia force/surface tension force), $F = \frac{U}{\sqrt{ga}}$ is the Froude number (= inertia force/gravity force) and $De = \frac{\lambda U}{L}$ is the Deborah number (= relaxation time /observation time). The equations therefore become

$$\frac{\partial v}{\partial r} + \varepsilon\frac{\partial u}{\partial z} + \frac{v}{r} = 0, \tag{5.10}$$

$$\left(\varepsilon\frac{\partial u}{\partial t} + v\frac{\partial u}{\partial r} + \varepsilon u\frac{\partial u}{\partial z}\right) = -\varepsilon\frac{\partial p}{\partial z} + \frac{\alpha_s}{Re}\left(\frac{1}{r}\frac{\partial u}{\partial r} + \frac{\partial^2 u}{\partial r^2} + \varepsilon^2\frac{\partial^2 u}{\partial z^2}\right) + \frac{1}{Re}\left(\varepsilon\frac{\partial T_{zz}}{\partial z}\right) + \frac{1}{F^2}, \tag{5.11}$$

$$\left(\varepsilon\frac{\partial v}{\partial t} + v\frac{\partial v}{\partial r} + \varepsilon u\frac{\partial v}{\partial z}\right) = -\frac{\partial p}{\partial r} + \frac{\alpha_s}{Re}\left(\frac{1}{r}\frac{\partial v}{\partial r} - \frac{v}{r^2} + \frac{\partial^2 v}{\partial r^2} + \varepsilon^2\frac{\partial^2 v}{\partial z^2}\right) + \frac{1}{Re}\left(\frac{T_{rr}}{r} + \frac{\partial T_{rr}}{\partial r}\right), \tag{5.12}$$

$$\frac{\partial T_{rr}}{\partial t}+\frac{v}{\varepsilon}\frac{\partial T_{rr}}{\partial r}+u\frac{\partial T_{rr}}{\partial z}-\frac{2}{\varepsilon}T_{rr}\frac{\partial v}{\partial r}=\frac{1}{De}\bigg(\frac{2(1-\alpha_s)}{\varepsilon}\frac{\partial v}{\partial r}-T_{rr}\bigg), \tag{5.13}$$

$$\frac{\partial T_{zz}}{\partial t}+\frac{v}{\varepsilon}\frac{\partial T_{zz}}{\partial r}+u\frac{\partial T_{zz}}{\partial z}-2T_{zz}\frac{\partial u}{\partial z}=\frac{1}{De}\bigg(2(1-\alpha_s)\frac{\partial u}{\partial z}-T_{zz}\bigg). \tag{5.14}$$

The normal stress condition is

$$\begin{aligned}&p-\frac{2\alpha_s}{Re}\bigg(\varepsilon^2\bigg(\frac{\partial R}{\partial z}\bigg)\bigg(\frac{\partial u}{\partial z}+\frac{T_{zz}}{2\alpha_s}\bigg)+\frac{1}{\varepsilon}\frac{\partial v}{\partial r}+\frac{T_{rr}}{2\alpha_s}-\\&\varepsilon\frac{\partial R}{\partial z}\bigg(\frac{1}{\varepsilon}\frac{\partial u}{\partial r}+\frac{\partial v}{\partial z}\bigg)\bigg)=\frac{\kappa}{We},\end{aligned} \tag{5.15}$$

where

$$\kappa=\frac{1}{r}\bigg(-\varepsilon^2\frac{\partial}{\partial z}\bigg(\frac{r}{E}\frac{\partial R}{\partial z}\bigg)+\frac{\partial}{\partial r}(\frac{r}{E})\bigg),$$

the tangential condition is

$$\bigg(1-\varepsilon^2\bigg(\frac{\partial R}{\partial z}\bigg)^2\bigg)\bigg(\varepsilon\frac{\partial v}{\partial z}+\frac{\partial u}{\partial r}\bigg)+2\varepsilon\frac{\partial R}{\partial z}\bigg(\varepsilon\frac{\partial u}{\partial z}-\frac{\partial v}{\partial r}-\frac{\varepsilon}{2}\bigg(T_{rr}-T_{zz}\bigg)\bigg)=0 \tag{5.16}$$

and the kinematic condition is

$$\varepsilon\frac{\partial R}{\partial t}-v+\varepsilon u\frac{\partial R}{\partial z}=0. \tag{5.17}$$

5.3 Asymptotic Analysis

We expand u, v, p in Taylor series in εr (see Eggers (1997) and Hohman *et al.* (1984)) and R, T_{zz}, T_{rr} in ε.

$$\begin{aligned}
u &= u_0(z,t) + (\varepsilon\, r)u_1(z,t) + ... \\
v &= (\varepsilon\, r)v_1(z,t) + (\varepsilon\, r)^2 v_2(z,t) + ... \\
p &= p_0(z,t) + (\varepsilon\, r)p_1(z,t) + ... \\
R &= R_0(z,t) + \varepsilon R_1(z,t) + ... \\
T_{zz} &= T^0_{zz}(z,t) + \varepsilon\, T^1_{zz}(z,t) + ... \\
T_{rr} &= T^0_{rr}(z,t) + \varepsilon\, T^1_{rr}(z,t) + ...
\end{aligned}$$

We substitute these asymptotic expansions in the equations of motion. We can therefore find from the equation of continuity

$$O(\varepsilon) : \frac{\partial u_0}{\partial z} = -2v_1. \tag{5.18}$$

We may also obtain from the equation of motion in axial direction at leading order,

$$\frac{\partial u_0}{\partial t} + u_0\frac{\partial u_0}{\partial z} = -\frac{\partial p_0}{\partial z} + \frac{\alpha_s}{Re}\left(4u_2 + \frac{\partial^2 u_0}{\partial z^2}\right) + \frac{1}{Re}\frac{\partial T^0_{zz}}{\partial z} + \frac{1}{F^2}. \tag{5.19}$$

From the tangential condition we have

$$\begin{aligned}
&u_1 = 0, \\
&u_2 = \frac{1}{4}\frac{\partial^2 u_0}{\partial z^2} + \frac{3}{2R_0}\frac{\partial R_0}{\partial z}\frac{\partial u_0}{\partial z} + \frac{1}{2R_0}\left(T^0_{zz} - T^0_{rr}\right).
\end{aligned} \tag{5.20}$$

from the normal stress condition we get

$$p_0 = -\frac{\alpha_s}{Re}\frac{\partial u_0}{\partial z} + \frac{1}{R_0 We} + \frac{T^0_{rr}}{Re},$$
$$p_1 = -\frac{R_1}{R_0^2} + \frac{4v_2}{R_0}. \tag{5.21}$$

Now we substitute p_0 and u_2 into Eq. (5.20), then it becomes

$$\frac{\partial u_0}{\partial t} + u_0\frac{\partial u_0}{\partial z} = -\frac{\partial}{\partial z}\left(\frac{1}{R_0 We}\right) + \frac{3\alpha_s}{R_0^2 Re}\frac{\partial}{\partial z}\left(R_0^2\frac{\partial u_0}{\partial z}\right) +$$
$$\frac{1}{R_0^2 Re}\frac{\partial}{\partial z}\left(R_0^2(T_{zz} - T_{rr})\right) + \frac{1}{F^2}. \tag{5.22}$$

And the kinematic condition is

$$O(\varepsilon): \quad \frac{\partial R}{\partial t} + \frac{\partial u_0}{2\partial z}R + u_0\frac{\partial R_0}{\partial z} = 0. \tag{5.23}$$

From the extra stress tensor in the radial and axial directions at leading order, we have

$$\frac{\partial T^0_{rr}}{\partial t} + u_0\frac{\partial T^0_{rr}}{\partial z} - \frac{2}{\varepsilon}T^0_{rr}\frac{\partial}{\partial r}(\varepsilon r v_1) = \frac{1}{De}\left(\frac{2(1-\alpha_s)}{\varepsilon}\frac{\partial}{\partial r}(\varepsilon r v_1) - T^0_{rr}\right), \tag{5.24}$$

$$\frac{\partial T^0_{zz}}{\partial t} + u_0\frac{\partial T^0_{zz}}{\partial z} - 2T^0_{zz}\frac{\partial u_0}{\partial z} = \frac{1}{De}\left(2(1-\alpha_s)\frac{\partial u_0}{\partial z} - T^0_{zz}\right), \tag{5.25}$$

which substituting from Eq. (5.19) into the last equation, we get

$$\frac{\partial T^0_{rr}}{\partial t} + u_0\frac{\partial T^0_{rr}}{\partial z} + T^0_{rr}\frac{\partial u_0}{\partial z} = \frac{1}{De}\left(-(1-\alpha_s)\frac{\partial u_0}{\partial z} - T^0_{rr}\right). \tag{5.26}$$

When $F \to \infty$, the equations (5.22), (5.25) and (5.26) are the same as those found by Clasen *et al.* (2006).

5.4 Steady State Solutions

Now we look for steady state solutions by considering all the variables to be a function of z. Thus, steady state solutions are given by solutions to

$$u_0\frac{\partial u_0}{\partial z} = -\frac{\partial}{\partial z}\left(\frac{1}{R_0We}\right) + \frac{3\alpha_s}{R_0^2\,Re}\frac{\partial}{\partial z}\left(R_0^2\frac{\partial u_0}{\partial z}\right) + \frac{1}{R_0^2Re}\frac{\partial}{\partial z}\left(R_0^2(T^0_{zz} - T^0_{rr})\right) + \frac{1}{F^2}. \tag{5.27}$$

$$\frac{1}{2}\frac{\partial u_0}{\partial z}R + u_0\frac{\partial R_0}{\partial z} = 0. \tag{5.28}$$

From Eq. (5.28), we can see that $R_0^2u_0 =$ constant, and now we use last expression to write our equations in the form

$$u_0\frac{\partial u_0}{\partial z} = -\frac{1}{2We}\frac{1}{\sqrt{u_0}}\frac{\partial u_0}{\partial z} + \frac{3\alpha_s}{Re}\left(\frac{\partial^2 u_0}{\partial z^2} - \frac{u_{0z}^2}{u_0}\right) + \frac{1}{Re}\left(\frac{\partial}{\partial z}(T^0_{zz} - T^0_{rr}) - \frac{1}{u_0}\frac{\partial u_0}{\partial z}(T^0_{zz} - T^0_{rr})\right) + \frac{1}{F^2}. \tag{5.29}$$

$$u_0\frac{\partial T^0_{rr}}{\partial z} + T^0_{rr}\frac{\partial u_0}{\partial z} = \frac{1}{De}\left(- (1-\alpha_s)\frac{\partial u_0}{\partial z} - T^0_{rr}\right), \tag{5.30}$$

$$u_0\frac{\partial T^0_{zz}}{\partial z} - 2T^0_{zz}\frac{\partial u_0}{\partial z} = \frac{1}{De}\left(2(1-\alpha_s)\frac{\partial u_0}{\partial z} - T^0_{zz}\right), \tag{5.31}$$

we can see that Eqs. (5.29)-(5.31) have three unknowns which are u_0, T^0_{zz} and T^0_{rr}. To solve this system of equations, we apply a second order finite difference scheme to discretize Eqs. (5.29)-(5.31). We also specify the boundary condition at the nozzle as

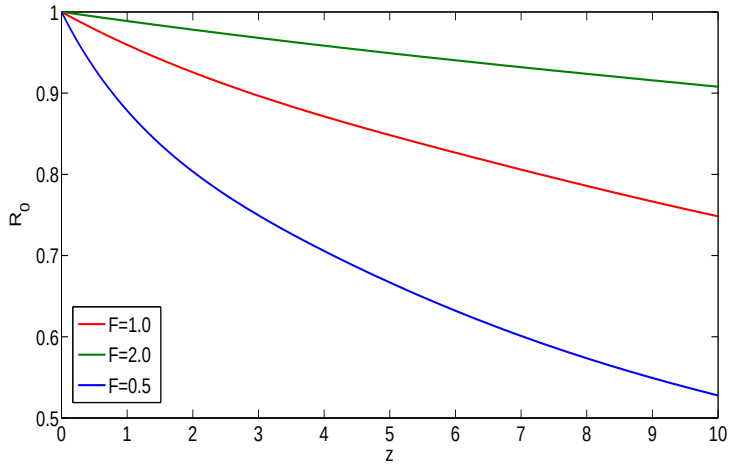

Figure 5.1: Graph showing the steady radius R_0 versus z for different values of the Froude number F for viscoelastic liquid jets. Here the parameters are $We = 10$, $Re = 20$,$De = 10$ and $\alpha_s = 0.20$.

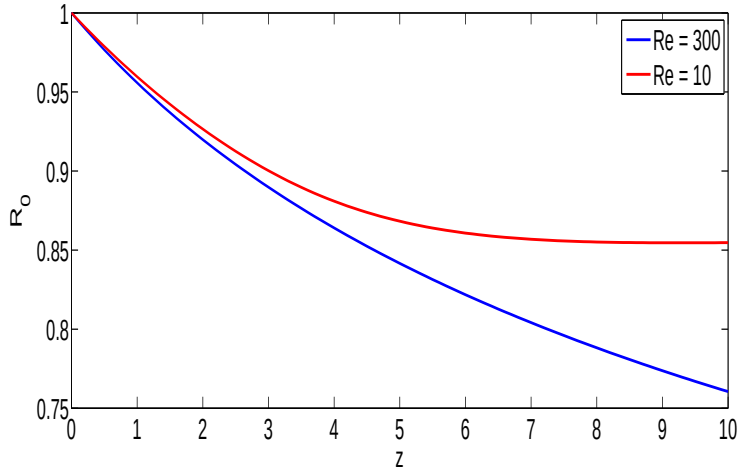

Figure 5.2: Graph showing the steady radius R_0 versus z for two different values of the Reynolds number Re for viscoelastic liquid jets. Here the parameters are $We = 10$, $De = 10$, $\alpha_s = 0.20$ and $F = 1$.

$u(0) = 1$ and $T^0_{zz}(0) = T^0_{rr}(0) = 0$ and the downstream boundary condition is obtained by quadratic extrapolation of the last interval mash point. The nonlinear Eqs. (5.29)-(5.31) are solved at each step using a modified Newton's method. Here we only compute the Jacobian for the first iteration, so the guess at the next step uses the previous calculated

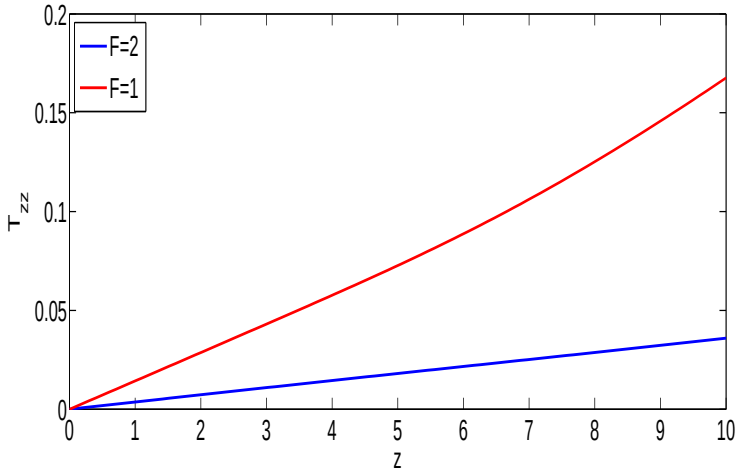

Figure 5.3: Graph showing the steady stress tensor T^0_{zz} versus z for two different values of the Froude number F for viscoelastic liquid jets. Here the parameters are $We = 10$, $Re = 20$, $De = 10$ and $\alpha_s = 0.20$.

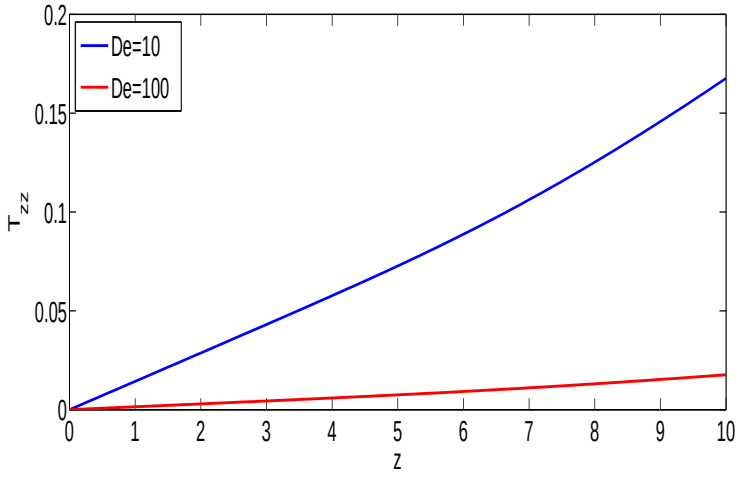

Figure 5.4: Graph showing the steady stress tensor T^0_{zz} versus z for two different values of the Deborah number De for viscoelastic liquid jets. Here the parameters are $We = 10$, $Re = 20$, $\alpha_s = 0.20$ and $F = 1$.

solution. A similar approach was used by Părău *et al.* (2007) for the case of spiralling liquid jets. The numerical accuracy can be checked by varying the grid interval ds and mash points M and it was found that the results are dependent of ds and M when $ds < 0.1$ and $M > 200$. In Figs. 5.1 to 5.6 we plot graphs to show the effects of gravity

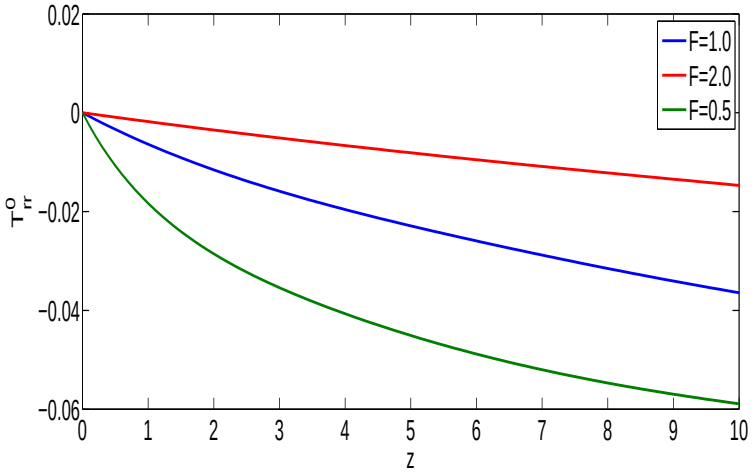

Figure 5.5: Graph showing the steady stress tensor T^0_{rr} versus z for two different values of the Froude number F for viscoelastic liquid jets. Here the parameters are $We = 10$, $Re = 20$, $De = 10$ and $\alpha_s = 0.20$.

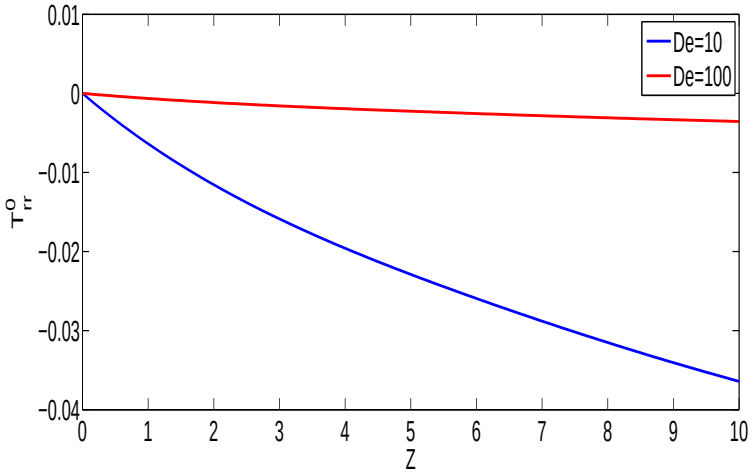

Figure 5.6: Graph showing the steady stress tensor T^0_{rr} versus z for two different values of the Deborah number De for viscoelastic liquid jets. Here the parameters are $We = 10$, $Re = 20$, $\alpha_s = 0.20$ and $F = 1$. It can be seen that when $De = 100$ the values of T^0_{rr} are very small which are not equal to 0.

on the radius and the extra stress tensor T^0_{rr} of viscoelastic liquid jets emerging from a nozzle as we move down the jet. We found from these graphs that when gravity increases (meaning the Froude number F decreases), the radius of the jet thins more quickly and this result shows that gravity affects the jet as expected. In Fig. 5.2 we investigate the

effect of viscosity. We can observe from this graph that when the viscosity increases, the jet becomes slower. In addition, we plot a graph to show the influence of varying the Froude number on the extra stress tensor T^0_{zz} along the jet and we notice that when the Froude number increases, the extra stress tensor T^0_{zz} decreases along the z-direction (see Fig. 5.3). Moreover, the relationship between T^0_{zz} and z for different values of the Deborah number De is plotted in Fig. 5.4. It can be noticed from this graph when the Deborah number increases, the extra stress tensor T^0_{zz} decreases. In Fig. 5.6 we can see that increasing the Deborah number leads to an increase in the extra stress tensor T^0_{rr} along the viscoelastic liquid jet.

5.5 Temporal Instability of the Steady State Solutions

We make a perturbation about the steady state solutions which are obtained from the previous section as follows

$$\mathbf{u} = \mathbf{u}(z, r) + \delta\widehat{\mathbf{u}}(z, r, t),$$

$$R = R(z) + \delta\widehat{R}(z, r, t),$$

$$T_{zz} = T_{zz}(z, r) + \delta\widehat{T}_{zz}(z, r, t),$$

$$T_{rr} = T_{rr}(z, r) + \delta\widehat{T}_{rr}(z, r, t),$$

$$p = p(z, r) + \delta\widehat{p}(z, r, t),$$

where $\mathbf{u} = \widehat{u}\mathbf{e_z} + \widehat{v}\mathbf{e_r}$ and δ is a small dimensionless number. Now we substitute these expressions into (5.10)-(5.17) and we keep terms of order delta, we therefore have

$$\frac{\partial \widehat{v}}{\partial r} + \varepsilon \frac{\partial \widehat{u}}{\partial z} + \frac{\widehat{v}}{r} = 0, \tag{5.32}$$

$$\left(\varepsilon \frac{\partial \widehat{u}}{\partial t} + v\frac{\partial \widehat{u}}{\partial r} + \widehat{v}\frac{\partial u}{\partial r} + \varepsilon u \frac{\partial \widehat{u}}{\partial z} + \varepsilon \widehat{u}\frac{\partial u}{\partial z}\right) = -\varepsilon \frac{\partial \widehat{p}}{\partial z} + \frac{\alpha_s}{Re}\left(\frac{1}{r}\frac{\partial \widehat{u}}{\partial r} + \frac{\partial^2 \widehat{u}}{\partial r^2} + \varepsilon^2 \frac{\partial^2 \widehat{u}}{\partial z^2}\right) + \frac{1}{Re}\left(\varepsilon \frac{\partial \widehat{T}_{zz}}{\partial z}\right), \tag{5.33}$$

$$\left(\varepsilon \frac{\partial \widehat{v}}{\partial t} + v\frac{\partial \widehat{v}}{\partial r} + \widehat{v}\frac{\partial v}{\partial r} + \varepsilon u \frac{\partial \widehat{v}}{\partial z} + \varepsilon \widehat{u}\frac{\partial v}{\partial z}\right) = -\frac{\partial \widehat{p}}{\partial r} + \frac{\alpha_s}{Re}\left(\frac{1}{r}\frac{\partial \widehat{v}}{\partial r} - \frac{\widehat{v}}{r^2} + \frac{\partial^2 \widehat{v}}{\partial r^2} + \varepsilon^2 \frac{\partial^2 \widehat{v}}{\partial z^2}\right) + \frac{1}{Re}\left(\frac{\widehat{T}_{rr}}{r} + \frac{\partial \widehat{T}_{rr}}{\partial r}\right), \tag{5.34}$$

$$\frac{\partial \widehat{T}_{rr}}{\partial t} + \frac{1}{\varepsilon}\left(v\frac{\partial \widehat{T}_{rr}}{\partial r} + \widehat{v}\frac{\partial T_{rr}}{\partial r}\right) + u\frac{\partial \widehat{T}_{rr}}{\partial z} + \widehat{u}\frac{\partial T_{rr}}{\partial z} - \frac{2}{\varepsilon}\left(T_{rr}\frac{\partial \widehat{v}}{\partial r} + \widehat{T}_{rr}\frac{\partial v}{\partial r}\right) = \frac{1}{De}\left(\frac{2(1-\alpha_s)}{\varepsilon}\frac{\partial \widehat{v}}{\partial r} - \widehat{T}_{rr}\right), \tag{5.35}$$

$$\frac{\partial T_{zz}}{\partial t} + \frac{1}{\varepsilon}\left(\widehat{v}\frac{\partial T_{zz}}{\partial r} + v\frac{\partial \widehat{T}_{zz}}{\partial r}\right) + \widehat{u}\frac{\partial T_{zz}}{\partial z} + u\frac{\partial \widehat{T}_{zz}}{\partial z} - 2\left(\widehat{T}_{zz}\frac{\partial u}{\partial z} + T_{zz}\frac{\partial \widehat{u}}{\partial z}\right) = \frac{1}{De}\left(2(1-\alpha_s)\frac{\partial \widehat{u}}{\partial z} - \widehat{T}_{zz}\right). \tag{5.36}$$

The normal stress condition is

$$\widehat{p} - \frac{2\alpha_s}{Re}\left(\frac{1}{\varepsilon}\frac{\partial \widehat{v}}{\partial r} + \frac{\widehat{T}_{rr}}{2\alpha_s}\right) = \frac{1}{We}\left(-\frac{\widehat{R}}{R_0^2} - \frac{\partial^2 \widehat{R}}{\partial z^2}\right). \tag{5.37}$$

The tangential condition is

$$\left(\frac{\partial \widehat{v}}{\partial z}+\frac{1}{\varepsilon}\frac{\partial \widehat{u}}{\partial r}\right)=0, \tag{5.38}$$

and the kinematic condition is

$$\varepsilon\frac{\partial \widehat{R}}{\partial t}-\widehat{v}+\varepsilon\left(u\frac{\partial \widehat{R}}{\partial z}+\widehat{u}\frac{\partial u}{\partial z}\right)=0. \tag{5.39}$$

The length scale over which the jet develops is $z = 0(1)$, but disturbances which are caused by instability are very small which is of order a (that is comparable with ε when $z = O(1)$) and this was used by many authors, such as Wallwork (2002b) and Uddin (2007). Then we consider the travelling wave modes of the form $exp(ik\overline{z} + \lambda\overline{t})$, where $\overline{z} = z/\varepsilon$, $\overline{t} = t/\varepsilon$, $k = k(z) = O(1)$ and $\lambda = \lambda(z) = O(1)$ then we make the substitutions

$$\begin{aligned}
\widehat{\mathbf{u}} &= \tilde{\mathbf{u}}(z,\overline{z},r,t,\overline{t}),\\
\widehat{R} &= \tilde{R}(z,\overline{z},t,\overline{t}),\\
\widehat{T}_{zz} &= \tilde{T_{zz}}(z,\overline{z},r,t,\overline{t}),\\
\widehat{T}_{rr} &= \tilde{T_{rr}}(z,\overline{z},r,t,\overline{t}),\\
\widehat{p} &= \tilde{p}(z,\overline{z},r,t,\overline{t}),
\end{aligned} \tag{5.40}$$

where $\widehat{\mathbf{u}} = \tilde{u}\mathbf{e_z}+\tilde{v}\mathbf{e_n}$. We substitute these expressions into Eqs.(5.34)-(5.42). We therefore

obtain at leading order

$$\frac{\partial \tilde{v}}{\partial r} + \frac{\partial \tilde{u}}{\partial \overline{z}} + \frac{\tilde{v}}{r} = 0, \tag{5.41}$$

$$\left(\frac{\partial \tilde{u}}{\partial \overline{t}} + u\frac{\partial \tilde{u}}{\partial \overline{z}}\right) = -\frac{\partial \tilde{p}}{\partial \overline{z}} + \frac{\alpha_s}{Re}\left(\frac{1}{r}\frac{\partial \tilde{u}}{\partial r} + \frac{\partial^2 \tilde{u}}{\partial r^2} + \frac{\partial^2 \tilde{u}}{\partial \overline{z}^2}\right) + \frac{1}{Re}\left(\frac{\partial \tilde{T}_{zz}}{\partial \overline{z}}\right), \tag{5.42}$$

$$\left(\frac{\partial \tilde{v}}{\partial \overline{t}} + u\frac{\partial \tilde{v}}{\partial z}\right) = -\frac{\partial \tilde{p}}{\partial r} + \frac{\alpha_s}{Re}\left(\frac{1}{r}\frac{\partial \tilde{v}}{\partial r} - \frac{\tilde{v}}{r^2} + \frac{\partial^2 \tilde{v}}{\partial r^2} + \frac{\partial^2 \tilde{v}}{\partial \overline{z}^2}\right) + \frac{1}{Re}\left(\frac{\tilde{T}_{rr}}{r} + \frac{\partial \tilde{T}_{rr}}{\partial r}\right), \tag{5.43}$$

$$\frac{\partial \tilde{T}_{rr}}{\partial \overline{t}} + u\frac{\partial \tilde{T}_{rr}}{\partial \overline{z}} - 2T_{rr}\frac{\partial \tilde{v}}{\partial r} = \frac{1}{De}\left(2(1-\alpha_s)\frac{\partial \tilde{v}}{\partial r}\right), \tag{5.44}$$

$$\frac{\partial \tilde{T}_{zz}}{\partial \overline{t}} + u\frac{\partial \tilde{T}_{zz}}{\partial \overline{z}} - 2T_{zz}\frac{\partial \tilde{u}}{\partial \overline{z}} = \frac{1}{De}\left(2(1-\alpha_s)\frac{\partial \tilde{u}}{\partial \overline{z}}\right), \tag{5.45}$$

the normal stress condition is

$$\tilde{p} - \frac{2\alpha_s}{Re}\left(\frac{\partial \tilde{v}}{\partial r} + \frac{\tilde{T}_{rr}}{2\alpha_s}\right) = \frac{1}{We}\left(-\frac{\tilde{R}}{R_0^2} - \frac{\partial^2 \tilde{R}}{\partial \overline{z}^2}\right). \tag{5.46}$$

The tangential condition is

$$\left(\frac{\partial \tilde{v}}{\partial \overline{z}} + \frac{\partial \tilde{u}}{\partial r}\right) = 0, \tag{5.47}$$

and the kinematic condition is

$$\frac{\partial \tilde{R}}{\partial \overline{t}} - \tilde{v} + \left(u\frac{\partial \tilde{R}}{\partial \overline{z}} + \tilde{u}\frac{\partial u}{\partial \overline{z}}\right) = 0. \tag{5.48}$$

We will look for general solutions by using the form

$$\tilde{u} = (exp(ik(z)\overline{z} + \lambda(z)\bar{t}))\overline{u},$$

$$\tilde{v} = i(exp(ik(z)\overline{z} + \lambda(z)\bar{t}))\overline{v},$$

$$\tilde{T}_{zz} = (exp(ik(z)\overline{z} + \lambda(z)\bar{t}))\overline{T}_{zz},$$

$$\tilde{T}_{rr} = (exp(ik(z)\overline{z} + \lambda(z)\bar{t}))\overline{T}_{rr},$$

$$\tilde{p} = (exp(ik(z)\overline{z} + \lambda(z)\bar{t}))\overline{p},$$

$$\tilde{R} = (exp(ik(z)\overline{z} + \lambda(z)\bar{t}))\overline{R}, \tag{5.49}$$

we substitute these expressions into the equations (5.41)-(5.48) and we find that

$$\frac{\partial\overline{v}}{\partial r} + ik\overline{u} + \frac{\overline{v}}{r} = 0, \tag{5.50}$$

$$(\lambda + iku_0)\overline{u} = -ik\overline{p} + \frac{\alpha_s}{Re}\left(\frac{1}{r}\frac{\partial\overline{u}}{\partial r} + \frac{\partial^2\overline{u}}{\partial r^2} - k^2\overline{u}\right) + \frac{1}{Re}\left(ik\overline{T}_{zz}\right), \tag{5.51}$$

$$(\lambda + iku_0)\overline{v} = -i\frac{\partial\overline{p}}{\partial r} + \frac{\alpha_s}{Re}\left(\frac{1}{r}\frac{\partial\overline{v}}{\partial r} - \frac{\overline{v}}{r^2} + \frac{\partial^2\overline{v}}{\partial r^2} - k^2\overline{v}\right) +$$
$$\frac{1}{Re}\left(\frac{\overline{T}_{rr}}{r} + \frac{\partial\overline{T}_{rr}}{\partial r}\right), \tag{5.52}$$

$$(\lambda + iku_0)\overline{T}_{zz} = \left(2ikT^0_{zz} + \frac{2}{De}(1-\alpha_s)ik\right)\overline{u}, \tag{5.53}$$

$$(\lambda + iku_0)\overline{T}_{rr} = \left(\frac{2(1-\alpha_s)}{De} + 2T^0_{rr}\right)\frac{\partial\overline{v}}{\partial r}, \tag{5.54}$$

$$\overline{p} - \frac{\overline{T}_{rr}}{Re} = \frac{1}{We}\left(-\frac{1}{R_0^2} + k^2\right)\overline{R}, \tag{5.55}$$

$$(\lambda + iku_0)\overline{R} = \overline{u}. \tag{5.56}$$

The solutions for these equations are

$$\overline{u} = A_1(z)I_0(kR_0) - A_2(z)\tilde{k}I_0(\tilde{k}R_0), \tag{5.57}$$

$$\overline{v} = A_1(z)\frac{1}{k}I_1(kR_0) - A_2(z)\frac{k}{\tilde{k}}I_1(\tilde{k}R_0), \tag{5.58}$$

$$\overline{p} = -A_1(z)\frac{\lambda + iku_0}{k}I_0(kR_0) - \frac{1}{Re(\lambda + iku_0)}\left(\frac{(1-\alpha_s)}{De} + T^0_{zz}\right)\Big(A_1I_1(kR_0) - A_2kI_1(\tilde{k}R_0)\Big), \tag{5.59}$$

where $\tilde{k} = k^2 + \frac{Re}{\alpha_s}(\lambda + iku_0)$, A_1 and A_2 are constants and I_0, I_1 are zeroth and first modified Bessel functions respectively. From the boundary conditions, we have

$$\overline{R} = \frac{\overline{u}}{\lambda + iku_0},$$

$$\overline{p} - \frac{2\alpha_s}{Re}\frac{\partial\overline{u}}{\partial r} - \frac{1}{Re(\lambda + iku_0)}\left(\frac{(1-\alpha_s)}{De} + T^0_{rr}\right)\frac{\partial\overline{u}}{\partial r} = \frac{\overline{R}}{We}\left(k^2 - \frac{1}{R^2}\right)$$

and

$$k\overline{u} + \frac{\partial\overline{v}}{\partial r} = 0.$$

Now we substitute the previous solutions into the boundary condition so that we obtain (after considerable algebra) the dispersion relation as follows

$$\tilde{\lambda^2} + \frac{2\alpha_s k^2}{Re}\left(1 + \frac{(1-\alpha_s)}{De\lambda} + T^0_{zz} + T^0_{rr}\right)\left\{\frac{I_1'(kR_0)}{I_0(kR_0)} - \frac{2k\tilde{k}I_1'(k'R_0)I_1(kR_0)}{I_1(k'R_0)(k^2+\tilde{k}^2)}\right\}\tilde{\lambda} = \frac{k}{We}\left(\frac{1}{R_0^2} - k^2\right)\frac{I_1(kR_0)(\tilde{k}^2 - k^2)}{I_0(kR_0)(\tilde{k}^2 + k^2)}, \tag{5.60}$$

where $\tilde{\lambda} = \lambda + iku_0$ and $\tilde{k} = k^2 + \frac{Re}{\alpha_s}(\lambda + iku_0)$.

When $\alpha_s = 1$ and $T^0_{zz} = T^0_{rr} = 0$, we have the same dispersion relation for Newtonian liquid jets as found by Weber (1931), namely

$$\left(\lambda + iku_0\right)^2 + \frac{2k^2}{Re}\left\{\frac{I_1'(kR_0)}{I_0(kR_0)} - \frac{2k\tilde{k}I_1'(k'R_0)I_1(kR_0)}{I_1(k'R_0)(k^2+\tilde{k}^2)}\right\}\left(\lambda + iku_0\right)$$
$$= \frac{k}{We}\left(\frac{1}{R_0^2} - k^2\right)\frac{I_1(kR_0)(\tilde{k}^2 - k^2)}{I_0(kR_0)(\tilde{k}^2 + k^2)}, \tag{5.61}$$

where

$$\tilde{k} = k^2 + Re(\lambda + iku_0).$$

In addition, our equation (5.60) can be reduced to inviscid liquid jets when $Re \to \infty$ and then we obtain Rayleigh's famous result

$$\left(\lambda + iku_0\right)^2 = \frac{k}{We}\left(\frac{1}{R_0^2} - k^2\right)\frac{I_1(kR_0)}{I_0(kR_0)}. \tag{5.62}$$

5.6 Results and Discussions

To investigate the temporal instability, the dispersion relation (5.60) has λ which is complex and k is real. Here we are interested in describing the temporal instability so that $\Re(\lambda) > 0$. Therefore, we solve this dispersion relation (5.60) by using Newton's method to find the most unstable wavenumber $k = k^*(z)$, which corresponds to the maximum growth rate for each z. It is known (see Wallwork (2002a) and Uddin (2007)) that the most unstable wavenumber varies along the jet. In Fig. 5.7 we show the relationship between the growth rate and the wavenumber of viscoelastic liquid jets for different values of the Reynolds number Re. We can notice from this graph that when we decrease the Reynolds number which means increasing the viscosity, the growth rate decreases, which will correspond to a longer jet. In addition, the effects of increasing the Reynolds number on the maximum growth rate have been plotted in Fig. 5.8. In this figure we choose

two different values of the Reynolds number which are $Re = 20$ and 40 and the rest of the parameter are fixed. We can also see from this figure that the maximum growth rate increases, when the Reynolds number decreases (see at $Re = 40$). Fig. 5.9 shows that increasing the Weber number We leads to a decrease in the growth rate. In Figs. 5.10 and 5.11 we can see that increasing the Weber number leads to a decrease in the wavenumber of the most unstable mode and the maximum growth rate along the viscoelastic jet.

To see how the Deborah number affects the linear instability behaviour, we plot graphs to show the relationship between the maximum growth rate disturbance and the wavenumber of the most unstable mode for different values of the Deborah number De (see Figs. 5.12 and 5.13). It can be observed from these graphs that when we increase the Deborah number, the maximum growth rate and the most unstable mode increase along the jet. Thus, these results confirm that when the Deborah number decreases, the growth rate decreases which means when the Deborah number is equal to 0, the corresponding disturbance growth rate of viscoelastic jets will return to Newtonian liquid jets. This was reported by Brenn *et al.* (2000).

Here we look at studying the viscosity ratio α_s on linear instability of viscoelastic liquid jets. We plot a graph to study the relationship between the growth rate and the wavenumber for different values of the viscosity ratio (see Fig. 5.14). In Fig. 5.15 we display the wavenumber of the most unstable mode against the axial direction. We can notice from this graph that when the viscosity ratio increases, the wavenumber of the most unstable mode decreases along the jet. We find the same result in the case of plotting the relationship between the maximum growth rate and the z direction (see Fig. 5.16). In order to examine the influence of the Froude number F on the linear instability behaviour, we display two graphs (Figs. 5.17 and 5.18) to investigate the wavenumber of the most unstable mode versus the axial direction z (see Fig. 5.17) and the maximum growth rate against the axial direction z for different values of the Froude number F. From these

graphs we can see that when the Froude number F decreases (meaning the gravitational force increases), the wavenumber of the most unstable mode and the maximum growth rate increase along the jet. For example, when the Froude number F is equal to 0.5, the wavenumber of the most unstable mode and the maximum growth rate have greater values in comparison with the Froude number F at 1. It can therefore be seen from Figs. 5.17 and 5.18 that gravity has affected the stability of viscoelastic liquid jets as we expected.

Furthermore, Fig. 5.19 shows that viscoelastic liquid jets exhibit a larger growth rate than a viscous liquid jet and a slower growth rate than an inviscid liquid jet. This result agrees with the same finding reported by Goldin *et al.* (1969). In general, viscosity and elasticity of non-Newtonian liquid jets are much more complicated in the behaviour to linear instability than Newtonian jets. Moreover, the viscosity stabilizes the jet in comparison with inviscid jets, as we can see in Fig. 5.19 the disturbance growth rate decreases for Newtonian jets, whereas viscoelastic jets result in a destabilization comparison with Newtonian jets.

The area between the growth rate of inviscid jets and viscoelastic jets is due to the interaction of the viscosity and elasticity on non-Newtonian fluids, which is called the viscoelasticity-induced region, whereas the area between viscous jets and viscoelastic jets are elasticity-induced region (see Brenn *et al.* (2000)).

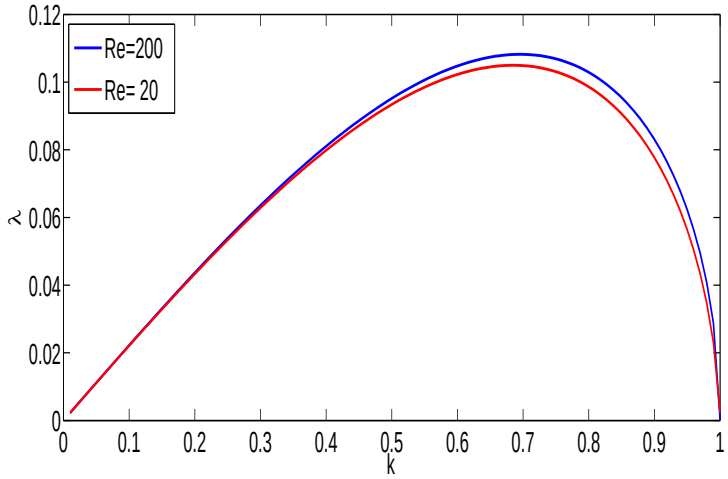

Figure 5.7: Graph showing the relationship between the growth rate λ and the wavenumber k of viscoelastic liquid jets for various Re. Here the parameters are $We = 10$, $Re = 30$, $De = 10$.

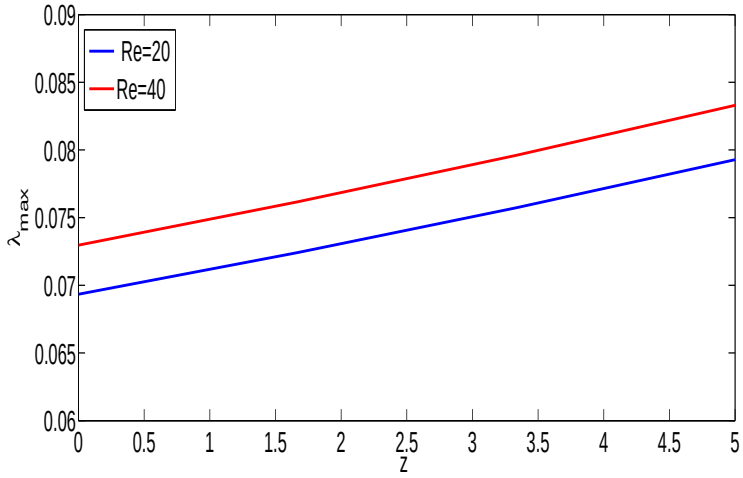

Figure 5.8: Graph showing the relationship between the maximum growth rate λ_{max} against z of viscoelastic liquid jets for different values of the Reynolds number Re. Here the parameters are $We = 10$, $De = 10$, $\alpha_s = 0.20$ and $F = 1$.

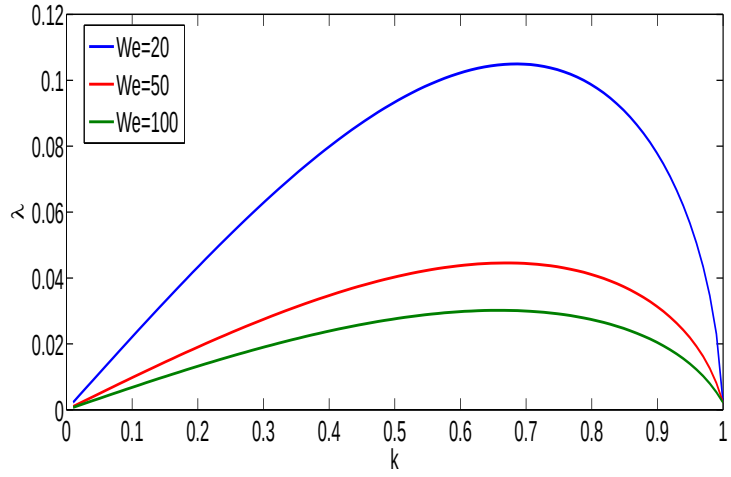

Figure 5.9: Graph showing the relationship between the growth rate λ and the wavenumber k of viscoelastic liquid jets for various We. Here the parameters are $We = 10$, $Re = 30$, $De = 10$.

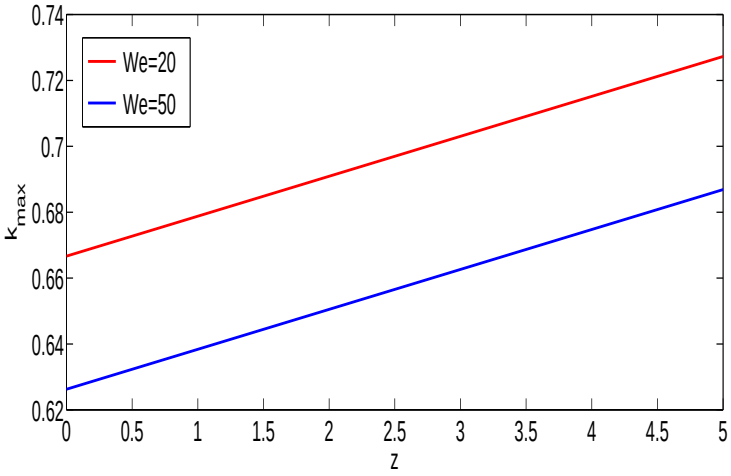

Figure 5.10: Graph showing the relationship between the wavenumber of the most unstable mode k_{max} against z of viscoelastic liquid jets for different values of the Weber number We. Here the parameters are $De = 10$, $Re = 20$, $\alpha_s = 0.20$ and $F = 1$.

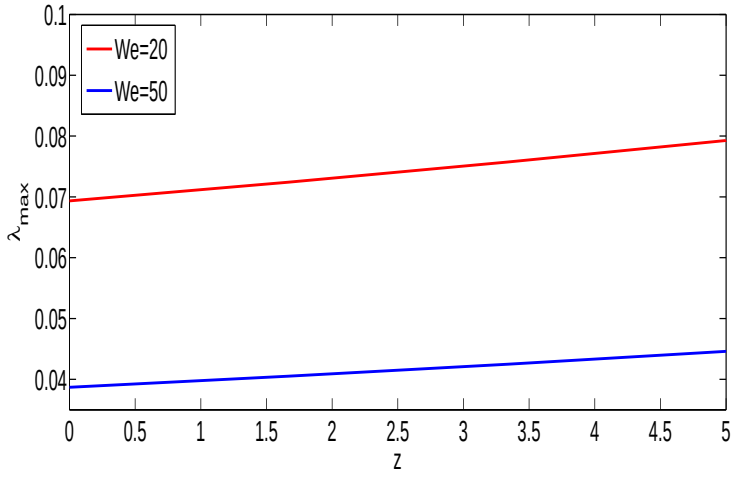

Figure 5.11: Graph showing the relationship between the maximum growth rate λ_{max} against z of viscoelastic liquid jets for different values of the Weber number We. Here the parameters are $De = 10$, $Re = 20$, $\alpha_s = 0.20$ and $F = 1$.

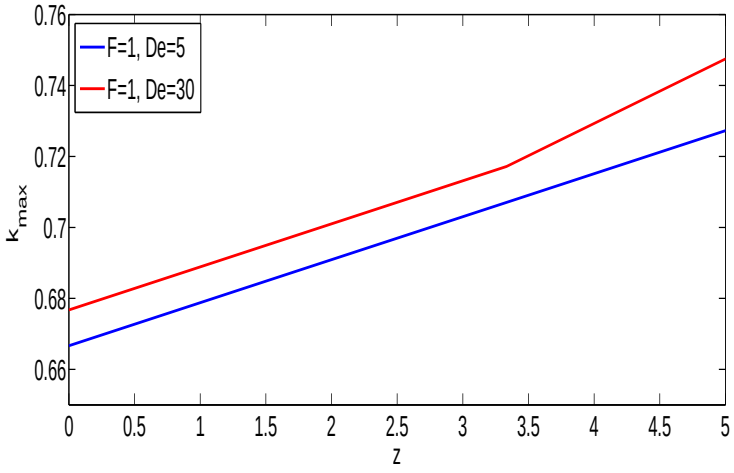

Figure 5.12: Graph showing the relationship between the wavenumber of the most unstable mode k_{max} against z of viscoelastic liquid jets for different values of the Weber number We. Here the parameters are $De = 10$, $Re = 20$, $\alpha_s = 0.20$ and $F = 1$.

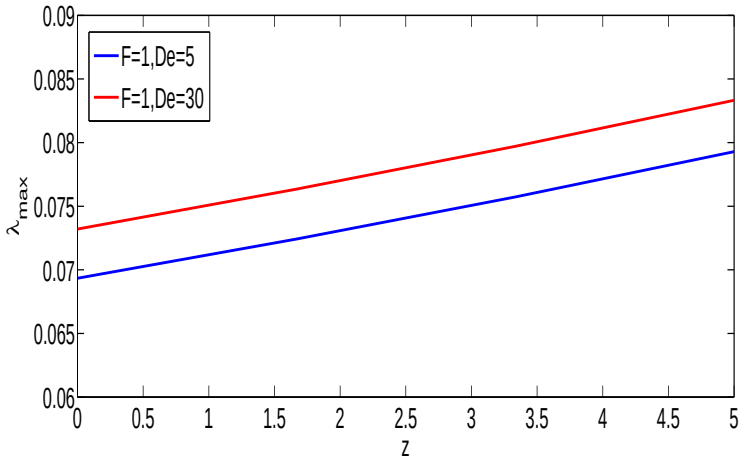

Figure 5.13: Graph showing the relationship between the maximum growth rate λ_{max} against z of viscoelastic liquid jets for different values of the Deborah number De. Here the parameters are $We = 10$, $Re = 20$, $\alpha_s = 0.20$ and $F = 1$..

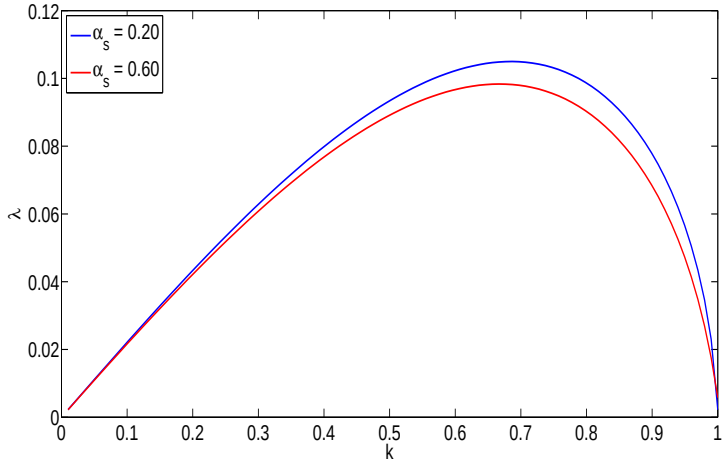

Figure 5.14: Graph showing the relationship between the growth rate λ and the wavenumber k of viscoelastic liquid jets for various α_s. Here the parameters are $We = 10$, $Re = 30$, $De = 10$.

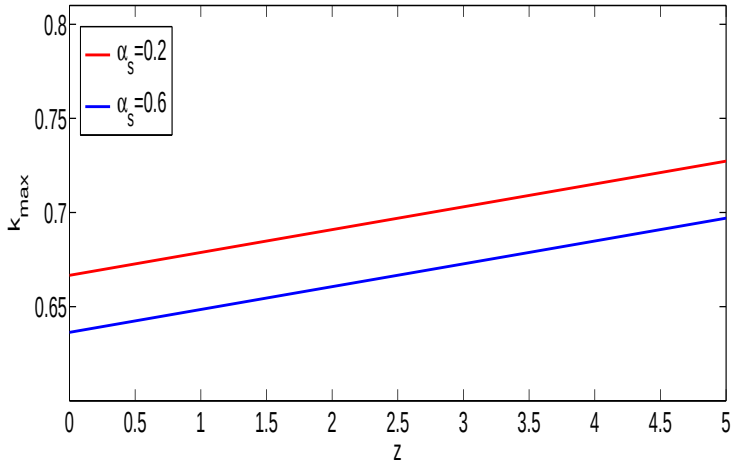

Figure 5.15: Graph showing the relationship between the wavenumber of the most unstable mode k_{max} against z of viscoelastic liquid jets for different values of the viscosity ratio α_s. Here the parameters are $We = 10$, $Re = 20$, $De = 10$ and $F = 1$.

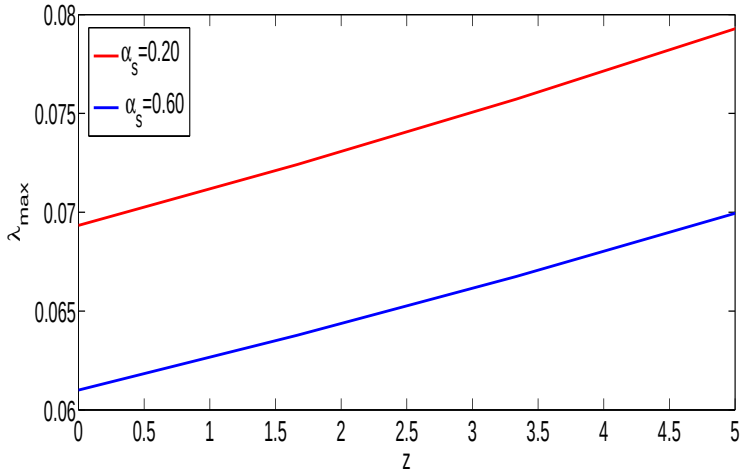

Figure 5.16: Graph showing the relationship between the maximum growth rate λ_{max} against z of viscoelastic liquid jets for different values of the viscosity ratio α_s. Here the parameters are $We = 10$, $Re = 20$, $De = 10$ and $F = 1$.

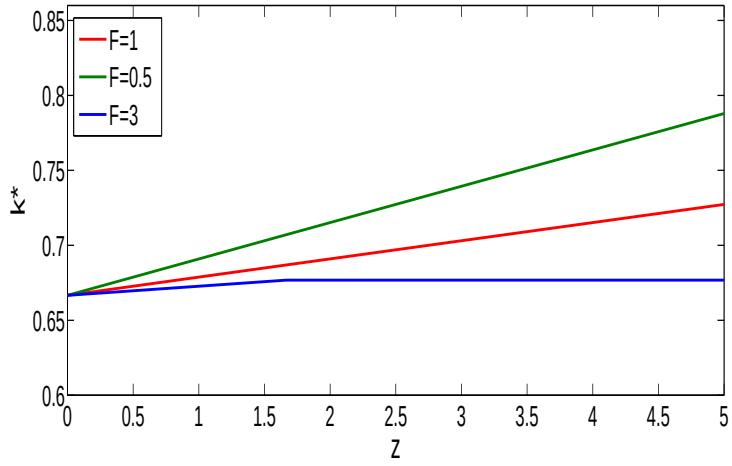

Figure 5.17: Graph showing the relationship between the wavenumber of the most unstable mode k_{max} against z of viscoelastic liquid jets for different values of the Froude number F. Here the parameters are $We = 10$, $De = 10$ and $\alpha_s = 0.20$.

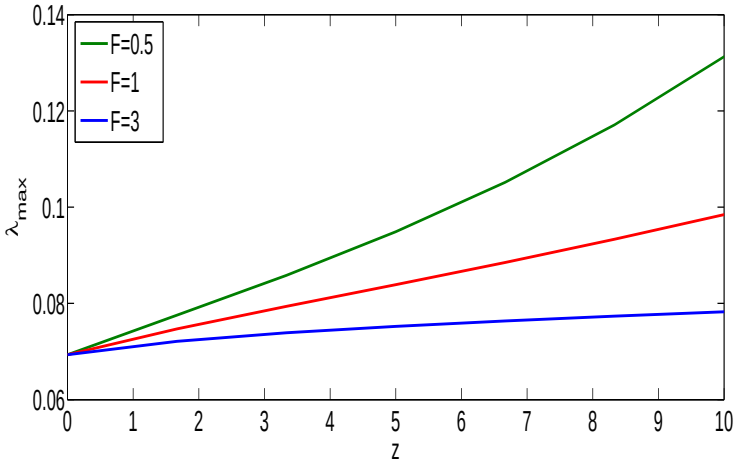

Figure 5.18: Graph showing the relationship between the maximum growth rate λ_{max} against z of viscoelastic liquid jets for different values of the Froude number F. Here the parameters are $We = 10$, $De = 10$ and $\alpha_s = 0.20$.

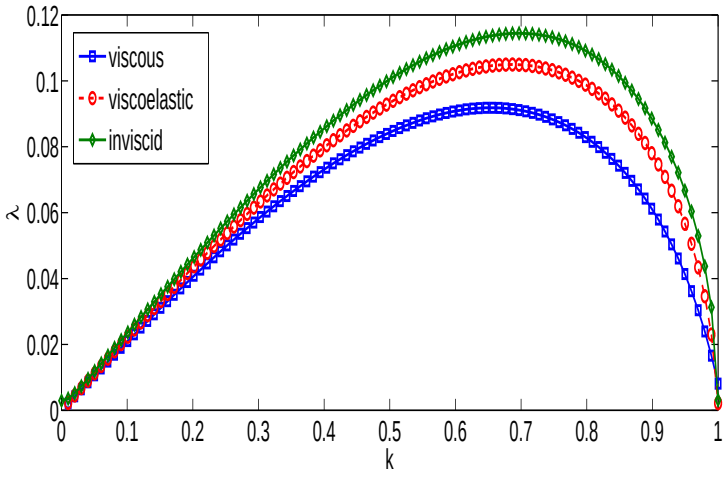

Figure 5.19: Graph showing the relationship between the growth rate and the wavenumber of inviscid liquid jets where $We = 10$, liquid jets viscous where $Re = 30$, $We = 10$ and viscoelastic liquid jets $Re = 30$, $We = 10$, $De = 10$ and $\alpha_s = 0.20$.

Chapter 6

Linear Instability of Viscoelastic Liquid Curved Jets

In the previous chapter we discussed the temporal instability of a straight viscoelastic jet falling under the influence of gravity. Here we will extend the previous chapter to investigate the linear instability of viscoelastic curved jets without including gravity. As we know, rotating liquid jets are used in prilling processes to produce fertilizer pellets (see Chapter 3). This process has been investigated by many authors (see Wallwork (2002a), Uddin (2007) and Parau (2006, 2007)). The liquids, which are used in this process, are normally viscoelastic fluids so that we are interested in studying this process mathematically which is much more complicated than straight jets.

6.1 Problem Formulation

Consider a large cylindrical container which has radius s_0 and rotates with angular velocity Ω. This container has an orifice at the bottom with radius a. This radius is very small compared with the radius of the container. This problem is examined by choosing a coordinate system (X, Y, Z) rotating with the container, having an origin at the axis of container and the position of the orifice is at $(s_0, 0, 0)$ as illustrated in Figs. 3.3 and

3.4. Due to the rotation of the container the liquid leaves the orifice in a curve. In this problem of the prilling process, we consider the centripetal acceleration of the jet is very large compared with the force of gravity. We can therefore assume the jet moves in the (X, Z) plane, so that the centerline can be described by coordinates $(X(s,t), 0, Z(s,t))$, where s is the arc-length along the middle of the jet which emerges from the orifice and t is the time (see Wallwork (2002a)). In any cross-section of the jet we also have plane polar coordinates (n, ϕ), which are the radial and azimuthal direction and have unit vectors which are $\mathbf{e_s}$, $\mathbf{e_n}, \mathbf{e}_\phi$. (see Decent *et al.* (2002)). The velocity components for this problem are $(\boldsymbol{u}, \boldsymbol{v}, \boldsymbol{w})$, where $\boldsymbol{u}$ is the tangential velocity, $\boldsymbol{v}$ is the radial velocity and $\boldsymbol{w}$ is the azimuthal velocity.

To begin with, we have to determine the equations of motion which are continuity equation, momentum equation and constitutive equation. We use the Oldroyd-B model to study the viscoelastic liquid jet. The equations of motion take the form

$$\boldsymbol{\nabla} \cdot \boldsymbol{u} = 0,$$

$$\rho\left(\frac{\partial \boldsymbol{u}}{\partial t} + \boldsymbol{u} \cdot \boldsymbol{\nabla} \boldsymbol{u}\right) = -\boldsymbol{\nabla} p + \boldsymbol{\nabla} \cdot \boldsymbol{\tau} \, - 2\,\boldsymbol{w} \times \boldsymbol{u} - \boldsymbol{w} \times (\boldsymbol{w} \times \boldsymbol{r}),$$

$$\boldsymbol{\tau} = \mu_s(\boldsymbol{\nabla} \boldsymbol{u} + (\boldsymbol{\nabla} \boldsymbol{u})^T) + \boldsymbol{T}$$

$$\lambda \boldsymbol{T}^{\triangledown} + \boldsymbol{T} = \mu_p \, \boldsymbol{\gamma}$$

$$\frac{\partial \boldsymbol{T}}{\partial t} + (\boldsymbol{u} \cdot \boldsymbol{\nabla})\boldsymbol{T} - \boldsymbol{T} \cdot \boldsymbol{\nabla} \boldsymbol{u} - (\boldsymbol{\nabla} \boldsymbol{u})^T \cdot \boldsymbol{T} = \frac{1}{\lambda}(\mu_p \boldsymbol{\gamma} - \boldsymbol{T}), \tag{6.1}$$

where $\boldsymbol{u}$ is the velocity in the form $\boldsymbol{u} = u\mathbf{e_s} + v\mathbf{e_n} + w\mathbf{e}_\phi$, ρ is the density of the fluid, p is the pressure, the angular velocity of the container is $\boldsymbol{w} = (0, w, 0)$, μ_s is the viscosity of the solvent, T is the extra stress tensor that represents the elastic contribution to the stresses and μ_p is the viscosity of the polymer. The equation $(6.1)_4$ is an upper convected derivative (see page 38). Then the equations of motion are

$$h_s\left(\frac{\partial u}{\partial t} + (v\cos\phi - w\sin\phi)(Z_{st}X_s - X_{st}Z_s) + v\frac{\partial u}{\partial n} + \frac{w}{n}\frac{\partial u}{\partial \phi}\right) + u\frac{\partial u}{\partial s} +$$

$$u(v\cos\phi - \sin\phi)(X_sZ_{ss} - Z_sX_{ss}) = -\frac{\partial p}{\partial s} + \left(2\Omega(v\cos\phi - \sin\phi) + \Omega^2((X + r_0)X_s + ZZ_s)\right)h_s$$

$$+\frac{\nu}{h_s}\left(\frac{-n\cos\phi(X_sZ_{sss} - Z_sX_{sss})}{h_s^2}\left(\frac{\partial u}{\partial s} + v\cos\phi(X_sZ_{ss} - Z_sX_{ss}) - w\sin\phi(X_sZ_{ss} - Z_sX_{ss})\right) +\right.$$

$$\frac{1}{h_s}\left(-u(X_sZ_{ss} - Z_sX_{ss})^2 + \frac{\partial^2 u}{\partial s^2} + \left(2\frac{\partial v}{\partial s}\cos\phi + v\cos\phi\right)(X_sZ_{sss} - Z_sX_{sss}) -\right.$$

$$\left.w\sin\phi(X_sZ_{sss} - Z_sX_{sss}) - 2\frac{\partial w}{\partial s}\sin\phi(X_sZ_{ss} - Z_sX_{ss})\right) +$$

$$\left.(1 + 2n\cos\phi(X_sZ_{ss} - Z_sX_{ss}))\frac{1}{n}\frac{\partial u}{\partial n} + nh_s\frac{\partial^2 u}{\partial n^2} + \frac{h_s}{n^2}\frac{\partial^2 u}{\partial \phi^2} - \frac{1}{n}\frac{\partial u}{\partial \phi}\sin\phi(X_sZ_{ss} - Z_sX_{ss})\right)$$

$$+\frac{1}{h_s}\left[\frac{\partial T_{ss}}{\partial s} + 2(v\cos\phi - w\sin\phi)(X_sZ_{ss} - Z_sX_{ss})\,T_{ss} + \frac{\partial T_{sn}}{\partial n}h_s + \frac{h_s}{n}\frac{\partial T_{s\phi}}{\partial \phi} + \frac{h_s v}{n}\,T_{s\phi}\right]. \qquad (6.2)$$

$$h_s\left(\frac{\partial v}{\partial t}+u\cos\phi(X_{st}Z_s-Z_{st}X_s)+v\frac{\partial v}{\partial n}+\frac{w}{n}\frac{\partial v}{\partial \phi}-\frac{w^2}{n}\right)+u\frac{\partial v}{\partial s}-$$

$$u^2\cos\phi(X_sZ_{ss}-X_{ss}Z_s)=-\frac{\partial p}{\partial n}h_s-2\Omega h_s u\cos\phi+$$

$$(\Omega^2\cos\phi((X+r_0)Z_s-ZX_s+n\cos\phi))h_s+$$

$$\frac{\nu}{h_s}\left(\frac{-n\cos\phi(X_sZsss-X_{sss}Z_s)}{h_s^2}\left(\frac{\partial v}{\partial s}-\ u\cos\phi(X_sZ_{ss}-X_{ss}Z_s)\right)+\right.$$

$$\frac{1}{h_s}\left(-v\cos^2\phi\,(X_sZ_{ss}-X_{ss}Z_s)^2+\frac{\partial^2 v}{\partial s^2}-2\frac{\partial u}{\partial s}\cos\phi\,(X_sZ_{ss}-X_{ss}Z_s)-\right.$$

$$\left.u\cos\phi(X_sZsss-X_{sss}Z_s)+w\sin\phi\cos\phi(X_sZ_{ss}-X_{ss}Z_s)^2\right)+$$

$$(1+2\varepsilon n\cos\phi(X_sZ_{ss}-X_{ss}Z_s))\frac{\partial v}{\partial n}+\ nh_s\frac{\partial^2 v}{\partial n^2}-(\frac{\partial v}{\partial \phi}-w)\sin\phi(X_sZ_{ss}-X_{ss}Z_s)+$$

$$\left.\frac{h_s}{n}(\frac{\partial^2 v}{\partial \phi^2}-v-2\frac{\partial w}{\partial \phi})\right)+\frac{1}{h_s}\left[\frac{\partial T_{sn}}{\partial s}+(v\cos\phi-w\sin\phi)(X_sZ_{ss}-X_{ss}Z_s)\,T_{sn}-\right.$$

$$\left.u\cos\phi T_{sn}+\frac{\partial T_{nn}}{\partial n}h_s+\frac{h_s}{n}\frac{\partial T_{n\phi}}{\partial \phi}+\frac{h_s v}{n}\,T_{n\phi}-\frac{w}{n}h_sT_{n\phi}\right]. \tag{6.3}$$

$$h_s\left(\frac{\partial w}{\partial t}+u\sin\phi(Z_{st}X_s-X_{st}Z_s)+v\frac{\partial w}{\partial n}+\frac{w}{n}\frac{\partial w}{\partial \phi}-\frac{vw}{n}\right)+u\frac{\partial w}{\partial s}+$$

$$u^2\sin\phi(X_sZ_{ss}-X_{ss}Z_s)=\left(-\frac{1}{n}\frac{\partial p}{\partial \phi}h_s+2\Omega u\sin\phi+\right.$$

$$\left.\Omega^2\sin\phi(ZX_s-(X+r_0)Z_s-n\cos\phi)\right)h_s+$$

$$\frac{\nu}{h_s}\left(\frac{-n\cos\phi(X_sZ_{sss}-X_{sss}Z_s)}{h_s^2}\left(\frac{\partial w}{\partial s}+u\sin\phi(X_sZ_{ss}-X_{ss}Z_s)\right)+\right.$$

$$\frac{1}{h_s}\left(-w\sin^2\phi\,(X_sZ_{ss}-X_{ss}Z_s)^2+\frac{\partial^2 w}{\partial s^2}+2\frac{\partial u}{\partial s}\sin\phi\,(X_sZ_{ss}-X_{ss}Z_s)+\right.$$

$$\left.\left.u\sin\phi(X_sZ_{sss}-X_{sss}Z_s)+v\sin\phi\cos\phi(X_sZ_{ss}-X_{ss}Z_s)^2\right)+\right.$$

$$(1+2n\cos\phi(X_sZ_{ss}-X_{ss}Z_s))\frac{\partial w}{\partial n}+nh_s\frac{\partial^2 w}{\partial n^2}-(\frac{\partial w}{\partial \phi}+v)\sin\phi(X_sZ_{ss}-X_{ss}Z_s)+$$

$$\left.\frac{h_s}{n}(\frac{\partial^2 w}{\partial \phi^2}-w+2\frac{\partial v}{\partial \phi})\right)+\frac{1}{h_s}\left[\frac{\partial T_{s\phi}}{\partial s}+(v\cos\phi-w\sin\phi)(X_sZ_{ss}-X_{ss}Z_s)\,T_{s\phi}-\right.$$

$$\left.\frac{u}{h_s}T_{s\phi}\sin\phi(X_sZ_{ss}-X_{ss}Z_s)+\frac{\partial T_{n\phi}}{\partial n}h_s+\frac{h_s}{n}\frac{\partial T_{\phi\phi}}{\partial \phi}+\frac{2h_sv}{n}\,T_{\phi\phi}\right]. \tag{6.4}$$

These equations are similar to Pătrău *et al.* (2007) except in this case we have some additional terms which are related to the extra stress tensor T. We note here again that the constitutive model used is Oldroyd-B model.

Owing to the fact that the components in the stress tensor are symmetrical, there are six expressions that may be derived as follows. These have been determined after lengthy algebra using (6.1).

$$\frac{\partial T_{ss}}{\partial t} + \frac{u}{h_s}\frac{\partial T_{ss}}{\partial s} + \frac{v}{\varepsilon}\frac{\partial T_{ss}}{\partial n} + \frac{w}{\varepsilon n}\frac{\partial T_{ss}}{\partial \phi} - \frac{2}{h_s}\left(\frac{\partial u}{\partial s} + v\,cos\phi - w\,\sin\phi\right)$$
$$(X_sZ_{ss} - Z_sX_{ss})T_{ss} - \frac{2}{h_s}\left(\frac{\partial v}{\partial s} + \frac{\partial u}{\partial n} - u\cos\phi\,(X_sZ_{ss} - Z_sX_{ss})\right)T_{sn} -$$
$$\frac{2}{h_s}\left(\frac{\partial w}{\partial s} + \frac{1}{n}\frac{\partial u}{\partial \phi} + u\,\sin\phi\,(X_sZ_{ss} - Z_sX_{ss})\right)T_{s\phi} =$$
$$\frac{1}{\lambda}\left[\frac{2\mu_p}{h_s}\left(\frac{\partial u}{\partial s} + (v\,\cos\phi - w\,\sin\phi)(X_sZ_{ss} - Z_sX_{ss})\right) - T_{ss}\right], \tag{6.5}$$

$$\frac{\partial T_{sn}}{\partial t} + \frac{u}{h_s}\frac{\partial T_{sn}}{\partial s} + \frac{v}{\varepsilon}\frac{\partial T_{sn}}{\partial n} + \frac{w}{\varepsilon n}\frac{\partial T_{sn}}{\partial \phi} - \frac{1}{h_s}\Big(\frac{\partial u}{\partial s} + v\,cos\phi(X_sZ_{ss} - Z_sX_{ss}) -$$
$$w\,\sin\phi(X_sZ_{ss} - Z_sX_{ss})\Big)T_{sn} - \frac{1}{h_s}\left(\frac{\partial v}{\partial s} + \frac{\partial u}{\partial n} - u\,\cos\phi\,(X_sZ_{ss} - Z_sX_{ss})\right)T_{nn} -$$
$$\frac{1}{\varepsilon}\frac{\partial v}{\partial n}T_{sn} - \frac{1}{h_s}\left(\frac{\partial w}{\partial s} + \frac{1}{n}\frac{\partial u}{\partial \phi} + u\,\sin\phi\,(X_sZ_{ss} - Z_sX_{ss})\right)T_{n\phi}$$
$$-\Big(\frac{1}{\varepsilon}\frac{\partial u}{\partial n} + \frac{1}{h_s}\frac{\partial v}{\partial s} - \frac{u}{h_s}\cos\phi\,(X_sZ_{ss} - Z_sX_{ss})\Big)T_{ss} - \Big(\frac{1}{\varepsilon}\frac{\partial w}{\partial n} - \frac{w}{\varepsilon n} + \frac{1}{\varepsilon n}\frac{\partial v}{\partial \phi}\Big)T_{s\phi}$$
$$= \frac{1}{\lambda}\left[\frac{\mu_p}{h_s}\Big(\frac{\partial v}{\partial s} + \frac{h_s}{\varepsilon}\frac{\partial u}{\partial n} - u\cos\phi(X_sZ_{ss} - Z_sX_{ss})\Big) - T_{sn}\right], \tag{6.6}$$

$$\frac{\partial T_{s\phi}}{\partial t} + \frac{u}{h_s}\frac{\partial T_{s\phi}}{\partial s} + \frac{v}{\varepsilon}\frac{\partial T_{s\phi}}{\partial n} + \frac{w}{\varepsilon n}\frac{\partial T_{s\phi}}{\partial \phi} - \frac{1}{h_s}\Big(\frac{\partial u}{\partial s} + v\,cos\phi(X_sZ_{ss} - Z_sX_{ss}) -$$
$$w\,\sin\phi(X_sZ_{ss} - Z_sX_{ss})\Big)T_{sn} - \frac{1}{\varepsilon}\left(\frac{\partial w}{\partial n} - \frac{w}{n} + \frac{1}{n}\frac{\partial v}{\partial \phi}\right)T_{s\phi}$$
$$-\Big(\frac{\partial u}{\varepsilon\partial n} + \frac{1}{h_s}\frac{\partial v}{\partial s} - \frac{u}{h_s}\cos\phi\,(X_sZ_{ss} - Z_sX_{ss})\Big)T_{ss} - \frac{1}{h_s}\Big(\frac{\partial v}{\partial s} + \frac{\partial u}{\varepsilon\partial n} -$$
$$u\,\cos\phi(X_sZ_{ss} - Z_sX_{ss})\Big)T_{nn} - \frac{1}{h_s}\Big(\frac{\partial w}{\partial s} + u\,\sin\phi(X_sZ_{ss} - Z_sX_{ss}) + \frac{1}{\varepsilon n}\frac{\partial u}{\partial \phi}\Big)T_{n\phi}$$
$$= \frac{1}{\lambda}\left[\mu_p\left(\frac{1}{\varepsilon n}\frac{\partial u}{\partial \phi} + \frac{u}{h_s}\sin\phi(X_sZ_{ss} - Z_sX_{ss}) + \frac{1}{h_s}\frac{\partial w}{\partial s}\right) - T_{s\phi}\right], \tag{6.7}$$

$$\frac{\partial T_{nn}}{\partial t}+\frac{u}{h_s}\frac{\partial T_{nn}}{\partial s}+\frac{v}{\varepsilon}\frac{\partial T_{nn}}{\partial n}+\frac{w}{\varepsilon n}\frac{\partial T_{nn}}{\partial \phi}$$
$$-2\Big(\frac{1}{\varepsilon}\frac{\partial u}{\partial n}+\frac{1}{h_s}\frac{\partial v}{\partial s}-\frac{u}{h_s}\cos\phi\,(X_sZ_{ss}-Z_sX_{ss})\Big)T_{sn}-\frac{2}{\varepsilon}\frac{\partial v}{\partial n}T_{nn}$$
$$-\frac{2}{\varepsilon}\Big(\frac{\partial w}{\partial n}-\frac{w}{n}+\frac{1}{n}\frac{\partial v}{\partial \phi}\Big)T_{n\phi}=-\frac{1}{\lambda}\left(\frac{2\mu_p}{\varepsilon}\frac{\partial v}{\partial n}-T_{nn}\right), \tag{6.8}$$

$$\frac{\partial T_{n\,\phi}}{\partial t}+\frac{u}{h_s}\frac{\partial T_{n\phi}}{\partial s}+\frac{v}{\varepsilon}\frac{\partial T_{n\phi}}{\partial n}+\frac{w}{\varepsilon n}\frac{\partial T_{n\phi}}{\partial \phi}$$
$$-\Big(\frac{1}{\varepsilon}\frac{\partial u}{\partial n}+\frac{1}{h_s}\frac{\partial v}{\partial s}-\frac{u}{h_s}\cos\phi\,(X_sZ_{ss}-Z_sX_{ss})\Big)T_{s\phi}-\frac{1}{\varepsilon}\Big(\frac{\partial v}{\partial n}+\frac{1}{n}\frac{\partial w}{\partial \phi}+\frac{v}{n}\Big)T_{n\phi}-$$
$$\frac{1}{\varepsilon}\Big(\frac{\partial w}{\partial n}-\frac{1}{n}\frac{\partial v}{\partial \phi}\Big)T_{\phi\phi}-\left(\frac{1}{\varepsilon n}\frac{\partial u}{\partial \phi}+\frac{u}{h_s}\sin\phi\,(X_sZ_{ss}-Z_sX_{ss})+\frac{1}{h_s}\frac{\partial w}{\partial s}\right)T_{sn}=$$
$$\frac{1}{\lambda}\left[\frac{\mu_p}{\varepsilon}\Big(\frac{\partial w}{\partial n}-\frac{w}{n}+\frac{1}{n}\frac{\partial v}{\partial \phi}\Big)-T_{n\phi}\right], \tag{6.9}$$

$$\frac{\partial T_{\phi\phi}}{\partial t}+\frac{u}{h_s}\frac{\partial T_{\phi\phi}}{\partial s}+\frac{v}{\varepsilon}\frac{\partial T_{\phi\phi}}{\partial n}+\frac{w}{\varepsilon n}\frac{\partial T_{\phi\phi}}{\partial \phi}-\frac{2}{\varepsilon n}\left(\frac{\partial v}{\partial \phi}-w+\frac{\partial w}{\partial n}\right)T_{n\phi}$$
$$-2\Big(\frac{1}{\varepsilon n}\frac{\partial u}{\partial \phi}+\frac{u}{h_s}\sin\phi\,(X_sZ_{ss}-Z_sX_{ss})+\frac{1}{h_s}\frac{\partial w}{\partial \phi}\Big)T_{s\phi}-\frac{2}{\varepsilon n}\left(\frac{\partial w}{\partial \phi}+v\right)T_{\phi\phi}=$$
$$\frac{1}{\lambda}\left[\frac{2\mu_p}{\varepsilon n}\left(\frac{\partial w}{\partial \phi}+v\right)-T_{\phi\phi}\right], \tag{6.10}$$

in which λ is the relaxation time, and $h_s = 1 + n\cos\phi(X_sZ_{ss} - Z_sZ_{ss})$. To solve the equation of motion, continuity equation and constitutive equation, we have to use suitable boundary conditions. The position of the free surface can be determined by $n - R(s,t,\phi) = 0$, and the normal vector is given by $\nabla(n - R(s,t,\phi))$, which gives

$$\boldsymbol{n} = \frac{1}{E}\left(-\frac{\partial R}{\partial s}\cdot\frac{1}{h_s}\cdot\boldsymbol{e_s} + \boldsymbol{e_n} - \frac{\partial R}{\partial \phi}\cdot\frac{1}{R}\cdot\boldsymbol{e_\phi}\right),$$

where

$$E = \left(1 + \frac{1}{h_s^2}\left(\frac{\partial R}{\partial s}\right)^2 + \frac{1}{R^2}\left(\frac{\partial R}{\partial \phi}\right)^2\right)^{\frac{1}{2}}.$$

The normal stress condition is $\boldsymbol{n}\cdot\boldsymbol{\Pi}\cdot\boldsymbol{n} = \sigma\kappa$, where Π is the total stress tensor given by $-p\boldsymbol{I} + \boldsymbol{\tau}$, where σ is the isotropic surface tension and κ is the curvature of the free surface;

$$\kappa = \frac{1}{nh_s}\left(-\frac{\partial}{\partial s}\left(\frac{n}{Eh_s}\frac{\partial R}{\partial s}\right) + \frac{\partial}{\partial n}\left(\frac{nh_s}{E}\right) - \frac{\partial}{\partial \phi}\left(\frac{h_s}{En}\frac{\partial R}{\partial \phi}\right)\right).$$

After some algebra the normal stress condition is given by

$$\begin{aligned}
&p - \frac{2\mu_s}{E^2}\left((\frac{\partial R}{\partial s})^2\frac{1}{h_s^3}\left(\frac{\partial u}{\partial s} + (v\,cos\phi - \sin\phi)(X_sZ_{ss} - Z_sX_{ss}) + \frac{h_s}{2\mu_s}T_{ss}\right)\right.\\
&+\frac{\partial v}{\partial n} + \frac{1}{2\mu_s}T_{nn} + \frac{1}{R^3}(\frac{\partial R}{\partial \phi})^2\left(\frac{\partial w}{\partial \phi} + v + \frac{1}{2\mu_s}T_{\phi\phi}\right) - \frac{\varepsilon}{h_s}\frac{\partial R}{\partial s}\left(\frac{1}{h_s}\frac{\partial v}{\partial s}\right.\\
&+\frac{\partial u}{\partial n} - \frac{u}{h_s}\,cos\phi(X_sZ_{ss} - Z_sX_{ss}) + \frac{1}{2\mu_s}T_{sn}\left.\right) + \frac{1}{Rh_s}\frac{\partial R}{\partial s}\frac{\partial R}{\partial \phi}\left(\frac{1}{R}\frac{\partial u}{\partial \phi}\right.\\
&+\frac{u}{h_s}\sin\phi(X_sZ_{ss} - Z_sX_{ss}) + \frac{1}{h_s}\frac{\partial u}{\partial s} + \frac{1}{2\mu_s}T_{s\phi}\left.\right)\\
&\left.-\frac{1}{R}\frac{\partial R}{\partial \phi}(R\frac{\partial w}{\partial n} - \frac{w}{R} + \frac{1}{R}\frac{\partial v}{\partial \phi})\right) = \frac{\kappa}{We}\ \text{on}\ n = R(s,t),
\end{aligned} \tag{6.11}$$

The tangential stress conditions are $\boldsymbol{t_i} \cdot \boldsymbol{\sigma} \cdot \boldsymbol{n} = 0$, where $i = 1, 2$ and $t_1 = \boldsymbol{e_s} + \frac{\partial R}{\partial s} . \frac{1}{h_s} . \boldsymbol{e_n}$, $t_2 = \frac{\partial R}{\partial \phi} . \frac{1}{R} . \boldsymbol{e_n} + \boldsymbol{e_\phi}$. So that, the first tangential stress condition is

$$\left(1 - \left(\frac{\partial R}{\partial s}\right)^2 \frac{1}{h_s^2}\right) \left\{ \frac{\partial v}{\partial s} + h_s \frac{\partial u}{\partial n} - u \cos\phi (Z_s Z_{ss} - X_{ss} Z_s) + \frac{T_{sn}}{\mu_s} \right\} + 2\frac{\partial R}{\partial s} \left\{ \frac{\partial v}{\partial n} - \frac{\partial u}{\partial s} \frac{1}{h_s} - \frac{1}{h_s} v \cos\phi - w \sin\phi (X_s Z_{ss} - X_{ss} Z_s) - \frac{1}{2\mu_s} (T_{ss} - T_{nn}) \right\} = 0, \tag{6.12}$$

and the second tangential stress condition is

$$\left(1 - \left(\frac{\partial R}{\partial \phi}\right)^2 \frac{1}{R^2}\right) \left(\frac{\partial w}{\partial n} - \frac{w}{R} + \frac{1}{R} \frac{\partial v}{\partial \phi} + \frac{T_{n\phi}}{\mu_s} \right) + \frac{2}{R} \frac{\partial R}{\partial \phi} \left(\frac{\partial v}{\partial n} - \frac{1}{R} (\frac{\partial w}{\partial \phi} + v) + \frac{1}{2\mu_s} (T_{nn} - T_{\phi\phi}) \right) = 0. \tag{6.13}$$

The kinematic condition is

$\frac{D}{Dt}(R(s,t,\phi) - n) = 0$ on $n = R(s, \phi, t)$. We can write the previous equation as

$$\frac{\partial R}{\partial t} + \frac{\partial R}{\partial s} \frac{\partial s}{\partial t} + \frac{\partial R}{\partial \phi} \frac{\partial \phi}{\partial t} - \frac{\partial n}{\partial t} = 0.$$

The pressure condition on the free surface is $p = \sigma\kappa$ on $n = R$.

6.2 Non-Dimensionalisation

We use the same transformation which is used in Uddin (2007) to make our equations dimensionless. Consequently, the momentum equation and the continuity equation are similar to Uddin (2007) but differ only in the terms of constitutive equations. In summary

we use the following scales

$$\overline{u} = \frac{u}{U}\ , \quad \overline{v} = \frac{v}{U}, \quad \overline{w} = \frac{w}{U}, \quad \overline{n} = \frac{n}{a}, \quad \varepsilon = \frac{a}{s_0}, \quad \overline{R} = \frac{R}{a},$$
$$\overline{T} = \frac{s_0}{U\mu_0}T, \quad \overline{s} = \frac{s}{s_0}, \quad \overline{t} = \frac{U}{s_0}\,t, \quad \overline{p} = \frac{p}{\rho U^2}, \quad \overline{X} = \frac{X}{s_0}, \quad \overline{Z} = \frac{Z}{s_0},$$

where u, v and w are the tangential, radial and azimuthal velocity components, U is the exit speed of the jet in the rotating frame, s_0 is the radius of the cylindrical drum, a is radius of the orifice, ε is the aspect ratio of the jet, T is the extra stress tensor and μ_0 is the total viscosity of the solvent and the polymer. After dropping overbars, the equation of motion is the same as found in Părău *et al.* (2007), but there are extra terms related to viscoelastic terms as follows

$$\varepsilon n\frac{\partial u}{\partial s} + h_s\left(v + n\frac{\partial v}{\partial n} + \frac{\partial w}{\partial \phi}\right) + \varepsilon n\left(v\cos\phi - w\sin\phi\right)\left(X_s Z_{ss} - Z_s X_{ss}\right) = 0, \qquad (6.14)$$

$$h_s\left(\varepsilon\frac{\partial u}{\partial t}+\varepsilon(v\cos\phi-w\sin\phi)(Z_{st}X_s-X_{st}Z_s)+v\frac{\partial u}{\partial n}+\frac{w}{n}\frac{\partial u}{\partial\phi}\right)+$$

$$\varepsilon u\frac{\partial u}{\partial s}+\varepsilon u(v\cos\phi-\sin\phi)(X_sZ_{ss}-Z_sX_{ss})=-\varepsilon\frac{\partial p}{\partial s}+$$

$$\left(\frac{2\varepsilon}{Rb}(v\cos\phi-\sin\phi)+\frac{\varepsilon}{Rb^2}((X+r_0)X_s+ZZ_s)\right)h_s+$$

$$\frac{\alpha_s}{h_sRe}\left(\frac{-n\varepsilon^3\cos\phi(X_sZ_{sss}-Z_sX_{sss})}{h_s^2}\left(\frac{\partial u}{\partial s}+v\cos\phi(X_sZ_{ss}-Z_sX_{ss})-\right.\right.$$

$$\left.w\sin\phi(X_sZ_{ss}-Z_sX_{ss})\right)+\frac{\varepsilon^2}{h_s}\Bigg(-u(X_sZ_{ss}-Z_sX_{ss})^2+$$

$$\frac{\partial^2u}{\partial s^2}+\left(2\frac{\partial v}{\partial s}\cos\phi+v\cos\phi\right)(X_sZ_{sss}-Z_sX_{sss})-w\sin\phi(X_sZ_{sss}-Z_sX_{sss})-$$

$$\left.2\frac{\partial w}{\partial s}\sin\phi(X_sZ_{ss}-Z_sX_{ss})\right)+(1+2\varepsilon n\cos\phi(X_sZ_{ss}-Z_sX_{ss}))\frac{1}{n}\frac{\partial u}{\partial n}$$

$$+nh_s\frac{\partial^2u}{\partial n^2}+\frac{h_s}{n^2}\frac{\partial^2u}{\partial\phi^2}-\frac{\varepsilon}{n}\frac{\partial u}{\partial\phi}\sin\phi(X_sZ_{ss}-Z_sX_{ss})\Bigg)+$$

$$\frac{1}{h_s\,Re}\left[\varepsilon\frac{\partial T_{ss}}{\partial s}+2\varepsilon(v\cos\phi-w\sin\phi)(X_sZ_{ss}-Z_sX_{ss})T_{ss}+\right.$$

$$\left.\frac{\partial T_{sn}}{\partial n}h_s+\frac{h_s}{n}\frac{\partial T_{s\phi}}{\partial\phi}+\frac{h_sv}{n}\,T_{s\phi}\right],\tag{6.15}$$

$$h_s\left(\varepsilon\frac{\partial v}{\partial t}+\varepsilon u\cos\phi(X_{st}Z_s-Z_{st}X_s)+v\frac{\partial v}{\partial n}+\frac{w}{n}\frac{\partial v}{\partial\phi}-\frac{w^2}{n}\right)+\varepsilon u\frac{\partial v}{\partial s}-$$

$$\varepsilon u^2\cos\phi(X_sZ_{ss}-X_{ss}Z_s)=-\frac{\partial p}{\partial n}h_s-\frac{2\varepsilon h_s}{Rb}h_s u\cos\phi+$$

$$\left(\frac{\varepsilon}{Rb^2}\cos\phi((X+r_0)Z_s-ZX_s+n\cos\phi)\right)h_s+$$

$$\frac{\alpha_s}{h_sRe}\left(\frac{-\varepsilon^3 n\cos\phi(X_sZsss-X_{sss}Z_s)}{h_s^2}\left(\frac{\partial v}{\partial s}-\,u\cos\phi(X_sZ_{ss}-X_{ss}Z_s)\right)+\right.$$

$$\frac{\varepsilon^2}{h_s}\left(-v\cos^2\phi\,(X_sZ_{ss}-X_{ss}Z_s)^2+\frac{\partial^2 v}{\partial s^2}-2\frac{\partial u}{\partial s}\cos\phi\,(X_sZ_{ss}-X_{ss}Z_s)-\right.$$

$$\left.u\cos\phi(X_sZsss-X_{sss}Z_s)+w\sin\phi\cos\phi(X_sZ_{ss}-X_{ss}Z_s)^2\right)+$$

$$(1+2\varepsilon n\cos\phi(X_sZ_{ss}-X_{ss}Z_s))\frac{\partial v}{\partial n}+\,nh_s\frac{\partial^2 v}{\partial n^2}-\varepsilon(\frac{\partial v}{\partial\phi}-w)\sin\phi(X_sZ_{ss}-X_{ss}Z_s)+$$

$$\left.\frac{h_s}{n}(\frac{\partial^2 v}{\partial\phi^2}-v-2\frac{\partial w}{\partial\phi})\right)+\frac{1}{h_sRe}\left[\varepsilon\frac{\partial T_{sn}}{\partial s}+\varepsilon(v\cos\phi-w\sin\phi)(X_sZ_{ss}-X_{ss}Z_s)\,T_{sn}-\right.$$

$$\left.\varepsilon u\cos\phi T_{sn}+\frac{\partial T_{nn}}{\partial n}h_s+\frac{h_s}{n}\frac{\partial T_{n\phi}}{\partial\phi}+\frac{h_sv}{n}\,T_{n\phi}-\frac{w}{n}h_sT_{n\phi}\right],\qquad(6.16)$$

$$h_s\left(\varepsilon\frac{\partial w}{\partial t}+\varepsilon u\sin\phi(Z_{st}X_s-X_{st}Z_s)+v\frac{\partial w}{\partial n}+\frac{w}{n}\frac{\partial w}{\partial\phi}-\frac{vw}{n}\right)+\varepsilon u\frac{\partial w}{\partial s}+$$

$$\varepsilon u^2\sin\phi(X_sZ_{ss}-X_{ss}Z_s)=\left(-\frac{1}{n}\frac{\partial p}{\partial\phi}h_s+\frac{2\varepsilon}{Rb}u\sin\phi+\right.$$

$$\left.\frac{\varepsilon}{Rb^2}\sin\phi(ZX_s-(X+r_0)Z_s-n\cos\phi)\right)h_s+$$

$$\frac{\alpha_s}{h_s\,Re}\left(\frac{-\varepsilon^3 n\cos\phi(X_sZ_{sss}-X_{sss}Z_s)}{h_s^2}\left(\frac{\partial w}{\partial s}+u\sin\phi(X_sZ_{ss}-X_{ss}Z_s)\right)+\right.$$

$$\frac{\varepsilon^2}{h_s}\left(-w\sin^2\phi\,(X_sZ_{ss}-X_{ss}Z_s)^2+\frac{\partial^2 w}{\partial s^2}+2\frac{\partial u}{\partial s}\sin\phi\,(X_sZ_{ss}-X_{ss}Z_s)+\right.$$

$$\left.\left.u\sin\phi(X_sZ_{sss}-X_{sss}Z_s)+v\sin\phi\cos\phi(X_sZ_{ss}-X_{ss}Z_s)^2\right)+\right.$$

$$(1+2\varepsilon n\cos\phi(X_sZ_{ss}-X_{ss}Z_s))\frac{\partial w}{\partial n}+nh_s\frac{\partial^2 w}{\partial n^2}-\varepsilon(\frac{\partial w}{\partial\phi}+v)\sin\phi(X_sZ_{ss}-X_{ss}Z_s)+$$

$$\left.\frac{h_s}{n}(\frac{\partial^2 w}{\partial\phi^2}-w+2\frac{\partial v}{\partial\phi})\right)+\frac{1}{h_s\,Re}\left[\varepsilon\frac{\partial T_{s\phi}}{\partial s}+\varepsilon(v\cos\phi-w\sin\phi)(X_sZ_{ss}-X_{ss}Z_s)\,T_{s\phi}-\right.$$

$$\left.\frac{\varepsilon u}{h_s}T_{s\phi}\sin\phi(X_sZ_{ss}-X_{ss}Z_s)+\frac{\partial T_{n\phi}}{\partial n}h_s+\frac{h_s}{n}\frac{\partial T_{\phi\phi}}{\partial\phi}+\frac{2h_sv}{n}\,T_{\phi\phi}\right]. \tag{6.17}$$

The equations of the extra stress tensor become

$$\frac{\partial T_{ss}}{\partial t} + \frac{u}{h_s}\frac{\partial T_{ss}}{\partial s} + \frac{v}{\varepsilon}\frac{\partial T_{ss}}{\partial n} + \frac{w}{\varepsilon n}\frac{\partial T_{ss}}{\partial \phi} - \frac{2}{h_s}\left(\frac{\partial u}{\partial s} + v\,cos\phi - w\,\sin\phi\right)$$
$$(X_sZ_{ss} - Z_sX_{ss})T_{ss} - \frac{2}{h_s}\left(\frac{\partial v}{\partial s} + \frac{\partial u}{\partial n} - u\cos\phi\,(X_sZ_{ss} - Z_sX_{ss})\right)T_{sn} -$$
$$\frac{2}{h_s}\left(\frac{\partial w}{\partial s} + \frac{1}{n}\frac{\partial u}{\partial \phi} + u\,\sin\phi\,(X_sZ_{ss} - Z_sX_{ss})\right)T_{s\phi} =$$
$$\frac{1}{De}\left[\frac{2(1-\alpha_s)}{h_s}\left(\frac{\partial u}{\partial s} + (v\,\cos\phi - w\,\sin\phi)(X_sZ_{ss} - Z_sX_{ss})\right) - T_{ss}\right], \quad (6.18)$$

$$\frac{\partial T_{sn}}{\partial t} + \frac{u}{h_s}\frac{\partial T_{sn}}{\partial s} + \frac{v}{\varepsilon}\frac{\partial T_{sn}}{\partial n} + \frac{w}{\varepsilon n}\frac{\partial T_{sn}}{\partial \phi} - \frac{1}{h_s}\Big(\frac{\partial u}{\partial s} + v\,cos\phi(X_sZ_{ss} - Z_sX_{ss}) -$$
$$w\,\sin\phi(X_sZ_{ss} - Z_sX_{ss})\Big)T_{sn} - \frac{1}{h_s}\left(\frac{\partial v}{\partial s} + \frac{\partial u}{\partial n} - u\,\cos\phi\,(X_sZ_{ss} - Z_sX_{ss})\right)T_{nn} -$$
$$\frac{1}{\varepsilon}\frac{\partial v}{\partial n}T_{sn} - \frac{1}{h_s}\left(\frac{\partial w}{\partial s} + \frac{1}{n}\frac{\partial u}{\partial \phi} + u\,\sin\phi\,(X_sZ_{ss} - Z_sX_{ss})\right)T_{n\phi}$$
$$-\Big(\frac{1}{\varepsilon}\frac{\partial u}{\partial n} + \frac{1}{h_s}\frac{\partial v}{\partial s} - \frac{u}{h_s}\cos\phi\,(X_sZ_{ss} - Z_sX_{ss})\Big)T_{ss} - \Big(\frac{1}{\varepsilon}\frac{\partial w}{\partial n} - \frac{w}{\varepsilon n} + \frac{1}{\varepsilon n}\frac{\partial v}{\partial \phi}\Big)T_{s\phi}$$
$$= \frac{1}{De}\left[\frac{(1-\alpha_s)}{h_s}\Big(\frac{\partial v}{\partial s} + \frac{h_s}{\varepsilon}\frac{\partial u}{\partial n} - u\cos\phi(X_sZ_{ss} - Z_sX_{ss})\Big) - T_{sn}\right], \quad (6.19)$$

$$\frac{\partial T_{s\phi}}{\partial t} + \frac{u}{h_s}\frac{\partial T_{s\phi}}{\partial s} + \frac{v}{\varepsilon}\frac{\partial T_{s\phi}}{\partial n} + \frac{w}{\varepsilon n}\frac{\partial T_{s\phi}}{\partial \phi} - \frac{1}{h_s}\Big(\frac{\partial u}{\partial s} + v\,cos\phi(X_sZ_{ss} - Z_sX_{ss}) -$$
$$w\,\sin\phi(X_sZ_{ss} - Z_sX_{ss})\Big)T_{sn} - \frac{1}{\varepsilon}\left(\frac{\partial w}{\partial n} - \frac{w}{n} + \frac{1}{n}\frac{\partial v}{\partial \phi}\right)T_{s\phi}$$
$$-\Big(\frac{\partial u}{\varepsilon\partial n} + \frac{1}{h_s}\frac{\partial v}{\partial s} - \frac{u}{h_s}\cos\phi\,(X_sZ_{ss} - Z_sX_{ss})\Big)T_{ss} - \frac{1}{h_s}\Big(\frac{\partial v}{\partial s} + \frac{\partial u}{\varepsilon\partial n} -$$
$$u\,\cos\phi(X_sZ_{ss} - Z_sX_{ss})\Big)T_{nn} - \frac{1}{h_s}\Big(\frac{\partial w}{\partial s} + u\,\sin\phi(X_sZ_{ss} - Z_sX_{ss}) + \frac{1}{\varepsilon n}\frac{\partial u}{\partial \phi}\Big)T_{n\phi}$$
$$= \frac{1}{De}\left[(1-\alpha_s)\left(\frac{1}{\varepsilon n}\frac{\partial u}{\partial \phi} + \frac{u}{h_s}\sin\phi(X_sZ_{ss} - Z_sX_{ss}) + \frac{1}{h_s}\frac{\partial w}{\partial s}\right) - T_{s\phi}\right], \quad (6.20)$$

$$\frac{\partial T_{nn}}{\partial t}+\frac{u}{h_s}\frac{\partial T_{nn}}{\partial s}+\frac{v}{\varepsilon}\frac{\partial T_{nn}}{\partial n}\ +\frac{w}{\varepsilon n}\frac{\partial T_{nn}}{\partial \phi}$$
$$-2\left(\frac{1}{\varepsilon}\frac{\partial u}{\partial n}+\frac{1}{h_s}\frac{\partial v}{\partial s}-\frac{u}{h_s}\cos\phi\,(X_sZ_{ss}-Z_sX_{ss})\right)T_{sn}-\frac{2}{\varepsilon}\frac{\partial v}{\partial n}T_{nn}$$
$$-\frac{2}{\varepsilon}\left(\frac{\partial w}{\partial n}-\frac{w}{n}+\frac{1}{n}\frac{\partial v}{\partial \phi}\right)T_{n\phi}=-\frac{1}{De}\left(\frac{2(1-\alpha_s)}{\varepsilon}\frac{\partial v}{\partial n}-T_{nn}\right), \tag{6.21}$$

$$\frac{\partial T_{n\,\phi}}{\partial t}+\frac{u}{h_s}\frac{\partial T_{n\phi}}{\partial s}+\frac{v}{\varepsilon}\frac{\partial T_{n\phi}}{\partial n}\ +\frac{w}{\varepsilon n}\frac{\partial T_{n\phi}}{\partial \phi}$$
$$-\left(\frac{1}{\varepsilon}\frac{\partial u}{\partial n}+\frac{1}{h_s}\frac{\partial v}{\partial s}-\frac{u}{h_s}\cos\phi\,(X_sZ_{ss}-Z_sX_{ss})\right)T_{s\phi}\ -\frac{1}{\varepsilon}\left(\frac{\partial v}{\partial n}+\frac{1}{n}\frac{\partial w}{\partial \phi}+\frac{v}{n}\right)T_{n\phi}\ -$$
$$\frac{1}{\varepsilon}\left(\frac{\partial w}{\partial n}-\frac{1}{n}\frac{\partial v}{\partial \phi}\right)T_{\phi\phi}-\left(\frac{1}{\varepsilon n}\frac{\partial u}{\partial \phi}+\frac{u}{h_s}\sin\phi\,(X_sZ_{ss}-Z_sX_{ss})\ +\frac{1}{h_s}\frac{\partial w}{\partial s}\right)T_{sn}=$$
$$\frac{1}{De}\left[\frac{(1-\alpha_s)}{\varepsilon}\left(\frac{\partial w}{\partial n}-\frac{w}{n}+\frac{1}{n}\frac{\partial v}{\partial \phi}\right)-T_{n\phi}\right], \tag{6.22}$$

$$\frac{\partial T_{\phi\phi}}{\partial t}+\frac{u}{h_s}\frac{\partial T_{\phi\phi}}{\partial s}+\frac{v}{\varepsilon}\frac{\partial T_{\phi\phi}}{\partial n}\ +\frac{w}{\varepsilon n}\frac{\partial T_{\phi\phi}}{\partial \phi}\ -\frac{2}{\varepsilon n}\left(\frac{\partial v}{\partial \phi}\ -w+\frac{\partial w}{\partial n}\right)T_{n\phi}$$
$$-2\left(\frac{1}{\varepsilon n}\frac{\partial u}{\partial \phi}+\frac{u}{h_s}\sin\phi\,(X_sZ_{ss}-Z_sX_{ss})+\frac{1}{h_s}\frac{\partial w}{\partial \phi}\right)T_{s\phi}-\frac{2}{\varepsilon n}\left(\frac{\partial w}{\partial \phi}\ +\ v\right)T_{\phi\phi}\ =$$
$$\frac{1}{De}\left[\frac{2(1-\alpha_s)}{\varepsilon n}\left(\frac{\partial w}{\partial \phi}\ +\ v\right)-T_{\phi\phi}\right], \tag{6.23}$$

where the dimensionless parameters are the Rossby number $Rb=\frac{U}{s_0\Omega}$, the Weber number $We=\frac{\rho U^2 a}{\sigma}$, the Reynolds number $Re=\frac{\rho U a}{\mu}$, the Deborah number $De=\frac{\lambda U}{s_0}$ and the ratio between the viscosity of the solvent and the total of the viscosity $\alpha_s=\frac{\mu_s}{\mu_0}=\frac{\mu_s}{\mu_s+\mu_p}$.

6.3 Non-Dimensionalisation of Boundary Conditions

It can be found that the normal stress condition is given by

$$p - \frac{2\alpha_s}{Re}\frac{1}{E^2}\Bigg(\varepsilon^2\left(\frac{\partial R}{\partial s}\right)^2\frac{1}{h_s^3}\left(\frac{\partial u}{\partial s} + (v\,cos\phi - \sin\phi)(X_sZ_{ss} - Z_sX_{ss}) + \frac{h_s}{2\alpha_s}T_{ss}\right)$$

$$+\frac{1}{\varepsilon}\frac{\partial v}{\partial n} + \frac{1}{2\alpha_s}T_{nn} + \frac{1}{\varepsilon\,R^3}\left(\frac{\partial R}{\partial \phi}\right)^2\left(\frac{\partial w}{\partial \phi} + v + RT_{\phi\phi}\right) - \frac{\varepsilon}{h_s}\frac{\partial R}{\partial s}\Bigg(\frac{1}{h_s}\frac{\partial v}{\partial s}$$

$$+\frac{1}{\varepsilon}\frac{\partial u}{\partial n} - \frac{u}{h_s}\,cos\phi(X_sZ_{ss} - Z_sX_{ss}) + \frac{1}{2\alpha_s}T_{sn}\Bigg) + \frac{\varepsilon}{Rh_s}\frac{\partial R}{\partial s}\frac{\partial R}{\partial \phi}\Bigg(\frac{1}{\varepsilon\,R}\frac{\partial u}{\partial \phi}$$

$$+\frac{u}{h_s}\sin\phi(X_sZ_{ss} - Z_sX_{ss}) + \frac{1}{h_s}\frac{\partial u}{\partial s} + \frac{1}{2\alpha_s}T_{s\phi}\Bigg)$$

$$-\frac{1}{R}\frac{\partial R}{\partial \phi}(R\frac{\varepsilon\partial w}{\partial n} - \frac{\varepsilon w}{R} + \frac{\varepsilon}{R}\frac{\partial v}{\partial \phi}\Bigg) = \frac{\sigma\,\kappa}{We}\text{ on } n = R(s,t), \tag{6.24}$$

where

$$\kappa = \frac{1}{h_s}\left(-\varepsilon^2\frac{\partial}{\partial s}\left(\frac{n}{Eh_s}\frac{\partial R}{\partial s}\right) + \frac{\partial}{\partial n}\left(\frac{nh_s}{E}\right) - \frac{\partial}{\partial \phi}\left(\frac{h_s}{En}\frac{\partial R}{\partial \phi}\right)\right).$$

$$E = \left(1 + \frac{\varepsilon^2}{h_s^2}\left(\frac{\partial R}{\partial s}\right)^2 + \frac{1}{R^2}\left(\frac{\partial R}{\partial \phi}\right)^2\right)^{\frac{1}{2}}.$$

$$h_s = 1 + \varepsilon n\cos\phi(X_sZ_{ss} - X_{ss}Z_s).$$

The first tangential stress condition is

$$\left(1-\varepsilon^2\left(\frac{\partial R}{\partial s}\right)^2\frac{1}{h_s^2}\right)\left\{\varepsilon\frac{\partial v}{\partial s}+h_s\frac{\partial u}{\partial n}-\varepsilon u\cos\phi(Z_sZ_{ss}-X_{ss}Z_s)+\frac{\varepsilon}{\alpha_s}T_{sn}\right\}+2\varepsilon\frac{\partial R}{\partial s}$$
$$\left\{\frac{\partial v}{\partial n}-\varepsilon\frac{\partial u}{\partial s}\frac{1}{h_s}-\frac{\varepsilon}{h_s}v\cos\phi-w\sin\phi(X_sZ_{ss}-X_{ss}Z_s)-\frac{\varepsilon}{2\alpha_s}(T_{ss}-T_{nn})\right\}=0, \quad (6.25)$$

and the second tangential stress condition is

$$\left(1-(\frac{\partial R}{\partial\phi})^2\frac{1}{R^2}\right)\left(\frac{\partial w}{\partial n}-\frac{w}{R}+\frac{1}{R}\frac{\partial v}{\partial\phi}+\frac{\varepsilon}{\alpha_s}T_{n\phi}\right)+$$
$$\frac{2}{R}\frac{\partial R}{\partial\phi}\left(\frac{\partial v}{\partial n}-\frac{1}{R}(\frac{\partial w}{\partial\phi}+v)+\frac{\varepsilon}{\alpha_s}(T_{nn}-T_{\phi\phi})\right)=0. \quad (6.26)$$

Another boundary condition is the arc-length condition $X_s^2+Z_s^2=1$ and also the kinematic condition is

$$h_s\left(\varepsilon\frac{\partial R}{\partial t}+(\cos\phi+\frac{1}{n}\frac{\partial R}{\partial t}\sin\phi)(X_tZ_s-X_sZ_t)-v+\frac{\partial R}{\partial\phi}\frac{w}{n}\right)$$
$$+\varepsilon u\frac{\partial R}{\partial s}-\varepsilon\frac{\partial R}{\partial s}(X_tZ_s-X_sZ_t+\varepsilon n\cos\phi(X_sZ_{ss}-Z_sX_{ss}))=0. \quad (6.27)$$

These boundary conditions (6.24) and (6.27) are applied at the free surface $n=R(s,\phi,t)$.

6.4 Asymptotic Analysis

We now examine the above set of equations in more detail. We begin by expanding u,v,w and p in Taylor's series in εn (see Eggers (1997) and Hohman *et al.* (1984)) and $R,X,Z,T_{ss},T_{nn},T_{\phi\phi}$ in asymptotic series in ε. We suppose that the leading order form of the axial component of the velocity is independent of ϕ. It is also assumed that small perturbations do not affect the centerline. Therefore, we have

$$
\begin{aligned}
u(s,n,\phi,t) &= u_0(s,t) + (\varepsilon\, n)u_1(s,\phi,t) + (\varepsilon\, n)^2 u_2(s,\phi,t) + ... \\
v(s,n,\phi,t) &= (\varepsilon\, n)v_1(s,\phi,t) + (\varepsilon\, n)^2 v_2(s,\phi,t) + ... \\
w(s,n,\phi,t) &= (\varepsilon\, n)w_1(s,\phi,t) + (\varepsilon\, n)^2 w_2(s,\phi,t) + ... \\
p(s,n,\phi,t) &= p_0(s,\phi,t) + (\varepsilon\, n)p_1(s,\phi,t) + ... \\
R(s,n,\phi,t) &= R_0(s,t) + (\varepsilon)R_1(s,\phi,t) + ... \\
X(s,n,\phi,t) &= X_0(s) + (\varepsilon)X_1(s,t) + ... \\
Z(s,n,\phi,t) &= Z_0(s) + (\varepsilon)Z_1(s,t) + ... \\
T_{ss}(s,n,\phi,t) &= T^0_{ss}(s,t) + \varepsilon\, T^1_{ss}(s,t) + ... \\
T_{nn}(s,n,\phi,t) &= T^0_{nn}(s,t) + \varepsilon\, T^1_{nn}(s,t) + ... \\
T_{\phi\phi}(s,n,\phi,t) &= \varepsilon T^1_{\phi\phi}(s,t) + \varepsilon^2\, T^2_{\phi\phi}(s,t) + \ ... \\
T_{sn}(s,n,\phi,t) &= \varepsilon\, T^1_{sn}(s,t) + \varepsilon^2\, T^2_{sn}(s,t) + ... \\
T_{s\phi}(s,n,\phi,t) &= \varepsilon\, T_{s\phi}(s,t) + \varepsilon^2\, T^2_{s\phi}(s,t) + ... \\
T_{n\phi}(s,n,\phi,t) &= \varepsilon\, T^1_{n\phi}(s,t) + \varepsilon^2\, T^2_{n\phi}(s,t) + ...
\end{aligned}
$$

It can be found from the continuity equation that

$$O(\varepsilon n): \quad u_{0s} + 2v_1 + w_{1\phi} = 0, \tag{6.28}$$

$$O(\varepsilon n)^2 : u_{1s} + 3v_2 + w_{2\phi} + 3v_1 + (w_{1\phi}\cos\phi - w_1 \sin\phi)\,(X_s Z_{ss} - X_{ss} Z_s) = 0. \tag{6.29}$$

By solving the second tangential stress condition, it can be found that

$$O(\varepsilon n): \quad R_0^3 v_{1\phi} = 0, \tag{6.30}$$

$$O(\varepsilon n)^2: \quad 3R_0^2 R_1 v_{1\phi} + R_0^4(w_2 + v_{2\phi}) - 2R_0^2 R_{1\phi} w_{1\phi} = 0. \tag{6.31}$$

From (6.30) we see that $v_{1\phi} = 0$, and by differentiating (6.28), we obtain $w_{1\phi\phi} = 0$. Because w_1 is periodic in ϕ we must have $w_1 = w_1(s,t)$. That leads to $v_1 = -\frac{u_{0s}}{2}$ and from (6.31) we obtain

$$w_2 + v_{2\phi} = 0. \tag{6.32}$$

Using the first tangential stress condition, we obtain

$$O(\varepsilon n): \quad u_1 = u_0 \cos\phi (X_s Z_{ss} - X_{ss} Z_s), \tag{6.33}$$

$$O(\varepsilon n)^2: \quad u_2 = \frac{3}{2} u_{0s} \frac{R_{0s}}{R_0} + \frac{u_{0ss}}{4} + \frac{R_{0s}}{2\alpha_s R_0}(T_{ss}^0 - T_{nn}^0). \tag{6.34}$$

By differentiating (6.32) with respect to ϕ we have

$$w_{2\phi} = -v_{2\phi\phi}, \tag{6.35}$$

so that

$$v_{2\phi\phi} - 3v_2 = u_{1s} + (3v_1 \cos\phi - w_1 \sin\phi)(X_s Z_{ss} - X_{ss} Z_s), \tag{6.36}$$

so when the expression for u_1 and v_1 are used, we obtain

$$v_{2\phi\phi} - 3v_2 = \left(u_0(X_s Z_{sss} - X_{sss} Z_s) - \frac{u_{0s}}{2}(X_s Z_{ss} - X_{ss} Z_s)\right) \cos\phi$$
$$-w_1 \sin\phi (X_s Z_{ss} - X_{ss} Z_s). \tag{6.37}$$

v_2 and w_2 are periodic solutions

$$v_2 = \frac{1}{4}\left(\frac{u_{0s}}{2}(X_s Z_{ss} - X_{ss} Z_s) - u_0(X_s Z_{sss} - X_{sss} Z_s)\right)\cos\phi + \frac{w_1}{4}\sin\phi(X_s Z_{ss} - X_{ss} Z_s), \tag{6.38}$$

$$w_2 = \frac{1}{4}\left(\frac{u_{0s}}{2}(X_s Z_{ss} - X_{ss} Z_s) - u_0(X_s Z_{sss} - X_{sss} Z_s)\right)\sin\phi + \frac{w_1}{4}\cos\phi(X_s Z_{ss} - X_{ss} Z_s). \tag{6.39}$$

Based on the momentum equation in the radial direction, we have at leading order $p_{0n} = 0$ and at order ε it gives

$$p_1 = \left(u_0^2(X_s Z_{ss} - X_{ss} Z_s) - \frac{2}{Rb}u_0 + \frac{(X_0+1)Z_{0s} - Z_0 X_{0s}}{Rb^2}\right)\cos\phi - \frac{\alpha_s}{Re}\left(\frac{5}{2}u_{0s}(X_s Z_{ss} - X_{ss} Z_s) + u_{0s}(X_s Z_{sss} - X_{sss} Z_s)\right)\cos\phi + \frac{\alpha_s}{Re}w_1\sin\phi(X_s Z_{ss} - X_{ss} Z_s). \tag{6.40}$$

We will henceforth use X and Z instead of X_0 and Z_0 for simplicity.

For the momentum equation in the azimuthal direction, we have at leading order, $p_{0\phi} = 0$. At next order, which is order ε, we obtain the equation given above. From the normal stress condition at leading order, we have

$$p_0 = -\frac{\alpha_s u_{0s}}{Re} + \frac{1}{R_0 We} + \frac{T^0_{nn}}{Re}, \tag{6.41}$$

and we also have at order ε

$$p_1 = \frac{1}{R_0 We}\left(-\frac{R_{1\phi\phi} + R_1}{R_0^2} + \cos\phi(X_s Z_{ss} - X_{ss} Z_s)\right) + \frac{4\alpha_s v_2}{Re}. \tag{6.42}$$

By substituting the expression v_2 in the last equation, we obtain

$$p_1 = \frac{1}{R_0 We}\left(-\frac{R_{1\phi\phi}+R_1}{R_0^2} + \cos\phi(X_s Z_{ss} - X_{ss} Z_s)\right) + \frac{\alpha_s}{Re}\left(\frac{u_{0s}}{2}(X_s Z_{ss} - X_{ss} Z_s) - u_0(X_s Z_{sss} - X_{sss} Z_s)\right)\cos\phi + \frac{\alpha_s w_1}{Re}\sin\phi(X_s Z_{ss} - X_{ss} Z_s). \tag{6.43}$$

If we substitute for p_1 from (6.40) into the previous equation, we obtain

$$(X_s Z_{ss} - X_{ss} Z_s)\left(u_0^2 - \frac{3\alpha_s}{Re}\,u_{0s} - \frac{1}{WeR_0}\right) - \frac{2}{Rb}\,u_0 + \frac{(X+1)Z_s - ZX_s}{Rb^2} = 0. \tag{6.44}$$

The momentum equation (6.15) in the axial direction at order ε is

$$u_{0t} + u_0 u_{0s} = -p_{0s} + \frac{(X+1)X_s + ZZ_s}{Rb^2} + \frac{\alpha_s}{Re}\left(u_{oss} + 4u_2 + u_{2\phi\phi}\right) + \frac{1}{Re}\,\frac{\partial T^0_{ss}}{\partial s}, \tag{6.45}$$

after substituting the expressions for u_2 and p_0, the previous equation becomes

$$u_{0t} + u_0 u_{0s} = -\frac{1}{We}\,\frac{\partial}{\partial s}\left(\frac{1}{R_0}\right) + \frac{(X+1)X_s + ZZ_s}{Rb^2} + \frac{3\alpha_s}{Re}\left(u_{0ss} + 2u_{0s}\frac{R_{0s}}{R}\right) + \frac{1}{Re}\left(\frac{1}{R_0^2}\frac{\partial}{\partial s}\,R_0^2\,(T^0_{ss} - T^0_{nn})\right). \tag{6.46}$$

From the kinematic condition at order ε, it can be obtained

$$R_{0t} + \frac{u_{0s}}{2}R_0 + u_0 R_{0s} = 0. \tag{6.47}$$

From the extra stress tensor, which is $T_{ss}, T_{sn}, T_{s\phi}, T_{nn}, T_{n\phi}, T_{\phi\phi}$,we have at leading order

as follows

$$\frac{\partial T^0_{ss}}{\partial t} + u_0 \frac{\partial T^0_{ss}}{\partial s} - 2\frac{\partial u_0}{\partial s} T^0_{ss} = \frac{1}{De}\left(2(1-\alpha_s)\frac{\partial u_0}{\partial s} - T^0_{ss}\right), \tag{6.48}$$

$$\frac{\partial T^0_{nn}}{\partial t} + u_0 \frac{\partial T^0_{nn}}{\partial s} + \frac{\partial u_0}{\partial s} T^0_{nn} = \frac{-1}{De}\left((1-\alpha_s)\frac{\partial u_0}{\partial s} + T^0_{nn}\right), \tag{6.49}$$

We have the last equation which is the arc-length at order ε

$$X_s^2 + Z_s^2 = 1. \tag{6.50}$$

we can see that the equations (6.46)-(6.49) and (6.50) reduce to Clasen *et al.* (2006) when $Rb \to \infty$.

6.5 Steady State Solutions

From the previous section, we have the six variables which are $u_0, R_0, X, Z, T^0_{ss}, T^0_{nn}$. These variables are functions of s only in the steady state. Hence, the steady state equations are

$$\begin{aligned} u_0 u_{0s} = -\frac{1}{We}\frac{\partial}{\partial s}\left(\frac{1}{R_0}\right) + \frac{(X+1)X_s + ZZ_s}{Rb^2} \\ +\frac{3\alpha_s}{Re}\left(u_{0ss} + 2u_{0s}\frac{R_{0s}}{R}\right) + \frac{1}{Re}\left(\frac{1}{R_0^2}\frac{\partial}{\partial s} R_0^2 \left(T^0_{ss} - T^0_{nn}\right)\right), \end{aligned} \tag{6.51}$$

$$u_0 \frac{\partial T^0_{ss}}{\partial s} - 2\frac{\partial u_0}{\partial s} T^0_{ss} = \frac{1}{De}\left(2(1-\alpha_s)\frac{\partial u_0}{\partial s} - T^0_{ss}\right), \tag{6.52}$$

$$u_0 \frac{\partial T^0_{nn}}{\partial s} + \frac{\partial u_0}{\partial s} T^0_{nn} = \frac{-1}{De}\left((1-\alpha_s)\frac{\partial u_0}{\partial s} + T^0_{nn}\right), \tag{6.53}$$

$$(X_s Z_{ss} - X_{ss} Z_s)\left(u_0^2 - \frac{3\alpha_s}{Re}\, u_{0s} - \frac{1}{WeR_0}\right) - \frac{2}{Rb}\, u_0 + \frac{(X+1)Z_s - ZX_s}{Rb^2} = 0, \quad (6.54)$$

$$\frac{u_{0s}}{2} R_0 + u_0 R_{0s} = 0, \quad (6.55)$$

$$X_s^2 + Z_s^2 = 1. \quad (6.56)$$

From (6.55) $R^2 u = constant$ is found. Now, we use the initial conditions $R(0) = 1$ and $u(0) = 1$, so that, we obtain $R^2 u = 1$ after using this expression, equation (6.46) becomes

$$\begin{aligned} u_0 u_{0s} = & -\frac{1}{2We}\,\frac{u_{0s}}{\sqrt{u}} + \frac{(X+1)X_s + ZZ_s}{Rb^2} \\ & + \frac{3\alpha_s}{Re}\left(u_{0ss} - \frac{u_{0s}^2}{u_0}\right) + \frac{1}{Re}\left(\frac{\partial}{\partial s}(T_{ss}^0 - T_{nn}^0) - \frac{u_{0s}}{u_0}(T_{ss}^0 - T_{nn}^0)\right), \end{aligned} \quad (6.57)$$

$$(X_s Z_{ss} - X_{ss} Z_s)\left(u_0^2 - \frac{3\alpha_s}{Re}\, u_{0s} - \frac{\sqrt{u}}{We}\right) - \frac{2}{Rb}\, u_0 + \frac{(X+1)Z_s - ZX_s}{Rb^2} = 0, \quad (6.58)$$

$$u_0 \frac{\partial T_{ss}^0}{\partial s} - 2\,\frac{\partial u_0}{\partial s}\, T_{ss}^0 = \frac{1}{De}\left(2(1-\alpha_s)\frac{\partial u_0}{\partial s} - T_{ss}^0\right), \quad (6.59)$$

$$u_0 \frac{\partial T_{nn}^0}{\partial s} + \frac{\partial u_0}{\partial s}\, T_{nn}^0 = \frac{-1}{De}\left((1-\alpha_s)\frac{\partial u_0}{\partial s} + T_{nn}^0\right), \quad (6.60)$$

$$X_s^2 + Z_s^2 = 1. \quad (6.61)$$

If we allow $De \to 0$ and $\alpha_s = 1$ (which implies $\mu_p = 0$) we have T_{ss}^0 and $T_{nn}^0 \to 0$

and (6.57)-(6.61) which produce the equivalent set of equations found in Părău *et al.* (2006,2007). Furthermore, if we let $Re \to \infty$ we obtain the inviscid equation of Decent *et al.* (2009). In the equations (5.57)-(5.61), we have five unknowns, which are X, Z, u_0, T^0_{ss} and T^0_{nn}. We solve these equations for high viscosity fluids by using the Runge-Kutta method. Părău *et al.* (2006, 2007) have used the Runge-Kutta method and Newton's method to solve the problem of viscous liquid curved jets and compared the results with the Runge-Kutta method for inviscid case. They found a good agreement between the two methods for the steady centerline and radius of the jet. Părău *et al.* (2006, 2007) also found that there is a very little difference with and without viscosity in numerical solutions. To find the steady state solutions for the equations (6.57)-(6.61), we make $Re \to \infty$ in the inviscid case, because we consider low viscosity fluids here. Decent *et al.* (2009) solved the Newtonian fluid by using this assumption. Therefore, we will use the same assumption in this paper to find the steady state solutions. However, if we consider that these equations are dependent of t, this means that $X_{0t} \neq 0$ and $Z_{0t} \neq 0$. This assumption leads to there being some extra unsteady terms in these equations in $E = Z_s X_t - Z_t X_s$. (see Părău *et al.* (2007)). Părău *et al.* (2007) have considered the case with $X(s,t) = X_0(s,t) + \widehat{X}(s,t)$ and $Z(s,t) = Z_0(s,t) + \widehat{Z}(s,t)$ and then found a set of equations linearized in $\widehat{X}$ and $\widehat{Z}$. Părău *et al.* (2007) also found the maximum deviation of order 10^{-2} of the perturbation of the steady state centerline. This value is small compared to the $O(1)$ values of $X_0(s)$ and $Z_0(s)$. Therefore, $E \approx 0$ is a very accurate assumption to be taken from the orifice to the break-up point. Experimentally Wong *et al.* (2004) observe that the centerline of the jet is steady, which means $X_{st} \approx 0$, $Z_{st} \approx 0$ and $E \approx 0$. As we mentioned earlier, we solve the equations (6.59)-(6.63) for inviscid centerline problem (which means $Re \to \infty$) using the Runge-Kutta method with the boundary conditions at the nozzle as $X(0) = Z(0) = Z_s(0) = T^0_{ss}(0) = T^0_{nn}(0) = 0$ and $u(0) = X_s(0) = 1$. In Figs. 6.1-6.5, we find the jet trajectory, the extra stress tensor

(T^0_{ss}, T^0_{nn}) and the jet radius for different values of Rossby and Weber numbers by using the Runge-Kutta method which is the ODE45 package in MATLAB. In the next paragraph, we will give more explanations about these figures.

For different values of the Rossby number (rotation rates), we plot a graph which is Fig 6.1 to see the effect of this number on the liquid jet. This graph shows that when the Rossby number is small, the liquid coils quickly. In Fig. 6.2 the graph shows that a small value of the Weber number makes the liquid coil very fast. This is obvious due to the inertia which means the speed of the jet is low, the liquid coils quickly. In addition, in Fig. 6.3 we display the relationship between the extra stress tensor, which is T^0_{ss}, and the arc-length for different values of the Rossby number and this graph shows when the rotation is very high the extra stress tensor has more effect on the jet. Moreover, in Figs. 6.4 and 6.5 these graphs correspond to different values of the Rossby number for the extra stress tensor, T^0_{nn} and the radius of the jet, R_0 along the arc-length$s$. From these figures, it can be seen that the jet becomes thin when the arc-length is increased.

6.6 Temporal Instability

Now we make small perturbations to the steady state solution, so that we have

$$u(s,t) = u_0(s) + \delta\widehat{u}\,\exp(i\kappa\overline{s} + \omega\overline{t}) + O(\delta\varepsilon) + cc., \tag{6.62}$$

$$R(s,t) = R_0(s) + \delta\widehat{R}\,\exp(i\kappa\overline{s} + \omega\overline{t}) + O(\delta\varepsilon) + cc., \tag{6.63}$$

$$p(s,t) = p_0(s) + \delta\widehat{p}\,\exp(i\kappa\overline{s} + \omega\overline{t}) + O(\delta\varepsilon) + cc., \tag{6.64}$$

$$T_{ss}(s,t) = T_{0ss}(s) + \delta\widehat{T}_{ss}\,\exp(i\kappa\overline{s} + \omega\overline{t}) + O(\delta\varepsilon) + cc., \tag{6.65}$$

$$T_{nn}(s,t) = T_{0nn}(s) + \delta\widehat{T}_{nn}\,\exp(i\kappa\overline{s} + \omega\overline{t}) + O(\delta\varepsilon) + cc., \tag{6.66}$$

$$X(s,t) = X(s) + \delta\varepsilon\widehat{X}(\overline{s}, s, \overline{t}, t) + cc., \tag{6.67}$$

$$Z(s,t) = Z(s) + \delta\varepsilon\widehat{Z}(\overline{s}, s, \overline{t}, t) + cc., \tag{6.68}$$

where $\overline{s} = s/\varepsilon$ is small length scales, $\overline{t} = t/\varepsilon$ is small time scales, $k = k(s)$ and $\omega = \omega(s)$ are the wavenumber and frequency of the disturbances, cc is complex conjugates and δ is a small constant which is $0 < \delta < \varepsilon^2$ (see Uddin (2007)). The symbols with subscripts denote steady state solutions. In order to prevent instability of wave modes with zero wavelength, we replace the leading order pressure term in (6.46) with the full expression of the mean curvature which is

$$\frac{1}{We}\left(\frac{1}{R(1+\varepsilon^2\,R_s^2)^{\frac{1}{2}}} - \frac{\varepsilon^2\,R_{ss}}{(1+\varepsilon^2\,R_s^2)^{\frac{3}{2}}}\right).$$

Many authors have used the complete mean curvature expression, such as Lee (1974) and Eggers (1997).

Then the axial equation of motion becomes

$$\begin{aligned} u_t + u_0 u_{0s} = & -\frac{1}{We}\frac{\partial}{\partial s}\left(\frac{1}{R(1+\varepsilon^2\,R_s^2)^{\frac{1}{2}}} - \frac{\varepsilon^2\,R_{ss}}{(1+\varepsilon^2\,R_s^2)^{\frac{3}{2}}}\right) + \frac{(X+1)X_s + ZZ_s}{Rb^2} \\ + & \frac{3\alpha_s}{Re}\left(u_{0ss} + 2u_{0s}\frac{R_{0s}}{R}\right) + \frac{1}{Re}\left(\frac{1}{R_0^2}\frac{\partial}{\partial s}\,R_0^2\,(T_{ss}^0 - T_{nn}^0)\right), \end{aligned} \tag{6.69}$$

with

$$\frac{\partial T_{ss}^0}{\partial t} + u_0\,\frac{\partial T_{ss}^0}{\partial s} - 2\,\frac{\partial u_0}{\partial s}\,T_{ss}^0 = \frac{1}{De}\left(2(1-\alpha_s)\frac{\partial u_0}{\partial s} - T_{ss}^0\right), \tag{6.70}$$

$$\frac{\partial T_{nn}^0}{\partial t} + u_0\,\frac{\partial T_{nn}^0}{\partial s} + \frac{\partial u_0}{\partial s}\,T_{nn}^0 = \frac{-1}{De}\left((1-\alpha_s)\frac{\partial u_0}{\partial s} + T_{nn}^0\right). \tag{6.71}$$

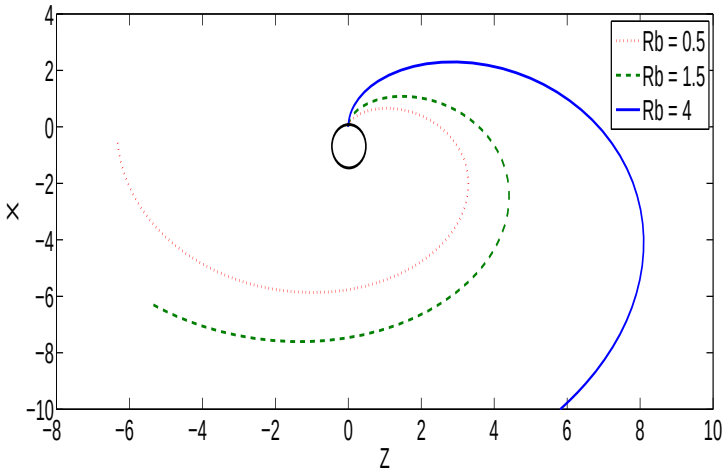

Figure 6.1: The trajectory of an inviscid liquid jet obtained by using a Runge-Kutta method and the orifice is placed at (0,0). The jet curves more when the Rossby number decreases (meaning high rotation rates). We use $We = 100$, $De = 10$ and $\alpha_s = 0.20$.

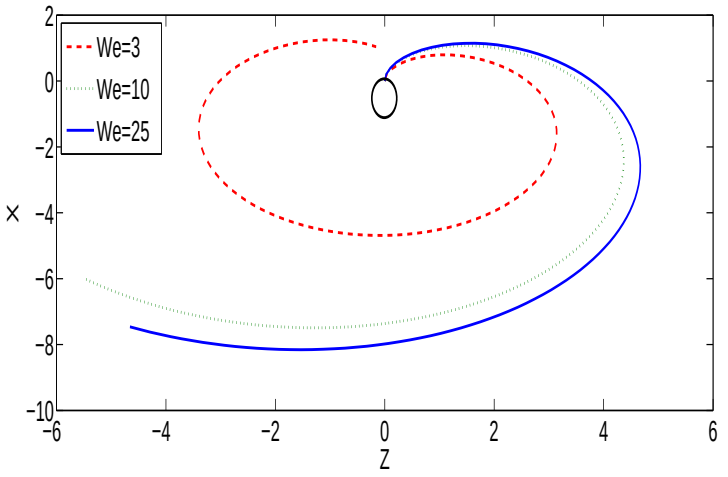

Figure 6.2: The trajectory of an inviscid liquid jet obtained by using the Runge-Kutta method and orifice is placed at (0,0). The jet curves more when the Weber number decreases. We use $Rb = 1.5$, $De = 10$ and $\alpha_s = 0.20$.

6.7 Dispersion Relation

The perturbation equations (6.62)-(6.68) are now substituted into the equations (6.69), (6.47), (6.70) and (6.71). The resulting set of equations may be written in matrix form

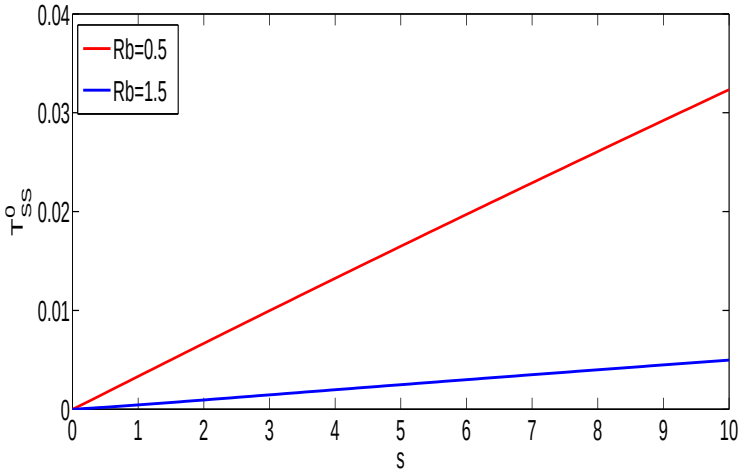

Figure 6.3: Graph showing the relationship between T^0_{ss} and arc-length s of a rotating liquid jets for different values of Rossby number at $We = 25$, $De = 10$ and $\alpha_s = 0.20$.

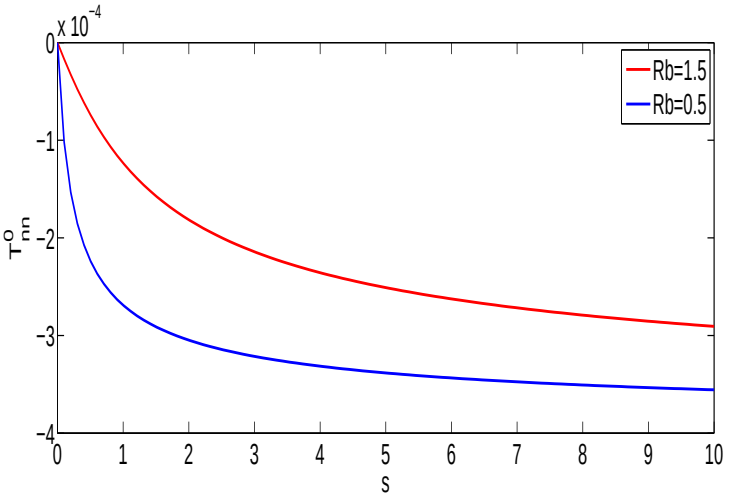

Figure 6.4: Graph showing the relationship between T^0_{nn} and arc-length s of rotating liquid jets for different values of Rossby number at $We = 25$, $De = 10$ and $\alpha_s = 0.20$.

$$\begin{pmatrix} \frac{3\tilde{\alpha_s}k^2}{Re} + \omega + iku_0 & -\frac{ik}{We}\left(\frac{1}{R_0^2} - k^2\right) + \frac{2ik}{R_0 Re}\left(T^0_{ss} - T^0_{nn}\right) & \frac{ik}{Re} & -\frac{ik}{Re} \\ \frac{ikR_0}{2} & \omega + iku_0 & 0 & 0 \\ -2ikT^0_{ss} - \frac{2ik}{De} & 0 & \omega + iku_0 & 0 \\ ikT^0_{nn} + \frac{ik}{De} & 0 & 0 & \omega + iku_0 \end{pmatrix}$$

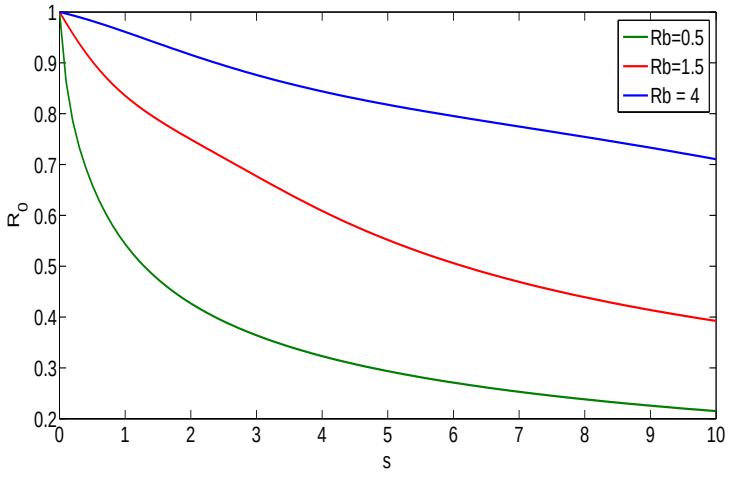

Figure 6.5: Graph showing the relationship between the radius, R, and the arc-length, s, for different values of the Rossby number where $We = 100$, $De = 10$ and $\alpha_s = 0.20$.

If we seek non-trivial solutions then the determinant of this matrix must be zero which yields

$$\left(\omega + iku_0\right)^2 + \frac{3\tilde{\alpha_s}k^2}{Re}\left(\omega + iku_0\right) - \frac{k^2 R_0}{2We}\left(\left(\frac{1}{R_0^2} - k^2\right) - \frac{2We}{R_0\, Re}(T^0_{ss} - T^0_{nn})\right) - \frac{k^2}{Re}\left(2T^0_{ss} + T^0_{nn} + \frac{3}{De}\right) = 0. \tag{6.72}$$

We note that there is a new scaling for the viscosity ratio which is $\tilde{\alpha_s} = \frac{\alpha_s}{\varepsilon}$. Without this new scaling, we cannot bring the viscous term into the dispersion relation. We mentioned earlier, $\alpha_s + \alpha_p = 1$, where α_s and α_p are the solvent viscosity and the polymeric viscosity respectively. After substituting the new scaling, the last equation becomes $\varepsilon\tilde{\alpha_s} + \alpha_p = 1$, which means that $\alpha_p \gg \alpha_s$. However, both the solvent viscosity and the polymeric viscosity are very small $\mu_s, \mu_p \ll 1$. By choosing $\omega_i = -ku_0$, we get

$$\omega_r^2 + \frac{3\tilde{\alpha_s}k^2}{Re}\omega_r - \frac{k^2 R_0}{2We}\left(\left(\frac{1}{R_0^2} - k^2\right) - \frac{2We}{R_0\, Re}(T^0_{ss} - T^0_{nn})\right) - \frac{k^2}{Re}\left(2T^0_{ss} + T^0_{nn} + \frac{3}{De}\right) = 0, \tag{6.73}$$

which becomes

$$\omega_r = \frac{-3\tilde{\alpha_s}k^2}{2Re} + \frac{k}{2}\sqrt{\frac{2}{R_0We}\left((1-(kR_0)^2 - \frac{2We}{R_0\,Re}B\right) + \frac{4}{Re}\left(2T^0_{ss} + T^0_{nn} + \frac{3}{De}\right) + \left(\frac{3\tilde{\alpha_s}k}{Re}\right)^2}. \tag{6.74}$$

We differentiate the last equation with respect to k to find the most unstable wavenumber $k = k^*$ which is given by

$$k^* = \frac{1}{(2R_0^3)^{1/4}} \frac{\left(\frac{R_0GWe}{2} + 1 - 2B\right)^{\frac{1}{2}}}{\sqrt{\left(3\tilde{\alpha_s}Oh + \sqrt{2R_0}\right)}}, \tag{6.75}$$

where $B = T^0_{ss} - T^0_{nn}$ and $G = \frac{4}{Re}\left(2T^0_{ss} + T^0_{nn} + \frac{3}{De}\right)$. For temporal instability, the growth rate ω_r is positive which occurs when $0 < kR_0 < 1$. When $De \to 0$, $\alpha_s = 1$ and $T^0_{ss} = T^0_{nn} = 0$ the dispersion relation is

$$k^* = \frac{1}{(2R_0^3)^{1/4}} \frac{1}{\sqrt{\left(3Oh + \sqrt{2R_0}\right)}}, \tag{6.76}$$

which is the same as for Newtonian liquid jets which was found by Decent *et al.* (2009).

6.8 Results and Discussion

From the dispersion relation (6.72), we can examine the linear instability of viscoelastic liquid curved jets in two ways; which are a spatial and temporal instability analysis. In the case of a spatial instability analysis, which grows in space along the jet, we consider that ω is imaginary and k is complex (*i.e.* $k = k_r + ik_i$, where k_r is the wavenumber of the wave and k_i is the spatial growth rate). The second instability, which we can investigate

from the dispersion relation (6.72), is the temporal instability where k is real and this kind of instability, which occurs when $\Re(\omega)>0$, will be examined throughout this thesis. In addition, to find the most unstable mode, which is referred here as k^*, of viscoelastic curved jets we use Eq. (6.75). In order to study the behavior of the growth rate and the wavenumber of viscoelastic liquid curved jets, there are four parameters that can affect the temporal instability, which are the Reynolds number, the Weber number, the Deborah number and the viscosity ratio. Firstly, we will discuss the effects of the Reynolds number on the jet for two different values and fix the rest of the parameters. Secondly, the explanations of the influence of different values of the Weber number (keeping the rest of parameters fixed) on the jet are induced in section 6.8.2. Thirdly, the effects of the Deborah number (change De and keeping all parameters fixed) on the jet is investigated in section 6.8.3. Finally, the effects of viscosity ratio on viscoelastic liquid curved jets are investigated in section 6.8.4.

6.8.1 The Effects of Reynolds Number on Viscoelastic Liquid Curved Jets

In Figs. 6.6 and 6.8, we chose different values of the Rossby number, $Rb = 0.5, 1.5$ and 4 for two values of the Reynolds number which are $Re = 1000$ and 3000 for obtaining the relationship between the growth rate of the most unstable mode and the arc-length s. From these figures, it can be noticed that when the Rossby number is small (meaning the rotation rate is high), the growth rate of the most unstable mode becomes large and as well when the Reynolds number is enhanced the growth rate of the most unstable mode is increased. Figs. 6.7 and 6.9 show the relationship between the maximum wave number for the most unstable k^* and the arc-length s for different values of Reynolds number, $Re = 1000$ and 3000 and found that high rotation rates lead to an increase in the maximum wavenumber. It can be seen in Figs. 6.10 and 6.11 that when the Reynolds number is

increased, the growth rate of the most unstable mode and the maximum wavenumber is increased at a constant $Rb = 0.5$. Figure 6.12 shows the relationship between the growth rate of disturbances and corresponding different values of the Reynolds number. We see that when we increase the Reynolds number the growth rate will also increase so that a reduction in viscosity leads to shorter jets.

6.8.2 The Effects of Weber Number on Viscoelastic Liquid Curved Jets

The correlation between the maximum growth rate and the arc-length s is represented in Figs. 6.13-6.15 and it can be noticed that when the rotation is increased the maximum growth rate is decreased for different values of the Weber number. However, the relationship between the maximum wavenumber for the most unstable mode k^* is plotted in Figs. 6.14-6.16 and it can be seen that when the Rossby number is increased the maximum wavenumber decreased. Figs. 6.17 and 6.18 show the effect of increasing Weber number on the maximum growth rate and the maximum wavenumber against the arc-length s respectively and this is the same result which is discussed about the maximum growth rate in Figs. 6.14-6.16. Fig. 6.19 indicates the relationship between the maximum growth rate and two values of the Weber number which means when we increase Weber number the maximum growth is decreased.

6.8.3 The Effects of Deborah Number on Viscoelastic Liquid Curved Jets

From Figs. 6.20-6.22, we can see that the relationship between the maximum growth rate and the arc-length s are plotted for two values of the Deborah number, $De = 15$ and 25. In Figs. 6.21-6.23 the maximum wavenumber of the most unstable mode k^* is plotted against the arc-length s, and it can be seen that increasing rotation rates decrease the

maximum wavenumber k^*. Fig. 6.24 shows that increasing the Deborah number decreases the maximum growth rate.

6.8.4 The Effects of Viscosity Ratio on Viscoelastic Liquid Curved Jets

In this section, we investigate the influence of the viscosity ratio α_s on the behavior of viscoelastic liquid curved jets. The relationship between the maximum growth rate and the arc-length s are plotted in Figs. 6.25-6.27 for different values of the viscosity ratio, $\alpha_s = 40$ and 60. In Figs. 6.26-6.28, we plot the maximum wavenumber against the arc-length along the jet and we see that when rotation rates are high, the maximum wavenumber becomes high. In Figs. 6.29 and 6.30, we make a comparison between the maximum growth rate and the maximum wavenumber and the arc-length for two different values of the viscosity ratio ($\tilde{\alpha_s} = 40$ and 60). It can be observed that when we increase the viscosity ratio the maximum growth and the wavenumber of the most unstable mode are decreased which means in this case the liquid becomes more elastic and in general increasing the viscosity ratio leads to decrease the growth rate (see Fig. 6.31). Furthermore, we plot a graph to show the relation between the growth rate and the wavenumber for various values of s (see Fig. 6.32). It can be observed from this graph that when we increase the arc-length s, the growth rate increases along the jet.

Moreover, the relationship between the growth rate and the wavenumber is plotted in Fig. 6.33 for three fluids, which are inviscid fluid, viscous fluid and viscoelastic fluid. It can be observed from this graph that viscoelastic jets are more unstable than Newtonian jets and less unstable than inviscid jets. This result agrees with Goldin's result (see Goldin 1969) where here $R_0 = 1$ for straight jets.

In order to examine the break-up of viscoelastic liquid curved jets, we will use nonlinear theory to investigate the break-up lengths and satellite droplets. This nonlinear theory

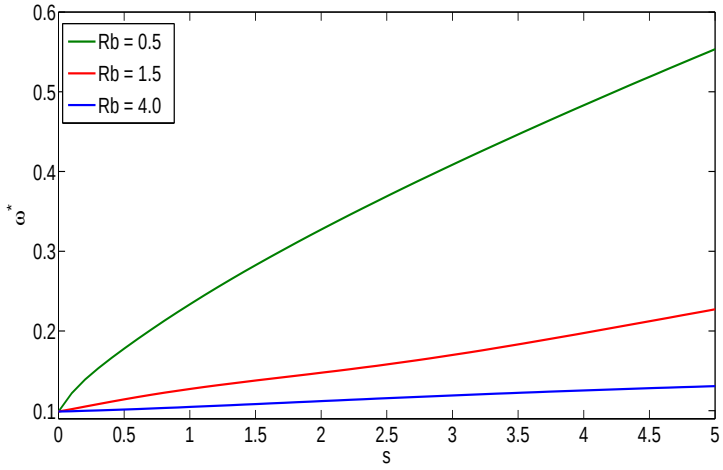

Figure 6.6: Graph showing the relationship between the growth rate ω_r^* for the most unstable mode and the arc-length s for a viscoelastic liquid jet for different values of the Rossby number Rb, where the dimensionless numbers are $Re = 1000$, $We = 10$, $De = 15$ and $\tilde{\alpha_s} = 20$.

will be studied in this thesis in Chapter 7.

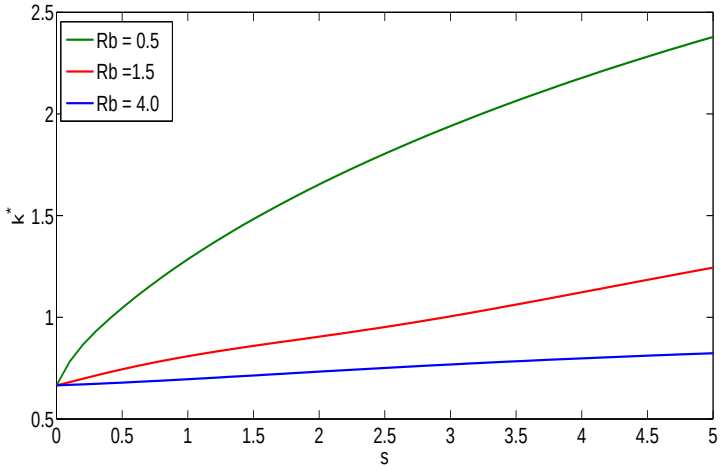

Figure 6.7: Graph showing the relationship between the wavenumber of the most unstable k^* and the arc-length s for a viscoelastic liquid jet for different values of the Rossby number Rb, where the dimensionless numbers are $Re = 1000$, $We = 10$, $De = 15$ and $\tilde{\alpha_s} = 20$.

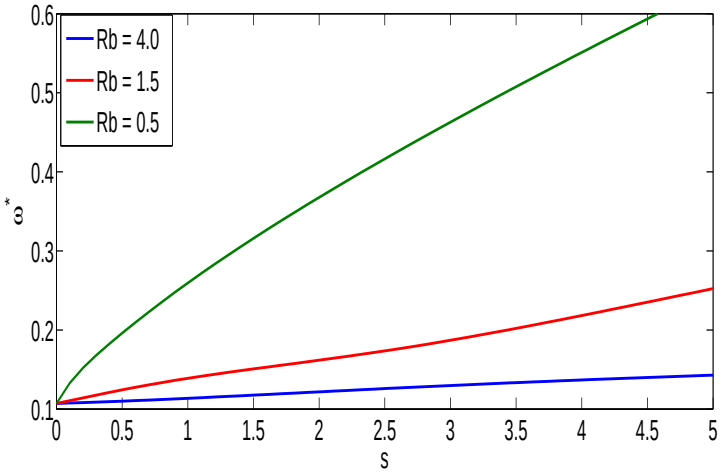

Figure 6.8: Graph showing the relation between the growth rate ω_r^* of the most unstable mode and the arc-length s for a viscoelastic liquid jet for different values of the Rossby number Rb, where the dimensionless numbers are $Re = 3000$, $We = 10$, $De = 15$ and $\tilde{\alpha_s} = 20$.

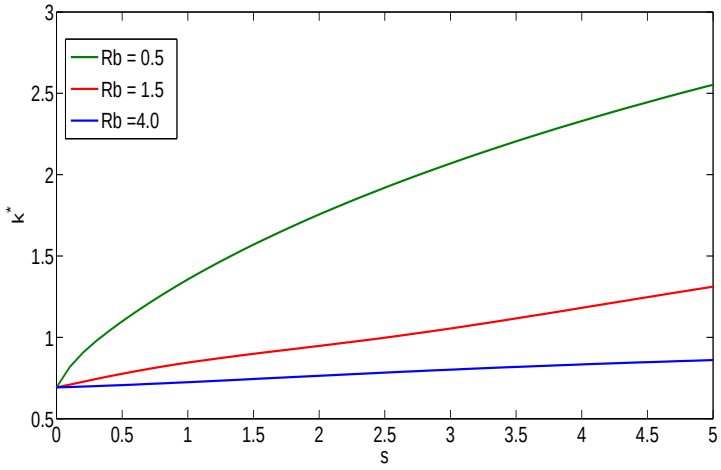

Figure 6.9: Graph showing the relationship between the maximum wavenumber of the most unstable k^* and the arc-length s for a viscoelastic liquid jet for different values of the Rossby number Rb, where the dimensionless numbers are $Re = 1000$, $We = 10$, $De = 15$ and $\tilde{\alpha_s} = 20$.

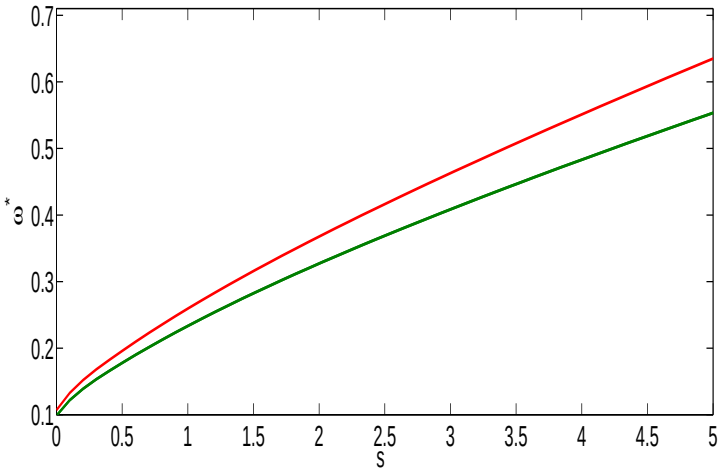

Figure 6.10: Graph showing the relationship between the growth rate ω_r^* and the arc-length s for a viscoelastic liquid jet for two values of the Reynolds number, $Re = 1000$ (green line), 3000 (red line), at $Rb = 0.5$, where the dimensionless numbers are $We = 10$, $De = 15$ and $\tilde{\alpha_s} = 20$.

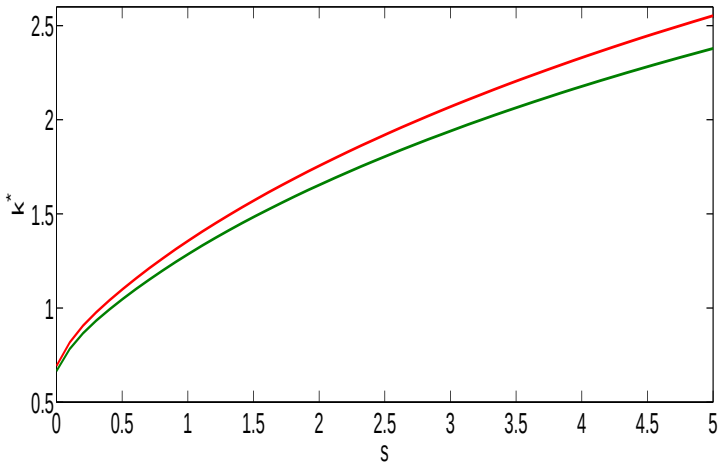

Figure 6.11: Graph showing the relationship between the maximum wavenumber of the most unstable k^* and the arc-length s for a viscoelastic liquid jet for two values of the Reynolds number, $Re = 1000$ (green line), 3000 (red line), at $Rb = 0.5$, where the dimensionless numbers are $We = 10$, $De = 15$ and $\tilde{\alpha_s} = 20$.

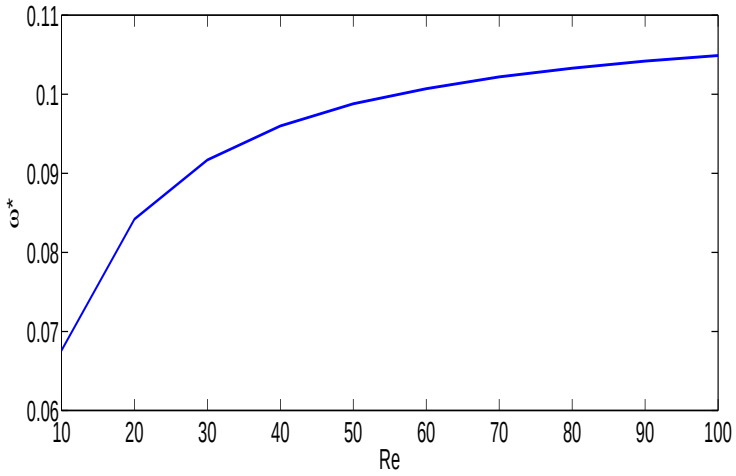

Figure 6.12: Graph showing the relation between the growth rate ω_r^* of the most unstable mode and the Reynolds number Re for a viscoelastic liquid jet, where the dimensionless numbers are $We = 10$, $De = 15$ and $\tilde{\alpha_s} = 20$.

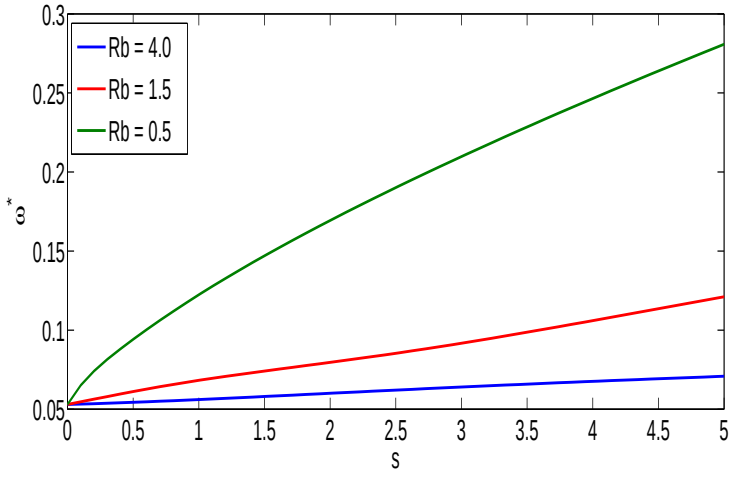

Figure 6.13: Graph showing the relationship between the growth rate ω_r^* of the most unstable mode and the arc-length k for a viscoelastic liquid jet for different values of the Rossby number Rb, where the dimensionless numbers are $Re = 1000$, $We = 30$, $De = 15$ and $\tilde{\alpha_s} = 20$.

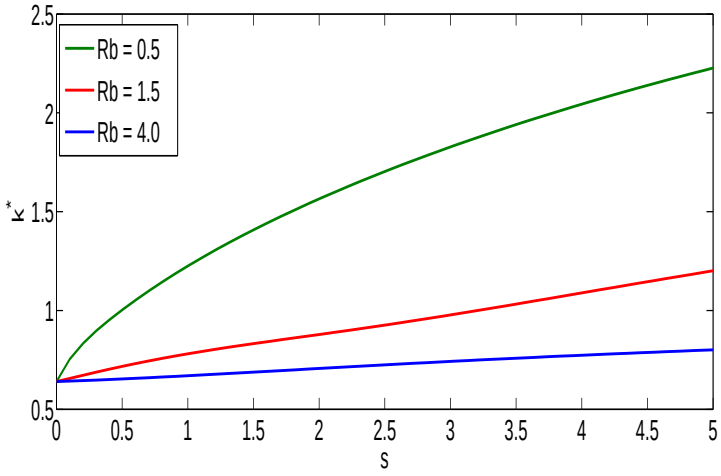

Figure 6.14: Graph showing the relationship between the maximum wavenumber of the most unstable k^* and the arc-length s for a viscoelastic liquid jet for different values of the Rossbt number Rb, where the dimensionless numbers are $Re = 1000$, $We = 30$, $De = 15$ and $\tilde{\alpha_s} = 20$.

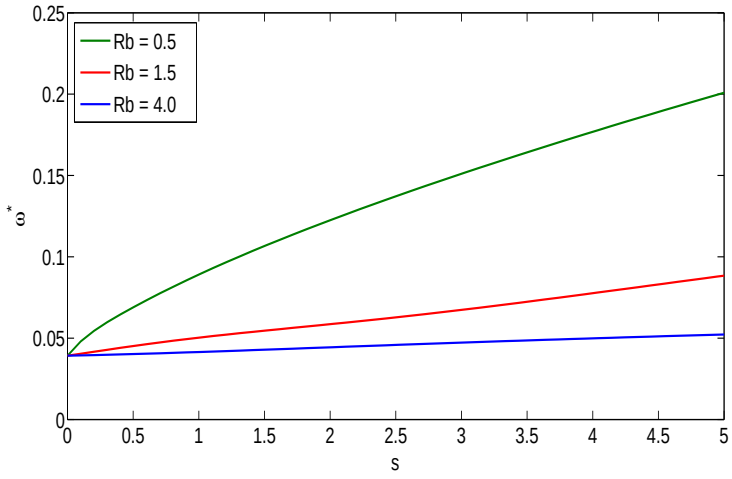

Figure 6.15: Graph showing the relationship between the growth rate ω_r^* of the most unstable mode and the arc-length s for a viscoelastic liquid jet for different values of the Rossby number Rb, where the dimensionless numbers are $Re = 1000$, $We = 50$, $De = 15$ and $\tilde{\alpha_s} = 20$.

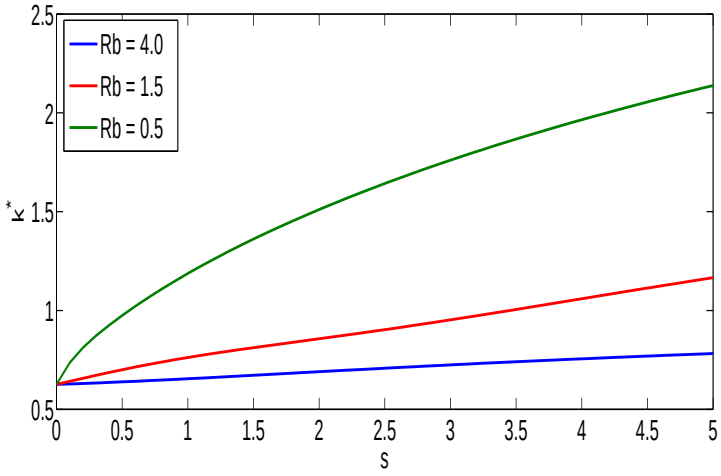

Figure 6.16: Graph showing the relationship between the maximum wavenumber of the most unstable k^* and the arc-length s for a viscoelastic liquid jet for different values of the Rossbt number Rb, where the dimensionless numbers are $Re = 1000$, $We = 50$, $De = 15$ and $\tilde{\alpha_s} = 20$.

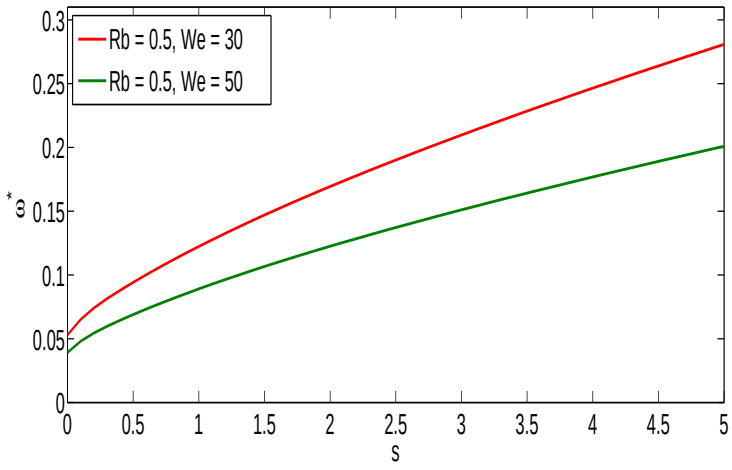

Figure 6.17: Graph showing the relationship between the growth rate ω_r^* and the arc-length s for a viscoelastic liquid jet, for two values of the Weber number, $We = 30, 50$ and $Rb = 0.5$, where the dimensionless numbers are $Re = 1000$, $De = 15$ and $\tilde{\alpha_s} = 20$.

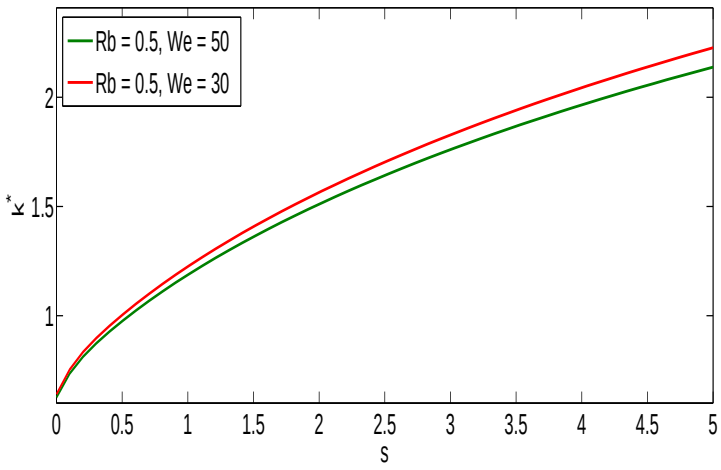

Figure 6.18: Graph showing the relationship between the maximum wavenumber k^* and the arc-length s for a viscoelastic liquid jet, for two values of the Weber number, $We = 30, 50$ and $Rb = 0.5$, where the dimensionless numbers are $Re = 1000$, $De = 15$ and $\tilde{\alpha_s} = 20$.

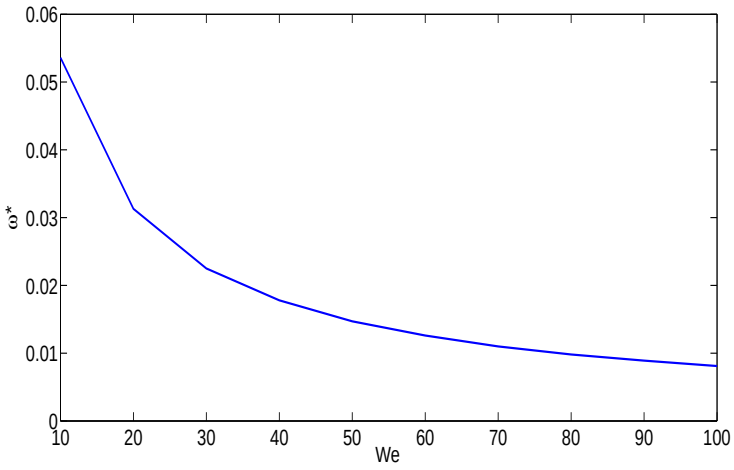

Figure 6.19: Graph showing the relationship between the growth rate ω_r^* of the most unstable mode and different values of the Weber number, We, for a viscoelastic liquid jet, where the dimensionless numbers are $Re = 1000$, $De = 15$ and $\tilde{\alpha_s} = 20$.

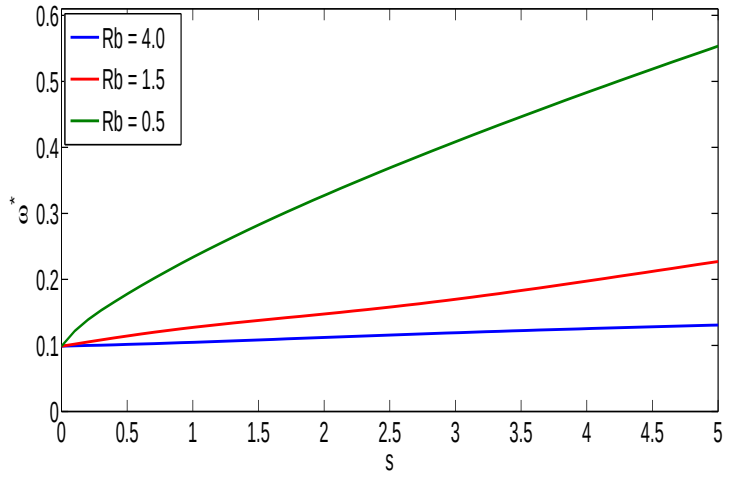

Figure 6.20: Graph showing the relationship between the growth rate ω_r^* of the most unstable mode and the arc-length s for a viscoelastic liquid jet for different values of the Rossby number, where the dimensionless numbers are $Re = 1000$, $We = 10$, $De = 15$ and $\tilde{\alpha_s} = 20$.

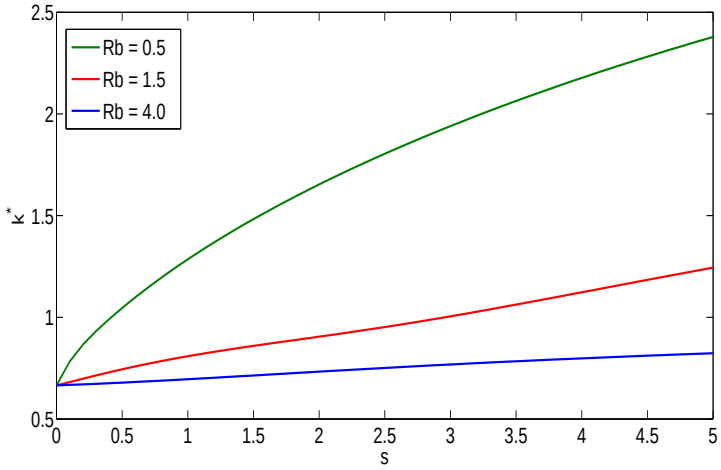

Figure 6.21: Graph showing the relationship between the maximum wavenumber k^* of the most unstable mode and the arc-length s for a viscoelastic liquid jet for different values of the Rossby number, where the dimensionless numbers are $Re = 1000$, $We = 10$, $De = 15$ and $\tilde{\alpha_s} = 20$.

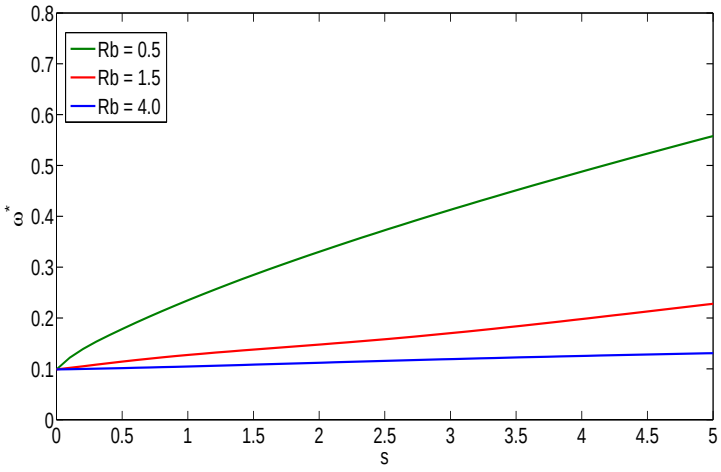

Figure 6.22: Graph showing the relationship between the growth rate ω_r^* and the arc-length s for a viscoelastic liquid jet, where the dimensionless numbers are $Re = 1000$, $We = 10$, $De = 25$ and $\tilde{\alpha_s} = 20$.

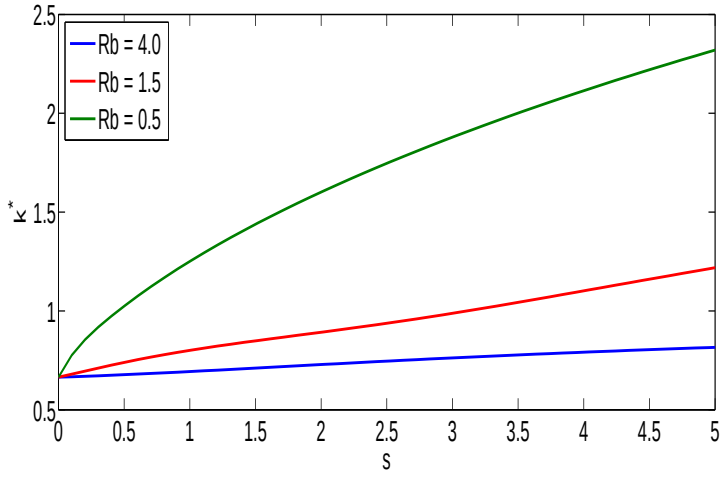

Figure 6.23: Graph showing the relationship between the maximum wavenumber k^* and the arc-length s for a viscoelastic liquid jet, where the dimensionless numbers are $Re = 1000$, $We = 10$, $De = 25$ and $\tilde{\alpha_s} = 20$.

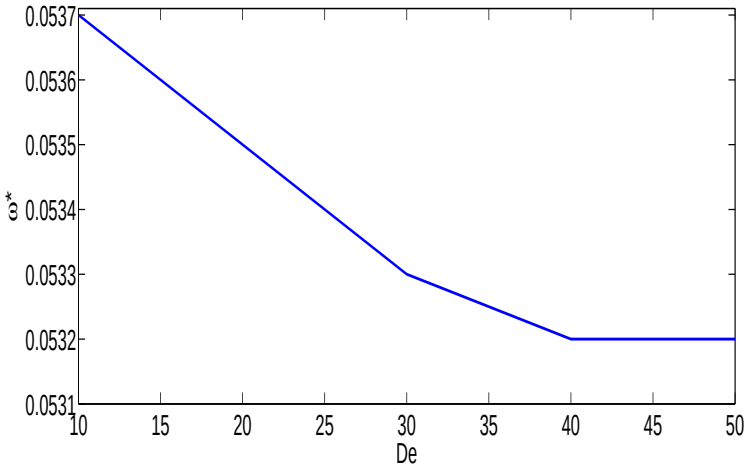

Figure 6.24: Graph showing the relationship between the growth rate ω_r^* of the most unstable mode and different values of the Deborah number De for a viscoelastic liquid jet, where the dimensionless numbers are $Re = 1000$, $We = 10$ and $\tilde{\alpha_s} = 20$.

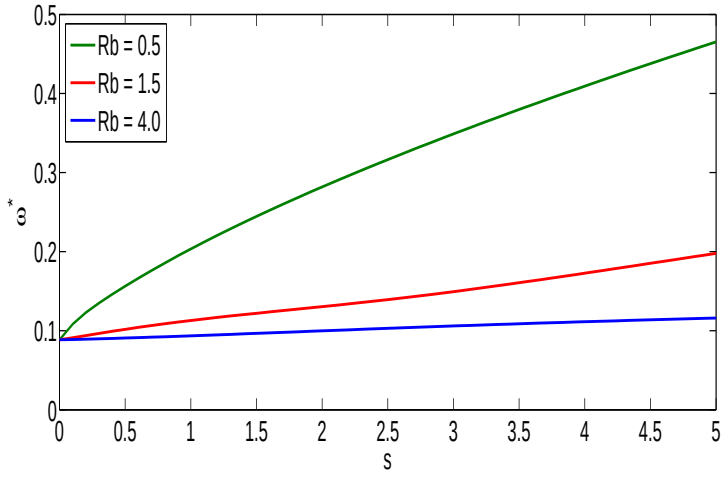

Figure 6.25: Graph showing the relationship between the growth rate ω_r^* and the arc-length s for a viscoelastic liquid jet, where the dimensionless numbers are $Re = 1000$, $We = 10$, $De = 15$ and $\tilde{\alpha_s} = 40$.

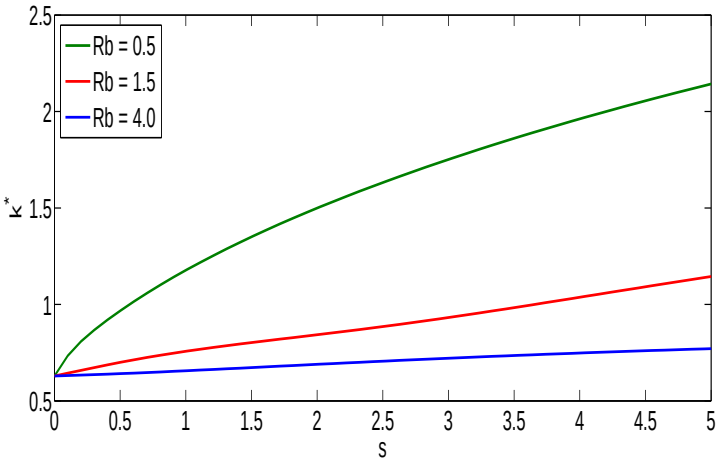

Figure 6.26: Graph showing the relationship between the maximum wavenumber k^* and the arc-length s for a viscoelastic liquid jet, where the dimensionless numbers are $Re = 1000$, $We = 10$, $De = 15$ and $\tilde{\alpha_s} = 40$.

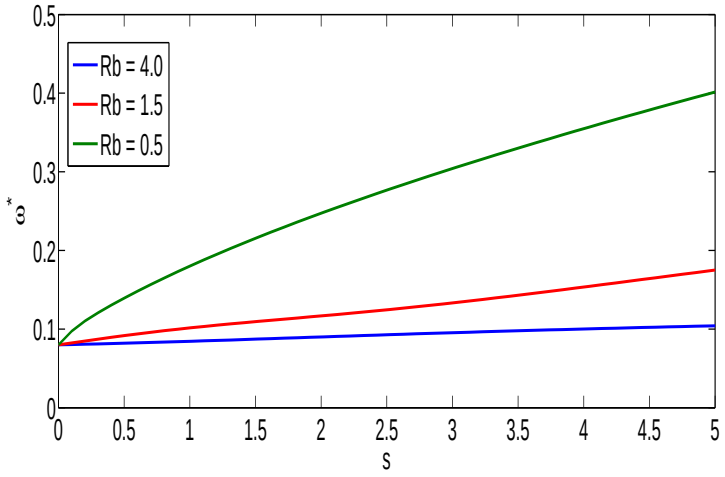

Figure 6.27: Graph showing the relationship between the growth rate ω_r^* and the arc-length s for a viscoelastic liquid jet, where the dimensionless numbers are $Re = 1000$, $We = 10$, $De = 15$ and $\tilde{\alpha_s} = 60$.

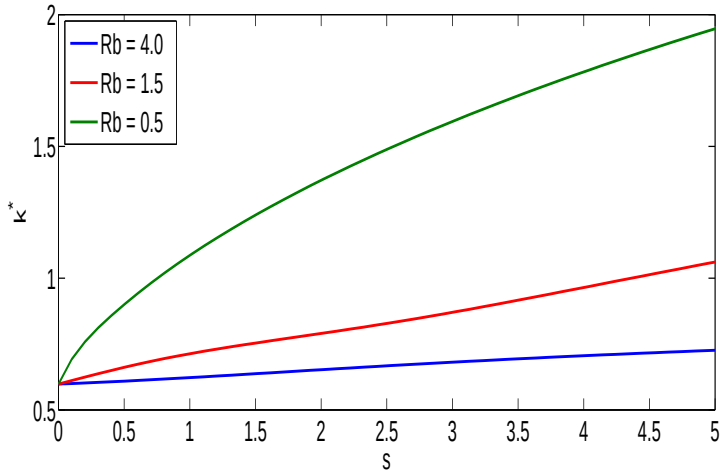

Figure 6.28: Graph showing the relationship between the maximum wavenumber k^* and the arc-length s for a viscoelastic liquid jet, where the dimensionless numbers are $Re = 1000$, $We = 10$, $De = 15$ and $\tilde{\alpha_s} = 60$.

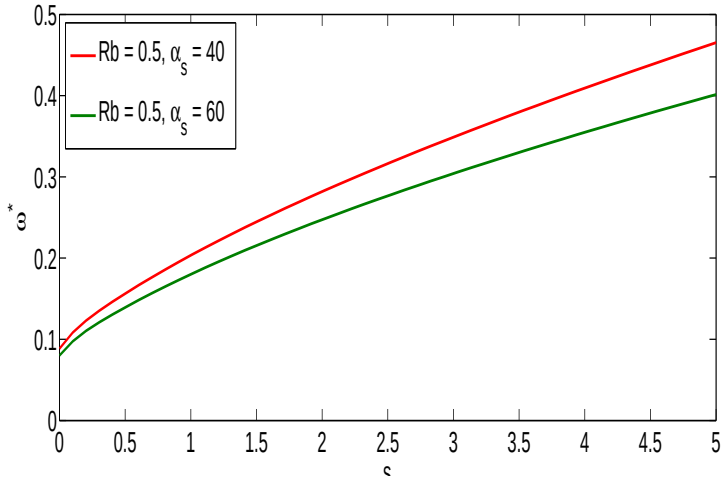

Figure 6.29: Graph showing the relationship between the growth rate ω_r^* and the arc-length s for a viscoelastic liquid jet, where the dimensionless numbers are $Re = 1000$, $We = 10$, $De = 15$ and $\tilde{\alpha_s} = 40$ and 60.

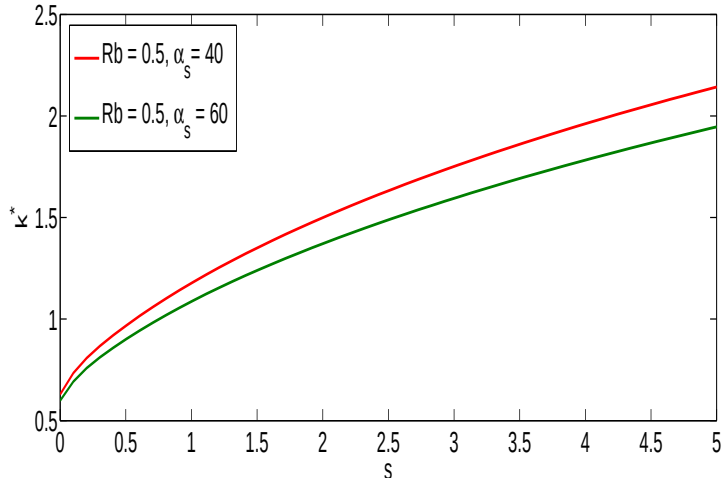

Figure 6.30: Graph showing the relationship between the maximum wavenumber k^* and the arc-length s for a viscoelastic liquid jet, where the dimensionless numbers are $Re = 1000$, $We = 10$, $De = 15$ and $\tilde{\alpha_s} = 40$ and 60.

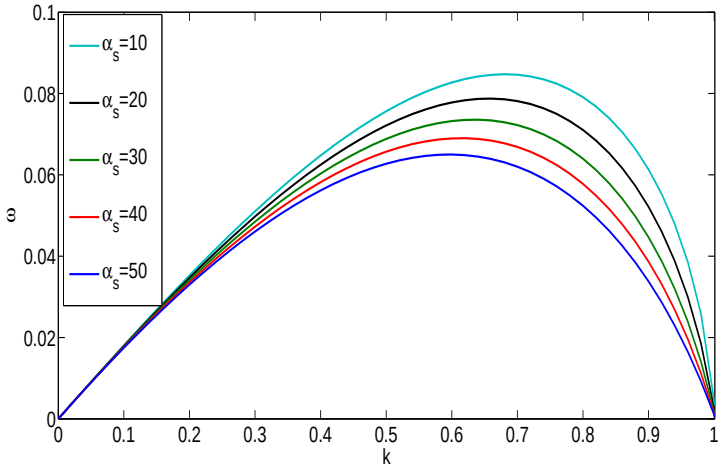

Figure 6.31: Graph showing the relationship between the growth rate ω_r^* of the most unstable mode and different values of the viscosity ratio $\tilde{\alpha_s}$ for a viscoelastic liquid jet, where the dimensionless numbers are $Re = 1000$, $We = 15$ and $De = 20$.

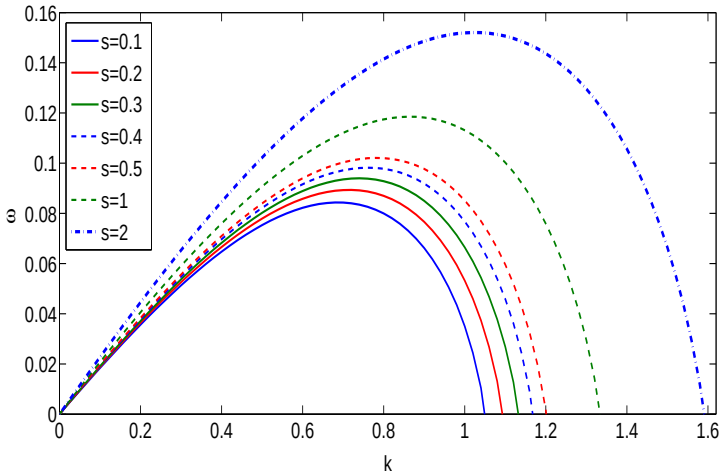

Figure 6.32: Graph showing the relationship between the growth rate against the wavenumber for various values of s at $Re = 1000$, $We = 15$, $De = 10$ and $\tilde{\alpha_s} = 20$.

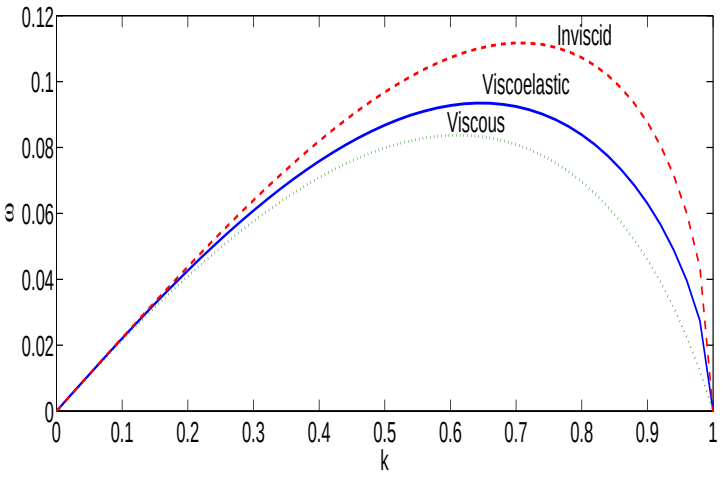

Figure 6.33: Graph showing the relationship between the growth rate against the wavenumber for three fluids, which are inviscid fluid where $We = 15$, viscoelastic fluid where $Re = 1000$, $We = 15$, $De = 15$ and $\tilde{\alpha_s} = 20$ and viscous fluid at $Re = 1000, We = 15$.

Chapter 7

Nonlinear Instability of Break-up of Viscoelastic Liquid Curved Jets

7.1 Introduction

In the previous chapter, we investigated the linear instability of viscoelastic liquid curved jets by using an asymptotic method to derive a set of one-dimensional equations. Using a temporal instability analysis, a dispersion relation was found and from this, we studied the growth rates and the wavenumber for the most unstable mode along the jet. In the case of straight jets, the growth rates and the wavenumber are constant therefore we can find the break-up length and drop sizes of the main droplets. However, the growth rates and the wavenumber are non-constant along the viscoelastic liquid curved jets. Thus, using linear theory, we cannot give a good prediction of the break-up and the droplet sizes of the prilling process. In addition, by using this theory, we cannot determine the satellite droplet size and the non uniformity in the break-up. In order to study these two phenomena, which are very important in terms of experiments, we will use the finite

difference method. It is very necessary close to break-up when the surface becomes more deformed to use the full curvature term which is

$$p = \frac{1}{We}((1+\varepsilon^2 R_s^2)^{-\frac{1}{2}} - \varepsilon^2 R_{ss}(1+\varepsilon^2 R_s^2)^{-\frac{3}{2}}),$$

because without using this term the jet is unstable to short wavelengths and it is found that a small droplet is connected by a slender neck. Many authors use the full term curvature for this form. For example, Li and Fontelos (2003) and Clasen *et al.* (2006) used it for studying the beads-on-string structure for viscoelastic jets. Brenner *et al.* (1997) used this curvature term to give a good equilibrium shape of break-up liquid jets at high Reynolds number. They also made comparisons between numerical simulations and experimental work on droplet sizes of liquid jets and found excellent agreement.

7.1.1 Lax-Wendroff Method

We can write the PDEs in the form of a flux conservative equation as

$$\frac{\partial \boldsymbol{u}}{\partial t} = -\frac{\partial \boldsymbol{F}(\boldsymbol{u})}{\partial s}, \tag{7.1}$$

where $\boldsymbol{F}$ is called the flux vector, which can depend on $\boldsymbol{u}$ and spatial derivatives of $\boldsymbol{u}$ (see Press *et al.* (2001) and Duchateau and Zachmann (1989)). Let consider that $\boldsymbol{F}$ is equal to $f(x,t)$, then we have one dimensional equation which is $u_t + f_x = 0$, so that an explicit scheme can be written as

$$\boldsymbol{u}_j^{n+1} - \boldsymbol{u}_j^n = -\frac{\sigma}{2}\left(\boldsymbol{F}_{j+1}^n - \boldsymbol{F}_{j-1}^n\right), \tag{7.2}$$

where σ is the Courant number, which is the ratio between time steps and space steps. This method can be unstable (see Hirsch(1990) Vol. 2), and therefore we use the approximation

$$\boldsymbol{u}_j^n \to \frac{1}{2}(\boldsymbol{u}_{j+1}^n + \boldsymbol{u}_{j-1}^n). \tag{7.3}$$

The finite difference approximation then is

$$\boldsymbol{u}_j^{n+1} = \frac{1}{2}(\boldsymbol{u}_{j+1}^n + u_{j-1}^n) - \frac{\sigma}{2}(\boldsymbol{F}_{j+1}^n - \boldsymbol{F}_{j-1}^n). \tag{7.4}$$

Now this method is called Lax Friedrichs scheme, which is stable and accurate in both time and space but only first order in those variables. In order to improve the accuracy of our approximation, second order space centered schemes are used. For nonlinear of PDEs, the Richtmyer scheme can be used. In this scheme, an intermediate time step is used and the solution is moved forward one time step in two steps and this scheme is also known as the two step Lax-Wendroff scheme (see Press *et al.* (2001)). This scheme can be written as

$$\boldsymbol{u}_{j+1/2}^{n+1/2} = \frac{1}{2}(\boldsymbol{u}_{j+1}^n + \boldsymbol{u}_j^n) - \frac{dt}{2ds}(\boldsymbol{F}_{j+1}^n - \boldsymbol{F}_j^n), \tag{7.5}$$

$$\boldsymbol{u}_j^{n+1} = \boldsymbol{u}_j^n - \frac{dt}{ds}(\boldsymbol{F}_{j+1/2}^{n+1/2} - \boldsymbol{F}_{j-1/2}^{n+1/2}), \tag{7.6}$$

where $\boldsymbol{F}_{j+1/2}^{n+1/2}$ is calculated by using Eq. 7.5.

This scheme (Eqs. 7.5 and 7.6) can be used to find the break-up of a liquid jet. We assume the jet will have broken, when the radius reaches a small value which we can

arbitrarily choose as 5% (for consistency with previous work, e.g. Părău *et al.* (2007)) of the initial radius; this method has been used by many authors (see Părău *et al.* (2006-2007) and Uddin (2007). We cannot use this approach downstream of the break-up point, because the jet can break up into droplets, and our numerical solution has no physical meaning.

7.1.2 Viscoelastic Jet Simulation

We use the two-step Lax-Wendroff scheme to find the break-up of a viscoelastic liquid jet. The equations, which derived in chapter 5 (5.71)-(5.73) and (5.47), are

$$u_t + u_0 u_{0s} = -\frac{1}{We}\frac{\partial}{\partial s}\left(\frac{1}{R(1+\varepsilon^2 R_s^2)^{\frac{1}{2}}} - \frac{\varepsilon^2 R_{ss}}{(1+\varepsilon^2 R_s^2)^{\frac{3}{2}}}\right) + \frac{(X+1)X_s + ZZ_s}{Rb^2}$$
$$+ \quad \frac{3\alpha_s}{Re}\left(u_{0ss} + 2u_{0s}\frac{R_{0s}}{R}\right) + \frac{1}{Re}\left(\frac{1}{R_0^2}\frac{\partial}{\partial s} R_0^2 \left(T_{ss}^0 - T_{nn}^0\right)\right), \tag{7.7}$$

$$\frac{\partial T_{ss}^0}{\partial t} + u_0 \frac{\partial T_{ss}^0}{\partial s} - 2\frac{\partial u_0}{\partial s} T_{ss}^0 = \frac{1}{De}\left(2(1-\alpha_s)\frac{\partial u_0}{\partial s} - T_{ss}^0\right), \tag{7.8}$$

$$\frac{\partial T_{nn}^0}{\partial t} + u_0 \frac{\partial T_{nn}^0}{\partial s} + \frac{\partial u_0}{\partial s} T_{nn}^0 = \frac{-1}{De}\left((1-\alpha_s)\frac{\partial u_0}{\partial s} + T_{nn}^0\right), \tag{7.9}$$

$$R_t + \frac{u_s}{2}R + uR_s = 0. \tag{7.10}$$

We now change the variable as follows $A = A(s,t)$, where $A(s,t) = R^2(s,t)$, and then we rewrite our equations as

$$\frac{\partial A}{\partial t} = -\frac{\partial}{\partial s}\Big(Au\Big), \tag{7.11}$$

$$u_t + \left(\frac{u^2}{2}\right)_s = -\frac{1}{We}\frac{\partial}{\partial s}\frac{4\Big(2A + (\varepsilon A_s)^2 - \varepsilon^2 A A_{ss}\Big)}{\Big(4A + (\varepsilon A_s)^2\Big)^{3/2}} + \frac{(X+1)X_s + ZZ_s}{Rb^2} +$$

$$\frac{3\alpha_s}{Re}\frac{(Au_s)_s}{A} + \frac{1}{Re}\frac{\Big(A(T_{ss} - T_{nn})\Big)_s}{A} \tag{7.12}$$

$$\frac{\partial T_{ss}}{\partial t} = -u\frac{\partial T_{ss}}{\partial s} + 2\frac{\partial u}{\partial s}T_{ss} + \frac{1}{De}\left(2(1-\alpha_s)\frac{\partial u}{\partial s} - T_{ss}\right), \tag{7.13}$$

$$\frac{\partial T_{nn}}{\partial t} = -\frac{\partial}{\partial s}(uT_{nn}) - \frac{1)}{De}\left((1-\alpha_s)\frac{\partial u}{\partial s} + T_{nn}\right). \tag{7.14}$$

We solve this system of equations as we did in Chapter 6 for the steady state by using the initial conditions at $t = 0$ which are $A(s, t = 0) = R_0^2(s),\ u(s, t = 0) = u_0(s),\ T_{ss}(s, t = 0) = 0,\ T_{nn}(s, t = 0) = 0$. At the nozzle, we use upstream boundary conditions

$$A(0, t) = 1,\ u(0, t) = 1 + \delta \sin\left(\frac{\kappa t}{\varepsilon}\right),$$

where κ is a non-dimensional wavenumber of the perturbation of frequency and δ (which is kept small) is the amplitude of the initial non-dimensional velocity disturbance. In the calculation, we have used the value of $\varepsilon(= \frac{a}{s_0})$ which can be measured from experiments using $\varepsilon = 0.01$. This value is the same as found in experiments and industrial problems (see Wong *et al.* (2004)). To represent the solution in the $X - Z$ plane, we have from the steady state solutions section 6.5 that $X(S) = X(s), Z(S) = Z(s)$ where $s = \varepsilon S$. We can therefore find $X_s(S)$ and $Z_s(S)$. By using the numerical method described above, we can calculate $R(s, t)$. To make sure that the numerical scheme is convergent, here we choose that the time step is very small which is less than half the square of the space

step (see Părău *et al.* (2007)). In order to display the curved jet, we are required to determine the normal vector along the centerline of the jet $(X(s), Z(s))$, which is in this case $n = (-Z_s(s), X_s(s)))$. Thereafter the free surface of the jet is given by $(X(s), Z(s)) + R(s,t)(-Z_s(s), X_s(s))$ and $(X(s), Z(s)) - R(s,t)(-Z_s(s), X_s(s))$. T determine size of main droplets, we need to integrate between two local minimums (which correspond to pinch points along the jet). If we label them as h_1 and h_2 then

$$V_{drop} = \pi \int_{h_1}^{h_2} R_0^2 ds,$$

where the drop radius R equates to a sphere, then

$$\widehat{R} = \left(\frac{3V_{drop}}{4\pi} \right)^{\frac{1}{3}}.$$

7.2 Results

As we mentioned before, the break-up is chosen to happen when the radius is less than 5%. In this simulation, we plot some profiles which are in Fig. 7.1 to see the effect of the Deborah number on the break-up length of a viscoelastic rotating liquid jet. From these graphs, it can be observed that when we increase the Deborah number the break-up length increases along the jet, meaning that the liquid in this case behaves more elastic in nature, which we expected to get from our results, because when the Deborah number is very high (say 2000), the liquid becomes purely elastic and will never break up.

We plot a graph to check the accuracy of our numerical solutions for various ds and various number of mesh points M (see Fig. 7.2) and in this thesis dt is equal to 5×10^{-6} (see Părău *et al.* (2007)). Figure 7.3 shows break-up lengths of viscoelastic liquid curved jets versus the Deborah number. It can be seen that when the Deborah number is increased, break-up lengths increase. The same findings are discovered for break-up time with the

Deborah number, which is in Fig. 7.4. The relationship between main and satellite droplet sizes and the Deborah number are shown in Fig. 7.5. From this graph, we can see that main and satellite droplet sizes increase with increasing the Deborah number.

In Fig. 7.6, we show some profiles which indicate the break-up for different values of the wavenumber where k is chosen as 0.3, 0.6 and 0.9. It can be noticed from these figures that when we increase the wavenumber, the break-up of the liquid is decreased. Moreover, we plot a graph to show the effect of the wavenumber κ on the break-up length for two values of the Rossby number, $Rb = 1$ and 3, which is in Fig. 7.7. It was found that the most unstable wavenumber increases, when κ is approximately to equal 0.60. It can also be seen from this figure that when the wavelength disturbances are short, we have a long break-up length.

Figure 7.8 is a graph showing the relationship between the droplet radius and the wavenumber κ for observing main and satellite droplet sizes. We can see that main and satellite droplet sizes decrease when the wavenumber increases. In Fig. 7.9, we find that when the initial perturbation (δ is chosen as 0.1 and 0.01) is large the break-up becomes short. In addition, the jet profile and the radius are plotted in Fig. 7.10 for two different values of the Rossby number ($Rb = 1$ and 8). It can be seen that the rotation rate has increased the break up length of the jet. In Fig. 7.11, we study the effect of the rotation rates on the break up length and find that when the rotation rates are very high, the break-up length increases, while in Fig. 7.12, we investigate the break-up time versus the Rossby number and we see that decreasing the Rossby number leads to an increase in the break-up time. We can therefore address from these Figs.7.11 and 7.12 that there is no monotonic relationship between the rotation rates and the break-up length and time respectively. Fig. 7.13 shows main and satellite droplet sizes versus the Rossby number for viscoelastic liquid curved jets. We can see that main droplet sizes do not change too much with increasing rotation rates, whereas satellite droplet sizes increase, and this

result agrees with the Newtonian spiralling jets. Furthermore, when the Reynolds number and the Deborah number are small we have a longer break-up length, as can be seen in Fig. 7.14. In these figures, we choose different values of the Reynolds number and the Deborah number. Another non-dimensionless parameter is the Weber number, We, which is plotted against the break-up length in Fig. 7.15. From this figure, it can be noticed that when the Weber number is increased, the break-up length is increased, especially for high rotation rates (see at $Rb = 1$).In Fig. 7.16, we show how the Reynolds number, Re, affects the break-up length. We found that the break-up length decreases when the Reynolds number increases. It can also be noticed that when the rotation rates are high, $Rb = 1$, we have a high break-up length.

We use the same method to study the influence of the viscosity ratio, α_s, on the break-up length and break-up time, as can be seen in Fig. 7.17 and Fig. 7.18. When we increase the viscosity ratio, the break-up length is increased and is more for high rotation rates, $Rb = 1$, while the break-up time is increased with low rotation rates when the viscosity is increased. Fig. 7.19 shows the effects of the viscosity ratio on the droplet radius for the main and satellite droplet sizes. We find that the viscosity ratio has a small effect on the main droplet size. However, the influence can be seen in the satellite droplet size, as when the viscosity ratio increases the satellite droplet size increases.

In Fig. 7.20, we show the difference between three types of liquids (inviscid, viscous and viscoelastic) in terms of breaking up lengths. It can be observed from this figure that the break-up of viscoelastic liquid jets occurs faster than viscous liquid jets and more slowly than inviscid liquid jets. P*ă*r*ă*u *et al.* (2007) plot a graph to show the relationship between the radius of the jet and the arc-length for inviscid and viscous liquids. They found that the inviscid jets break-up faster than the Newtonian jet.

7.3 Discussion

There are many applications of break-up liquid jets which emerge from an orifice, assuming that the centerline of the jet is straight, with ink-jet printing. However, it can be considered that the centerline is curved, which is known as the prilling process. This case is investigated here for viscoelastic liquid curved jets by using the Oldroyd-B model. It is also important in this process to study the effect of the rotation on the break-up lengths and drop sizes.

We have made an assumption, which is that the viscosity does not affect the trajectory of the centerline (see Decent *et al.* (2005) and Uddin (2007)) and this is taken as an inviscid liquid jet. It was found that decreasing the Reynolds number, which corresponds to high viscosity, increases the break-up length (see Fig. 7.16). It was also observed that increasing the viscosity ratio, which is the total of the solvent and polymeric liquid, increases the break-up length (see Fig. 7.17). When the Reynolds number and the Deborah number are small, we have a longer break-up length, which means the liquid is highly viscoelastic (see Fig. 7.14). The main and satellite droplets are examined for different values of the Rossby number and it is found that satellite droplet sizes are decreased with decreasing rotation rates in $0.5 \leqslant Rb \leqslant 2$.

It was noticed that the non-Newtonian (viscoelastic) liquid jet breaks up earlier than Newtonian liquid jets and later than inviscid jets (see Fig. 7.20), and this result agrees with the linear instability which is found in Chapter 6.

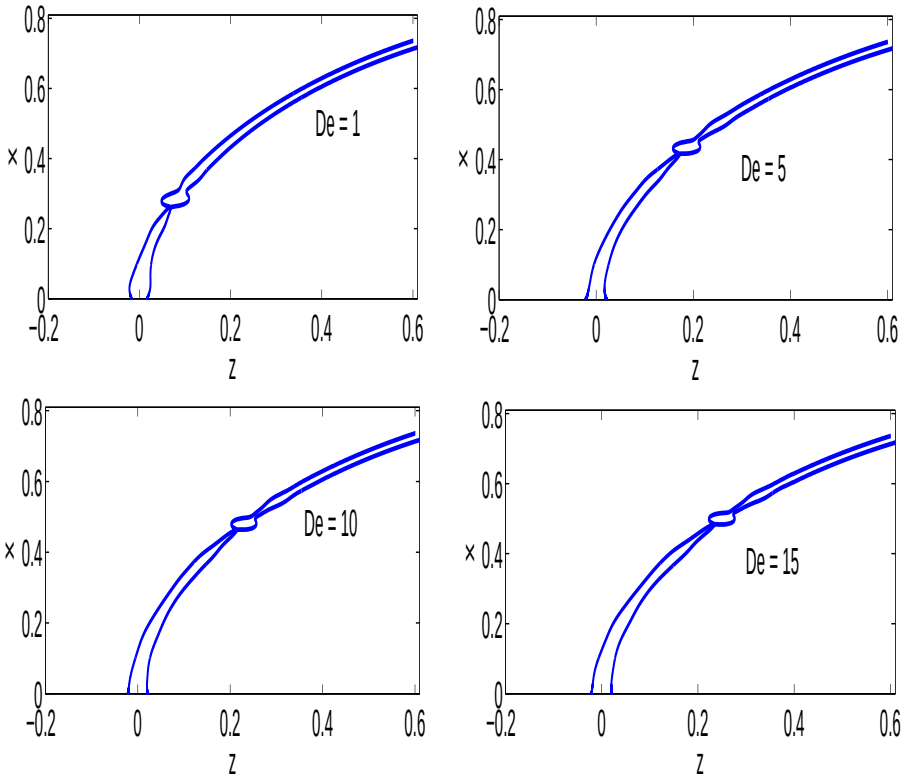

Figure 7.1: Graph showing the relationship between the break-up length and De where $Re = 1000$, $We = 10$, $k = 0.5$, $\delta = 0.01$ and $\alpha_s = 0.2$. We can see that the break-up length increases when the Deborah number is increased.

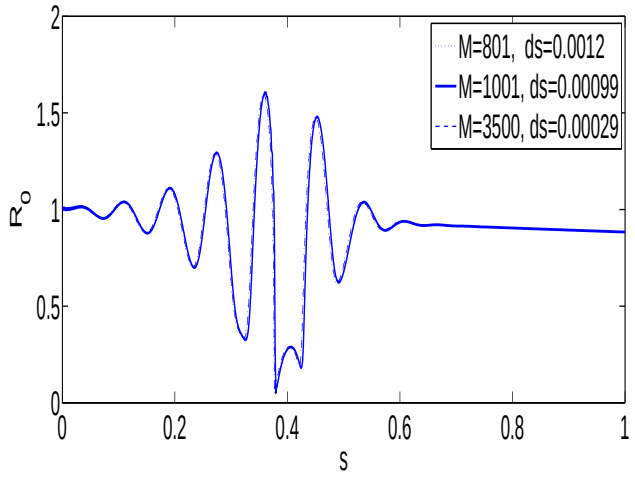

Figure 7.2: Accuracy check for various ds and various number of mesh points M, where $Re = 2800$, $We = 10$, $Rb = 1$, $k = 0.8$, $\delta = 0.01$, $\alpha_s = 0.2$, $dt = 5 \times 10^{-6}$, which is greater than $\frac{1}{2}\, ds^2$, and the final time $t_f = 0.4250$.

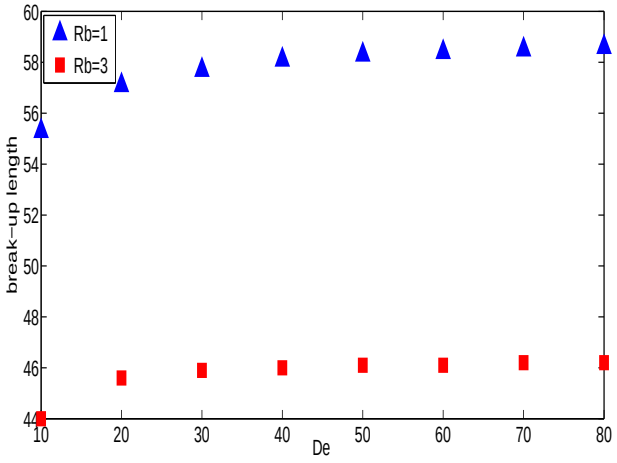

Figure 7.3: Graph showing the relationship between break-up lengths and the Deborah number De for two values of the Rossby number. Here we have $Re = 3000$, $We = 10$, $k = 0.5$, $\delta = 0.01$ and $\alpha_s = 0.2$. It can be noticed that break-up lengths is increased when the Deborah number is increased.

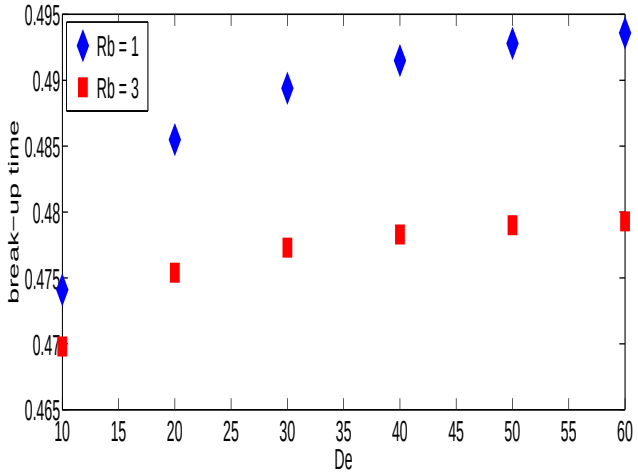

Figure 7.4: Graph showing the relationship between break-up time and the Deborah number De for two values of the Rossby number. Here we have $Re = 3000$, $We = 10$, $k = 0.5$, $De = 10$, $\delta = 0.01$ and $\alpha_s = 0.2$. It can be noticed that the break up time is increased when the Deborah number is decreased.

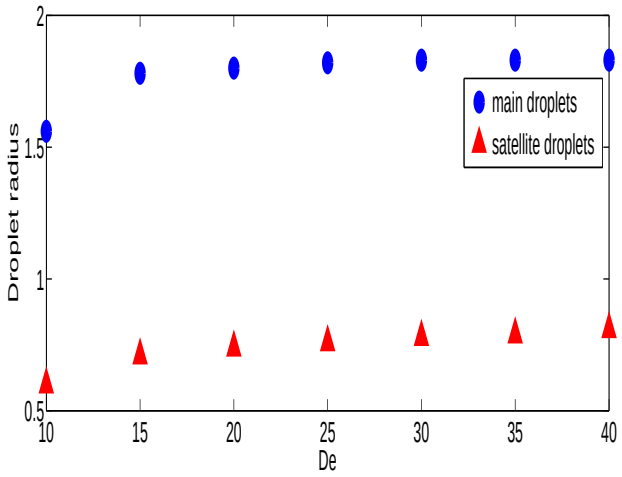

Figure 7.5: Graph showing the relationship between main and satellite droplet sizes and the Deborah number De. Here we use $Re = 1000$, $We = 10$, $k = 0.5$, $\delta = 0.01$, $\alpha_s = 0.2$ and $Rb = 1$.

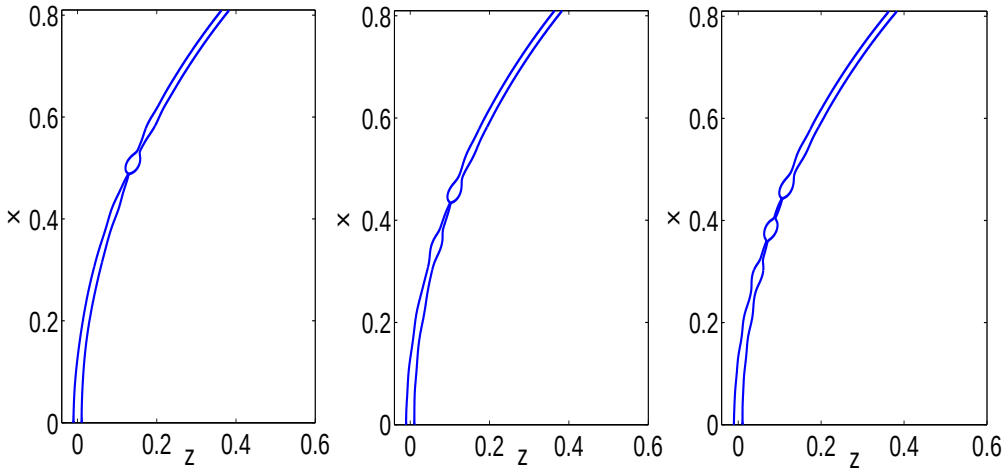

Figure 7.6: Graph showing the influence of wavenumber, k, on the viscoelastic liquid curve jet. From left to right for these figures, we use $k = 0.3$, 0.6 and 0.9 respectively. Here we have $Re = 1000$, $Rb = 2$, $We = 10$, $De = 10$, $\delta = 0.01$ and $\alpha_s = 0.20$. We can be seen that when the wavenumber is increased the break-up is decreased.

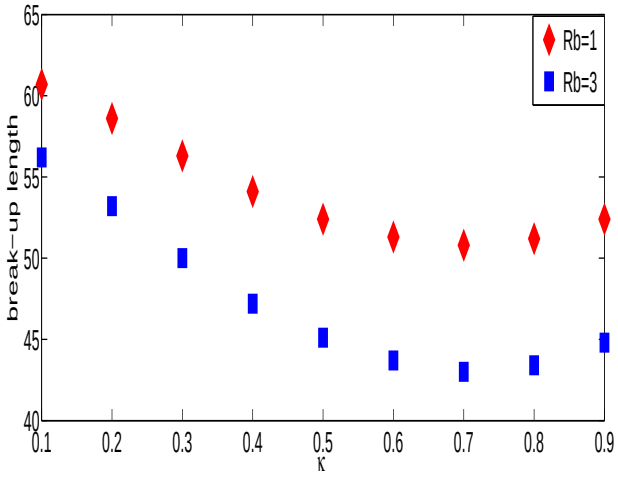

Figure 7.7: Break-up lengths of viscoelastic liquid curved jets versus the wavenumber, k, for two different values of Rb. In this case we have $Re = 3000$, $We = 10$, $De = 10$, $\delta = 0.01$ and $\alpha_s = 0.2$. When the rotation rate is high, we obtain longer jets for short wavelength disturbances.

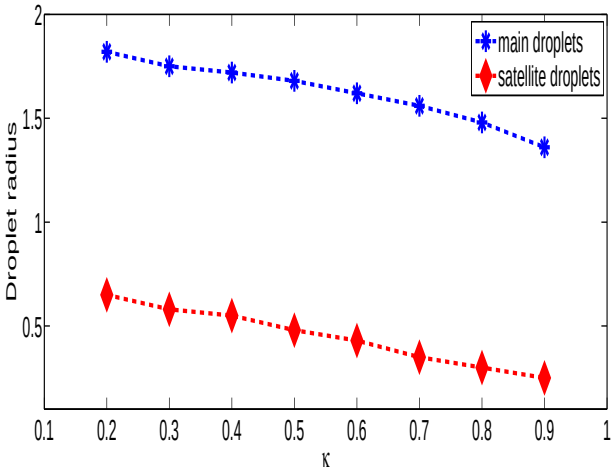

Figure 7.8: Graph showing the relationship between the main and satellite droplet radius of the jet and the wavenumber, κ. We can notice that satellite droplets radius decrease with increasing the wavenumber. Here we use $Re = 1000$, $We = 10$, $De = 10$, $\delta = 0.01$, $\alpha_s = 0.2$ and $Rb = 1$.

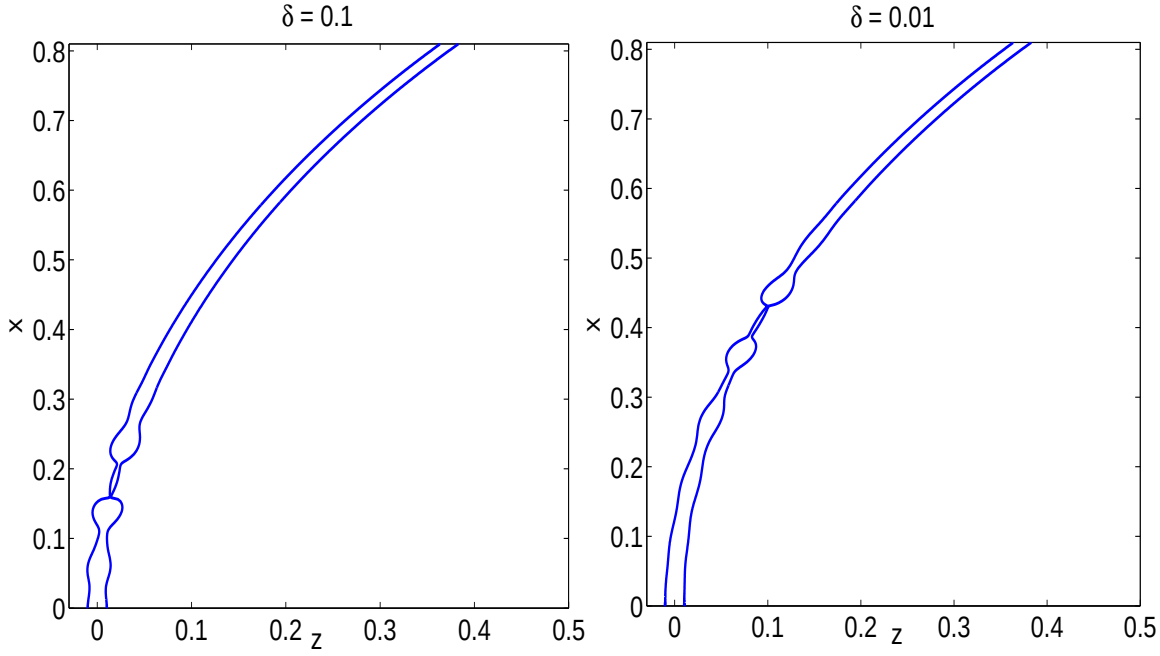

Figure 7.9: The profile of the break-up of viscoelastic liquid jets for two different values of δ, where $Re = 1000$, $Rb = 2$, $We = 10$, $De = 10$, $k = 0.8$ and $\alpha_s = 0.20$. It can be noticed that shorter break-up length occurs when the initial disturbance is large.

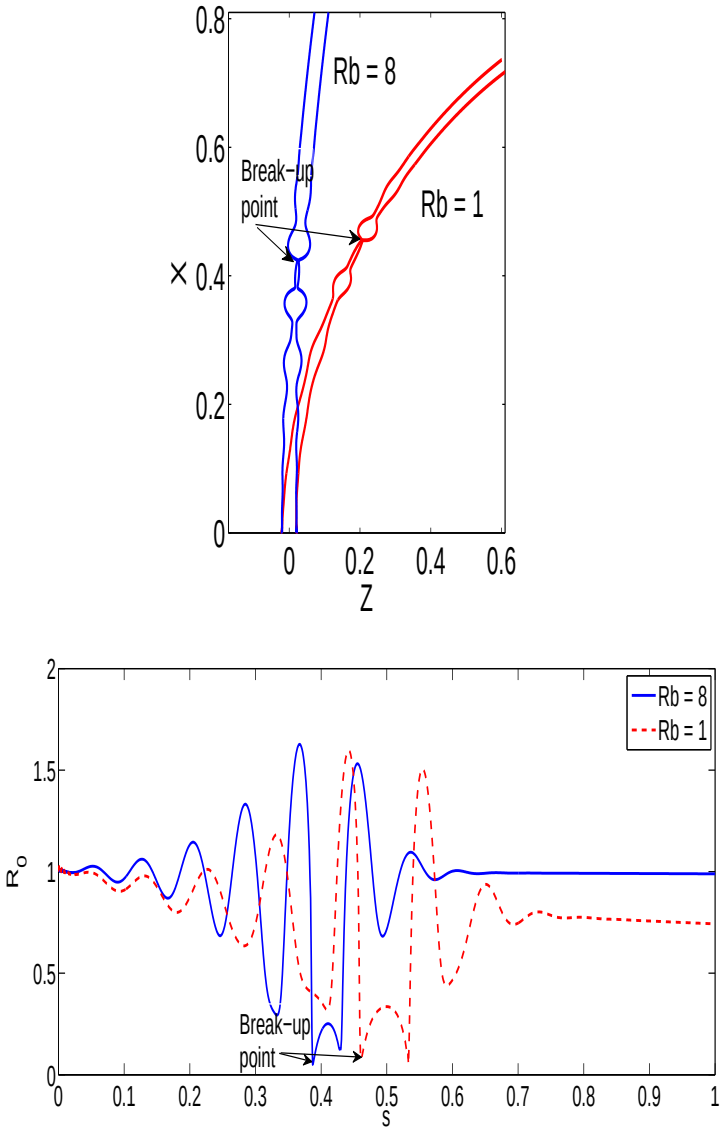

Figure 7.10: The profile of two different values of the Rossby number, where the values of the parameters here are $Re = 1000$, $We = 10$, $De = 10$, $k = 0.8$, $\alpha_s = 0.20$ and$\delta = 0.01$. We notice that when we increase the rotation rate, the break-up length increases

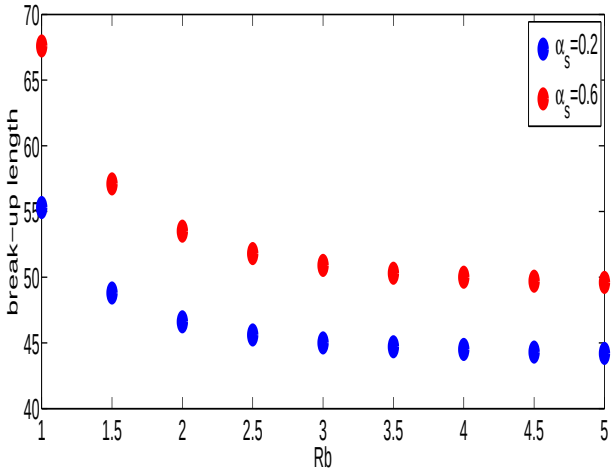

Figure 7.11: Graph showing the relationship between the break-up length and Rb where $Re = 3000$, $We = 10$, $k = 0.5$, $De = 10$ and $\delta = 0.01$. We can see that the break-up length increases when the rotation rate is increased.

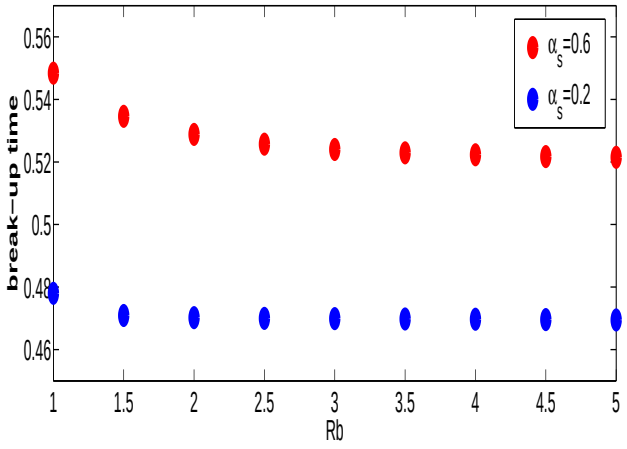

Figure 7.12: Graph showing the relationship between the break-up time and Rb. Here we have $Re = 3000$, $We = 10$, $k = 0.5$, $De = 10$ and $\delta = 0.01$. It can be noticed that the break-up time is increased when the rotation rate is decreased.

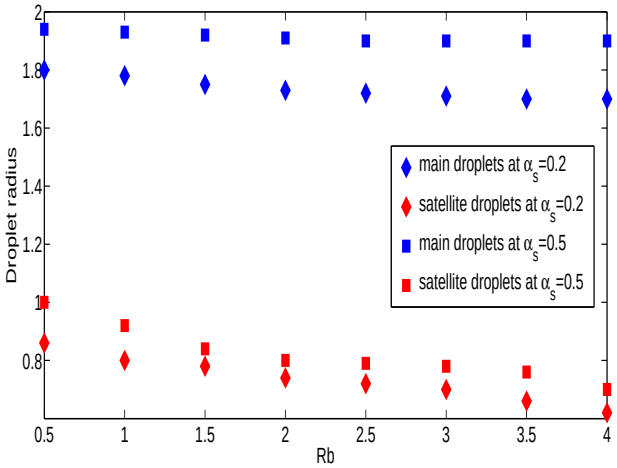

Figure 7.13: Graph showing the relationship between the main and satellite droplet radius of a viscoelastic rotating liquid jet and the Rossby number, Rb, we can observe that satellite droplets decrease when the Rossby number is decreased, whereas main droplets remain steady. Her we use $Re = 1000$, $We = 10$, $De = 10$, $\delta = 0.1$, $k = 0.6$ and $\alpha_s = 0.2$.

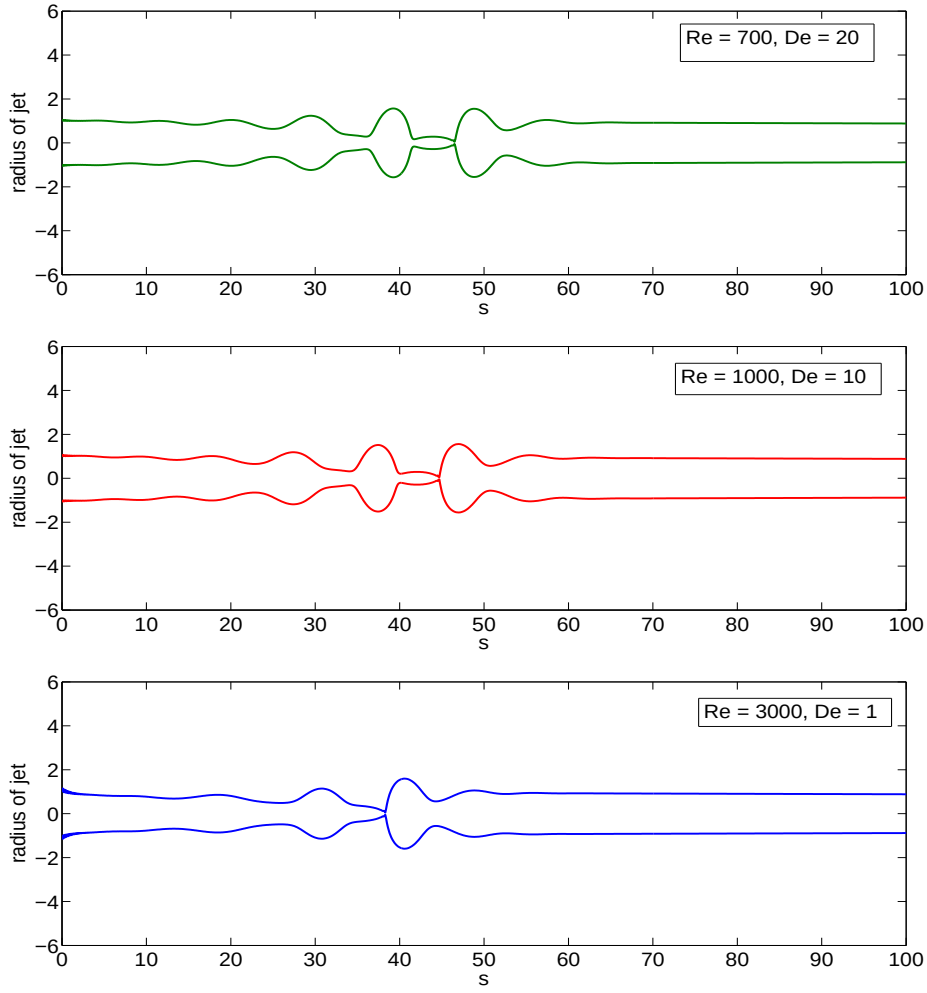

Figure 7.14: The profile of the break up of viscoelastic liquid jets for different values of the Reynolds number and the Deborah number can be seen in these figures. We observe that when these two numbers are small, we have longer break up. Here we use $Rb = 2$, $We = 10$, $k = 0.8$, $\delta = 0.01$ and $\alpha_s = 0.1$

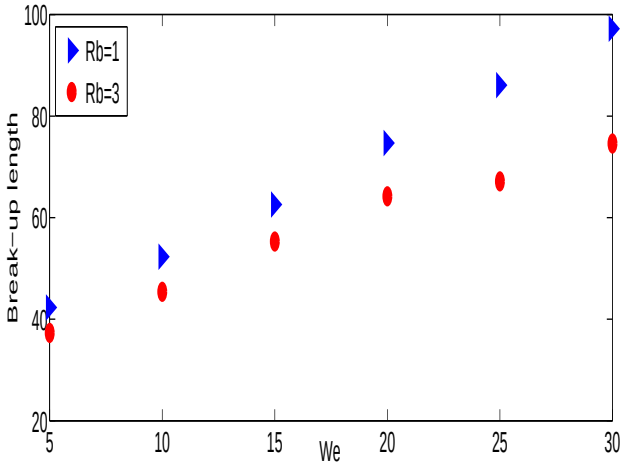

Figure 7.15: Break-up lengths of viscoelastic liquid curved jets against the Weber number for two different values of the Rossby number. Here we use the parameters $Re = 3500$, $De = 10$, $\kappa = 0.84$, $\delta = 0.001$ and $\alpha_s = 0.2$. When the Weber number is increased, the break-up length is increased and when the rotation rate is high, we have longer jets.

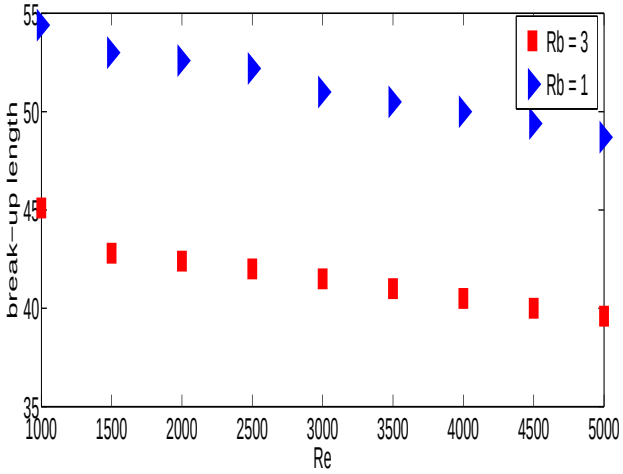

Figure 7.16: Break-up lengths of viscoelastic liquid curved jets plotted against the Reynolds number for two values of Rb. Here the parameters are $We = 10$, $De = 10$, $k = 0.65$, $\delta = 0.01$ and $\alpha_s = 0.2$. It can be noticed that when the Reynolds number is small, we obtain longer jets.

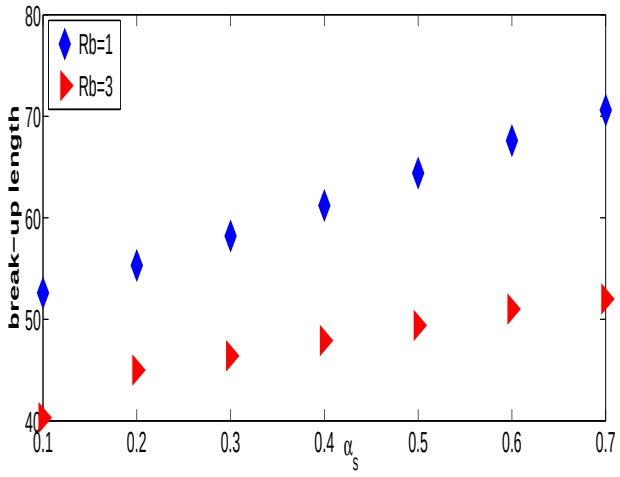

Figure 7.17: Break-up lengths of viscoelastic liquid curved jets plotted against the viscosity ratio α_s for two values of $Rb = 1$ and 3. The parameters are $Re = 3000$, $We = 10$, $De = 10$, $k = 0.5$ and $\delta = 0.01$. We observe that when we increase the viscosity ratio, the break-up increases.

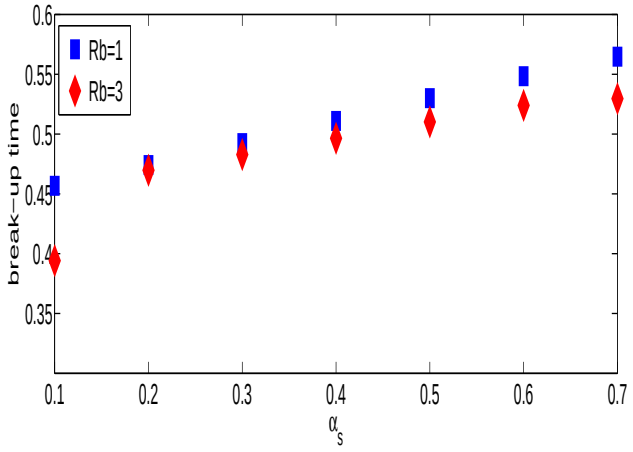

Figure 7.18: Graph showing the relationship between the break-up time and the viscosity ratio α_s. It can be seen that increasing the viscosity ratio leads to increase the break-up time. Her we use $Re = 3000$, $We = 10$, $De = 10$, $k = 0.5$ and $\delta = 0.01$.

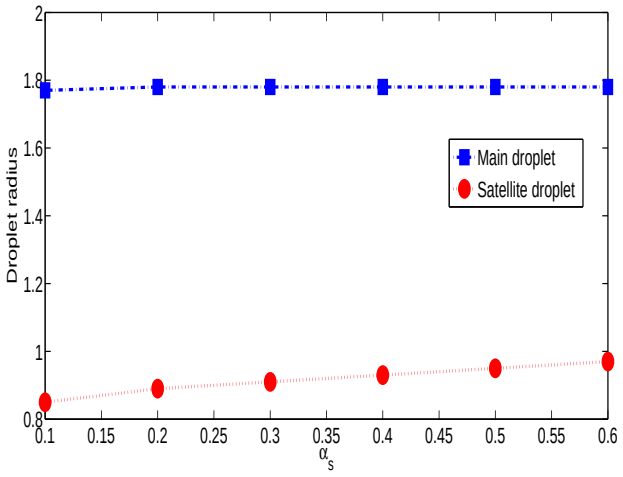

Figure 7.19: Graph showing the relationship between the main and the satellite droplet radius of the jet and the viscosity ratio α_s of viscoelastic liquid curved jets. As can be seen satellite droplet sizes increase with increasing the viscosity ratio. Here we use $Re = 1000$, $We = 10$, $De = 10$, $k = 0.6$, $\delta = 0.01$ and $Rb = 1$.

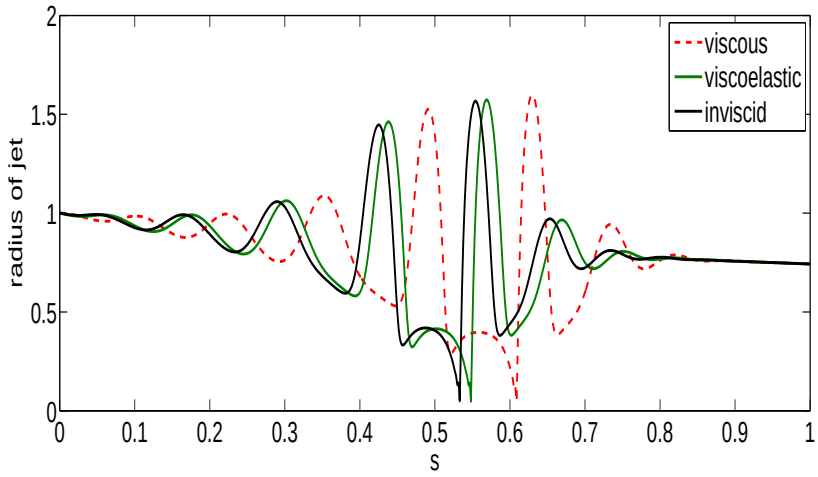

Figure 7.20: Graph showing the relationship between the radius of the jet and the arc-length for three different liquids. We notice that the break-up lengths of non-Newtonian liquid jets (viscoelastic) occur closer to the nozzle than Newtonian liquid jets and after the inviscid liquid jets. We use $Re = 3000$, $We = 10$, $De = 20$, $k = 0.62$, $\delta = 0.01$, $\alpha_s = 0.2$ and $Rb = 1$.

Chapter 8

The Influence of Gravity on the Break-up of Viscoelastic Liquid Curved Jets

8.1 Introduction

In Chapter 6, we neglected gravity because the can rotates very fast. However, if we make an assumption that the can rotates slowly, this means gravity will affect the break-up, so that there is another function, which is $Y(s)$ has to be considered in the vertical direction as illustrated in Fig. 8.1.

Wallwork (2002a) investigated the influence of gravity for the inviscid case and viscous case. Decent *et al*. (2002) and Partridge (2006) conducted the influence of gravity for a rotating liquid jet. However, Uddin & Decent (2010) studied instability of non-Newtonian liquid curved jets under gravity. Uddin (2007) has also investigated the influence of gravity of non-Newtonian liquid curved jet by adding surfactants. The equations of motion and

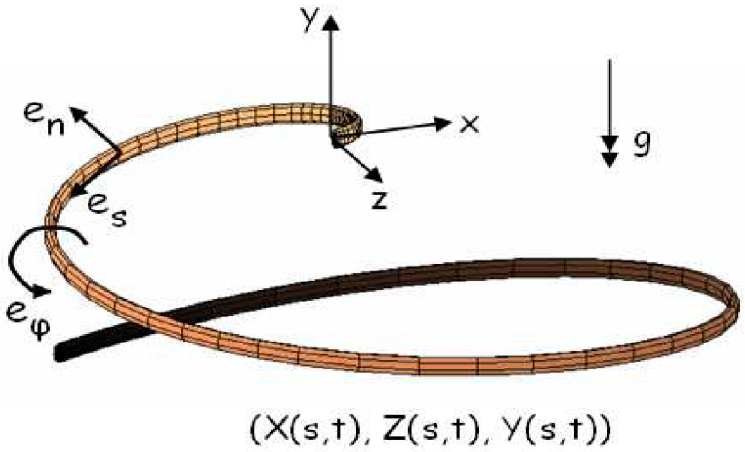

Figure 8.1: This image shows the rotating orifice at (0, 0, 0) in the coordinate system (X, Y, Z) falling under the effect of gravity and $(X(s,t), Y(s,t), Z(s,t)$ describes the centerline of the jet.

the Oldroyd-B model are

$$\boldsymbol{\nabla} \cdot \boldsymbol{u} = 0, \tag{8.1}$$

$$\rho\left(\frac{\partial \boldsymbol{u}}{\partial t} + \boldsymbol{u} \cdot \boldsymbol{\nabla} \boldsymbol{u}\right) = -\boldsymbol{\nabla} p + g + \boldsymbol{\nabla} \cdot \boldsymbol{\tau} - 2\,\boldsymbol{w} \times \boldsymbol{u} - \boldsymbol{w} \times (\boldsymbol{w} \times \boldsymbol{r}), \tag{8.2}$$

$$\boldsymbol{\tau} = \mu_s(\boldsymbol{\nabla} \boldsymbol{u} + (\boldsymbol{\nabla} \boldsymbol{u})^T + \boldsymbol{T}, \tag{8.3}$$

$$\lambda \boldsymbol{T}^{\triangledown} + \boldsymbol{T} = \mu_p\, \boldsymbol{\gamma}, \tag{8.4}$$

$$\frac{\partial \boldsymbol{T}}{\partial t} + (\boldsymbol{u} \cdot \boldsymbol{\nabla})\boldsymbol{T} - \boldsymbol{T} \cdot \boldsymbol{\nabla} \boldsymbol{u} - (\boldsymbol{\nabla} \boldsymbol{u})^T \cdot \boldsymbol{T} = \frac{1}{\lambda}(\mu_p \boldsymbol{\gamma} - \boldsymbol{T}). \tag{8.5}$$

We have two boundary conditions which are the kinematic condition which takes the form

$$\frac{\partial R}{\partial t} + u \cdot \nabla R = 0, \tag{8.6}$$

and the dynamic condition which is

$$\boldsymbol{n} \cdot \boldsymbol{\Pi} \cdot \boldsymbol{n} = \sigma\kappa, \text{ and } \boldsymbol{t_i} \cdot \boldsymbol{\Pi} \cdot \boldsymbol{n} = \boldsymbol{t_i} \cdot \nabla\sigma, \tag{8.7}$$

and the arc-length condition is

$$X_s^2 + Y_s^2 + Z_s^2 = 1,$$

where $\boldsymbol{\Pi} = -p\boldsymbol{I} + (\nabla\boldsymbol{u} + (\nabla\boldsymbol{u})^T) + \boldsymbol{T}$.

These equations are similar to Decent *et al.* (2002) and Partridge (2006). However, the differences are in the equations of the extra-stress term which is T.

We expand u, v, w, p in Taylor series in εn and $R, X, Z, T_{ss}, T_{nn}, T_{\phi\phi}, T_{sn}, T_{s\phi}, T_{n\phi}$ in ε.

$u = u_0(s,t) + (\varepsilon\, n)u_1(s,\phi,t) + ...$

$v = (\varepsilon\, n)v_1(s,\phi,t) + (\varepsilon\, n)^2 v_2(s,\phi,t) + ...$

$p = p_0(s,\phi,t) + (\varepsilon\, n)p_1(s,\phi,t) + ...$

$R = R_0(s,t) + (\varepsilon)R_1(s,\phi,t) + ...$

$X = X_0(s) + (\varepsilon)X_1(s,t) + ...$

$Y = Y_0(s) + (\varepsilon)Y_1(s,t) + ...$

$Z = Z_0(s) + (\varepsilon)Z_1(s,t) + ...$

$T_{ss} = T_{ss}^0(s,t) + \varepsilon\, T_{ss}^1(s,t) + ...$

$T_{nn} = T_{nn}^0(s,t) + \varepsilon\, T_{nn}^1(s,t) + ...$

$T_{\phi\phi} = \varepsilon T_{\phi\phi}^1(s,t) + \varepsilon^2\, T_{\phi\phi}^2(S,T) + ...$

$T_{sn} = \varepsilon\, T_{sn}^1(s,t) + \varepsilon^2\, T_{sn}^2(s,t) + ...$

$$T_{s\phi} = \varepsilon T^1_{s\phi}(s,t) + \varepsilon^2 T^2_{s\phi}(s,t) + ...$$

$$T_{n\phi} = \varepsilon T^1_{n\phi}(s,t) + \varepsilon^2 T^2_{n\phi}(s,t) + ...$$

We use the same asymptotic expansion which was discussed in the previous chapter, including Y, which is the same as the expansion of X and Z.

We substitute these asymptotic expansions in the equations of motion. We can therefore find from the equation of continuity at leading order

$$v_1 = -\frac{u_{0s}}{2}. \tag{8.8}$$

It can be also obtained that from the equation of motion in s-direction at leading order

$$\begin{aligned} u_{0t} + u_0 u_{0s} &= -p_{0s} + \frac{(X+1)X_s + ZZ_s}{Rb^2} \\ &+ \frac{3\alpha_s}{Re}(u_{0ss} - \frac{u_{0s}^2}{u_0}) - \frac{Y_s}{F^2} + \frac{1}{R_0^2 Re}\left((\frac{\partial}{\partial s}R_0^2(T^0_{ss} - T^0_{nn})\right). \end{aligned} \tag{8.9}$$

and in n-direction the equation of motion at leading order is $\frac{\partial p_0}{\partial n} = 0$.

The equation of motion in $\boldsymbol{n}$-direction at $O(\varepsilon)$ is (as seen in Wallwork (2002a))

$$\begin{aligned} &u_0^2 \cos\phi (X_{ss}^2 + Y_{ss}^2 + Z_{ss}^2)^{\frac{1}{2}} = -p_{1n} - \frac{1}{F^2}\frac{Z_s(X_{ss}^2 + Y_{ss}^2 + Z_{ss}^2)^{\frac{1}{2}}}{(\cos\phi(Y_{ss}Z_s - Y_sZ_{ss}) - X_{ss}\sin\phi)} \\ &+ \frac{1}{F^2}\frac{(\sin\phi(Y_{ss}Z_s - Z_{ss}Y_s) + X_{ss}\cos\phi)(\cos\phi(X_{ss}Z_s - X_sZ_{ss}) + Y_{ss}\sin\phi)}{(\cos\phi(Y_{ss}Z_s - Z_{ss}Y_s) - X_{ss}\sin\phi)(X_{ss}^2 + Y_{ss}^2 + Z_{ss}^2)^{\frac{1}{2}})} \\ &+ \left(-\frac{2u_0Z_s}{Rb} + \frac{X+1}{Rb^2}\right)\frac{(\sin\phi(Y_{ss}Z_s - Y_sZ_{ss}) + X_{ss}\cos\phi)}{(X_{ss}^2 + Y_{ss}^2 + Z_{ss}^2)^{\frac{1}{2}}} \\ &+ \left(\frac{2u_0X_s}{Rb} + \frac{Z}{Rb^2}\right)\frac{(\cos\phi(Y_sX_{ss} - Y_{ss}X_s) - Z_{ss}\sin\phi)(\sin\phi(Y_{ss}Z_s - Y_sZ_{ss}) + X_{ss}\cos\phi)}{(\cos\phi(Y_{ss}Z_s - Z_{ss}Y_s) - X_{ss}\sin\phi)(X_{ss}^2 + Y_{ss}^2 + Z_{ss}^2)^{\frac{1}{2}}} - \\ &\left(\frac{2u_0X_s}{Rb} + \frac{Z}{Rb^2}\right)\left(\frac{Y_s(X_{ss}^2 + Y_{ss}^2 + Z_{ss}^2)^{\frac{1}{2}}}{\cos\phi(Y_{ss}Z_s - Z_{ss}Y_s) - X_{ss}\sin\phi)}\right) + \\ &\frac{1}{Re}\left(\frac{1}{n}\frac{\partial v_1}{\partial n} + \frac{\partial^2 v_1}{\partial n^2} + \frac{1}{n^2}\left(-v_1 + \frac{\partial^2 v_1}{\partial\phi^2}\right)\right). \end{aligned} \tag{8.10}$$

The equation of motion in ϕ-direction at leading order is $\frac{\partial p_0}{\partial t} = 0$, and in ϕ-direction at leading order is (as seen in Wallwork (2002a))

$$-u_0^2 \sin\phi (X_{ss}^2 + Y_{ss}^2 + Z_{ss}^2)^{\frac{1}{2}} = -\frac{1}{n} p_{1\phi} + \frac{1}{F^2} \left(\frac{\cos\phi (X_{ss} Z_s - Z_{ss} X_s) + Y_{ss} \sin\phi}{(X_{ss}^2 + Y_{ss}^2 + Z_{ss}^2)^{\frac{1}{2}}} \right)$$
$$+ \left(-\frac{2u_0 Z_s}{Rb} + \frac{X+1}{Rb^2} \right) \left(\frac{\cos\phi (Y_{ss} Z_s - Z_{ss} Y_s) - \sin\phi X_{ss}}{(X_{ss}^2 + Y_{ss}^2 + Z_{ss}^2)^{\frac{1}{2}}} \right)$$
$$+ \left(\frac{2u_0 X_s}{Rb} + \frac{Z}{Rb^2} \right) \left(\frac{\cos\phi (Y_s X_{ss} - X_s Y_{ss}) - \sin\phi Z_{ss}}{(X_{ss}^2 + Y_{ss}^2 + Z_{ss}^2)^{\frac{1}{2}}} \right) + \frac{1}{Re} \left(\frac{2}{n^2} \frac{\partial v_1}{\partial \phi} \right), \tag{8.11}$$

$$u_{0t} + u_0 u_{0s} = -\frac{1}{We} (\frac{1}{R_0})_s + \frac{(X+1)X_s + Z Z_s}{Rb^2}$$
$$+ \frac{3\alpha_s}{Re} (u_{0ss} - \frac{u_{0s}^2}{u_0}) - \frac{Y_s}{F^2} + \frac{1}{R_0^2 Re} \left(\frac{\partial}{\partial s} R_0^2 (T_{ss}^0 - T_{nn}^0) \right), \tag{8.12}$$

$$(X_{ss}^2 + Y_{ss}^2 + Z_{ss}^2) \left(u_0^2 - \frac{3\alpha_s}{Re} u_{0s} - \frac{\sqrt{u}}{We} \right)$$
$$= -\frac{Y_{ss}}{F^2} + \frac{2}{Rb} u_0 (X_s Z_{ss} - Z_s X_{ss}) + \frac{(X+1)X_{ss} + Z Z_{ss}}{Rb^2} = 0, \tag{8.13}$$

$$\frac{\partial T_{ss}^0}{\partial t} + u_0 \frac{\partial T_{ss}^0}{\partial s} - 2 \frac{\partial u_0}{\partial s} T_{ss}^0 = \frac{1}{De} \left(2(1-\alpha_s) \frac{\partial u_0}{\partial s} - T_{ss}^0 \right), \tag{8.14}$$

$$\frac{\partial T_{nn}^0}{\partial t} + u_0 \frac{\partial T_{nn}^0}{\partial s} + \frac{\partial u_0}{\partial s} T_{nn}^0 = \frac{-1}{De} \left((1-\alpha_s) \frac{\partial u_0}{\partial s} + T_{nn}^0 \right), \tag{8.15}$$

$$\frac{Z_s X_{ss} - Z_{ss} X_s}{F^2} - \frac{2 Y_{ss} u_0}{Rb} + \frac{(X+1)(Y_{ss} Z_s - Y_s Z_{ss})}{Rb^2} + \frac{Z(Y_s X_{ss} - Y_{ss} X_s)}{Rb^2} = 0, \tag{8.16}$$

$$\frac{\partial R_0}{\partial t} + u_0 R_{0s} + \frac{R_0}{2} u_{0s} = 0. \tag{8.17}$$

8.2 Steady State Solutions

By using the steady state of the equations (8.12)-(8.16), we have the governing equations for this system as

$$\begin{aligned} u_0 u_{0s} = & -\frac{1}{2We}\,\frac{u_{0s}}{\sqrt{u}} + \frac{(X+1)X_s + ZZ_s}{Rb^2} \\ & + \frac{3\alpha_s}{Re}(u_{0ss} - \frac{u_{0s}^2}{u_0}) - \frac{Y_s}{F^2} + \frac{1}{Re}\left(\frac{\partial}{\partial s}(T_{ss}^0 - T_{nn}^0) - \frac{u_{0s}}{u_0}(T_{ss}^0 - T_{nn}^0)\right), \end{aligned} \tag{8.18}$$

$$\begin{aligned} & (X_{ss}^2 + Y_{ss}^2 + Z_{ss}^2)\left(u_0^2 - \frac{3\alpha_s}{Re}\,u_{0s} - \frac{\sqrt{u}}{We}\right) \\ & = -\frac{Y_{ss}}{F^2} + \frac{2}{Rb}\,u_0(X_s Z_{ss} - Z_s X_{ss}) + \frac{(X+1)X_{ss} + ZZ_{ss}}{Rb^2} = 0, \end{aligned} \tag{8.19}$$

$$u_0\,\frac{\partial T_{ss}^0}{\partial s} - 2\,\frac{\partial u_0}{\partial s}\,T_{ss}^0 \;=\; \frac{1}{De}\,\left(2(1-\alpha_s)\frac{\partial u_0}{\partial s} \;-\; T_{ss}^0\right), \tag{8.20}$$

$$u_0\,\frac{\partial T_{nn}^0}{\partial s} + \frac{\partial u_0}{\partial s}\,T_{nn}^0 \;=\; \frac{-1}{De}\,\left((1-\alpha_s)\frac{\partial u_0}{\partial s} \;+\; T_{nn}^0\right), \tag{8.21}$$

$$\frac{Z_s X_{ss} - Z_{ss} X_s}{F^2} - \frac{2Y_{ss}u_0}{Rb} + \frac{(X+1)(Y_{ss}Z_s - Y_s Z_{ss})}{Rb^2} + \frac{Z(Y_s X_{ss} - Y_{ss} X_s)}{Rb^2} = 0, \tag{8.22}$$

and finally the arc-length condition is

$$X_s^2 + Y_s^2 + Z_s^2 = 1. \tag{8.23}$$

These are a system of six equations in six unknowns which are X, Y, Z, u_0,T^0_{ss} and T^0_{nn}. We solve these equations in the inviscid limit for obtaining the trajectory of the jet with the following initial conditions as $u_0(0) = R_0(0) = X_s(0) = 1$ and $Y(0) = X(0) = Z(0) = Z_s(0) = Y_s(0) = T^0_{ss} = T^0_{nn} = 0$.

We use the same assumptions used in the previous chapter to solve these set of equations and find the corresponding trajectory of the viscoelastic curved jet which is similar to Uddin & Decent (2010) who studied the effect of gravity on non-Newtonian liquid jets. Uddin (2007) also investigated the influence of gravity on non-Newtonian liquid curved jets with surfactant by considering $Re \to \infty$ which means the viscosity has a negligible effect on the steady state solutions. Figs. 8.2 and 8.3 show the influence of changing the Froude number and the Rossby number on the trajectory of a viscoelastic liquid jet which means when we decrease the Froude number the effect of gravity becomes stronger on the trajectory. We find the relationship between the extra stress tensor, T^0_{ss} and T^0_{nn} and the arc-length s for different values of Rossby number and Froude number which are in Figs. 8.4-8.7. Fig. 8.8 shows the solutions of a liquid jet emerging from an orifice and falling under the influence of gravity for different values of the Weber number.

8.3 Linear Analysis

In Chapter 6 we did not establish an explicit relationship between the most unstable wavenumber and rotation. By changing the initial steady state solutions for u_0 and R_0, we determined the linear stability. We follow the same approach for finding linear stability under influence of gravity. As before, the Rossby number and Weber, and in this case the Froude number, are non-dimensional parameters which are manifested only in the steady state solution.

It can be noticed in Fig. 8.9 the radius of the jet decreases with an increasing arc-length s. This Figure also shows when the Froude number is increased with constant Rossby

number, $F = 0.5, 1$ and 3, $Rb = 8$, the radius of the jet increases which means the liquid jet becomes thinner and moves slowly. In Figs. 8.10 and 8.11, we plot the correlation between the growth rate and the wavenumber of the most unstable modes and the arc-length for different values of Froude number.

In Fig. 8.12, we chose a different value of the Rossby number, making Froude number as a constant, showing that when we increase the Rossby number the radius of the jet increases as well. The same procedure is applied in Figs. 8.13 and 8.14 to find the relationship between the growth rate and the most unstable mode for the wavenumber and arc-length s. It can also be seen that when the Rossby number increases the growth rate and the wavenumber increases.

In Fig. 8.15, we make the Rossby number and the Froude number changeable. The same results were found when finding the growth rate and the wavenumber for the most unstable mode with arc-length s in Figs. 8.16 and 8.17.

From Fig. 8.18, we make the Rossby number very high and the Froude number varies which means no rotation for determining the radius of the jet against arc-length s. In Figs. 8.19 and 8.20, we see that when the Rossby number is very high and the Froude number is changeable the growth rate for the most unstable mode and the maximum wavenumber against arc-length increase when the Froude number is decreased.

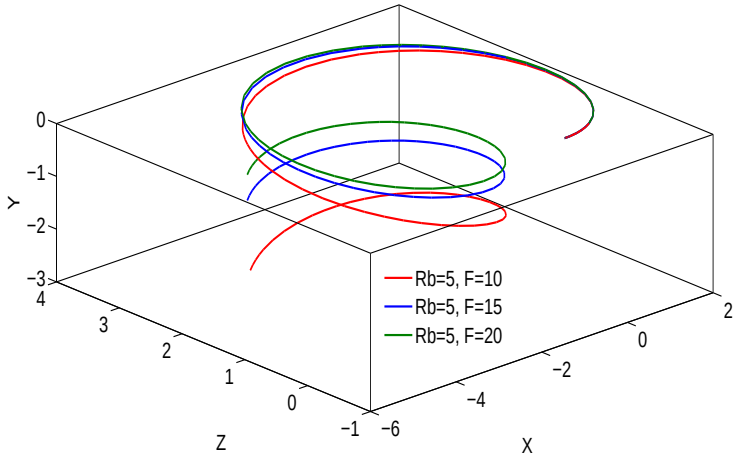

Figure 8.2: Graph showing the trajectory of a rotating liquid jet under the effect of gravity and rotation for different values of Froude number at $We = 10$, $\alpha_s = 0.2$ and $De = 2$.

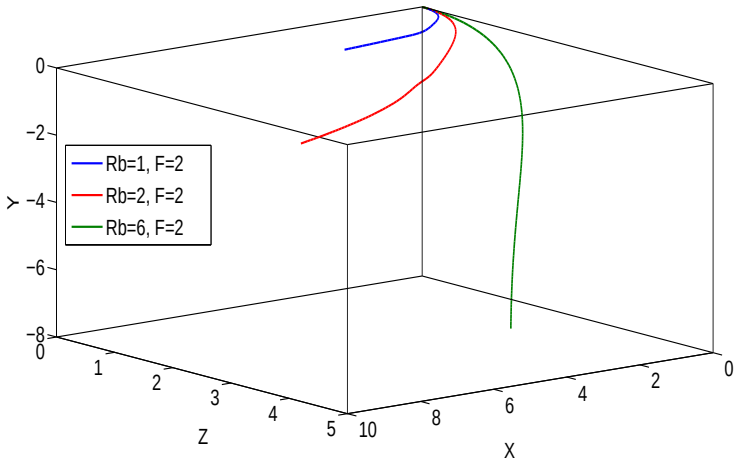

Figure 8.3: Graph showing the trajectory of a rotating liquid jet under the effect of gravity and rotation for different values of Rossby number at $We = 10$, $\alpha_s = 0.2$ and $De = 2$.

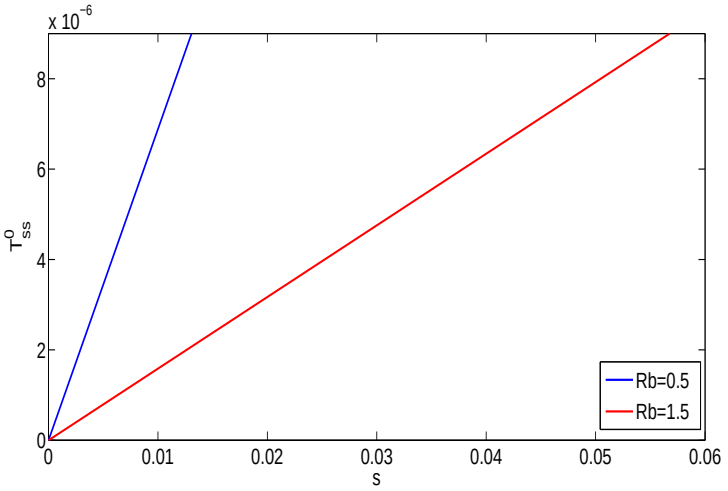

Figure 8.4: Graph showing the relationship between T^0_{ss} and arc-length s of a rotating liquid jets under the effect of gravity for different values of Rossby number number at $F = 3$, $We = 25$, $\alpha_s = 0.2$ and $De = 2$.

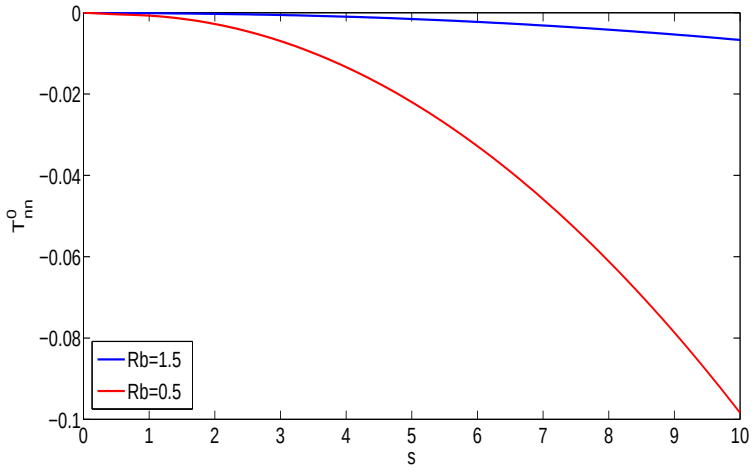

Figure 8.5: Graph showing the relationship between T^0_{nn} and arc-length s of a rotating liquid jets under the effect of gravity for different values of Rossby number number at $F = 3$, $We = 25$, $\alpha_s = 0.2$ and $De = 2$.

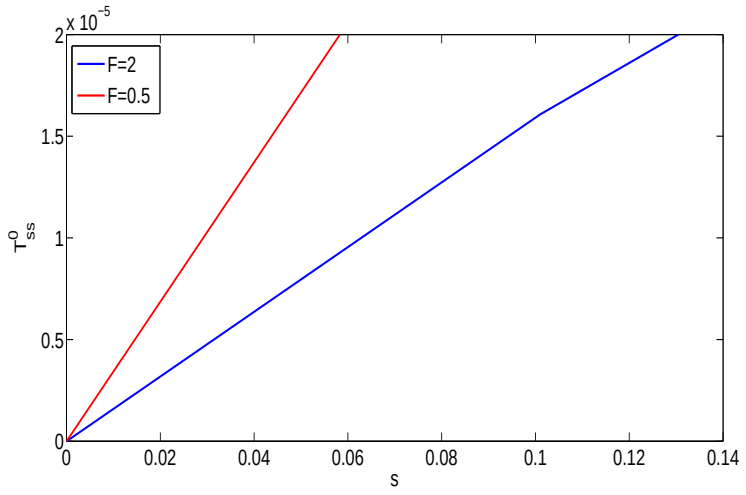

Figure 8.6: Graph showing the relationship between T^0_{ss} and arc-length s of a rotating liquid jets under the effect of gravity for different values of Froude number number at $Rb = 1.5$, $We = 25$, $\alpha_s = 0.2$ and $De = 2$.

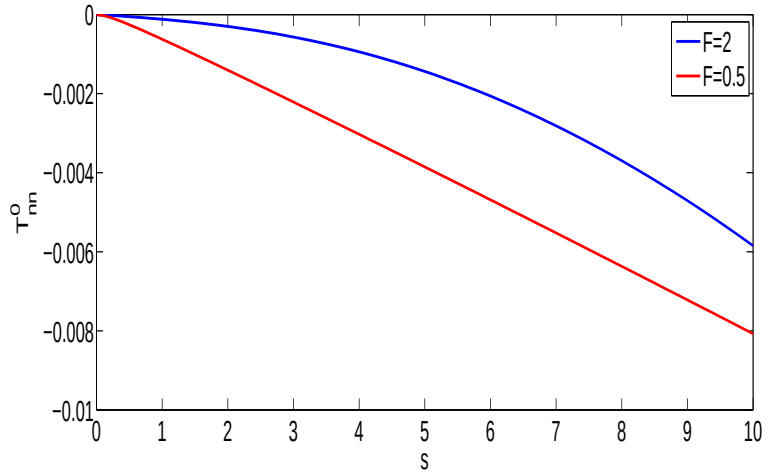

Figure 8.7: Graph showing the relationship between T^0_{nn} and arc-length s of a rotating liquid jets under the effect of gravity for different values of Froude number number at $Rb = 1.5$, $We = 25$, $\alpha_s = 0.2$ and $De = 2$.

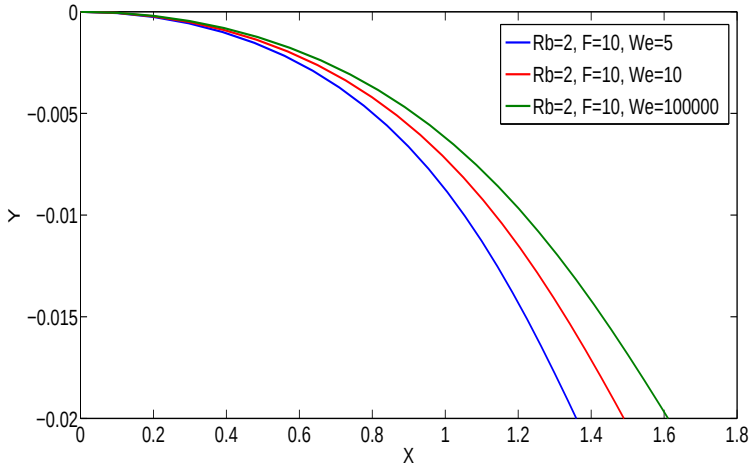

Figure 8.8: Graph showing the trajectory of a rotating liquid jets under the effect of gravity and rotation for different values of the surface tension at $\alpha_s = 0.2$ and $De = 2$.

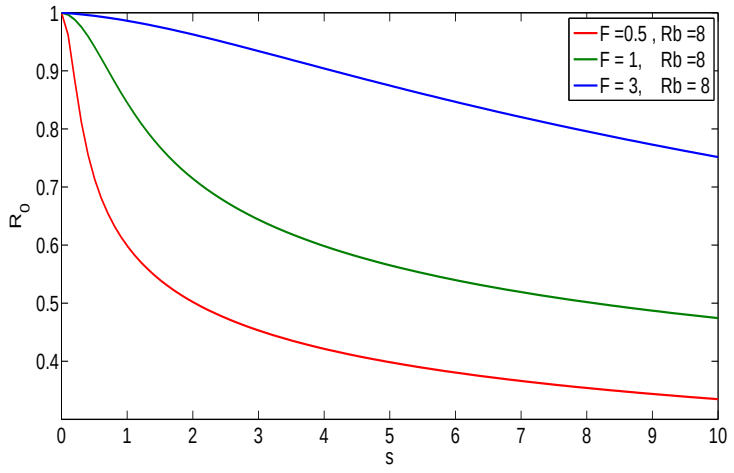

Figure 8.9: Graph showing the relationship between the radius and the arc-length s for different values of Froude number and Rossby number when $We = 15$, $\alpha_s = 0.2$ and $De = 2$.

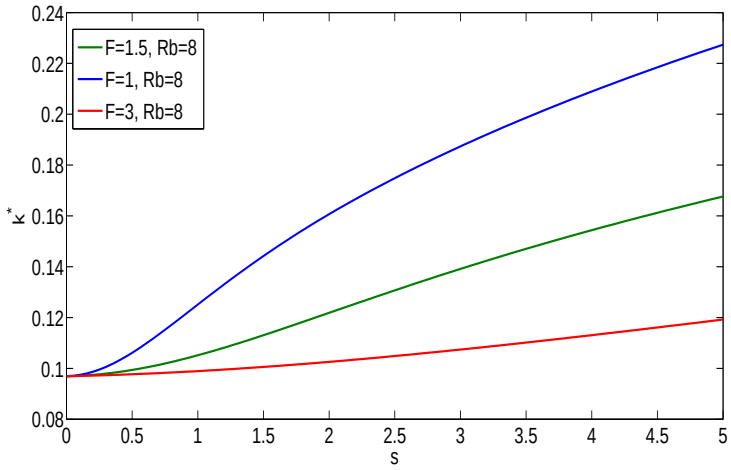

Figure 8.10: Graph showing the relationship between the growth rate ω_r^* of the most unstable mode against the arc-length s for a viscoelastic liquid jet, where the dimensionless numbers are $Re = 1000$, $We = 10$, $De = 15$ and $\tilde{\alpha_s} = 20$.

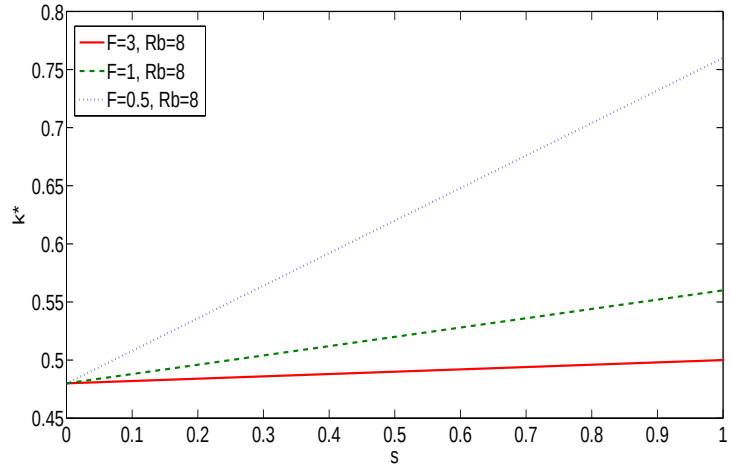

Figure 8.11: Graph showing the relationship between the most unstable mode k^* and the arc-length s for a viscoelastic liquid jet, where the dimensionless numbers are $Re = 1000$, $We = 10$, $De = 15$, and $\tilde{\alpha_s} = 20$.

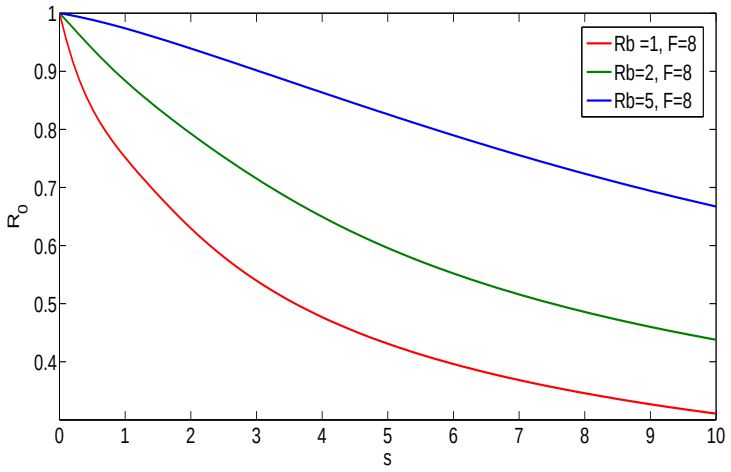

Figure 8.12: Graph showing the relationship between the radius and the arc-length s for different values of Froude number and Rossby number when $We = 15$.

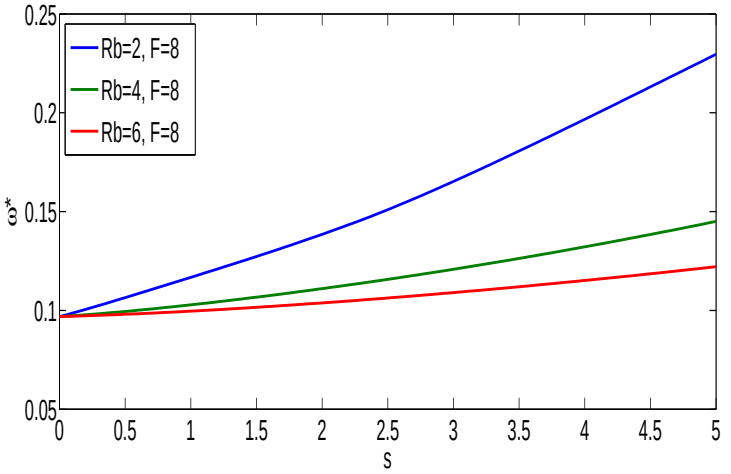

Figure 8.13: Graph showing the relationship between the growth rate ω_r^* of the most unstable mode against the arc-length s for a viscoelastic liquid jet, where the dimensionless numbers are $Re = 1000$, $We = 10$, $De = 15$ and $\tilde{\alpha_s} = 20$.

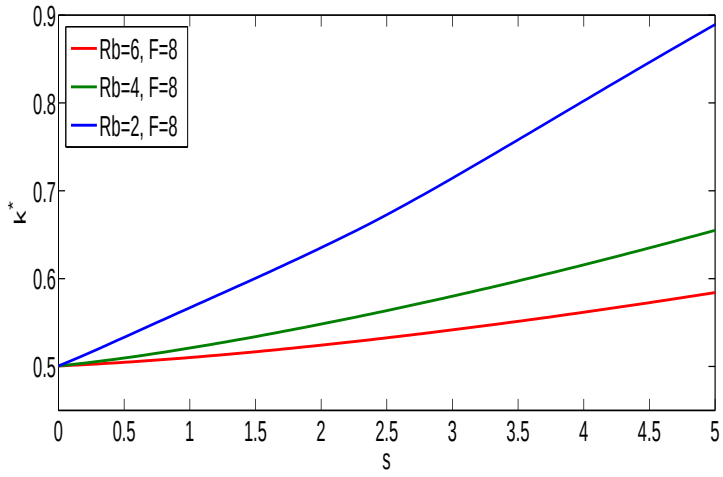

Figure 8.14: Graph showing the relationship between the most unstable mode k^* and the arc-length s for a viscoelastic liquid jet, where the dimensionless numbers are $Re = 1000$, $We = 10$, $De = 15$ and $\tilde{\alpha}_s = 20$.

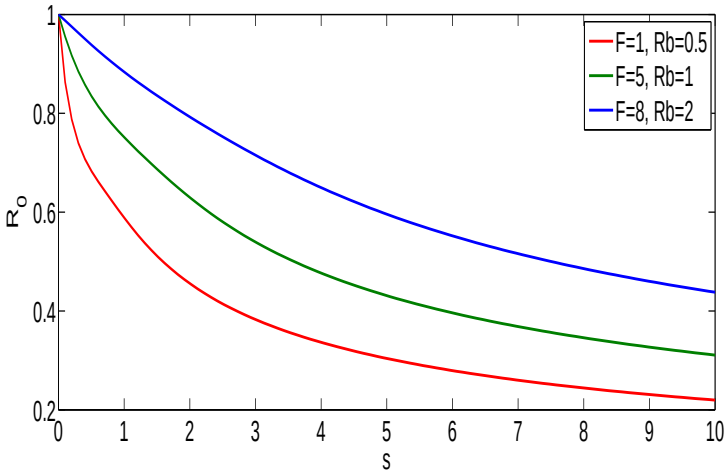

Figure 8.15: Graph showing the relationship between the radius and the arc-length s for different values of Froude number and Rossby number when $We = 15$.

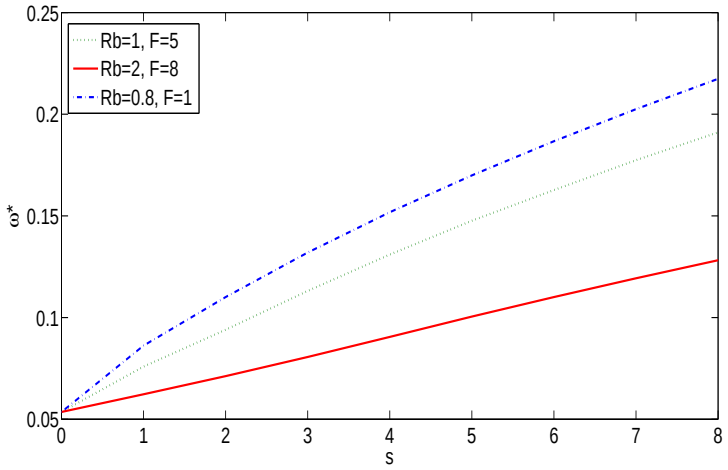

Figure 8.16: Graph showing the relationship between the growth rate ω_r^* of the most unstable mode against the arc-length s for a viscoelastic liquid jet, where the dimensionless numbers are $Re = 1000$, $We = 10$, $De = 15$ and $\tilde{\alpha_s} = 20$.

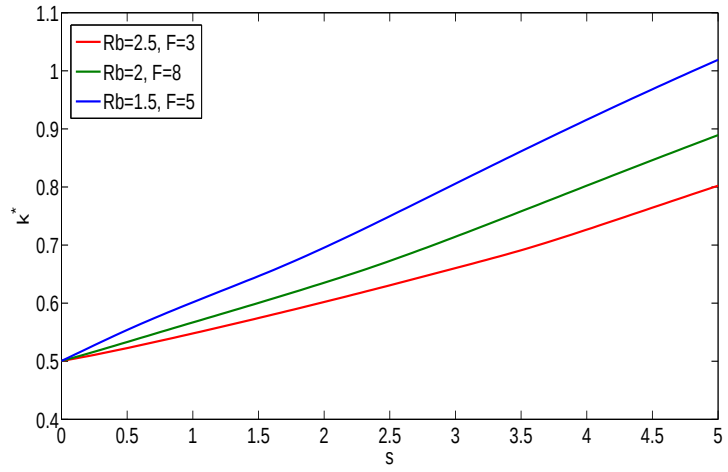

Figure 8.17: Graph showing the relationship between the most unstable mode k^* and the arc-length s for a viscoelastic liquid jet, where the dimensionless numbers are $Re = 1000$, $We = 10$, $De = 15$ and $\tilde{\alpha_s} = 20$.

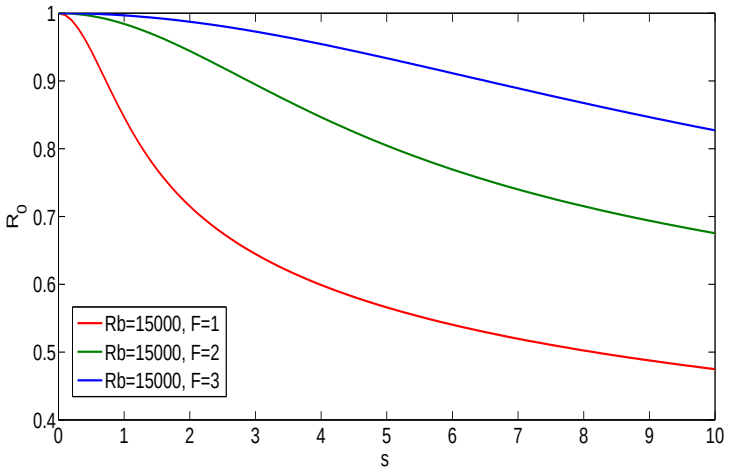

Figure 8.18: Graph showing the relationship between the radius and the arc-length s for different values of Froude number and Rossby number when $We = 15$.

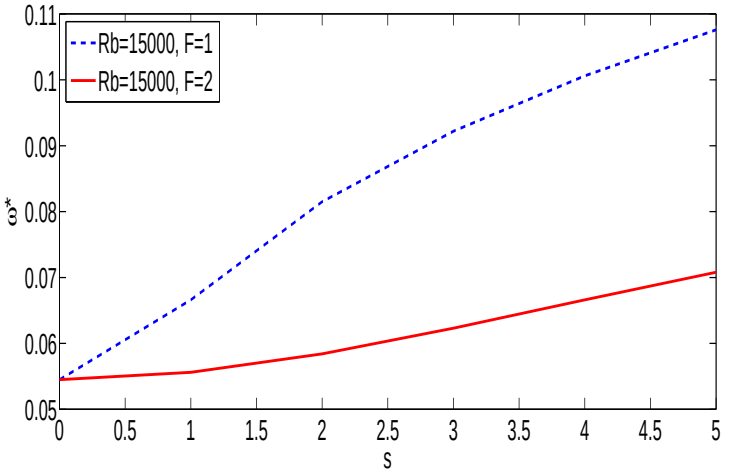

Figure 8.19: Graph showing the relationship between the growth rate ω_r^* of the most unstable mode against the arc-length s for a viscoelastic liquid jet, where the dimensionless numbers are $Re = 1000$, $We = 10$, $De = 15$ and $\tilde{\alpha_s} = 20$.

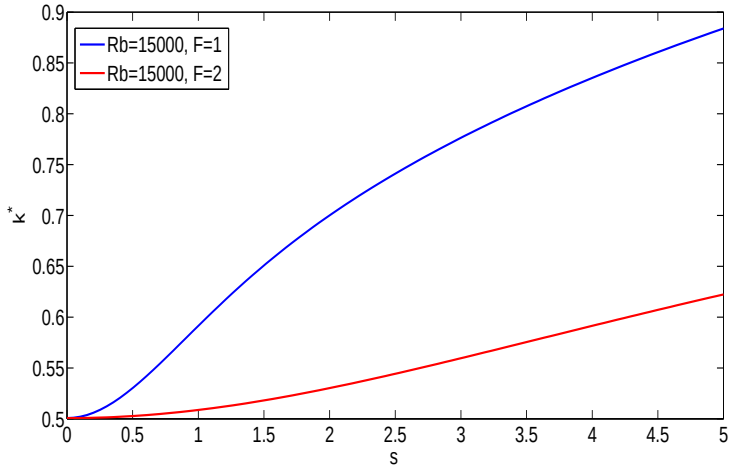

Figure 8.20: Graph showing the relationship between the most unstable mode k^* and the arc-length s for a viscoelastic liquid jet, where the dimensionless numbers are $Re = 1000$, $We = 10$, $De = 15$ and $\tilde{\alpha} = 20$.

Chapter 9

Linear Instability of Viscoelastic Liquid Curved Jets with Surfactants

9.1 Background on Surfactants

In liquid jets, surface tension plays an important role in instability. Therefore, in this chapter, we will be interested in investigating the influence of using surfactants on the break-up of viscoelastic curved jets. A surfactant, known as a surface active agent, is a chemical material which tends to reduce the surface tension of the droplets.

Surfactants have many forms which they can come in; however, there are generally three categories, which are: Ionic, Non-ionic and Amphoteric (see Walker (2012)).
Ionic surfactants have molecules which have charged (negative or positive) heads. These kind of surfactants are the most common, and are found in products such as soaps and shampoos. Non-Ionic surfactants are not charged, but they contain two parts, which are polar head and non-polar tail (see Fig. 9.1). These two parts of the molecular surfactant with liquid in free surface can be disregarded, as the head point will go inside the liquid

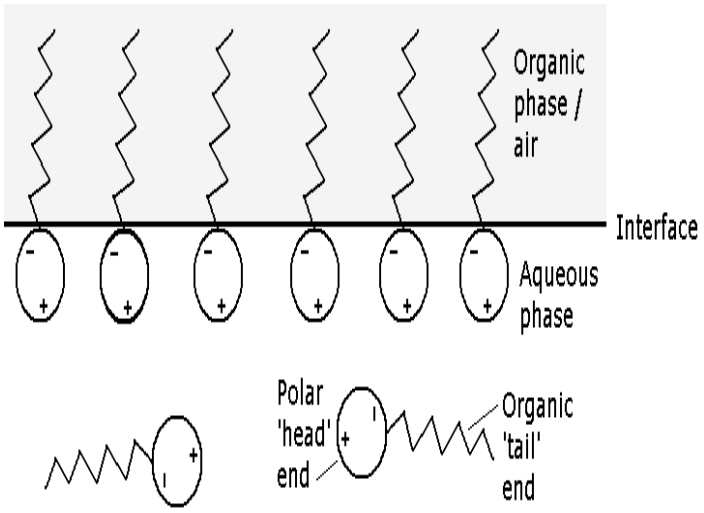

Figure 9.1: Surfactants geometry

while the tail point is in the free surface. Amphoteric surfactants have polar heads which are charged either negatively or positively depending on the measurement of the acidity or basicity of the aqueous solution (pH). These kinds of surfactants are not in common use.

9.1.1 Effect of Surfactants on Break-Up of Liquid Jets

Many authors have studied the effects of adding small amounts of surfactants on straight liquid jets. For example, Whitaker (1976) examined the instability of inviscid liquid jets with surfactants. The linear instability of viscous liquid jets and a surfactant has been carried out by Hansen *et al*. (1999). They have found that the growth rate decreases with including surfactants; this is clear, because the surfactant slows the growth rate of disturbances.

Anshus (1973) investigated theoretically the effect of surfactants on liquid jets in two cases which are compressible and incompressible. He found that the surfactants decrease the growth rate, especially in the case of incompressible liquid jets. Craster *et al.* (2002) studied Newtonian liquid jets with surfactants by using a one-dimensional model. The case of weakly viscoelastic jets with surfactants has been examined by Zhang *et al.* (2002) in a study in which they discussed the influence of the viscosity ratio, using the Oldroyd-B model.

Timmermans and Lister (2002) have used a nonlinear analysis to study a surfactant laden thread in inviscid liquid jets. They used a one-dimensional nonlinear model to examine the effect of the surfactant on the change of surface tension gradients. Uddin (2007) investigated the effects of surfactants on the instability of rotating liquid jets. He discovered that surfactants reduce the growth rate of liquid curved jets and found that adding surfactants in non-Newtonian liquid curved jets delay the break-up. He also examined the steady state trajectories and noticed that when the concentration of surfactants is increased, the liquid jet curves less and the radius along the jet decays more quickly. Uddin (2007) discussed the effects of gravity on the liquid curved jets with surfactants and from the linear instability found that the wavenumber of the most unstable mode increases as gravity is increased.

Stone and Leal (1990) examined the break-up of liquid jets with surfactants by extending the work of Stone *et al.* (1986) to include insoluble surfactants. Viscous liquid jets and soluble surfactants have been studied by Milliken *et al.* (1993) and Milliken & Leal (1994). They observed that Marangoni stress decreased with increasing the viscosity and surfactant solubility.

9.2 Problem Formulation

As we have modelled the spiralling process in Chapter 6, here we consider the same assumption by supposing that we have a large cylindrical container which has radius s_0 and rotates with angular velocity Ω. We also assume that the liquid which emerges from the orifice has a layer of an insoluble surfactant and the concentration of the surfactant is fixed. This problem is examined by choosing a coordinate system (X, Y, Z) rotating with the container, having an origin at the axis of the container; the position of the orifice is at $(s_0, 0, 0)$. Initially, we outline the continuity, momentum and constitutive equations of motion. Due to the surfactant concentration, we have a convection-diffusion equation along the liquid interface. We use the Oldroyd-B model for the viscoelastic term. These equations therefore take the form

$$\boldsymbol{\nabla} \cdot \boldsymbol{u} = 0,$$

$$\rho\left(\frac{\partial \boldsymbol{u}}{\partial t} + \boldsymbol{u} \cdot \boldsymbol{\nabla} \boldsymbol{u}\right) = -\boldsymbol{\nabla} p + \boldsymbol{\nabla} \cdot \boldsymbol{\tau} - 2\,\boldsymbol{w} \times \boldsymbol{u} - \boldsymbol{w} \times (\boldsymbol{w} \times \boldsymbol{r}),$$

$$\boldsymbol{\tau} = \mu_s(\boldsymbol{\nabla} \boldsymbol{u} + (\boldsymbol{\nabla} \boldsymbol{u})^T) + \boldsymbol{T}$$

$$\lambda \boldsymbol{T}^{\triangledown} + \boldsymbol{T} = \mu_p \boldsymbol{\gamma}$$

$$\frac{\partial \boldsymbol{T}}{\partial t} + (\boldsymbol{u} \cdot \boldsymbol{\nabla})\boldsymbol{T} - \boldsymbol{T} \cdot \boldsymbol{\nabla} \boldsymbol{u} - (\boldsymbol{\nabla} \boldsymbol{u})^T \cdot \boldsymbol{T} = \frac{1}{\lambda}(\mu_p \boldsymbol{\gamma} - \boldsymbol{T}), \tag{9.1}$$

where $(\boldsymbol{u})$ is the velocity in the form $(\boldsymbol{u}) = (\boldsymbol{u})e_s + (\boldsymbol{v})e_n + (\boldsymbol{w})e_\phi$, ρ is the density of the fluid, p is the pressure, the angular velocity of the container is $(\boldsymbol{w}) = (0, w, 0)$, μ_s is the viscosity of the solvent, $(\boldsymbol{T})$ is the extra stress tensor that represents the viscoelastic

contribution, and μ_p is the viscosity of the polymer. The surfactant concentration along the jet is given by (see Stone & Leal (1990) and Blyth & Pozrikidis (2004))

$$\Gamma_t + \boldsymbol{\nabla_s} \cdot (\Gamma \boldsymbol{u_s}) + \Gamma(\boldsymbol{\nabla_s} \cdot \boldsymbol{n})(\boldsymbol{u} \cdot \boldsymbol{n}) = S(\Gamma, B_s) + D_s \boldsymbol{\nabla_s^2} \Gamma, \tag{9.2}$$

where Γ is the surfactant concentrations at the interface, $\boldsymbol{\nabla_s} = (I - \mathbf{nn}) \cdot \nabla$ is the surface gradient operator, D_s is the surface diffusivity of surfactant, $\boldsymbol{u_s} = (I - \mathbf{nn}) \cdot \boldsymbol{u}$ is the surface or tangential velocity, and $\boldsymbol{\nabla_s} \cdot \mathbf{n} = 2\kappa$ where κ is the mean curvature of the free surface. The surfactant source term, S, takes absorption from the free surface into account, and acts as a function of surfactant concentration on the surface Γ and the bulk B_s. The third term on the left of (9.2) relates to the effect of normal forces on dilatation by expansion (see Blyth & Pozrikidis (2004)).

We consider in this study that the diffusivity of surfactant is small ($D_s = 0$) and the surfactant is insoluble ($S = 0$). For example, if surfactants with typical diffusivity 10^{-10}-10^{-9} $mm^2\ s^{-1}$ (see Tricot (1997)) were added to the liquid-bridge experiments of Zhang, Padgett & Basaran (1995), so that the Peclet number would be at least 10^3-10^4. This approach has been taken by Timmermans & Lister (2002) for investigating the linear stability of a liquid thread with surfactants. Uddin (2007) examined linear and nonlinear instability of non-Newtonian liquid curved jets with surfactants by using the model

$$\Gamma_t + \boldsymbol{u} \cdot \boldsymbol{\nabla_s} \Gamma - \Gamma \mathbf{n} \cdot ((\boldsymbol{n} \cdot \boldsymbol{\nabla}) \boldsymbol{u}) = 0. \tag{9.3}$$

The boundary conditions are

$$\frac{\partial R}{\partial t} + \mathbf{u} \cdot \nabla R = 0, \tag{9.4}$$

normal and tangential conditions are

$$p + \mathbf{n} \cdot \mathbf{\Pi} \cdot \mathbf{n} = \sigma \nabla \cdot \mathbf{n}, \tag{9.5}$$

and

$$\mathbf{t_i} \cdot \mathbf{\Pi} \cdot \mathbf{n} = \mathbf{t_i} \cdot \nabla \sigma, \tag{9.6}$$

where

$$\mathbf{\Pi} = -p\mathbf{I} + \mu\left(\nabla \mathbf{u} + (\nabla \mathbf{u})^T\right) + \mathbf{T},$$

the normal vector is

$$\mathbf{n} = \frac{1}{E}\left(-\frac{\partial R}{\partial s}\frac{1}{h_s}\mathbf{e_s} + \mathbf{e_n} - \frac{\partial R}{\partial \phi}\frac{1}{R}\mathbf{e}_\phi\right), \tag{9.7}$$

tangential vectors are

$$\mathbf{t_1} = \mathbf{e_s} + \frac{1}{h_s}\frac{\partial R}{\partial s}\mathbf{e_n} \text{ and } \mathbf{t_2} = \frac{1}{R}\frac{\partial R}{\partial \phi}\mathbf{e_n} + \mathbf{e}_\phi,$$

and the arc-length condition is

$$X_s^2 + Z_s^2 = 1. \tag{9.8}$$

Moreover, in order to incorporate the dependence of the surface tension on the surfactant concentration, we use the surfactant equation of state which is the Szyskowski equation that is given by

$$\sigma = \tilde{\sigma} + \Gamma_\infty R_g T \log\left[\frac{\Gamma_\infty - \Gamma}{\Gamma_\infty}\right], \tag{9.9}$$

which is a special case from the Frumkin equation of state (see Tricot (1997))

$$\sigma = \tilde{\sigma} + \Gamma_\infty R_g T(\log(1 - \frac{\Gamma_\infty}{\Gamma}) + \frac{A\Gamma_\infty^2}{2\Gamma^2}),$$

where $\tilde{\sigma}$ is the surface tension of the liquid in the absence ($\Gamma = 0$) of any surfactant, Γ_∞ is the maximum packing concentration of surfactant, R_g is the universal gas constant, T is the temperature and A is the molecular interaction parameter.

This equation gives the relation between the surfactant concentration Γ and the surface tension of the liquid-gas interface.

9.3 Non-Dimensionalisation

We can express our equations in dimensionless terms by using the following transformations

$$\begin{aligned}
&\overline{u} = \frac{u}{U}\ , \quad \overline{v} = \frac{v}{U}, \quad \overline{w} = \frac{w}{U}, \quad \overline{n} = \frac{n}{a}, \quad \varepsilon = \frac{a}{s_0}, \\
&\overline{R} = \frac{R}{a}, \quad \overline{T} = \frac{s_0}{U\mu_0}T, \quad \overline{s} = \frac{s}{s_0}, \quad \overline{t} = \frac{U}{s_0}\,t, \quad \overline{p} = \frac{p}{\rho U^2}, \\
&\overline{X} = \frac{X}{s_0}, \quad \overline{Z} = \frac{Z}{s_0}, \quad \overline{\sigma} = \frac{\sigma}{\tilde{\sigma}}, \quad \overline{\Gamma} = \frac{\Gamma}{\Gamma_\infty},
\end{aligned} \tag{9.10}$$

where u, v and w are the tangential, radial and azimuthal velocity components, U is the exit speed of the jet in the rotating frame, s_0 is the radius of the cylindrical drum, a is radius of the orifice, ε is the aspect ratio of the jet, T is the extra stress tensor, μ_0 is the total viscosity of the solvent and the polymer and σ and Γ are dimensionless with respect to the surface tension and the surfactant concentration, then dropping over bars. The equations of motion are the same as in Chapter 6, which means that the continuity

equation is

$$\varepsilon n\frac{\partial u}{\partial s}+h_s\left(v+n\frac{\partial v}{\partial n}+\frac{\partial w}{\partial \phi}\right)+\varepsilon n\left(v\cos\phi-w\sin\phi\right)\left(X_sZ_{ss}-Z_sX_{ss}\right)=0, \quad (9.11)$$

the rest of the equations are found in Chapter 6 (6.15)-(6.23).

The surfactant concentration equation is (see Uddin (2007))

$$\begin{aligned}\Gamma_t \;=\; & -\frac{u}{h_s}\frac{\partial \Gamma}{\partial s}-\frac{v}{\varepsilon}\frac{\partial \Gamma}{\partial n}-\frac{w}{\varepsilon n}\frac{\partial \Gamma}{\partial \phi}+\\ & \frac{\Gamma}{E}\left(\frac{\varepsilon^2}{h_s^2}\left(\frac{\partial R}{\partial s}\right)^2\frac{\partial u}{\partial s}-\frac{1}{h_s}\left(\frac{\partial R}{\partial s}\right)\frac{\partial u}{\partial n}+\frac{1}{nRh_s}\frac{\partial R}{\partial \phi}\frac{\partial R}{\partial s}\frac{\partial u}{\partial \phi}-\frac{\varepsilon}{h_s^2}\left(\frac{\partial R}{\partial s}\right)\frac{\partial v}{\partial s}+\right.\\ & \left.\frac{1}{\varepsilon}\frac{\partial v}{\partial n}-\frac{1}{\varepsilon nR}\frac{\partial R}{\partial \phi}\frac{\partial v}{\partial \phi}+\frac{\varepsilon}{Rh_s^2}\frac{\partial R}{\partial \phi}\frac{\partial R}{\partial s}\frac{\partial w}{\partial s}-\frac{1}{R}\frac{\partial R}{\partial \phi}\frac{\partial w}{\partial n}+\frac{1}{\varepsilon nR^2}\left(\frac{\partial R}{\partial \phi}\right)^2\frac{\partial w}{\partial \phi}\right). \quad (9.12)\end{aligned}$$

9.4 The Non-dimensionalisation of Boundary Conditions

It can be found that the normal stress condition is

$$\begin{aligned}& p-\frac{2\alpha_s}{Re}\frac{1}{E^2}\left(\varepsilon^2\left(\frac{\partial R}{\partial s}\right)^2\frac{1}{h_s^3}\left(\frac{\partial u}{\partial s}+(v\,cos\phi-\sin\phi)(X_sZ_{ss}-Z_sX_{ss})+\frac{h_s}{2\alpha_s}T_{ss}\right)\right.\\ & +\frac{1}{\varepsilon}\frac{\partial v}{\partial n}+\frac{1}{2\alpha_s}T_{nn}+\frac{1}{\varepsilon\,R^3}\left(\frac{\partial R}{\partial \phi}\right)^2\left(\frac{\partial w}{\partial \phi}+v+RT_{\phi\phi}\right)-\\ & \frac{\varepsilon}{h_s}\frac{\partial R}{\partial s}\left(\frac{1}{h_s}\frac{\partial v}{\partial s}+\frac{1}{\varepsilon}\frac{\partial u}{\partial n}-\frac{u}{h_s}\,cos\phi(X_sZ_{ss}-Z_sX_{ss})+\frac{1}{2\alpha_s}T_{sn}\right)+\\ & \frac{\varepsilon}{Rh_s}\frac{\partial R}{\partial s}\frac{\partial R}{\partial \phi}\left(\frac{1}{\varepsilon\,R}\frac{\partial u}{\partial \phi}+\frac{u}{h_s}\sin\phi(X_sZ_{ss}-Z_sX_{ss})+\frac{1}{h_s}\frac{\partial u}{\partial s}+\frac{1}{2\alpha_s}T_{s\phi_s}\right)\\ & \left.-\frac{1}{R}\frac{\partial R}{\partial \phi}(R\frac{\varepsilon\partial w}{\partial n}-\frac{\varepsilon w}{R}+\frac{\varepsilon}{R}\frac{\partial v}{\partial \phi}\right)=\frac{\sigma\,\kappa}{We}\ \text{on}\ n=R(s,t), \quad (9.13)\end{aligned}$$

where

$$\kappa = \frac{1}{h_s}\left(-\varepsilon^2\frac{\partial}{\partial s}\left(\frac{n}{Eh_s}\frac{\partial R}{\partial s}\right) + \frac{\partial}{\partial n}\left(\frac{nh_s}{E}\right) - \frac{\partial}{\partial \phi}\left(\frac{h_s}{En}\frac{\partial R}{\partial \phi}\right)\right).$$

$$E = \left(1 + \frac{\varepsilon^2}{h_s^2}\left(\frac{\partial R}{\partial s}\right)^2 + \frac{1}{R^2}\left(\frac{\partial R}{\partial \phi}\right)^2\right)^{\frac{1}{2}}.$$

$$h_s = 1 + \varepsilon n\cos\phi(X_s Z_{ss} - X_{ss}Z_s).$$

The first tangential stress condition is

$$\left(1 - \varepsilon^2\left(\frac{\partial R}{\partial s}\right)^2\frac{1}{h_s^2}\right)\left\{\varepsilon\frac{\partial v}{\partial s} + h_s\frac{\partial u}{\partial n} - \varepsilon u\cos\phi(Z_s Z_{ss} - X_{ss}Z_s) + \frac{\varepsilon}{\alpha_s}T_{sn}\right\} + 2\varepsilon\frac{\partial R}{\partial s}$$
$$\left\{\frac{\partial v}{\partial n} - \varepsilon\frac{\partial u}{\partial s}\frac{1}{h_s} - \frac{\varepsilon}{h_s}v\cos\phi - w\sin\phi(X_s Z_{ss} - X_{ss}Z_s) - \frac{\varepsilon}{2\alpha_s}(T_{ss} - T_{nn})\right\} =$$
$$\frac{\varepsilon Re}{We}\left(\frac{\varepsilon}{h_s}\frac{\partial\sigma}{\partial s} + \frac{1}{h_s}\frac{\partial R}{\partial s}\frac{\partial\sigma}{\partial n}\right), \tag{9.14}$$

and the second tangential stress condition is

$$\left(1 - (\frac{\partial R}{\partial\phi})^2\frac{1}{R^2}\right)\left(\frac{\partial w}{\partial n} - \frac{w}{R} + \frac{1}{R}\frac{\partial v}{\partial\phi} + \frac{\varepsilon}{\alpha_s}T_{n\phi}\right) +$$
$$\frac{2}{R}\frac{\partial R}{\partial\phi}\left(\frac{\partial v}{\partial n} - \frac{1}{R}(\frac{\partial w}{\partial\phi} + v) + \frac{\varepsilon}{\alpha_s}(T_{nn} - T_{\phi\phi})\right) = \frac{\varepsilon Re}{We}\left(\frac{1}{R}\frac{\partial R}{\partial\phi} + \frac{1}{n}\frac{\partial\sigma}{\partial\phi}\right). \tag{9.15}$$

Another boundary condition is the arc-length condition $X_s^2 + Z_s^2 = 1$ and also the kinematic condition is

$$h_s\left(\varepsilon\frac{\partial R}{\partial t} + (\cos\phi + \frac{1}{n}\frac{\partial R}{\partial t}\sin\phi(X_t Z_s - X_s Z_t) - v + \frac{\partial R}{\partial\phi}\frac{w}{n}\right)$$
$$+\varepsilon u\frac{\partial R}{\partial s} - \varepsilon\frac{\partial R}{\partial s}(X_t Z_s - X_s Z_t + \varepsilon n\cos\phi(X_s Z_{ss} - Z_s X_{ss})) = 0. \tag{9.16}$$

These boundary conditions (9.13) and (9.16) are applied at the free surface $n = R(s, \phi, t)$.

9.5 Asymptotic Analysis

As discussed earlier, u, v, w and p are expanded in εn (see Eggers (1997) and Hohman *et al.* (1984)) and $R, X, Z, T_{ss}, T_{nn}, T_{\phi\phi}$ in asymptotic series in ε. We assume that the leading order of the axial component of the velocity is independent of ϕ. It is also assumed that small perturbations do not affect the centerline. Therefore, we have

$$
\begin{aligned}
u(s,n,\phi,t) &= u_0(s,t) + (\varepsilon\, n)u_1(s,\phi,t) + (\varepsilon\, n)^2 u_2(s,\phi,t) + ... \\
v(s,n,\phi,t) &= (\varepsilon\, n)v_1(s,\phi,t) + (\varepsilon\, n)^2 v_2(s,\phi,t) + ... \\
w(s,n,\phi,t) &= (\varepsilon\, n)w_1(s,\phi,t) + (\varepsilon\, n)^2 w_2(s,\phi,t) + ... \\
p(s,n,\phi,t) &= p_0(s,\phi,t) + (\varepsilon\, n)p_1(s,\phi,t) + ... \\
R(s,n,\phi,t) &= R_0(s,t) + (\varepsilon)R_1(s,\phi,t) + ... \\
X(s,n,\phi,t) &= X_0(s) + (\varepsilon)X_1(s,t) + ... \\
Z(s,n,\phi,t) &= Z_0(s) + (\varepsilon)Z_1(s,t) + ... \\
T_{ss}(s,n,\phi,t) &= T^0_{ss}(s,t) + \varepsilon\, T^1_{ss}(s,t) + ... \\
T_{nn}(s,n,\phi,t) &= T^0_{nn}(s,t) + \varepsilon\, T^1_{nn}(s,t) + ... \\
T_{\phi\phi}(s,n,\phi,t) &= \varepsilon T^1_{\phi\phi}(s,t) + \varepsilon^2\, T^2_{\phi\phi}(s,t) + ... \\
T_{sn}(s,n,\phi,t) &= \varepsilon\, T^1_{sn}(s,t) + \varepsilon^2\, T^2_{sn}(s,t) + ... \\
T_{s\phi}(s,n,\phi,t) &= \varepsilon\, T_{s\phi}(s,t) + \varepsilon^2\, T^2_{s\phi}(s,t) + ... \\
T_{n\phi}(s,n,\phi,t) &= \varepsilon\, T^1_{n\phi}(s,t) + \varepsilon^2\, T^2_{n\phi}(s,t) + ...
\end{aligned}
$$

The following expansions have been used for the surfactant concentration Γ and the surface tension σ as

$$\Gamma = \Gamma_0(s) + \varepsilon\Gamma_1(s) + O(\varepsilon^2),$$
$$\sigma = \sigma_0(s) + \varepsilon\sigma_1(s) + O(\varepsilon^2).$$

It can be found from the continuity equation that

$$O(\varepsilon n): \quad u_{0s} + 2v_1 + w_{1\phi} = 0 \tag{9.17}$$
$$O(\varepsilon n)^2: \; u_{1s} + 3v_2 + w_{2\phi} + ((3v_1 + w_{1\phi})\cos\phi - w_1 \sin\phi)$$
$$(X_s Z_{ss} - X_{ss} Z_s) = 0. \tag{9.18}$$

By solving the second tangential stress condition, it can be found that

$$O(\varepsilon n): \quad R_0^3 v_{1\phi} = 0 \tag{9.19}$$
$$O\Big((\varepsilon n)^2\Big): \quad 3R_0^2 R_1 v_{1\phi} + R_0^4(w_2 + v_{2\phi}) - 2R_0^2 R_{1\phi} w_{1\phi} = 0 \tag{9.20}$$

It can be seen that $v_{1\phi} = 0$, and by differentiating (9.17), we obtain $w_{1\phi\phi} = 0$. Because w_1 is periodic in ϕ we must have $w_1 = w_1(s,t)$. That leads to $v_1 = -\frac{u_{0s}}{2}$ and from (9.20) we obtain

$$w_2 + v_{2\phi} = 0. \tag{9.21}$$

Using the first tangential stress condition, it can be obtained that

$$O(\varepsilon n): \quad u_1 = u_0 \cos\phi (X_s Z_{ss} - X_{ss} Z_s) \tag{9.22}$$
$$O\Big((\varepsilon n)^2\Big): \quad u_2 = \frac{3}{2} u_{0s} \frac{R_{0s}}{R_0} + \frac{u_{0ss}}{4} + \frac{R_{0s}}{2\alpha_s R_0}(T^0_{ss} - T^0_{nn}) + \left(\frac{Re}{We}\right)\frac{\sigma_{0s}}{2R_0}. \tag{9.23}$$

By differentiating (9.21) with respect to ϕ we have

$$w_{2\phi} = -v_{2\phi\phi}, \tag{9.24}$$

so that

$$v_{2\phi\phi} - 3v_2 = u_{1s} + (3v_1 \cos\phi - w_1 \sin\phi)(X_s Z_{ss} - X_{ss} Z_s), \tag{9.25}$$

and when the expressions for u_1 and v_1 are used, we obtain

$$\begin{aligned} v_{2\phi\phi} - 3v_2 = &\Big(u_0(X_s Z_{sss} - X_{sss} Z_s) - \frac{u_{0s}}{2}(X_s Z_{ss} - X_{ss} Z_s)\Big)\cos\phi \\ &-w_1 \sin\phi (X_s Z_{ss} - X_{ss} Z_s). \end{aligned} \tag{9.26}$$

Periodic solutions for v_2 and w_2 are

$$\begin{aligned} v_2 = &\frac{1}{4}\Big(\frac{u_{0s}}{2}(X_s Z_{ss} - X_{ss} Z_s) - u_0(X_s Z_{sss} - X_{sss} Z_s)\Big)\cos\phi + \\ &\frac{w_1}{4}\sin\phi (X_s Z_{ss} - X_{ss} Z_s), \end{aligned} \tag{9.27}$$

and

$$\begin{aligned} w_2 = &\frac{1}{4}\Big(\frac{u_{0s}}{2}(X_s Z_{ss} - X_{ss} Z_s) - u_0(X_s Z_{sss} - X_{sss} Z_s)\Big)\sin\phi - \\ &\frac{w_1}{4}\cos\phi (X_s Z_{ss} - X_{ss} Z_s). \end{aligned} \tag{9.28}$$

Based on the momentum equation in the radial direction, we have at leading order

$p_{0n} = 0$ and at order ε is given by

$$p_1 = \left(u_0^2 (X_s Z_{ss} - X_{ss} Z_s) - \frac{2}{Rb} u_0 + \frac{(X_0 + 1) Z_{0s} - Z_0 X_{0s}}{Rb^2} \right) \cos\phi$$
$$- \frac{\alpha_s}{Re} \left(\frac{5}{2} u_{0s} (X_s Z_{ss} - X_{ss} Z_s) + u_{0s} (X_s Z_{sss} - X_{sss} Z_s) \right) \cos\phi -$$
$$\frac{\alpha_s}{Re} w_1 \sin\phi (X_s Z_{ss} - X_{ss} Z_s). \tag{9.29}$$

We will use X and Z instead of X_0 and Z_0 for simplicity.

For the momentum equation in the azimuthal direction, we have at leading order $p_{0\phi} = 0$, and obtain the above equation at order ε for p_1. From the normal stress condition at leading order, we have

$$p_0 = -\frac{u_{0s}}{Re} + \frac{\sigma_0}{R_0 We} + \frac{T^0_{nn}}{Re}, \tag{9.30}$$

and we also have at order ε

$$p_1 = \frac{\sigma_0}{R_0 We} \left(-\frac{R_{1\phi\phi} + R_1}{R_0^2} + \cos\phi (X_s Z_{ss} - X_{ss} Z_s) \right) + \frac{4\alpha_s v_2}{Re}. \tag{9.31}$$

By substituting the expression v_2 in the last equation, we obtain

$$p_1 = \frac{\sigma_0}{R_0 We} \left(-\frac{R_{1\phi\phi} + R_1}{R_0^2} + \cos\phi (X_s Z_{ss} - X_{ss} Z_s) \right) +$$
$$\frac{\alpha_s}{Re} \left(\frac{u_{0s}}{2} (X_s Z_{ss} - X_{ss} Z_s) - u_0 (X_s Z_{sss} - X_{sss} Z_s) \right) \cos\phi +$$
$$\frac{\alpha_s w_1}{Re} \sin\phi (X_s Z_{ss} - X_{ss} Z_s). \tag{9.32}$$

If we substitute p_1 from (9.31) into the previous equation, we obtain

$$(X_s Z_{ss} - X_{ss} Z_s) \left(u_0^2 - \frac{3\alpha_s}{Re} u_{0s} - \frac{\sigma}{We R_0} \right) - \frac{2}{Rb} u_0 + \frac{(X + 1) Z_s - Z X_s}{Rb^2} = 0. \tag{9.33}$$

The momentum equation in the axial direction at order ε is

$$u_{0t} + u_0 u_{0s} = -p_{0s} + \frac{(X+1)X_s + ZZ_s}{Rb^2} + \frac{\alpha_s}{Re}\left(u_{oss} + 4u_2 + u_{2\phi\phi}\right) + \frac{1}{Re}\frac{\partial T^0_{ss}}{\partial s}. \tag{9.34}$$

After substituting the expressions u_2 and p_0, the previous equation becomes

$$u_{0t} + u_0 u_{0s} = -\frac{1}{We}\frac{\partial}{\partial s}\left(\frac{\sigma_0}{R_0}\right) + \frac{(X+1)X_s + ZZ_s}{Rb^2} + \frac{3\alpha_s}{Re}\left(u_{0ss} + 2u_{0s}\frac{R_{0s}}{R}\right) + \frac{1}{Re}\left(\frac{1}{R_0^2}\frac{\partial}{\partial s}R_0^2\left(T^0_{ss} - T^0_{nn}\right)\right) + \frac{2\sigma_{0s}}{We\,R_0}. \tag{9.35}$$

From the kinematic condition at order ε, it can be obtained

$$R_{0t} + \frac{u_{0s}}{2}R_0 + u_0 R_{0s} = 0. \tag{9.36}$$

From the extra stress tensor, which is $T_{ss}, T_{sn}, T_{s\phi}, T_{nn}, T_{n\phi}, T_{\phi\phi}$,we have at leading order as follows

$$\frac{\partial T^0_{ss}}{\partial t} + u_0\frac{\partial T^0_{ss}}{\partial s} - 2\frac{\partial u_0}{\partial s}T^0_{ss} = \frac{1}{De}\left(2(1-\alpha_s)\frac{\partial u_0}{\partial s} - T^0_{ss}\right), \tag{9.37}$$

$$\frac{\partial T^0_{nn}}{\partial t} + u_0\frac{\partial T^0_{nn}}{\partial s} + \frac{\partial u_0}{\partial s}T^0_{nn} = \frac{-1}{De}\left((1-\alpha_s)\frac{\partial u_0}{\partial s} + T^0_{nn}\right). \tag{9.38}$$

We have the arc-length at order ε

$$X_s^2 + Z_s^2 = 1. \tag{9.39}$$

The last equation which is the surfactant transport equation at leading order is

$$\Gamma_{0t} + u_0\Gamma_{0s} + \frac{u_{0s}}{2}\Gamma_0 = 0. \tag{9.40}$$

There is another equation related to the surfactant concentration Γ to the surface tension of the liquid-gas interface, which is Szyskowski equation (see Tricot(1997))

$$\sigma = 1 + \beta log(1 - \Gamma), \tag{9.41}$$

where the parameter $\beta = \Gamma_\infty R_g T/\tilde{\sigma}$ is known as the effectiveness of surfactants. However, if we consider that these equations are not independent of t, then $X_{0t} \neq 0$ and $Z_{0t} \neq 0$. This assumption leads to there being some extra unsteady terms in these equations in $E = Z_s X_t - Z_t X_s$ (see Părău *et al.* (2007)). Părău *et al.* (2007) have used that $X(s,t) = X_0(s,t) + \widehat{X}(s,t)$ and $Z(s,t) = Z_0(s,t) + \widehat{Z}(s,t)$ and then solved the linearized equations. They also found the maximum deviation of order 10^{-2} of the perturbation of the steady state centerline. This value is small compared to the $O(1)$ values of $X_0(s)$ and $Z_0(s)$. Therefore, $E \approx 0$ is a very accurate assumption to be taken from the orifice to the break-up point. Experimentally Wong *et al.* (2004) observed that the centerline of the jet is steady, which means $X_{st} \approx 0$, $Z_{st} \approx 0$ and $E \approx 0$.

9.6 Steady State Solutions

From the previous section, we have six variables which are u_0, R_0, X, Z, T^0_{ss} and T^0_{nn}. These variables are functions of s only in the steady state. Hence, the steady state

equations are

$$u_0 u_{0s} = -\frac{\sigma_0}{We}\frac{\partial}{\partial s}\left(\frac{1}{R_0}\right) + \frac{(X+1)X_s + ZZ_s}{Rb^2}$$
$$+\frac{3\alpha_s}{Re}\left(u_{0ss} + 2u_{0s}\frac{R_{0s}}{R}\right) + \frac{1}{Re}\left(\frac{1}{R_0^2}\frac{\partial}{\partial s}\,R_0^2\,(T^0_{ss} - T^0_{nn})\right) + \frac{2\sigma_{0s}}{We\,R_0}, \qquad (9.42)$$

$$u_0\,\frac{\partial T^0_{ss}}{\partial s} - 2\,\frac{\partial u_0}{\partial s}\,T^0_{ss} \;=\; \frac{1}{De}\,\left(2(1-\alpha_s)\frac{\partial u_0}{\partial s} \;-\; T^0_{ss}\right), \qquad (9.43)$$

$$u_0\,\frac{\partial T^0_{nn}}{\partial s} + \frac{\partial u_0}{\partial s}\,T^0_{nn} \;=\; -\frac{1}{De}\,\left((1-\alpha_s)\frac{\partial u_0}{\partial s} \;+\; T^0_{nn}\right), \qquad (9.44)$$

$$(X_s Z_{ss} - X_{ss} Z_s)\left(u_0^2 - \frac{3\alpha_s}{Re}\,u_{0s} - \frac{1}{WeR_0}\right) - \frac{2}{Rb}\,u_0 + \frac{(X+1)Z_s - ZX_s}{Rb^2} = 0, \qquad (9.45)$$

$$X_s^2 + Z_s^2 = 1, \qquad (9.46)$$

$$\frac{u_{0s}}{2}R_0 + u_0 R_{0s} = 0, \qquad (9.47)$$

and

$$\frac{u_{0s}}{2}\Gamma_0 + u_0\Gamma_{0s} = 0. \qquad (9.48)$$

From (9.47) and (9.48), we can notice that R^2u and $\Gamma_0^2 u_0$ are constants. Now, we use the initial conditions $R(0) = 1 = u(0)$ and $\Gamma_0(0) = \zeta$, where ζ is the initial surfactant concentration ($0 \le \zeta \le 1$), we therefore obtain $R^2u = 1$ and $\Gamma_0^2 u_0 = \zeta^2$. After using these

expressions, the previous equations (9.42)-(9.46) become

$$u_0 u_{0s} = -\frac{(1+\beta log(1-\zeta u_0^{\frac{-1}{2}}))}{We}\frac{u_{0s}}{2\sqrt{u_0}} + \frac{\beta\zeta}{2u_0 We}\frac{u_{os}}{(1-\zeta u_0^{\frac{-1}{2}})} + \frac{(X+1)X_s + ZZ_s}{Rb^2}$$
$$+\frac{3\alpha_s}{Re}\left(u_{0ss} - \frac{u_{0s}^2}{u_0}\right) + \frac{1}{Re}\left(\frac{\partial}{\partial s}(T_{ss}^0 - T_{nn}^0) - \frac{u_{0s}}{u_0}(T_{ss}^0 - T_{nn}^0)\right), \tag{9.49}$$

$$u_0\,\frac{\partial T_{ss}^0}{\partial s} - 2\,\frac{\partial u_0}{\partial s}\,T_{ss}^0 = \frac{1}{De}\left(2(1-\alpha_s)\,\frac{\partial u_0}{\partial s} - T_{ss}^0\right), \tag{9.50}$$

$$u_0\,\frac{\partial T_{nn}^0}{\partial s} + \frac{\partial u_0}{\partial s}\,T_{nn}^0 = \frac{-1}{De}\left((1-\alpha_s)\frac{\partial u_0}{\partial s} + T_{nn}^0\right), \tag{9.51}$$

$$(X_s Z_{ss} - X_{ss} Z_s)\left(u_0^2 - \frac{3\alpha_s}{Re}\,u_{0s} - \frac{1}{We}\left(1+\beta log(1-\zeta u_0^{\frac{-1}{2}})\right)\sqrt{u_0}\right) -$$
$$\frac{2}{Rb}\,u_0 + \frac{(X+1)Z_s - ZX_s}{Rb^2} = 0, \tag{9.52}$$

and

$$X_s^2 + Z_s^2 = 1. \tag{9.53}$$

From the equations (9.49)-(9.53), we have five unknowns which are X, Z, u_0, T_{ss}^0 and T_{nn}^0. This system of non-linear differential equations can be solved by using a finite difference scheme. Părău *et al.* (2006, 2007) have used this method and Newton's method to solve the previous equations with viscosity and compared the results with the Runge-Kutta method for the inviscid case and found a good agreement between the two for the steady centerline and radius of the jet. Equations (9.49)-(9.53) with the viscous terms form a very stiff differential equation and are difficult to solve in general even without the viscoelastic

terms. We therefore, given the analysis which is to come, show that the centerline is unaffected at leading order, by viscous terms, using the limit $Re \to \infty$ to solve (9.49)-(9.53) to obtain our centerline. Decent *et al*. (2009) found the centerline of viscous liquid jets by using the limit $Re \to \infty$ to find the steady state solutions. Uddin (2007) and Uddin *et al* (2008b) also used this assumption to find the centerline of non-Newtonian liquid jets with and without surfactants. Therefore, we will use the same assumption in this thesis to find the steady state solutions. In order to show that the centerline is independent of viscosity to leading order, let us consider that the expansions take the form

$$u = u_0(s) + \varepsilon u_1(s,n,\phi) + O(\varepsilon^2),\ v = v_0(s) + \varepsilon v_1(s,n,\phi) + O(\varepsilon^2),$$
$$T_{ss} = T^0_{ss}(s) + \varepsilon T^1_{ss}(s,n,\phi) + O(\varepsilon^2),\ T_{nn} = T^0_{nn}(s) + \varepsilon T^1_{nn}(s,n,\phi) + O(\varepsilon^2),$$
$$R = R_0(s) + \varepsilon R_1(s,n,\phi) + O(\varepsilon^2),\ p = p_0(s) + \varepsilon p_1(s,n,\phi) + O(\varepsilon^2),$$
$$\sigma = \sigma_0(s) + \varepsilon \sigma_1(s,n,\phi) + O(\varepsilon^2),\ \Gamma = \Gamma_0(s) + \varepsilon \Gamma_1(s,n,\phi) + O(\varepsilon^2),$$

and set $w = 0$ which means there is no azimuthal velocity. We substitute them into the the governing equation, and therefore obtain at leading order

$$v_1 = -\frac{n}{2}\frac{du_0}{ds}, \tag{9.54}$$

$$\frac{\partial u_0}{\partial t} + u_0\frac{\partial u_0}{\partial s} = -\frac{\partial p_0}{\partial s} + \frac{1}{Rb^2}\left((X+1)X_s + ZZ_s\right) + \frac{\alpha_s Oh}{\sqrt{We}}\left(\frac{1}{n}\frac{\partial u_1}{\partial n} + \frac{\partial^2 u_1}{\partial n^2} + \frac{1}{n^2}\frac{\partial^2 u_1}{\partial \phi^2}\right) + \frac{Oh}{\sqrt{We}}\left(\frac{\partial T^0_{ss}}{\partial s}\right), \tag{9.55}$$

$$\frac{\partial p_0}{\partial n} = 0 \text{ and } \frac{\partial p_0}{\partial \phi} = 0,$$

$$u_0 \frac{\partial T^0_{ss}}{\partial s} - 2 \frac{\partial u_0}{\partial s} T^0_{ss} = \frac{1}{De} \left(2(1-\alpha_s) \frac{\partial u_0}{\partial s} - T^0_{ss} \right), \tag{9.56}$$

$$u_0 \frac{\partial T^0_{nn}}{\partial s} + \frac{\partial u_0}{\partial s} T^0_{nn} = \frac{-1}{De} \left((1-\alpha_s) \frac{\partial u_0}{\partial s} + T^0_{nn} \right), \tag{9.57}$$

$$-\cos\phi(X_s Z_{ss} - X_{ss} Z_s) u_0^2 = -\frac{\partial p_1}{\partial n} - \frac{2u_0 \cos\phi}{Rb} + \frac{\cos\phi}{Rb^2} \Big((X+1) Z_s - Z X_s \Big), \tag{9.58}$$

$$\sin\phi(X_s Z_{ss} - X_{ss} Z_s) u_0^2 = -\frac{\partial p_1}{\partial n} - \frac{2u_0 \sin\phi}{Rb} - \frac{\sin\phi}{Rb^2} \Big((X+1) Z_s - Z X_s \Big), \tag{9.59}$$

$$u_0 \frac{\partial R_0}{\partial s} = v_1 \text{ on } n = R_0$$

$$p_1 - \frac{2Oh}{\sqrt{We}} \frac{\partial v1}{\partial n} = \frac{\sigma_0}{We} \Big(- \frac{1}{R_0^2} \Big(R_1 + \frac{\partial^2 R_1}{\partial \phi^2} \Big) + \cos\phi(X_s Z_{ss} - X_{ss} Z_s) \Big) \text{ on } n = R_0 \tag{9.60}$$

and

$$\frac{\partial u_1}{\partial n} = u_0 \cos\phi(X_s Z_{ss} - X_{ss} Z_s) + \frac{Oh^{-1}}{We^{\frac{1}{2}}} \frac{\partial \sigma_0}{\partial s}. \tag{9.61}$$

We have

$$u_0 \frac{\partial u_0}{\partial s} + \frac{\partial p_0}{\partial s} - \frac{(X+1)X_s + Z Z_s}{Rb^2} = \frac{\alpha_s Oh}{\sqrt{We}} \Big(\nabla^2_{n,\phi} u_1 \Big) + \frac{Oh}{\sqrt{We}} \frac{\partial T_{ss}}{\partial s}, \tag{9.62}$$

where

$$\nabla^2_{n,\phi} = \frac{1}{n} \frac{\partial}{\partial n} + \frac{\partial^2}{\partial n^2} + \frac{1}{n^2} \frac{\partial^2}{\partial \phi^2}.$$

Suppose that

$$f(s) = \frac{\sqrt{(We)}}{\alpha_s Oh} \Big(u_0 \frac{\partial u_0}{\partial s} + \frac{\partial p_0}{\partial s} - ((X+1)X_s + Z Z_{ss})/Rb^2) \Big) - \frac{1}{\alpha_s} \frac{\partial T^0_{ss}}{\partial s},$$

so that $f(s) = \nabla^2_{n,\phi} u_1$, which is a Neumann problem on a circular domain, where s is a parameter. We determine the solvability condition by multiplying the above equation by $\widehat{u}(s, n, \phi)$ and integrating over the domain S ($0 \leqslant n \leqslant R_0$, $0 \leqslant \phi \leqslant 2\pi$) then we have

$$\iint\limits_S \left(\widehat{u} \nabla^2_{n\phi} u_1 \right) dS = \iint\limits_S \widehat{u} f(s)\, dS,$$

where $\widehat{u}$ satisfies the homogeneous Neumann problem such that

$$\nabla^2_{n\phi} u = 0 \text{ with } \frac{\partial \widehat{u}}{\partial n} = 0 \text{ on } n = R_0.$$

Greens identity gives

$$\iint\limits_S \left(\widehat{u} \nabla^2_{n\phi} u_1 \right) dS = \int\limits_B u \frac{\partial u_1}{\partial n}\, d\Omega_S,$$

where Ω_S is the boundary of S. Then we get

$$\int\limits_0^{2\pi} \int\limits_0^{R_0} \widehat{u} n f(s) dn d\phi = \int\limits_0^{2\pi} \left[\widehat{u} \frac{\partial u_1}{\partial n} \right]_{n=R_0} R_0 d\phi$$

$$= \int\limits_0^{2\pi} [\widehat{u}]_{n=R_0} \left(u_0 \cos\phi (X_s Z_{ss} - X_{ss} Z_s) + \frac{Oh^{-1}}{\sqrt{We}} \frac{\partial \sigma_0}{\partial s} \right) R_0 d\phi$$

$$= \int\limits_0^{2\phi} [\widehat{u}]_{n=R_0} (g(s) \cos\phi + h(s)) R_0 d\phi, \tag{9.63}$$

where $g(s) = u_0(X_s Z_{ss} - X_{ss} Z_s)$ and $h(s) = \frac{Oh^{-1}}{\sqrt{We}} \frac{\partial \sigma_0}{\partial s}$. The general solution to the homogeneous Neumann problem which is bounded in $0 \leqslant n \leqslant R_0$ and is periodic in ϕ with period 2π is $\widehat{u} = \gamma(s)$, which means that this result cannot be a function of the radial or

azimuthal direction. Then we have

$$\gamma(s)R_0g(s)[\sin\phi]_0^{2\pi}+\gamma(s)R_0h(s)[\phi]_0^{2\pi}=\gamma(s)f(s)[\frac{n^2}{2}]_0^{R_0}[\phi]_0^{2\pi}$$

where $R_0\neq 0$, we thus have $f(s)=\frac{2h(s)}{R_0}$ so that

$$f(s)=\frac{1}{Oh\sqrt{We}}\frac{2}{R_0}\frac{\partial\sigma_0}{\partial s}.$$

Then we have

$$\frac{\partial u_0}{\partial t}+u_0\frac{\partial u_0}{\partial s}-\frac{(X+1)X_s+ZZ_s}{Rb^2}=-\frac{\partial p_0}{\partial s}+\frac{2}{R_0We}\frac{\partial\sigma_0}{\partial s}. \tag{9.64}$$

To obtain p_1, we solve the equations (9.58),(9.59) and (9.60),

$$p_1=\frac{\sigma_0 n}{R_0We}\cos\phi(X_sZ_{ss}-X_{ss}Z_s)-\frac{Oh}{\sqrt{We}}\frac{\partial u_0}{\partial s}+h_1(s), \tag{9.65}$$

where $h_1(s)$ is an arbitrary function of s. We can see that there are no viscous terms in the equation (9.64), which means that we obtain the same leading order equations for the trajectory in the inviscid case.

The boundary conditions at the nozzle are $X(0)=Z(0)=Z_s(0)=T^0_{ss}(0)=T^0_{nn}(0)=0$ and $u(0)=X_s(0)=1$. In Figs. 9.2-9.7, we find the jet trajectory, the extra stress tensor T^0_{ss}, T^0_{nn} and the jet radius for different values of ζ and β by using the Runge-Kutta method which is the ODE45 package in MATLAB. In the next paragraph, we will give more explanations about these figures.

In Figs. 9.2 and 9.4, we show the effects of the initial surfactant concentration ζ and the parameter β on trajectories of the liquid jet respectively. From these figures, it can be observed that when ζ and β are increased liquid jets coil slowly. We also plot graphs,

which are in Figs. 9.3 and 9.5 to see the influence of increasing the initial surfactant concentration ζ and the parameter β on the arc-length s. We observe that greater values of these parameters lead to a decrease in the radius of the jet which means that the jet becomes thin when the arc-length s is increased. Moreover, on Figs. 9.6 and 9.7 we find the relationship between the extra stress tensors, which are T^0_{ss} and T^0_{nn} and the arc-length for different values of the parameter β, and these graphs show that when this parameter increases, the extra stress tensors have more effect on the jet. Fig. 9.8 shows the effects of the Rossby number on the surface tension for viscoelastic liquid curved jets and we can see that when rotation rates increase, the surface tension increases.

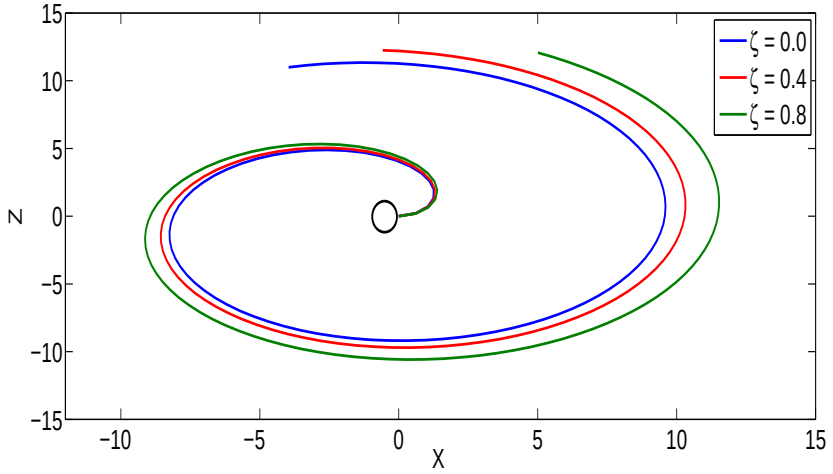

Figure 9.2: The trajectory of rotating liquid jets with the effect of surfactants, which is solved by using the Runge-Kutta method and emerging from an orifice placed at (0,0). The jet curves increase when the initial surfactant concentration increases. The parameters here are $We = 8$, $Rb = 2$, $De = 20$, $\alpha_s = 0.2$ and $\beta = 0.4$.

9.7 Temporal Instability

In this section we consider small temporal perturbations of our steady state solutions as we did in Chapter 6. However, here we linearize the surface tension by using a Taylor

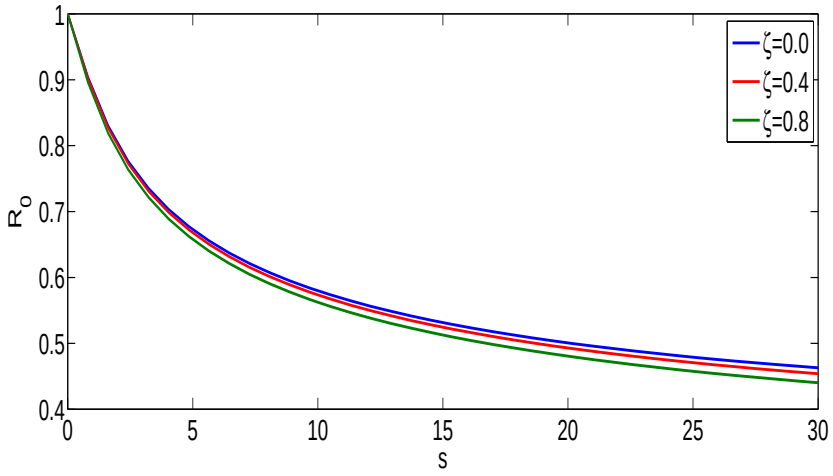

Figure 9.3: The radius of rotating liquid jets with changing the initial surfactant concentration versus the arc-length s. Here we have $We = 8$, $Rb = 2$, $De = 20$, $\alpha_s = 0.2$ and $\beta = 0.4$. It can be seen that increasing the initial surfactant concentration increases the radius of the jet along the jet.

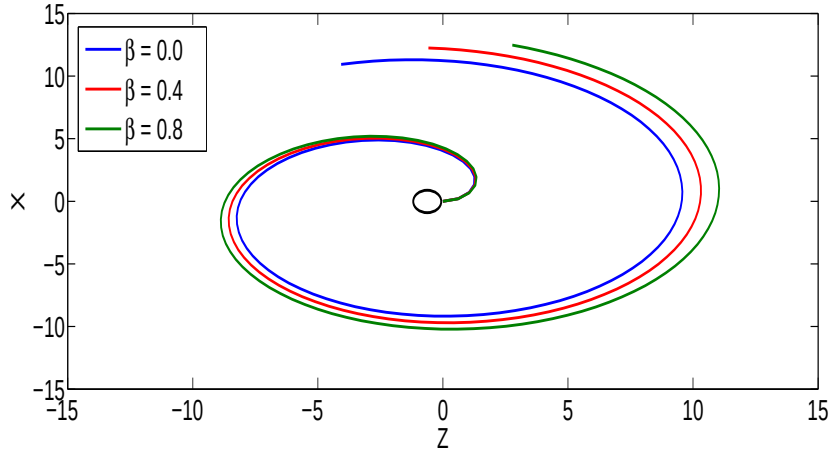

Figure 9.4: The trajectory of rotating liquid jets, which is solved by using the Runge-Kutta method and emerging from an orifice placed at (0,0). The jet curves increase when the parameter β increases. Here we have $We = 8$, $Rb = 2$, $De = 20$, $\alpha_s = 0.2$ and $\zeta = 0.4$.

series to expand Eq. (9.41), we therefore get

$$\begin{aligned} \sigma &= (1 + \beta log(1-\zeta)) + \sigma^{'}(\zeta)(\Gamma - \zeta) \\ &= (1 + \beta log(1-\zeta)) - \frac{\beta}{(1-\zeta)}(\Gamma - \zeta) \\ &= \sigma_e - E\Gamma \end{aligned} \tag{9.66}$$

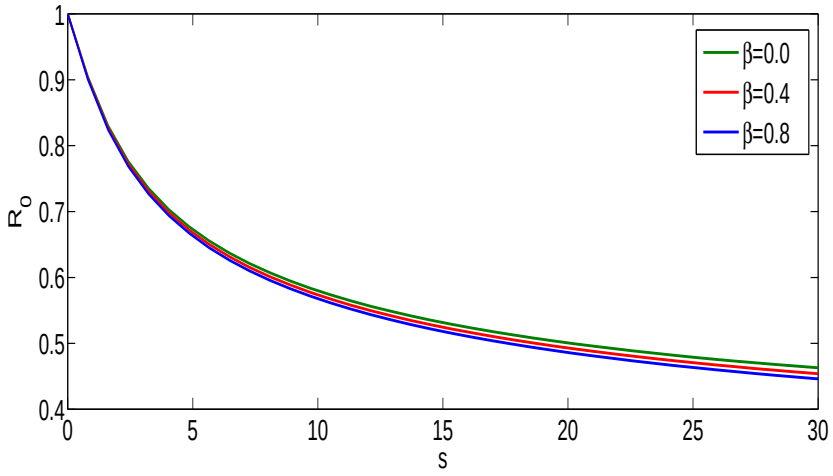

Figure 9.5: The radius of rotating liquid jets with changing the parameter β versus the arc-length s. Here we have $We = 8$, $Rb = 2$, $De = 20$, $\alpha_s = 0.2$ and $\beta = 0.4$. It can be observed that increasing the parameter β increases the radius of the jet along the jet.

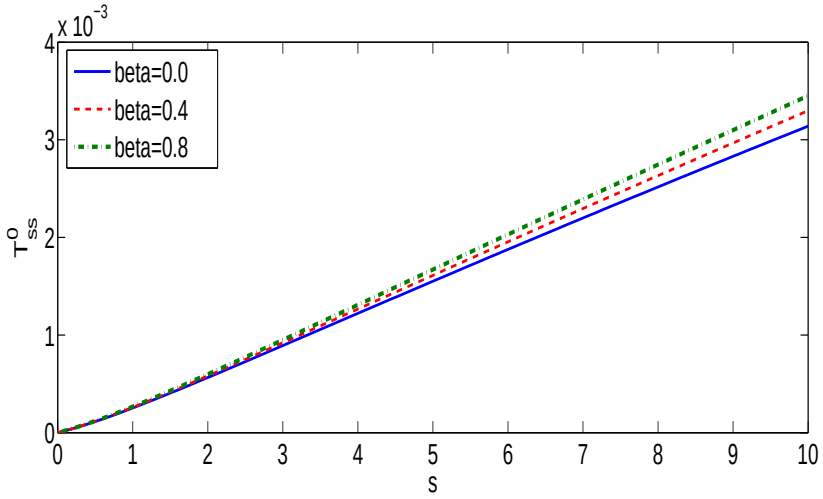

Figure 9.6: The effect of changing the parameter β of a rotating liquid jet on the extra stress tensor T^0_{ss} along the jet.Here we use $We = 8$, $De = 20$, $\beta = 0.4$, $\tilde{\alpha_s} = 0.2$ and $Rb = 2$.

where $\sigma_e = (1 + \beta log(1 - \zeta)) + \frac{\beta\zeta}{(1-\zeta)}$ is the surface tension of the undisturbed liquid jet and $E = \beta/(1 - \zeta)$ is the Gibbs elasticity (see Uddin (2007)).

The radius of the jet is of order a, which is comparable to ε when $s = O(1)$, when we make perturbations along the jet then we consider the travelling wave modes of the form

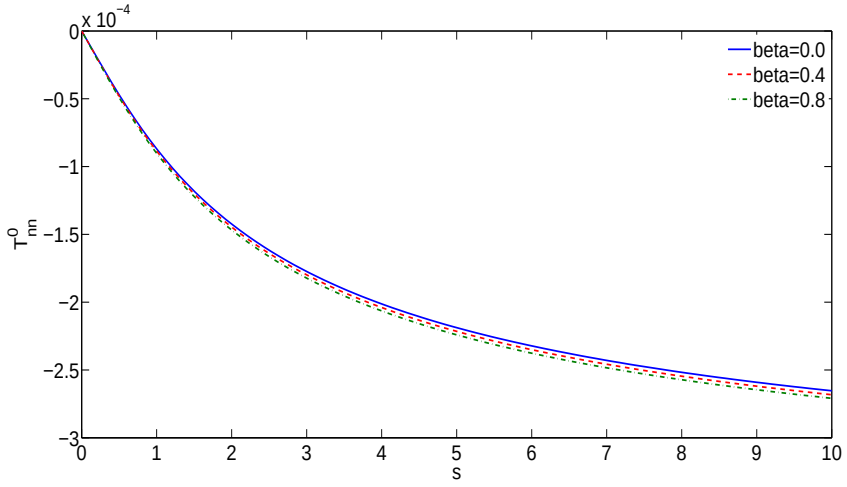

Figure 9.7: The effect of changing the parameter β of a rotating liquid jet on the extra stress tensor T^0_{nn} along the jet.Here we use $We = 8$, $De = 20$, $\beta = 0.4$, $\tilde{\alpha_s} = 0.2$ and $Rb = 2$.

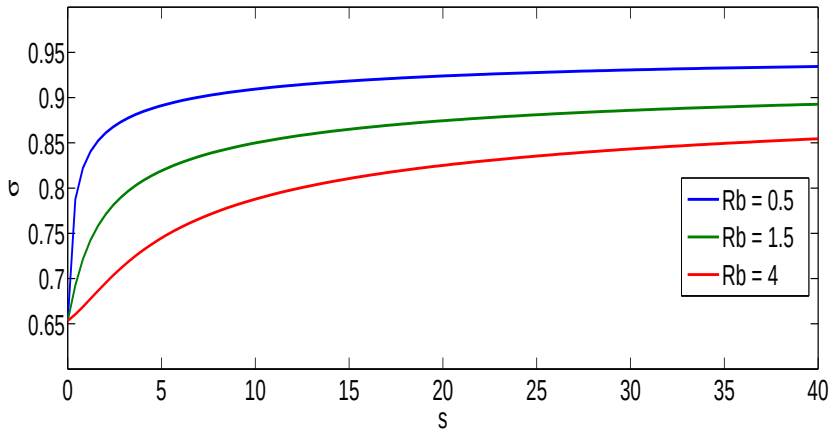

Figure 9.8: The relationship between the surface tension and the arc-length s of a rotating viscoelastic liquid jet. Here we use $We = 10$, $De = 20$, $\beta = 0.25$ and $\alpha_s = 0.20$.

$$(u, R, T_{ss}, T_{nn}, \Gamma) = (u_0, R_0, T^0_{ss}, T^0_{nn}, \Gamma_0) + \delta(\widehat{u}, \widehat{R}, \widehat{T}_{ss}, \widehat{T}_{nn}, \widehat{\Gamma})\, exp(i\kappa\bar{s} + \omega\bar{t}), \quad (9.67)$$

where $\overline{s} = s/\varepsilon$ is small length scales, $\overline{t} = t/\varepsilon$ is small time scales, $k = k(s)$ and $\omega = \omega(s)$ are the wavenumber and frequency of the disturbances and δ is a small constant which is $0 \ll \delta \ll \varepsilon^2$ (see Uddin (2007)). We have to use the full expression for the mean curvature (see Lee (1974) and Eggers (1997)) to prevent instability to waves with zero wavelength which is

$$\frac{1}{We}\left(\frac{1}{R(1+\varepsilon^2\,R_s^2)^{\frac{1}{2}}} - \frac{\varepsilon^2\,R_{ss}}{(1+\varepsilon^2\,R_s^2)^{\frac{3}{2}}}\right).$$

The axial equation of motion becomes

$$u_t + u_0 u_{0s} = -\frac{1}{We}\frac{\partial}{\partial s}\left(\sigma\left(\frac{1}{R(1+\varepsilon^2\,R_s^2)^{\frac{1}{2}}} - \frac{\varepsilon^2\,R_{ss}}{(1+\varepsilon^2\,R_s^2)^{\frac{3}{2}}}\right)\right) + \frac{(X+1)X_s + ZZ_s}{Rb^2}$$
$$+ \quad \frac{3\alpha_s}{Re}\left(u_{0ss} + 2u_{0s}\frac{R_{0s}}{R}\right) + \frac{1}{Re}\left(\frac{1}{R_0^2}\frac{\partial}{\partial s}\,R_0^2\,(T_{ss}^0 - T_{nn}^0)\right), \tag{9.68}$$

$$\frac{\partial T_{ss}^0}{\partial t} + u_0\,\frac{\partial T_{ss}^0}{\partial s} - 2\,\frac{\partial u_0}{\partial s}\,T_{ss}^0 = \frac{1}{De}\left(2(1-\alpha_s)\,\frac{\partial u_0}{\partial s} - T_{ss}^0\right), \tag{9.69}$$

$$\frac{\partial T_{nn}^0}{\partial t} + u_0\,\frac{\partial T_{nn}^0}{\partial s} + \frac{\partial u_0}{\partial s}\,T_{nn}^0 = -\frac{1}{De}\left((1-\alpha_s)\frac{\partial u_0}{\partial s} + T_{nn}^0\right). \tag{9.70}$$

9.8 Dispersion Relation

The perturbation equations (9.67) are now substituted into the equations (9.68), (9.36), (9.69), (9.70) and (9.40), which has the following matrix

$$\begin{pmatrix} \frac{3k^2\tilde{\alpha_s}}{Re}+\omega+iku_0 & -\frac{ik\sigma_0}{We}\left(\frac{1}{R_0^2}-k^2\right)+\frac{2ik}{R_0Re}(T^0_{ss}-T^0_{nn}) & \frac{ik}{Re} & -\frac{ik}{Re} & \frac{ikE}{We\,R_0} \\ \frac{ikR_0}{2} & \omega+iku_0 & 0 & 0 & 0 \\ -2ikT^0_{ss}-\frac{2ik}{De} & 0 & \omega+iku_0 & 0 & 0 \\ ikT^0_{nn}+\frac{ik}{De} & 0 & 0 & \omega+iku_0 & 0 \\ \frac{ik\Gamma_0}{2} & 0 & 0 & 0 & \omega+iku_0 \end{pmatrix}$$

There is a new scaling for the viscosity ratio which is $\tilde{\alpha_s}=\frac{\alpha_s}{\varepsilon}$. Without this new scaling, we cannot bring the viscous term into the equations which derived the dispersion relation. We mentioned earlier, $\alpha_s+\alpha_p=1$, where α_s and α_p are the solvent viscosity and the polymeric viscosity respectively. After substituting the new scaling, the last equation becomes $\varepsilon\tilde{\alpha_s}+\alpha_p=1$, which means that $\alpha_p \gg \alpha_s$. However, both the solvent viscosity and the polymeric viscosity are very small $\mu_s, \mu_p \ll 1$. Now, we find non-trivial solutions for the above system and, therefore, we obtain

$$\left(\omega+iku_0\right)^2+\frac{3k^2\tilde{\alpha_s}}{Re}\left(\omega+iku_0\right)-\frac{k^2\sigma_0R_0}{2We}\left[\left(\frac{1}{R_0^2}-k^2\right)-\frac{2We}{R_0Re}\left(T^0_{ss}-T^0_{nn}\right)\right]- \frac{k^2}{Re}\left(2T^0_{ss}+T^0_{nn}+\frac{3}{De}\right)+\frac{k^2E\Gamma_0}{2We\,R_0}=0, \tag{9.71}$$

here $\omega=\omega_r+i\omega_i$, where ω_r is the growth rate of disturbances and ω_i is the wavenumber of disturbances. Then

$$\omega_r^2+\frac{3k^2\tilde{\alpha_s}}{Re}\omega_r-\frac{k^2\sigma_0R_0}{2We}\left(\frac{1}{R_0^2}-k^2-\frac{2We}{R_0Re}\left(T^0_{ss}-T^0_{nn}\right)\right) -\frac{k^2}{Re}\left(2T^0_{ss}+T^0_{nn}+\frac{3}{De}\right)+\frac{k^2E\Gamma_0}{2We\,R_0}=0, \tag{9.72}$$

which becomes

$$\omega_r = \frac{-3k^2\tilde{\alpha_s}}{2Re} + \frac{k}{2}\sqrt{\frac{2\sigma_0}{R_0We}\left(1-(kR_0)^2-\frac{2We}{R_0Re}\right)+\frac{4}{Re}\left(2T^0_{ss}+T^0_{nn}+\frac{3}{De}\right)+\left(\frac{3k\tilde{\alpha_s}}{Re}\right)^2-\frac{2E\Gamma_0}{WeR_0}}, \tag{9.73}$$

where

$$\frac{2\sigma_0}{R_0We}\left(1-(kR_0)^2-\frac{2We}{R_0Re}\right)+\frac{4}{Re}\left(2T^0_{ss}+T^0_{nn}+\frac{3}{De}\right)+\left(\frac{3k\tilde{\alpha_s}}{Re}\right)^2-\frac{2E\Gamma_0}{WeR_0} > 0,$$

we differentiate Eq. 9.73 with respect to k to find the most unstable wavenumber $k = k^*$ which is given

$$k^* = \frac{\sqrt{\frac{R_0GWe}{2}-2B+(\sigma_0-\Gamma_0E)}}{\sqrt{\sqrt{2R_0^3\sigma_0}\left(3\tilde{\alpha_s}\frac{\sqrt{We}}{Re}+\sqrt{2\sigma_0R_0}\right)}}, \tag{9.74}$$

where $B = T^0_{ss} - T^0_{nn}$, $G = \frac{4}{\tilde{\alpha_s}Re}\left(2T^0_{ss}+T^0_{nn}+\frac{3}{De}\right)$. For temporal instability, the growth rate ω_r is positive which happens when $0 < kR < 1$ where $k = k^*$, and R_0 found from the steady state solutions. When $De = 0$ and $T^0_{ss} = T^0_{nn} = 0$ the dispersion relation is

$$k^* = \frac{(\sigma_0-\Gamma_0E)^{\frac{1}{2}}}{\sqrt{\sqrt{2R_0^3\sigma_0}\left(3Oh+\sqrt{2\sigma_0R_0}\right)}}, \tag{9.75}$$

where $Oh = \frac{\sqrt{We}}{Re}$ which is the same as for Newtonian liquid jets with surfactant, as found by Uddin (2007).

9.9 Discussion

In order to determine the break-up of liquid jets from the linear instability analysis, we seek to find the largest value of the growth rate which corresponds to the wavenumber of k (referred as k^* in this work) from the nozzle to downstream the jet. However, as mentioned earlier in this thesis, we can use the linear instability to find the size of main droplets, but not satellite droplets. From the dispersion relation (9.72), we find the wavenumber (k^*) and the growth rate of the most unstable mode against the arc-length s for a number of cases;

in Fig. 9.9 we plot the growth rate of a viscoelastic liquid jet with surfactant against the wavenumber for different distances from the nozzle. It can be noticed that at the nozzle (meaning $s = 0$) the growth rate starts to increase with distance along the jet. The effect of surfactants on viscoelastic liquid curved jets has been examined in Fig. 9.10. We can see from this figure that when we increase the initial surfactant concentration ζ the growth rate decreases. This is a result to be expected as surfactants dampen or reduce the growth of disturbances.

Figs. 9.11 and 9.12 show that when the wavenumber of the most unstable mode k^* increases along the liquid jet, rotation rates are increased (meaning that Rb decreases). In addition, we can see in Fig. 9.13 that when we increase the effectiveness of surfactants β, the wavenumber of the most unstable mode of viscoelastic liquid curved jets is decreased, which means that when the parameter $\beta = 0.25$ the most unstable mode k^* is equal 0.6, whereas with $\beta = 0.5$ the most unstable mode is equal 0.50 at the nozzle. Similarly, we do the same thing for the growth rate of the most unstable mode which can be seen in Figs. 9.14-9.16, so that in Figs. 9.14 and 9.15, we show the effect of changing the parameter β for two different values (0.25 and 0.5) on the maximum growth rate. We make a comparison to see how these two values of β affect the growth rate of the most

unstable mode and we find that when the parameter β is increased the maximum growth rate is decreased (see Fig. 9.16). In Figs. 9.17 and 9.18, we study the effect of the Reynolds number Re on the viscoelastic liquid curved jets with surfactants where the parameter β is fixed. From these figures, it can be observed that when we decrease the Reynolds number the wavenumber and the growth rate of the most unstable mode are decreased and this means that the liquid becomes more viscous and it will take more time to break-up.

Here we plot graphs to see the relationship between the maximum growth rate and the wavenumber of the most unstable mode against the arc-length s for two different values of the Deborah number ($De = 5$ and 20) which are in Figs 9.19 and 9.20. It can be observed from these graphs that when the Deborah number is increased the growth rate and the wavenumber are increased.

When we increase the viscosity ratio $\tilde{\alpha_s}$ the maximum wavenumber and the growth rate are decreased which means the liquid is more elastic. These results are shown in Figs. 9.21 and 9.22. In Figs. 9.23 and 9.24 show that when we increase the initial surfactant concentration ζ and the parameter β is fixed the growth rate and the wavenumber of the most unstable mode are decreased which means the liquid becomes thicker along the arc-length s.

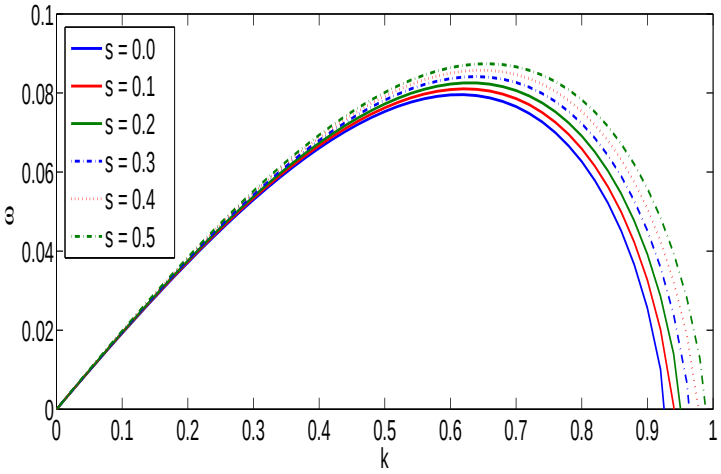

Figure 9.9: Graph showing the growth rate versus the wavenumber of viscoelastic liquid curved jets with surfactants from a nozzle at $s = 0$ to $s = 0.5$ along the jet. The other parameters here are $We = 10$, $Re = 1000$, $Rb = 2$, $\zeta = 0.2$, $\beta = 0.5$, $De = 20$ and $\tilde{\alpha_s} = 20$.

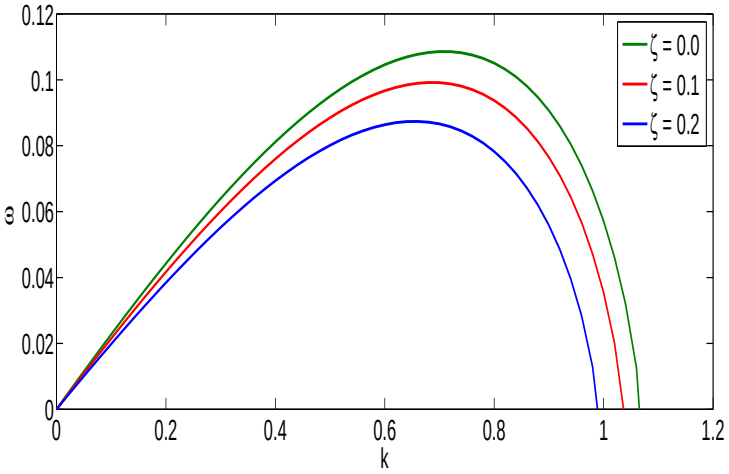

Figure 9.10: Graph showing the growth rate versus the wavenumber of viscoelastic liquid curved jets with surfactants at the nozzle for different values of the initial surfactant concentration. The other parameters here are $We = 10$, $Re = 1000$, $Rb = 2$, $\zeta = 0.2$, $\beta = 0.5$, $De = 20$ and $\tilde{\alpha_s} = 20$.

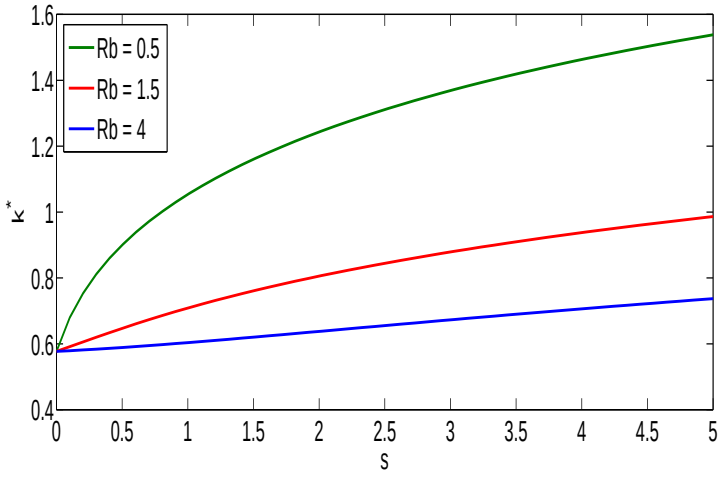

Figure 9.11: The wavenumber of the most unstable mode k^* versus the arc-length s for different values of the Rossby number. The other parameters here are $We = 15$, $Re = 1000$, $\zeta = 0.5$, $De = 20$, $\tilde{\alpha}_s = 20$ and $\beta = 0.25$.

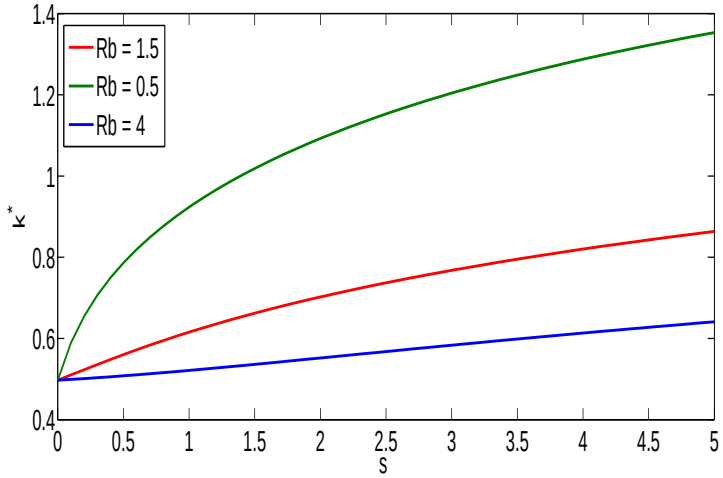

Figure 9.12: The wavenumber of the most unstable mode k^* versus the arc-length s for different values of the Rossby number. The other parameters here are $We = 15$, $Re = 1000$, $\zeta = 0.5$, $De = 20$, $\tilde{\alpha}_s = 20$ and $\beta = 0.5$.

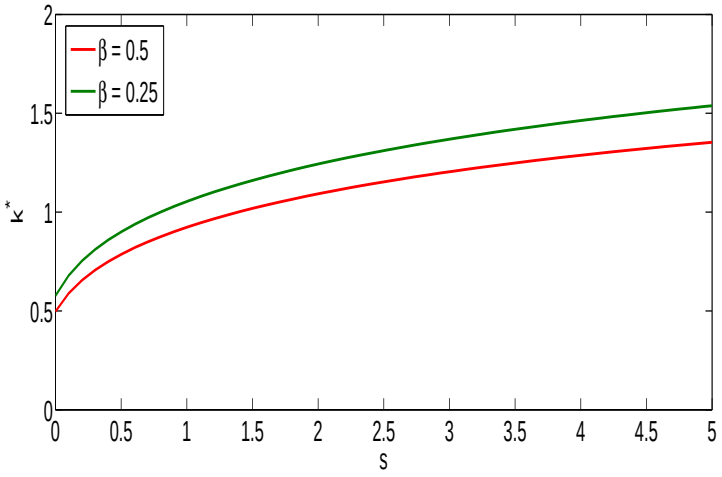

Figure 9.13: The wavenumber of the most unstable mode k^* versus the arc-length s for two different values of the parameter β. The other parameters are $We = 15$, $Re = 1000$, $\zeta = 0.5$, $De = 20$, $\tilde{\alpha}_s = 20$ and $Rb = 0.5$.

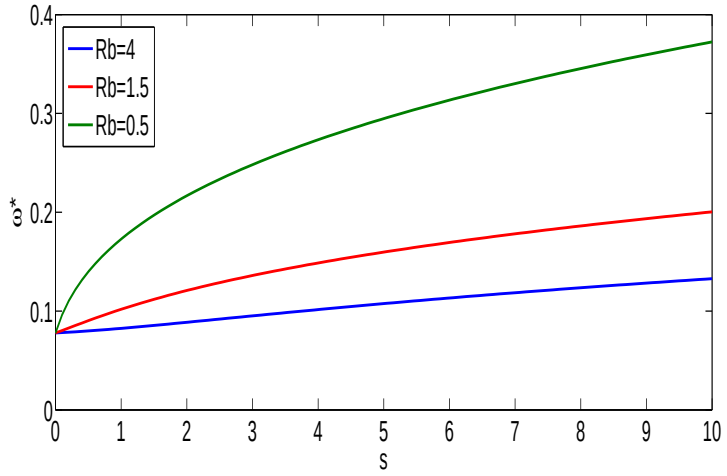

Figure 9.14: The maximum growth rate ω^* versus the arc-length s for different values of the Rossby number. The other parameters here are $We = 15$, $Re = 1000$, $\zeta = 0.5$, $De = 20$, $\tilde{\alpha}_s = 20$ and $\beta = 0.25$.

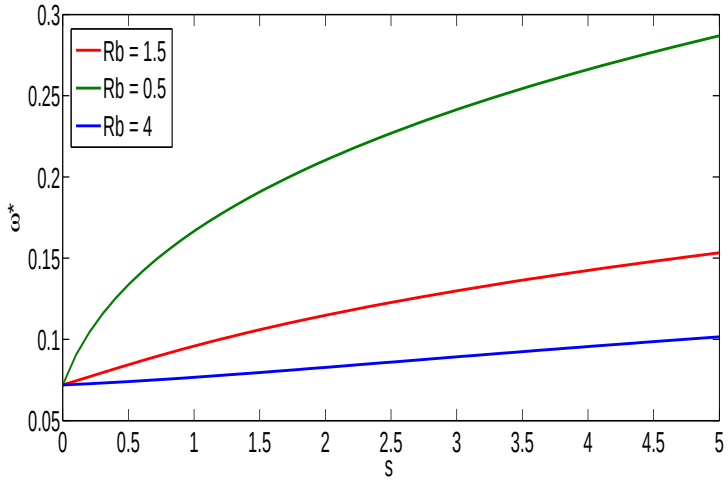

Figure 9.15: The maximum growth rate ω^* versus the arc-length s for two different values of the parameter β . The other parameters here are $We = 15$, $Re = 1000$, $\zeta = 0.5$, $De = 20$, $\tilde{\alpha_s} = 20$ and $\beta = 0.5$.

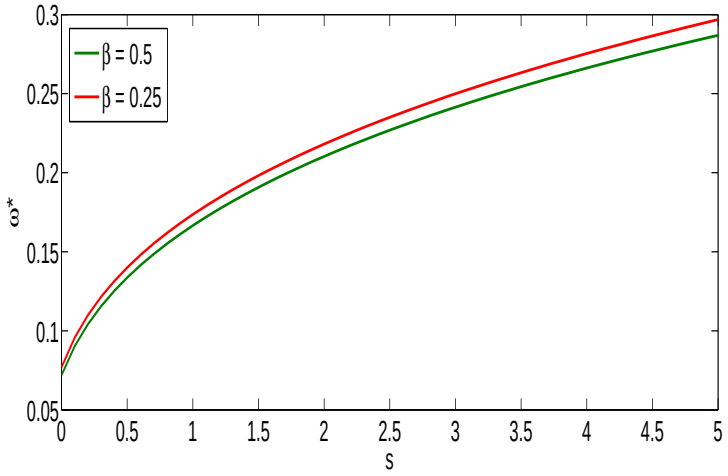

Figure 9.16: The maximum growth rate ω^* versus the arc-length s for two different values of the Rossby number. The other parameters here are $We = 15$, $Re = 1000$, $\zeta = 0.5$, $De = 20$, $\tilde{\alpha_s} = 20$ and $Rb = 0.5$.

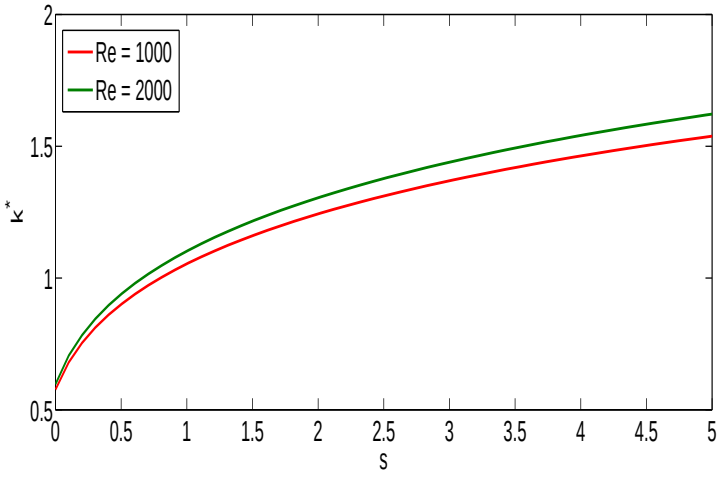

Figure 9.17: The maximum wavenumber k^* versus the arc-length s for two different values of the Reynolds number. The other parameters here are $We = 15$, $Rb = 0.5$, $\zeta = 0.5$, $De = 20, \tilde{\alpha_s} = 20$ and $\beta = 0.25$.

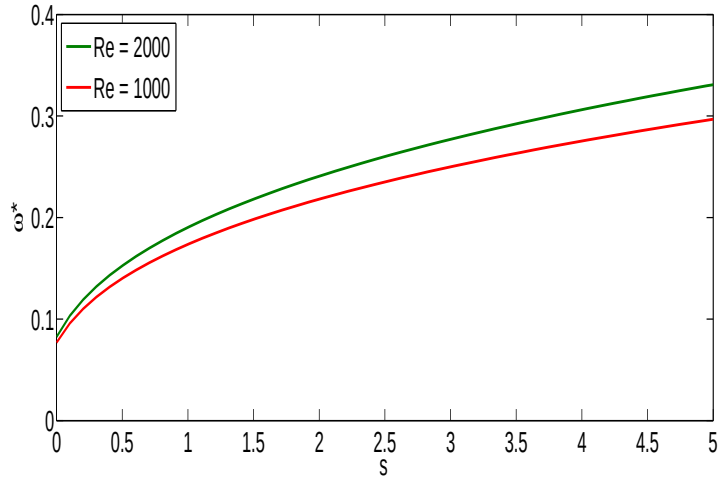

Figure 9.18: The maximum growth rate ω^* versus the arc-length s for two different values of the Reynolds number. The other parameters here are $We = 15$, $Rb = 0.5$, $\zeta = 0.5$, $De = 20$, $\tilde{\alpha_s} = 20$ and $\beta = 0.25$.

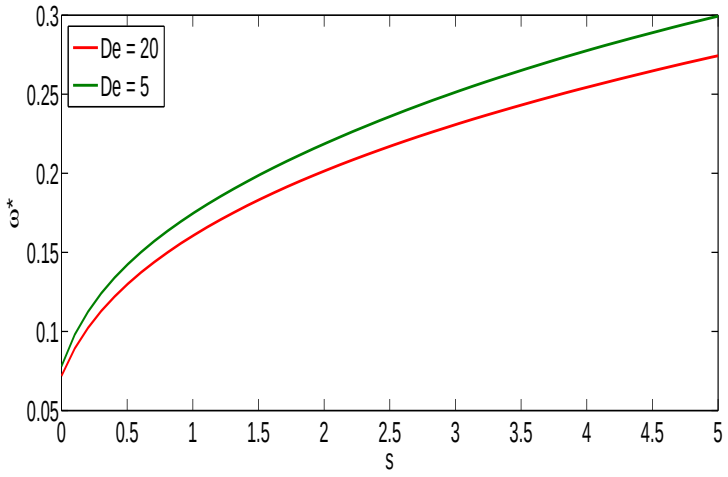

Figure 9.19: Graph showing the relationship between the maximum growth rate ω_r^* and the arc-length s for viscoelastic liquid curved jets with surfactants for two different values of the Deborah De, where the other parameters here are $We = 15$, $Re = 1000$, $\zeta = 0.5$, $Rb = 0.5$, $\tilde{\alpha_s} = 20$ and $\beta = 0.25$.

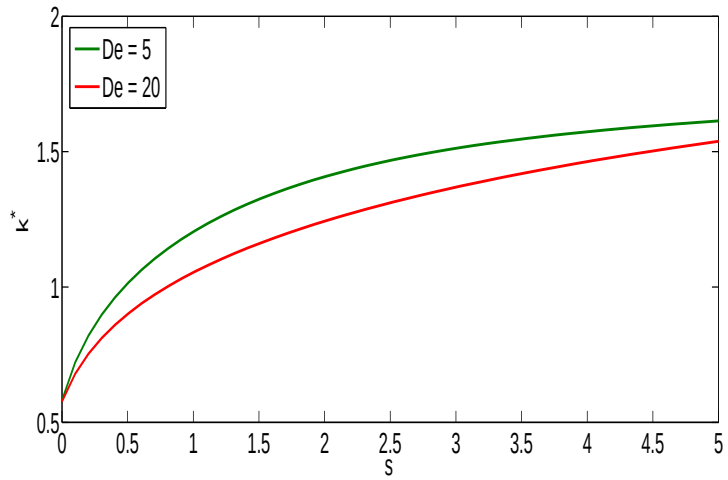

Figure 9.20: Graph showing the relationship between the wavenumber of the most unstable k^* and the arc-length s for viscoelastic liquid curved jets with surfactants for two different values of the Deborah number De , where the other parameters here are $We = 15, Re = 1000, \zeta = 0.5, Rb = 0.5, \tilde{\alpha_s} = 20$ and $\beta = 0.25$.

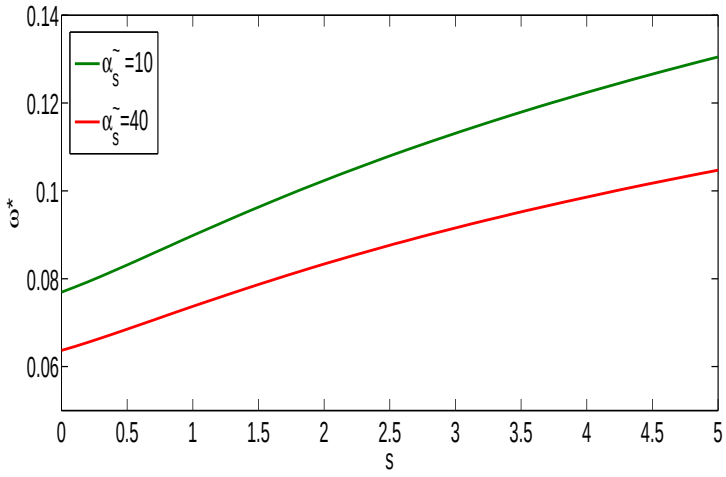

Figure 9.21: Graph showing the relationship between the growth rate of the most unstable mode ω_r^* and the arc-length s for viscoelastic liquid curved jets with surfactants for two different values of the viscosity ratio $\tilde{\alpha_s}$, where the other parameters here are $We = 15, Re = 1000, \zeta = 0.5, De = 20$ and $\beta = 0.25$.

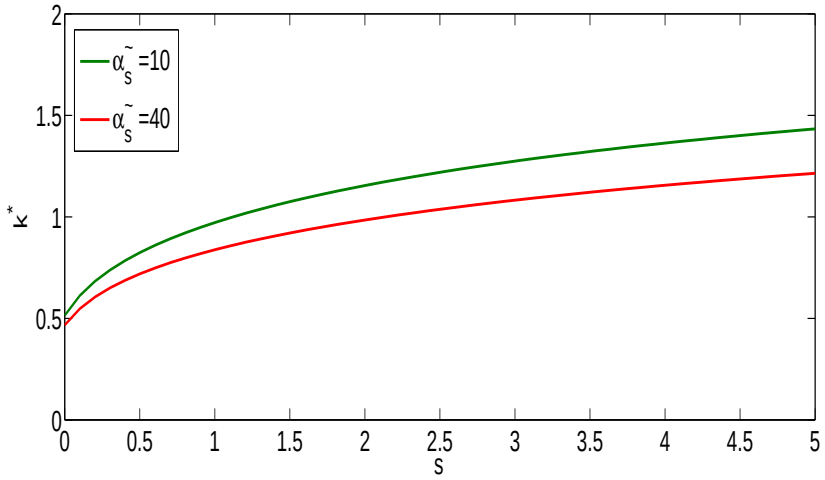

Figure 9.22: Graph showing the wavenumber of the most unstable mode k^* and the arc-length s of viscoelastic rotating liquid jets with surfactants for two different values of the viscosity ratio $\tilde{\alpha_s}$, where the other parameters here are $We = 15, Re = 1000, \zeta = 0.5, De = 20$ and $\beta = 0.25$.

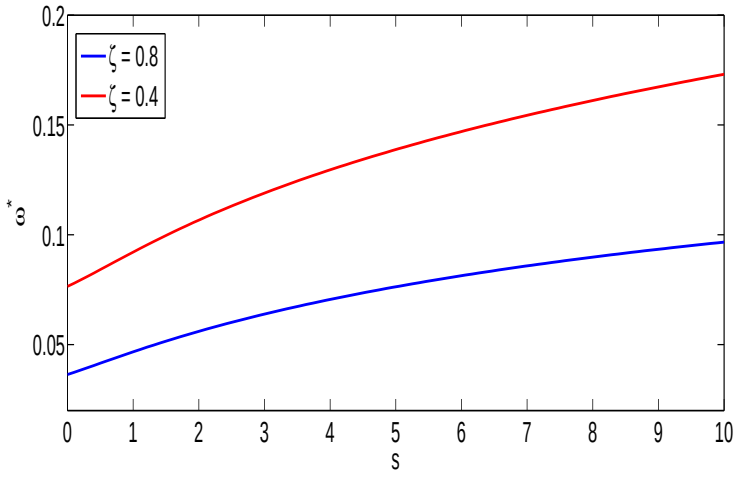

Figure 9.23: Graph showing the growth rate of the most unstable mode ω^* and the arc-length s of viscoelastic rotating liquid jets with surfactants for two different values of the initial surfactant concentration ζ, where the other parameters here are $We = 15$, $Re = 1000$, $\zeta = 0.5$, $De = 20$ and $\beta = 0.5$.

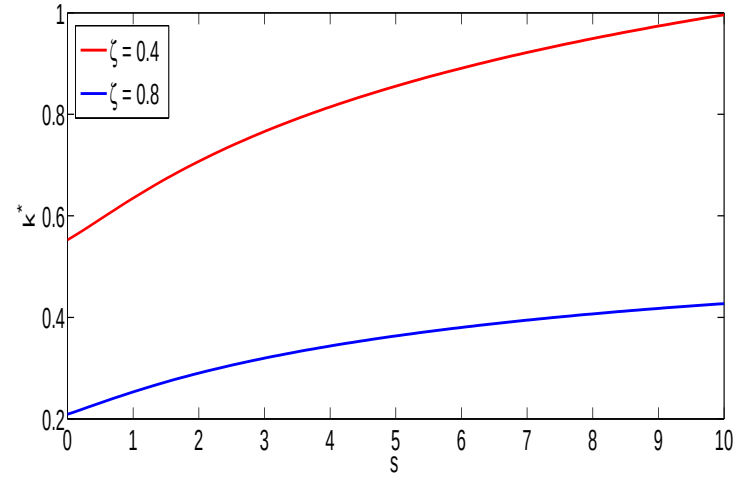

Figure 9.24: Graph showing the wavenumber of the most unstable mode k^* and the arc-length s of viscoelastic rotating liquid jets with surfactants for two different values of the initial surfactant concentration ζ, where the other parameters here are $We = 15$, $Re = 1000$, $\zeta = 0.5$, $De = 20$ and $\beta = 0.5$.

9.10 Nonlinear Temporal Solutions

Linear instability analysis predicts that liquid jets break-up and produce uniform drop sizes along the axis of approximately the same wavelength of initial disturbances. However, it can be observed that a number of smaller satellite droplets appeared in this case which are not equal in size. Therefore, we use nonlinear temporal analysis to examine the break-up length and the formation of the satellite droplets. We replace the leading order pressure term $p_0 = \frac{\sigma}{We}\frac{1}{R_0}$ with the expression for the full curvature term which contains only R_0 and is not ϕ-dependent, namely

$$p = \frac{\sigma}{We}\left[\frac{1}{R_0(1+\varepsilon^2 R_{0s}^2)^{1/2}} - \frac{\varepsilon^2 R_{0ss}}{(1+\varepsilon^2 R_{0s}^2)^{3/2}}\right]. \tag{9.76}$$

For simplicity, we denote $A = A(s,t)$, where $A(s,t) = R^2(s,t)$ and $G = \Gamma_0^2$; then we rewrite our equations (9.36), (6.38), (9.39) and (9.41) as

$$\frac{\partial u}{\partial t} = -\left(\frac{u^2}{2}\right)_s - \frac{1}{We}\frac{\partial}{\partial s}\left(\sigma\frac{4(2A+(\varepsilon A_s)^2 - \varepsilon^2 A A_{ss})}{(4A+(\varepsilon A_s)^2)^{3/2}}\right) + \frac{(X+1)X_s + ZZ_s}{Rb^2} + \frac{2\sigma_s}{A^{\frac{1}{2}}We} + \frac{3\alpha_s}{Re}\frac{(Au_s)_s}{A} + \frac{1}{Re}\frac{\left(A(T_{ss}-T_{nn})\right)_s}{A}, \tag{9.77}$$

$$\frac{\partial T_{ss}}{\partial t} = -\frac{\partial}{\partial s}(uT_{ss}) + 3\frac{\partial u}{\partial s}T_{ss} + \frac{1}{De}\left(2(1-\alpha_s)\frac{\partial u}{\partial s} - T_{ss}\right), \tag{9.78}$$

$$\frac{\partial T_{nn}}{\partial t} = -\frac{\partial}{\partial s}(uT_{nn}) - \frac{1}{De}\left((1-\alpha_s)\frac{\partial u}{\partial s} + T_{nn}\right), \tag{9.79}$$

$$\frac{\partial A}{\partial t} = -\frac{\partial}{\partial s}(Au), \tag{9.80}$$

$$\frac{\partial G}{\partial t} = -\frac{\partial}{\partial s}(Gu). \tag{9.81}$$

We solve this nonlinear system of equations as we did in section 6 for the steady state by using the initial conditions at $t = 0$ which are

$$A(s, t = 0) = R_0^2(s),\ u(s, t = 0) = u_0(s), G(s, o) = \Gamma_0^2(s), T_{ss}(s, t = 0) = 0,\ T_{nn}(s, t = 0) = 0.$$

At the nozzle, we use upstream boundary conditions

$$u(0, t) = 1 + \delta \sin\left(\frac{\kappa t}{\varepsilon}\right),\ \Gamma(0, t) = \zeta,\ A(0, t) = 1,$$

where κ is a non-dimensional wavenumber of the perturbation of frequency and δ (of which we used a small size) is the amplitude of the initial non-dimensional velocity disturbance. In the calculation, we have used the value of $\varepsilon\,(= \frac{a}{s_0})$ which can be measured from experiments using $\varepsilon = 0.01$. This value is the same as found in experiments and industrial problems (see Wong *et al* (2004)).

9.11 Results and Discussions

A profile has been plotted (Fig. 9.25) to show the effect of increasing the concentration of initial surfactants on the break-up of viscoelastic liquid curved jets. From this profile we see that when we enhance the initial surfactant concentration, the liquid jet becomes longer in terms of breaking up. In Fig. 9.26 we make a compression to see the effect of adding surfactant on the break-up of viscoelastic liquid curved jets. It can be observed that adding surfactants on liquid jets delay the break-up of viscoelastic liquid jets. These results are the same found by Uddin (2007) for spiralling liquid jets with surfactants. Furthermore, we plot profiles to see the effects of increasing the viscosity ratio on viscoelastic curved jets with surfactants, which is in Fig. 9.27. We can see from these

profiles that when we increase the viscosity ratio, the break-up length will increase. In Fig. 9.28 we make a profile to see the effect of rotating liquid jets with surfactant for two values of rotation rates which are high rotation rates ($Rb = 2$) and very small rotation rates ($Rb = 100$, meaning straight liquid jets) and we can see that when we have high rotation rates, viscoelastic liquid curved jets with surfactants will break up later than straight jets.

A graph has been plotted to check the accuracy of the numerical simulation for various ds and various mesh points M (see Fig. 9.29). Moreover, we discuss the break-up length versus the Rossby number Rb with and without adding surfactants (see Fig. 9.30). From this figure we notice that when rotation rates are increased the break-up increases and when we have a surfactant on liquid jets that leads to an increase in the break-up as well. In Fig. 9.31 we show that when we add surfactants on viscoelastic liquid curved jets satellite droplet sizes are decreased. It can be also observed that decreasing rotation rates imply to small satellite droplet sizes and this result agrees with Parau *et al.* (2007). Furthermore, we plot a graph (Fig. 9.32) to see variations of wavenumber κ on main droplet sizes for viscoelastic jets with and without surfactants. From this figure we find that increasing the wavenumber decreases main droplet sizes and we also see that adding surfactants to liquid curved jets leads to an increase in the main droplet size of viscoelastic liquid curved jets. In Fig. 9.33 we see that when we have viscoelastic liquid curved jets with surfactant this leads to an increase in satellite droplet sizes with a variation in the wavenumber. From this figure as well, when we decrease the wavenumber, satellite droplet sizes are increased either with surfactants or without it for liquid jets. We plot a graph (Fig. 9.34) to find the break-up length of viscoelastic liquid curved jets with surfactants with making the wavenumber variation. From this figure we notice that when we add surfactants to liquid jets this leads to an increase in the break-up length.

In Fig. 9.35 we observe that increasing the viscosity ratio α_s makes the liquid jet have a

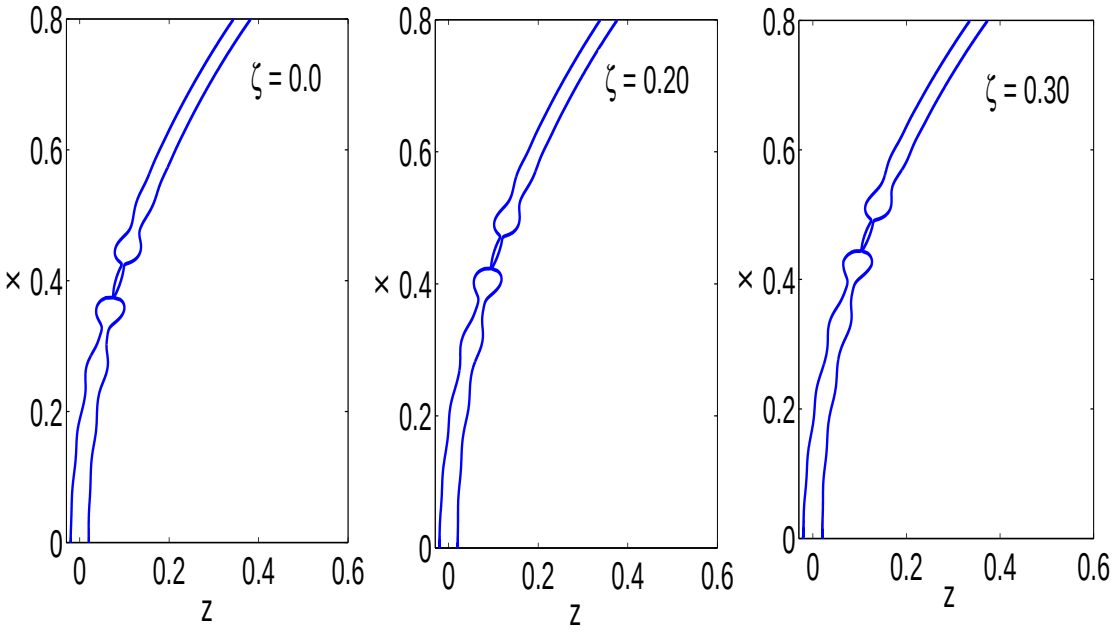

Figure 9.25: Graph showing viscoelastic liquid curved jets with surfactants by changing the initial surfactant concentration ζ. The parameters here are $Re = 2000$, $We = 10$, $Rb = 2$, $k = 0.7$, $De = 20$, $\delta = 0.01$, $\beta = 0.5$ and $\alpha_s = 0.20$.

longer break-up length both in the presence of surfactants and without it. Moreover, we plot a graph (Fig. 9.36) to find main droplet sizes when the viscosity ratio is varied and we see that main droplet sizes are not changed too much. However, In Fig. 9.37 it can be noticed that satellite droplet sizes increase when the viscosity ratio is increased.

Now we turn our attention to study the effectiveness of surfactants (β). In order to do this, we see in Fig. 9.38 that increasing the parameter β leads to an increase in the break-up length. In addition, the relationship between main droplet sizes and the parameter β is shown in Fig. 9.39 and we see that high rotation rates imply to increase the main droplet sizes. In Fig. 9.40 we show that when the rotation rates are high, satellite droplet sizes decrease with increasing the parameter β. These results agree with Uddin (2007).

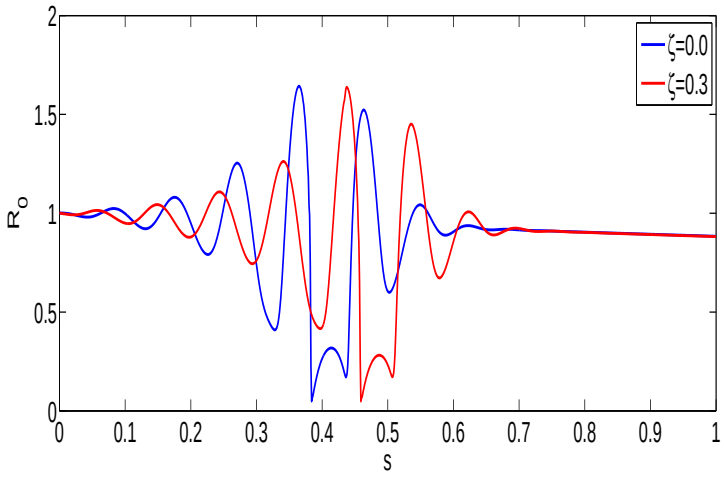

Figure 9.26: Graph showing the relationship between the radius R_0 and the distance along the jet s with and without surfactants for viscoelastic liquid curved jets. The parameters here are $Re = 2000$, $We = 10$, $Rb = 2$, $k = 0.7$, $De = 20$, $\delta = 0.01$, $\beta = 0.5$ and $\alpha_s = 0.20$.

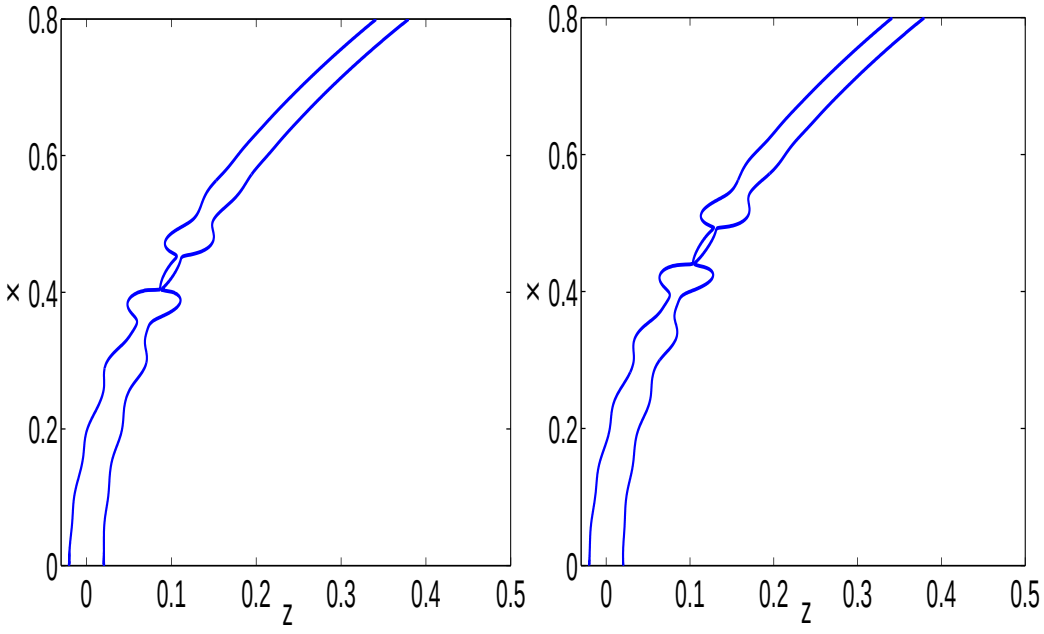

Figure 9.27: Rotating viscoelastic liquid jets with surfactants when the viscosity ratio α_s is varied (0.20 and 0.60 respectively). The parameters here are $Re = 2000$, $We = 10$, $Rb = 2$, $k = 0.7$, $De = 20$, $\delta = 0.01$, $\beta = 0.5$ and $\zeta = 0.1$.

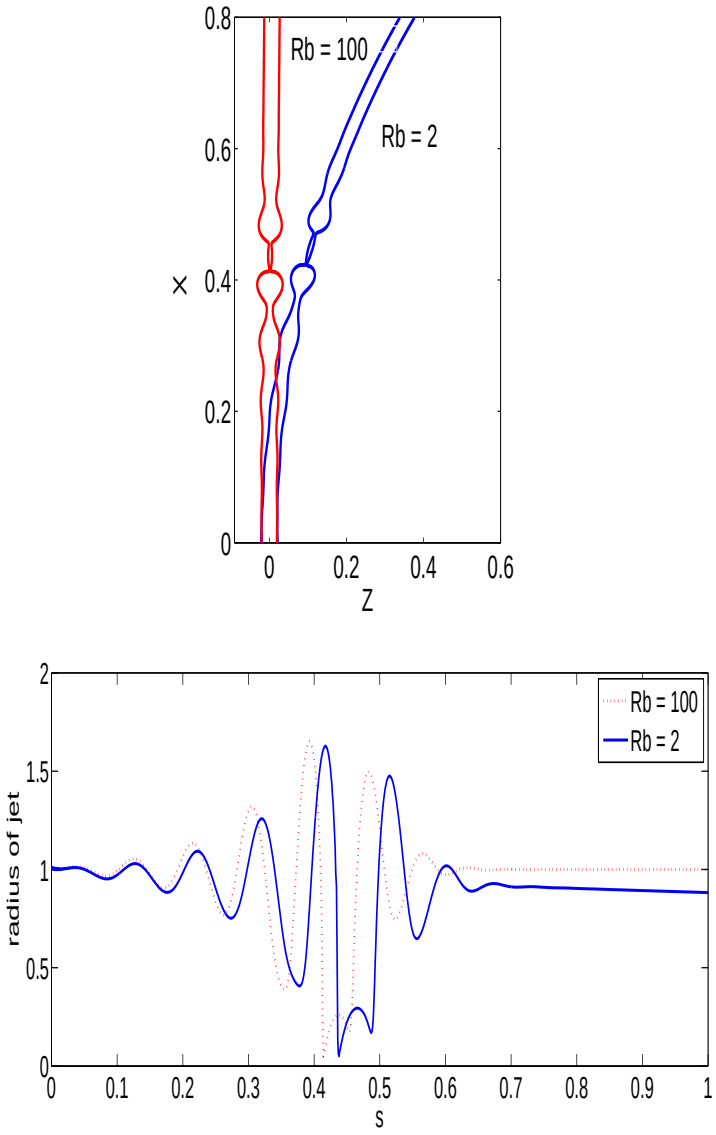

Figure 9.28: The profile of two different values of the Rossby number Rb, where the other parameters here are $Re = 2000, We = 10, k = 0.7, De = 20, \delta = 0.01\,, \zeta = 0.2, \beta = 0.5$ and $\alpha_s = 0.20$.

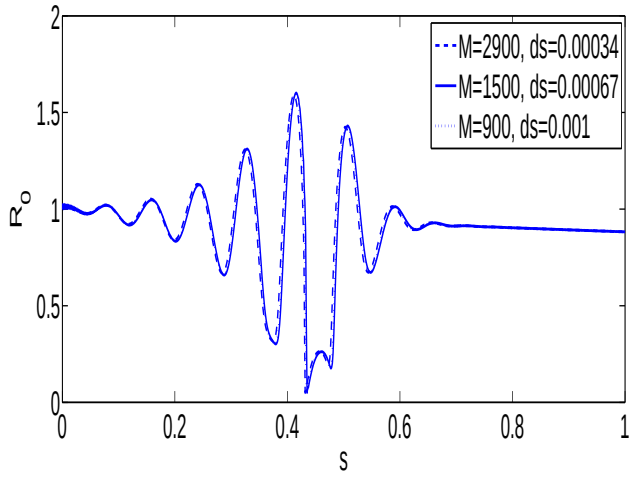

Figure 9.29: Accuracy check for various ds and various number of mesh points M, where $Re = 2000, We = 10, Rb = 1, k = 0.8, \zeta = 0.2, \beta = 0.5, De = 10, \delta = 0.01$, $\alpha_s = 0.2$, $dt = 5 \times 10^{-6}$ and the final time $t_f = 0.4728$.

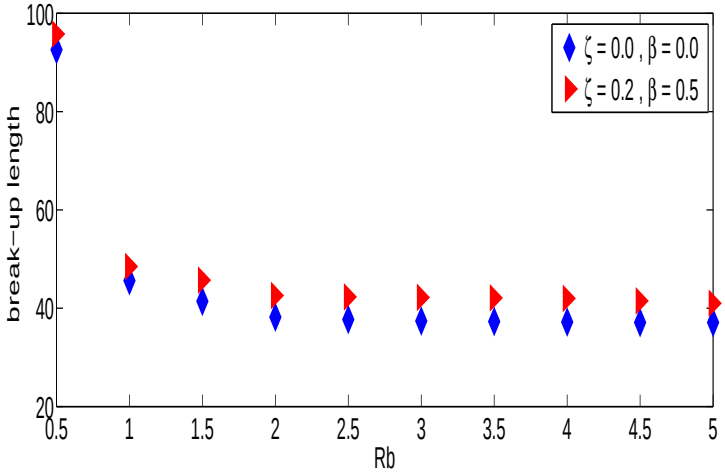

Figure 9.30: Graph showing break-up lengths for different values of the Rossby number Rb for viscoelastic rotating liquid jets with and without surfactants. The parameters here are $Re = 2000$, $We = 10$, $k = 0.8$, $De = 20$, $\delta = 0.01$ and $\alpha_s = 0.20$.

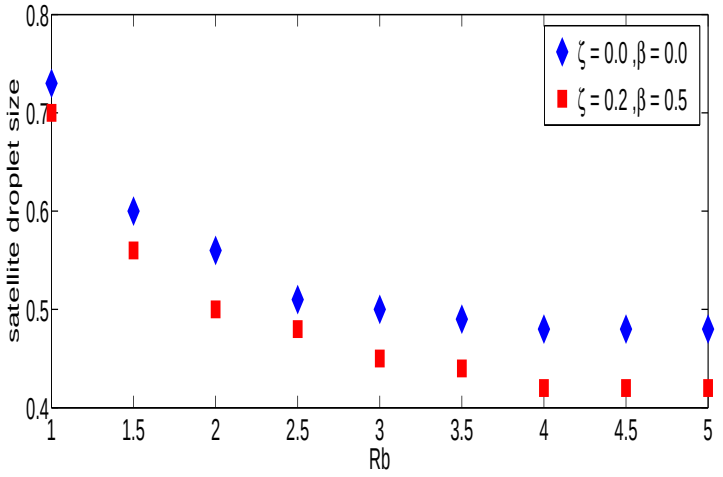

Figure 9.31: Satellite droplet sizes versus different rotation rates Rb for viscoelastic liquid curved jets with and without surfactants. The parameters here are $Re = 2000$, $We = 10$, $k = 0.8$, $De = 20$, $\delta = 0.01$ and $\alpha_s = 0.20$.

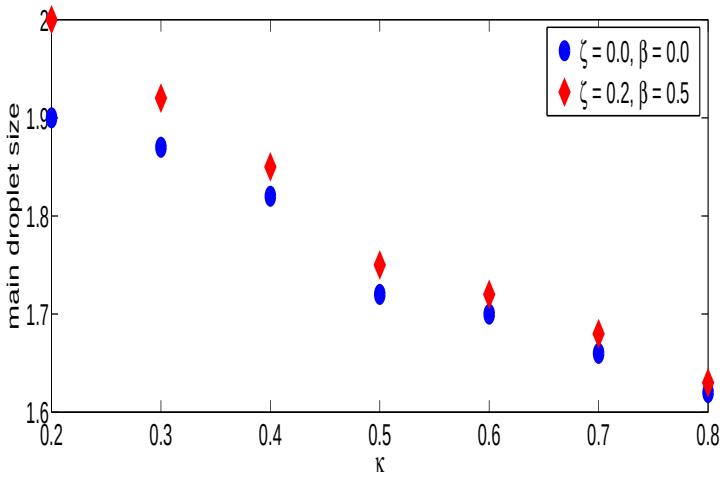

Figure 9.32: Graph showing main droplet sizes and the wavenumber of disturbances κ for viscoelastic liquid curved jets with and without surfactants. The parameters here are $Re = 2000$, $We = 10$, $Rb = 2$, $De = 20$, $\delta = 0.01$ and $\alpha_s = 0.20$.

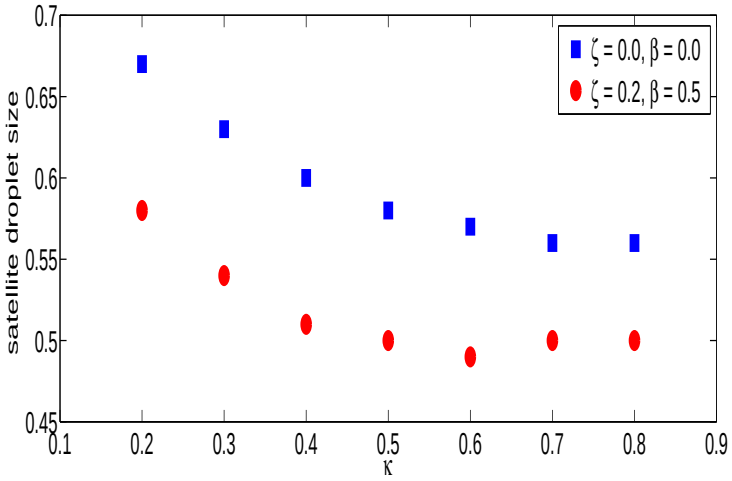

Figure 9.33: Graph showing satellite droplet sizes and the wavenumber of disturbances κ for viscoelastic liquid curved jets with and without surfactants. The parameters here are $Re = 2000$, $We = 10$, $Rb = 2$, $De = 20$, $\delta = 0.01$ and $\alpha_s = 0.20$.

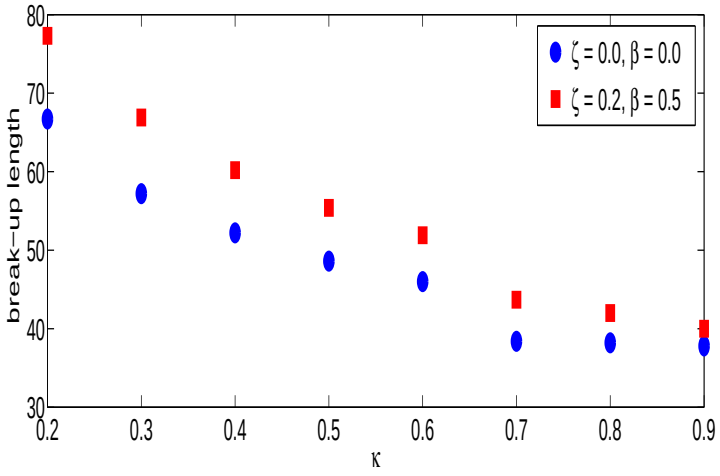

Figure 9.34: Break-up lengths versus the wavenumber of disturbances κ of viscoelastic liquid curved jets with and without surfactants. The parameters are $Re = 2000$, $We = 10$, $Rb = 2$, $De = 20$, $\delta = 0.01$ and $\alpha_s = 0.20$.

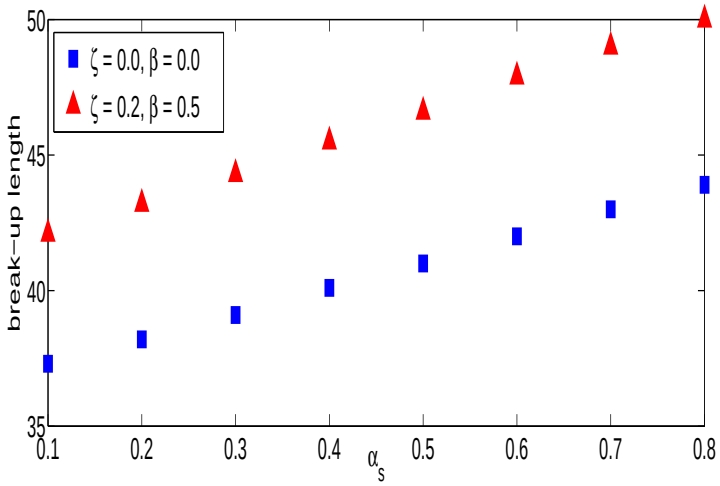

Figure 9.35: Break-up lengths versus the viscosity ratio α_s of viscoelastic liquid curved jets with and without surfactants. The parameters here are $Re = 2000$, $We = 10$, $Rb = 2$, $De = 20$ and $\delta = 0.01$.

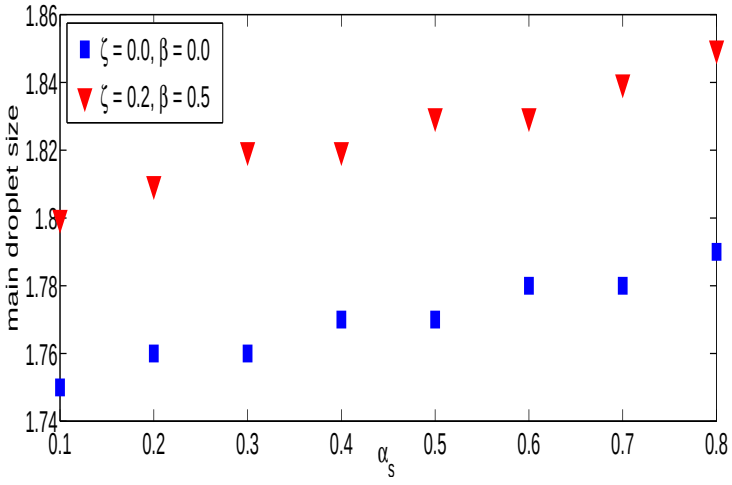

Figure 9.36: Graph showing the relationship between main droplet sizes and the viscosity ratio α_s with and without the effect of surfactants on viscoelastic liquid curved jets. The parameters here are $Re = 2000, We = 10, Rb = 2, k = 0.8, De = 20$ and $\delta = 0.01$.

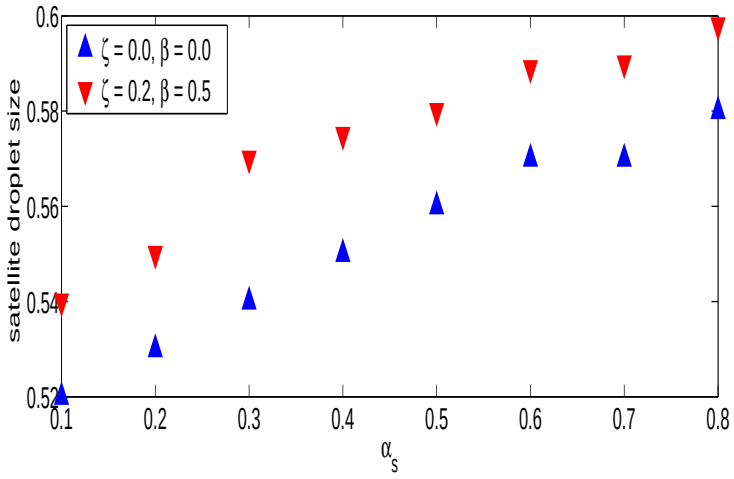

Figure 9.37: Graph showing the relationship between satellite droplet sizes and the viscosity ratio α_s with and without the effect of surfactants on viscoelastic liquid curved jets. The parameters here are $Re = 2000, We = 10, Rb = 2, k = 0.8, De = 20$ and $\delta = 0.01$.

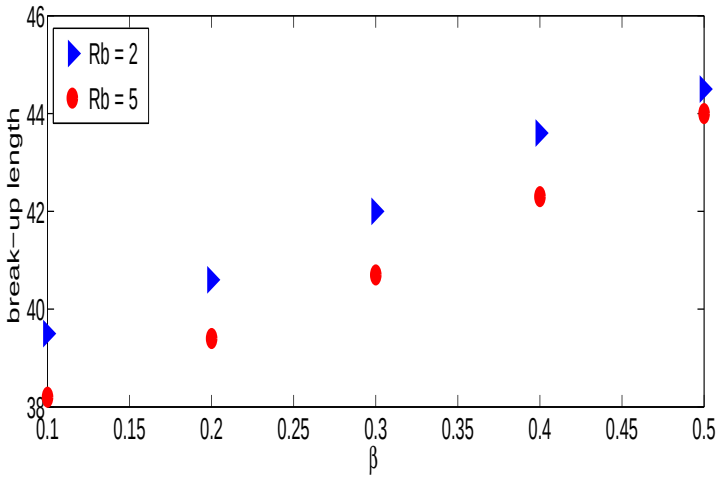

Figure 9.38: Graph showing the relationship between break-up lengths and the parameter β for two different values of rotation rates Rb with and without the effect of surfactants on viscoelastic liquid curved jets. The parameters here are $Re = 2000$, $We = 10$, $k = 0.8$, $De = 20$, $\zeta = 0.3$, $\delta = 0.01$ and $\alpha_s = 0.20$.

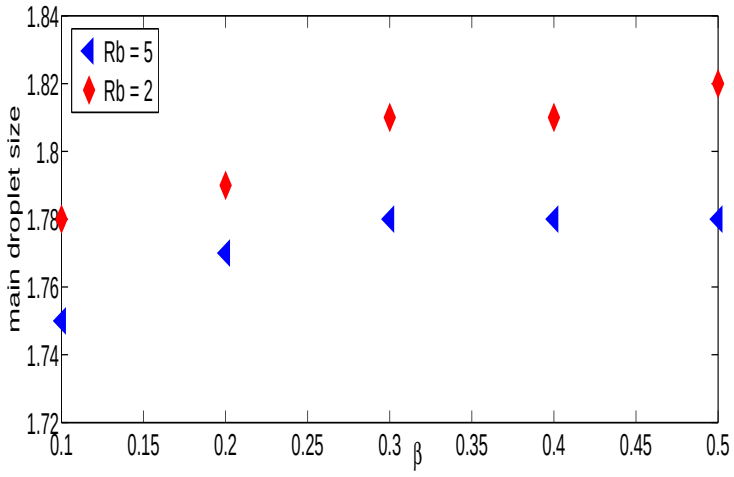

Figure 9.39: Graph showing the relationship between main droplet sizes versus the parameter β for two different values of rotation rates Rb with and without the effect of surfactants on viscoelastic liquid curved jets. The parameters here are $Re = 2000$, $We = 10$, $k = 0.8$, $De = 20$, $\zeta = 0.3$, $\delta = 0.01$ and $\alpha_s = 0.20$.

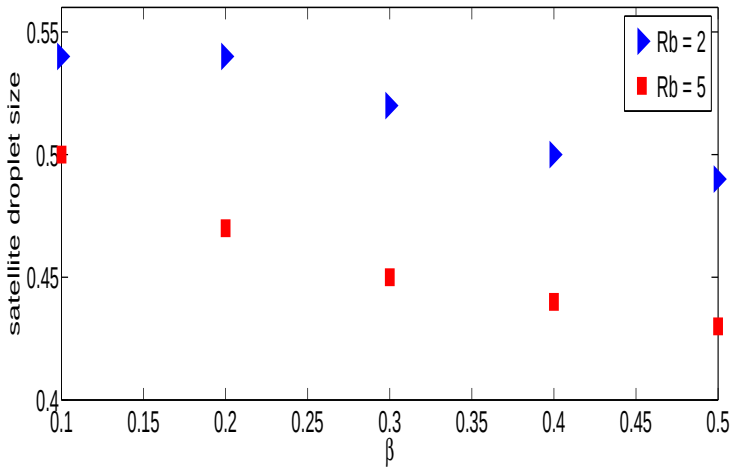

Figure 9.40: Graph showing the relationship between satellite droplet sizes versus the parameter β for two different values of rotation rates Rb with and without the effect of surfactants on viscoelastic liquid curved jets. The parameters here are $Re = 2000$, $We = 10$, $k = 0.8$, $De = 20$, $\zeta = 0.3$, $\delta = 0.01$ and $\alpha_s = 0.20$.

Chapter 10

Conclusion and Future Work

10.1 Conclusion

The purpose of this thesis is to extend the work done by Uddin (2007), by incorporating viscoelasticity into the model. There are many researchers who have studied the prilling process in different cases for both the Newtonian case (see Wallwork (2002a)) and for the non-Newtonian case (see Uddin (2007)). A theoretical analysis of a slender liquid jet which emerges from an orifice of a rotating container was considered.

In Chapters 1 and 2, we started by giving a general meaning of liquid jets and looked at the background of inviscid jets, viscous jets and viscoelastic liquid jets. Whilst looking at some experiments which were done by Wong (2004), and giving brief details of the theoretical work that was investigated by Wallwork (2002a) for the prilling process, we used similar equations to those used by Wallwork (2002a) and by Părău *et al*. (2007) but with extra terms, as discussed in Chapter 6.

There are many models for studying viscoelastic liquid jets, although some of them are extremely difficult to use for constitutive equations, especially for the prilling process, such as the Oldroyd 8-constant model, which was discussed in Chapter 4.

In Chapter 5 we examined the temporal linear instability of viscoelastic straight liquid jets falling under the influence of gravity. We solved the set of equations in two-dimensional models. We found the steady state solutions of this problem by using Newton's method. Moreover, we derived the dispersion relation of viscoelastic liquid jets. From this dispersion relation, the findings were:

• When the Froude number F decreases ($i.e$ meaning gravity is increased (see Figs. 5.22 and 5.23 respectively)), the wavenumber of the most unstable mode and growth rate increase.

• Decreasing the Weber number We and the viscosity ratio α_s leads to an increase in the growth rate (see Figs. 5.14 and 5.19 respectively).

• Viscoelastic liquid jets exhibited a larger growth rate than viscous liquid jets and a slower growth rate than an inviscid liquid jet (see Fig. 5.24), which agrees with the same finding reported by Goldin *et al.* (1969).

In Chapter 6, we used the Maxwell upper-convected model (Oldroyd-B) for investigating the temporal instability of viscoelastic liquid curved jets. The linear instability gives a better understanding for predicting main droplet sizes, so we used an asymptotic analysis at leading order to derive the governing equations for this problem. We also used the normal model to derive the dispersion relation for studying linear stability theory and found the growth rate and wavenumber of the most unstable mode along the jet. We also made a comparison between the dispersion relation of viscoelastic jets, Newtonian and inviscid liquid jets as done by Wallwork (2002). He considered steady state solutions, obtained from solving a nonlinear set of equations using the Runge-Kutta method, and found that the radius along the jet decreases against the arc-length. The trajectory was plotted on the $X-Z$ plane for different values of the Rossby and Weber numbers, and it was observed that when we decrease the Rossby number (meaning high rotation rates) the liquid curves more, which was seen in Fig. 6.1, confirming the results of Wallwork (2002a).

The growth rate and the wavenumber of the most unstable mode were plotted against the arc-length for different values of the non-dimensional parameter Reynolds number, the Weber number, the Deborah number and the Rossby number, and the findings were:

• Increasing the Reynolds number leads to an increase in the growth rate of viscoelastic liquid jets.

• Increasing the Weber number and the Deborah number decreases the growth of viscoelastic liquid jets.

• When the Rossby number is decreased, the growth rate and the wavenumber of the most unstable mode is increased.

• When the viscosity ratio is increased, the growth rate and the wavenumber of the most unstable mode is decreased.

In Chapter 7, we examined break-up lengths and main and satellite droplet sizes of viscoelastic rotating liquid jets by using a finite difference scheme based on the two-step Lax-Wendroff method. We found that decreasing the Reynolds number, which corresponds to high viscosity, leads to an increase in the break-up length (see Fig.7.11). Moreover, increasing the viscosity ratio α_s, which is the total of the solvent and polymeric liquid, was found to increase the break-up length (see Fig. 7.12). In addition, we found that the non-Newtonian (viscoelastic) liquid jet breaks up earlier than Newtonian liquid jets and later than inviscid jets (see Fig. 7.15), which agrees with the linear instability which is found in Chapter 5. We also noticed that when we increase rotation rates, this leads to an increase in main droplet sizes. Furthermore, we found that when we increase the Deborah number De, break-up lengths and main and satellite droplet sizes increase.

In Chapter 8, we included the influence of gravity (the Froude number) on viscoelastic liquid curved jets by considering the velocity of the can which was very slow, so the same analysis, which was presented in Chapter 6, followed. Many cases are considered in this chapter, such as those in which the Froude number is variable and the Rossby number is

constant and vice versa, where the Froude number and the Rossby number vary and the Froude number is variable but without rotation. It can be noticed from the last cases that the Froude number has affected the jet and makes it more stable. These results are the same as demonstrated in Chapter 6, without including gravity, and support the findings that were obtained by Wallwork (2002a). The trajectory for the liquid curved jet was also found in three dimensions (X, Y, Z).

In Chapter 9, we extended Chapter 6 by including surfactants. In this chapter, we investigated the linear and nonlinear instability of viscoelastic rot instability of viscoelastic rotating liquid jets by adding surfactants. We found a number of interesting findings, which are:

• Increasing the initial surfactant concentration ζ and the effectiveness of surfactant β lead the jet to coil slowly.

• When we increase the initial surfactant concentration ζ, the growth rate of viscoelastic rotating liquid jets decreases (see Fig. 9.10).

• Increasing the effectiveness of surfactants β was found to decrease the maximum growth rate and the most unstable mode along the jet (see Figs. 9.16 and 9.17 respectively).

These results agree with the same finding reported by Uddin (2007) in the case of non-Newtonian liquid curved jets with surfactants. In the presence of viscoelastic rotating liquid jets with adding surfactants, there are two extra parameters which are the Deborah number and the viscosity ratio. Therefore, we found that:

• When we increase the Deborah number, the growth rate decreases.

• Increasing the viscosity ratio leads to an increase in break-up lengths and main and satellite droplet sizes.

10.2 Future Work

Viscoelastic liquid jets have a great number of potential applications, due to the many practical and engineering processes in which they are used. Therefore, there are many constitutive equations (as mentioned in Chapter 4) which we can use to study this subject.

10.2.1 Prilling Processes

In Chapter 6, we investigated the temporal instability of viscoelastic curved jets by using the Maxwell Upper Convected (MUC) model. However, in future, we can examine the same problem by using Giesekus's model and we can make a comparison between these two models.

Decent *et al.* (2009) investigated the temporal and spatial instability (the second being more realistic) for Newtonian liquid jets, so that it is possible to examine the spatial instability for viscoelastic curved jets. We can also extend Chapter 9 by studying the effects of gravity on the instability of viscoelastic liquid rotating jets with surfactants.

In prilling processes, an ambient gas can affect the jet break-up and therefore this is another possible extension to investigate the effect of an ambient gas on viscoelastic straight and curved jets.

10.2.2 Electrospinning Processes

This phenomenon has been considerably investigated in the last two decades owing to its potential applications, such as producing ink jet printers and ultra-fine nanofibers. Viscoelasticity plays an important role in this process, because a liquid fiber has high molecular polymer solutions, and viscoelasticity affects the instability and break-up of liquid jets for this reason.

There are few articles in this subject in terms of mathematical analysis (see Hohman *et al.* (2001), Feng (2003) and Caroll and Joo(2008)) due to the complexity of this problem, which consists of coupling between the elastic field and viscoelastic liquid jets. For instance, if we look at Caroll and Joo (2003), we can see the same contributions made by the equations of viscoelastic liquid jets as we got in this thesis, but without the rotational force. Therefore, we can include the rotational force to study the instability of electrospinning of viscoelastic liquid jets and we can also investigate the non-linear instability to see the effects of the electrical force on break-up lengths and drop formation. Caroll and Joo (2003) used the Oldroyd-B model to examine the linear instability of electrically viscoelastic jets, so we can use another model, which is the Giesekus model, to investigate the linear instability of a straight and a curved electrically charged viscoelastic liquid jet. Furthermore, Hohmann *et al.* (2001) and Caroll and Joo (2003) found that when the electrical conductivity is very low, the instability occurs at low wavenumber. However, we can consider this linear instability of electrical charged viscoelastic curved jets at a high electrical conductivity. We can also examine the instability of curved electrically charged viscoelastic jets with surfactant. In this project we can find drop formations and how the electric field affects the trajectory of a liquid jet, main and satellite droplets and break-up length.

10.2.3 Compound Liquid Jets

Uddin (2007) examined the linear and nonlinear instability of inviscid compound jets, it would be worth investigating the instability of compound rotating jets. We can also find the drop formation and discuss the effect of the rotation rates on the break-up the inner and outer jet. In addition to this, my colleague Faheem Afzaal and I are to submit an article to the Journal of Physics of Fluids relating to the effects of an ambient gas on the temporal instability of inviscid compound jets falling under gravity. Furthermore,

we can extend this article to investigate the linear instability of Newtonian compound liquid jets falling under the influence of gravity with an ambient gas. The last point to make is that some experiments relating to viscoelastic liquid jets could be conducted in the department of Chemical Engineering in the King Abdullah University of Science and Technology.

Bibliography

[1] Anshus, B., E., 1973, The Effect of Surfactants on the Breakup of Cylinders and Jets. Journal of Colloid and Interface Science, 43, 113-121.

[2] Ardekani, A. M., Sharma, V., and Mckinley, G. H., 2010, Dynamics of bead formation, filament thinning and breakup in weakly viscoelastic jets. J. Fluid Mech. 665, 46-56

[3] Ashgriz, N. and Mashayek, F., 1995. Temporal analysis of capillary jet breakup. J. Fluid Mech. 291, 163-190.

[4] Batchelor, G. K., 1967, An Introduction to Fluid Dynamics. Cambridge University Press.

[5] Bird, R. B., and Armstrong, A., 1987, Dynamics of polymeric liquids: Vol 1, Fluid Mechanics, Wiley, Nwe York.

[6] Blyth, M., G., and Pozrikidis, C., 2004, Evolution Equation for the Surface Concentration of an Insoluble Surfactant; Application to the Stability of an Elongating Thread and a Stretched Interface. Theoret. Comput. Fluid Dynamics. 17, 147-164.

[7] Bousfield, D. W., Marrucci, G., and Denn, M. M., 1986, Nonlinear analysis of the surface tension driven breakup of viscoelastic filaments. Journal of Non-Newtonian Fluid Mechanics, 21, 79-97.

[8] Brenn, G., Liu, Z., and Durst, F., 2000, Linear analysis of the temporal instability of axisymmetrical non-Newtonian liquid jets, International Journal of Multiphase Flow, 26, 1621-1644

[9] Brenner, M., P., Eggers, J., Joseph, K., Nagel., S., R., and Shi, X., D., 1997, Breakdown of scaling in droplet fission at high Reynolds number. Phys. Fluids, 9, 1573-1590.

[10] Chang, Hsueh-Chia, Demekhin, E. A., and Kalaiden, E., 1999, Iterated stretching of viscoelastic jets, Phys. Fluids, 11,1717-1737

[11] Chaudhary, K. C., and Maxworthy, T., 1980, The nonlinear capillary instability of a liquid jet. Part 2. Experiments on jet behaviour before droplet formation. J. Fluid Mech. 96, 275-286.

[12] Chaudhary, K. C., and Maxworthy, T., 1980, The nonlinear capillary instability of a liquid jet. Part 3. Experiments on satellite drop formation and control. J. Fluid Mech. 96, 287-297.

[13] Cheong, B. S., Howes, T., 2004, Capillary jet instability under influence of gravity, Chemmical Engineering Science, 59, 2145-2157

[14] Chhabra, R. P., and Richardson, J. F., 2008, Non-Newtonian flow and applied rheology. Elsevier Ltd.

[15] Chilcott, M. D. and Rallison, J. M., 1988, Creeping flow of dilute polymer solutions past cylinders and spheres. J. Non-Newtonian Fluid Mech. 29:381-432.

[16] Clasen, C., Eggers, J., Fonlelos, M. A., Li, j., and Mckinley, G. H., 2006, The beads-on-string structure of viscoelastic threads. J. Fluid Mech., 556, 283-308

[17] Cooper-White, J. J., Fagan, J. E., Tirtaatmadja, V., Lastert, D. R., and Boger, D. V., 2002, Drop formation dynamics of constant low-viscosity, elastic fluids, J. Non-Newtonian fluid Mech., 106,29-59

[18] Craster, R., V., Matar, O., K., and Papageorgiou, D., T., 2002, Pinch off and satellite formation in surfactant covered viscous thread. Phys. Fluids, 14, 1364-1376.

[19] Davidson, M. R., Harvie, J. E., and Cooper-White, J. J., 2006, Simulation of pendant drop formation of a viscoelastic liquid, Korea-Australia Rheology Journal, 18, (2), 41-49

[20] Decent, S. P., King, A. C. and Wallwork, I. M., 2002, Free jets spun from a prilling tower, Journal of Engineering Mathematics, 42, 265-282

[21] Decent, S. P., King, A. C., Simmons, M. H., Părău, E. I., Wong, D. C. Y., Wallwork, I. M., Gurney, C., and Uddin, J., 2009, The trajectory and stability of a spiralling liquid jet: Part II. Viscous Theory, Appl. Math. Modelling, 33, (12), 4283-4302

[22] DuChateau, P., and Zachmann, D., 1989, Applied Partial Differential Equations, Harper & Row Publishers, New York.

[23] Eggers, J., and Dupont, T. F., 1994. Drop formation in a one-dimensional approximation of the Navier Stokes equation. J. Fluid Mech., 262, 205221.

[24] Eggers, J., 1997. Nonlinear dynamics and breakup of free surface flows. Rev. Mod. Physis, 69, (3), 865-929.

[25] Eggers, J., and Villermaux, E., 2008, Physics of liquid jets. Rep. Prog. Phys, 71, 036601(79pp).

[26] Fontelos, M. A., 2003, Break-up and no break-up in a family for the evolution of viscoelastic jets, Z. angew. Math. Phys.,54,84-111

[27] Fontelos, M. A., and Li, J., 2004, On the evolution and rupture of filaments in Giesekus and FENE models, J. Non-Newtonian Fluid Mech., 118, 1-16

[28] Funda, T., Joseph, D. D., 2003, Viscoelastic potential flow analysis of capillary instability, J. Non-Newtonian Fluid Mech., 111, 87-105

[29] Giesekus, H., 1982, A simple constitutive equation for polymer fluids based on the concept of deformation-dependant tensorial mobility, J. Non-Newtonian Fluid Mech., 11, 69-109

[30] Goldin, M., Yerushalmi, J., Pfeffer, R., and Shinner, R., 1969, Breakup of a viscoelastic fluid. J. Fluid Mech. 38, 689-711.

[31] Goren, S. L., and Gottlieb, M. 1982, Surface-tension driven breakup of viscoelastic liquid threads. J. Fluid Mech. 120, 245-266.

[32] Grant, R. P., and Middleman, S., 1965, Newtonian jet stability. A. I. Ch. E. Journal, 2, 669.

[33] Gunawan, A., Y., Molenaar, J., and Van de Van, A. A. F., 2005, Temporal stability of a viscoelastic immersed thread in a confined region, J. Non-Newtonian Fluid Mech., 126, 83-92

[34] Hansen, S., Peters, G., W., M. and Meijer, H., E., H., 1999, The effect of surfactant on the stability of a fluid filament embedded in a viscous fluid, J. Fluid Mech., 382, 331-349.

[35] Hawkins, V. L., 2010. Curved liquid jets : effect of scale, rheology and forced disturbances. PhD thesis, University of Birmingham.

[36] Hirsch, C., 1988, Numerical computation of internal and external flows; volume 2, computational methods for inviscid and viscous flows, John Wiley & Sons.

[37] Hohman, M. M., Shin, M., Rutledge, G. abd Brenner, M. P., 1984, Electrospinning and electrically forced jets. II. Application. Phys. Fluids, 13, 8, 2221-2236.

[38] Hohman, M. M., Rutledge, M. S., Brenner, M. P., 2001, Electrospinning and electrically forced jets : I. Stability theory, Phys. Fluids, 13, 2201-2220.

[39] Hohman, M. M., Rutledge, M. S., Brenner, M. P., 2001, Electrospinning and electrically forced jets : II. Applications, Phys. Fluids, 13, 2221-2236.

[40] Kang, F., and Chen, K. P., 1995, Nonlinear elastic instability of gravity-driven flow of a thin viscoelastic film down an inclined plane. J. Non-Newtonian Fluid Mech. 57, 243-252.

[41] Keller, J. B., Rubinow, S. I., and Tu, Y. O., 1973, Spatial instability of a jet, Phys. Fluids, 16, 2052-2055

[42] Larson, R. G., 1988. Constitutive equation for polymer melts and solutions. AT and T Bell Laboratories, Incorporate.

[43] Larson, R. G., 1992, Instabilities in viscoelastic flows, Rheol., Acta,31

[44] Lee, H. C., 1974, Drop formation in a liquid jet. IBM J. Res. Dev. 18,364.

[45] Li, J., and Fontelos, M. A., 2003, Drop dynamics on the beads-on string structure for viscoelastic jets : a numerical study, Phys. Fluids, 15, (4), p. 922

[46] Li, F., Yin, Xie-Yuan, Yin, Xie-Zhen, 2011, Axisymmetric and non-axisymmetric instability of an electrically charged viscoelastic liquid jets, J. Non-Newtonian Fluid Mech., 166, 1024-1032

[47] Lin, S. P., 2003, Breakup of Liquid Sheets and Jets, Cambridge University Press, United Kingdom.

[48] Lin, S. P., and Reitz, R. D., 1998. Drop and spray formation from a liquid jet. Annu. Rev. Fluid Mech. 30, 85-105.

[49] Liu, Z., and Liu, Z., 2008, Instability of a viscoelastic liquid jet with axisymmetric and asymmetric disturbance, International Journal of Multiphase Flow, 34, 42-60

[50] Magda, J. J., and Larson, R. G., 1988, Atransition occurring in ideal elastic liquids during shear flow, J. Non-Newtonian Fluid Mech., 30,1-19

[51] Malkin, A. Y., 2008, Surface Instabilities, Colloid Journal, 70, (6), 673-689

[52] Middleman, S., 1965, Stability of a viscoelastic jet, Chem. Eng. Sci. 20, 1037-1040.

[53] Middleman, S., 1995, Modeling Axisymmetric flows; dynamics of films, jets and drops, Academic Press.

[54] Milliken, W., J., Stone, H., A., and Leal, L. G., 1993, The effect of surfactant on the transient motion of Newtonian drops. Phys. Fluids, 5, 69-79.

[55] Milliken, W., J., and Leal., G., 1994, The Influence of Surfactant on the Deformation and Breakup of a Viscous Drop : The Effect of Surfactant Solubility. Journal of Colloid and Interface Science, 166, 275-285.

[56] Morrison, F. A., 2001, Understanding Rhelogy, Oxford University Press.

[57] Morrison, N. F., Harlen, O. G. 2010, Viscoelasticity in inkjet printing, Rheol., Acta, 49, 619-632

[58] Oldroyd, J. G., 1950, On the formation of rheological equations of state. Proc. Roy. Soc. A200, 523-541.

[59] Papageorgiou, D. T., 1995, On the breakup of viscous liquid threads, Phys. Fluids, 7, 1529

[60] Părău, E. I., Decent, S. P., King, A. C., Simmons, M. J. H., Wong, D. C. Y., 2006, Nonlinear travelling waves on a spiralling liquid jet, Wave Motion, 43, 599-613.

[61] Părău, E. I., Decent, S. P., Simmons, M. J. H., Wong, D. C. Y. and King, A. C., 2007, Nonlinear viscous liquid jets from a rotating orifice, J. Of Eng. Maths., 57, 159-179

[62] Partridge, L., 2006, An experimental and theoretical investigation into the break-up of curved liquid jets in the prilling process. PhD Thesis, University of Birmignham.

[63] Pimbley, W. T., and Lee., H. C., 1977, Satellite droplet formation in a liquid jet. IBM J. Res. Dev. 21, 21-25.

[64] Plateau, J., 1873, Statique experimentale et theortique des liquides soumis aux seules forces moleculaires. Gauthier Villars, Paris II, 319.

[65] Press, W. H., Teukolsky, S. A., Vetterling, W. T., and Flannery, B. P. 2001, Numerical Recipes in Fortran 77: The art if scientific computing. Cambridge University Press.

[66] Rayleigh, W. S., 1878, On the instability of jets, Proc. Lond. Math. Soc 10,4.

[67] Renardy, M., 1995, A numerical study of the asymptotic evolution and breakup of Newtonian and viscoelastic jets, J. Non-Newtonian Fluid Mech., 59, 267-282

[68] Renardy, M., 2008, Stability of viscoelastic shear flows in the limit of high Weissenberg and Reynolds numbers, J. Non-Newtonian Fluid Mech., 155, 124-129

[69] Roy, A., Mahadevan, L., and Thiffeault, J., 2006, Fall and Rise of a viscoelastic filament, Journal of Fluid Mech., 563, pp. 283-292

[70] Rutland, D. F., and Jameson, G. J., 1971, A non-linear effect in the capillary instability of liquid jets. J. Fluid Mech. 46, 267-271.

[71] Sauter, U., S. & Buggisch, H., W., 2005, Stability of initially slow viscous jets driven by gravity. J. Fluid Mech. 533, 237-257.

[72] Savart, F., 1833, Annal, Chim. 53 337.

[73] Stone, H., A., Bentley, B., J., and Leal, L., G., 1986, An experimental study of transient effects in the breakup of viscous drops. J . Fluid Mech. 173, 131-158. Press, W., H., Teukolsky, S., A., Vetterling, W., T., and Flannery, B., P. 2001, Numerical Recipes in Fortran 77: The art if scientific computing, Cambridge University Press.

[74] Stone, H., A., and Leal, L., G., 1990, The effects of surfactants on drop deformation and breakup. J. Fluid Mech., 220, 161-186.

[75] Schummer, P., and Thelen, H. G., 1988, Break-up of a viscoelastic liquid jets, Rheol., Acta, 27, 39-43

[76] Timmermans, M., E., and Lister, J., R., 2002, The effect of surfactant on the stability of a liquid thread. J. Fluid Mech., 459, 289-306.

[77] Tomotika, S., 1935, On the instability of a cylindrical thread of a viscous liquid surrounded by another viscous fluid. Proceedings of the Royal Society of London Series A, Mathematical and Physical Science, 150 (870) : 322-337.

[78] Tricot, Y. M., 1997, Surfactants: static and dynamic surface tension. In Liquid Film Coating (ed. S. F. Kistler & P. M. Schweizer), pp. 100-136. Chapman & Hall.

[79] Uddin, J., 2007. An investigation into methods to control breakup and droplet formation in single and compound liquid jets. PhD thesis, University of Birmingham.

[80] Uddin, J., Decent, S. P., and Simmons. M. J. H., 2006, The instability of shear thinning and shear thickening spiralling liquid jets: Linear theory. ASME J. of Fluids Eng., 128, 968975.

[81] Uddin, J., Decent, S. P., and Simmons. M. J. H., 2008a, Non-linear waves along rotating non-Newtonian liquid jets. Int. J. Eng. Sci, 46.

[82] Uddin, J. Decent, S. P., and Simmons, M. J. H., 2008b, The effect of surfactants on the instability of a rotating liquid jet. Fluid Dyn. Res., 40, 827851.

[83] Uddin, J., and Decent, S. P., 2010, Instability of non-Newtonian liquid jets curved by gravity. Mathematics in industry, 15, 597-602.

[84] Uddin, J., and Decent, S. P., 2012, Drop formation in rotating non-Newtonian jets with surfactants. IMA Journal of Applied Mathematics, 77, 86-96.

[85] Walker, J. R., 2012, The effect of surfactants on the breakup of an axisymmetric laminar liquid jet. Ph. D Thesis, University of Maryland, Maryland USA.

[86] Wallwork, I. M., 2002a, The trajectory and stability of a spiralling liquid jet, Ph.D. Thesis, University of Birmingham, Birmingham.

[87] Wallwork, I. M., Decent, S.P., King, A. C. and Schulkes, R. M. S., 2002b, The trajectory and stability of a spiralling liquid jet. Part 1, Inviscid Theory, J. Fluid Mech., 459,43-65.

[88] Weber, C., 1931, Zum Zerfall eines Flussigkeitsstrahles. Z. Angew. Math. Mech, 11, 136-154.

[89] Whitaker, S., 1976, Studies of the Drop-Weight Method for Surfactant Solutions III. Drop Stability, the Effect of Surfactants on the Stability of Column of Liquid. Journal of Colloid and Interface Science, 54, 2.

[90] Wong, D. C. Y., Simmons, M. J. H., Decent, S. P., Parau, E. I. and King, A. C., 2004, Break-up dynamics and drop sizes distributions created from spiralling liquid jets, International Journal of Multiphase Flow, 30, 5, 499-520.

[91] Yamaguchi, H., 2010, Engineering Fluid Mechanics, Springer.

[92] Yarin, L. A., 1993, Free liquid jets and films : hydrodynamics and rheology. John Wiley and Sons Inc.

[93] Yuen, M. C., 1968, Non-linear capillary instability of a liquid jet. J. Fluid Mech., 33, 151163.

[94] Zhang, X., Padgett, R. S. & Basaran, O. A.,1996, Nonlinear deformation and breakup of stretching liquid bridges. J. Fluid Mech. 329, 207.

[95] Zhang, Y. L., Matar, O. K., Craster, R. V., 2002, Surfactant spreading on a thin weakly viscoelastic film. J. Non-Newtonian Fluid Mech., 105, 53-78.